Platinum-group elements in the ultrabasic rocks of the Braganca and Morais massifs, northern Portugal

Thesis

Platinum-Group Elements in the ultrabasic rocks of the Bragança and Morais massifs, northern Portugal

A thesis presented for the degree of Doctor of Philosophy

by

John Charles Bridges

B.Sc. (hons.) University of Edinburgh 1988

Department of Earth Sciences

The Open University

February 1992

PAGINATED
BLANK PAGES
ARE SCANNED AS
FOUND IN
ORIGINAL
THESIS

NO
INFORMATION
MISSING

CONTAINS

PULLOUTS

Platinum-Group Elements in the ultrabasic rocks of the Bragança and Morais massifs, northern Portugal

A thesis presented for the degree of Doctor of Philosophy

by

John Charles Bridges
B.Sc. (hons.) University of Edinburgh 1988

Department of Earth Sciences
The Open University

February 1992

Frontispiece

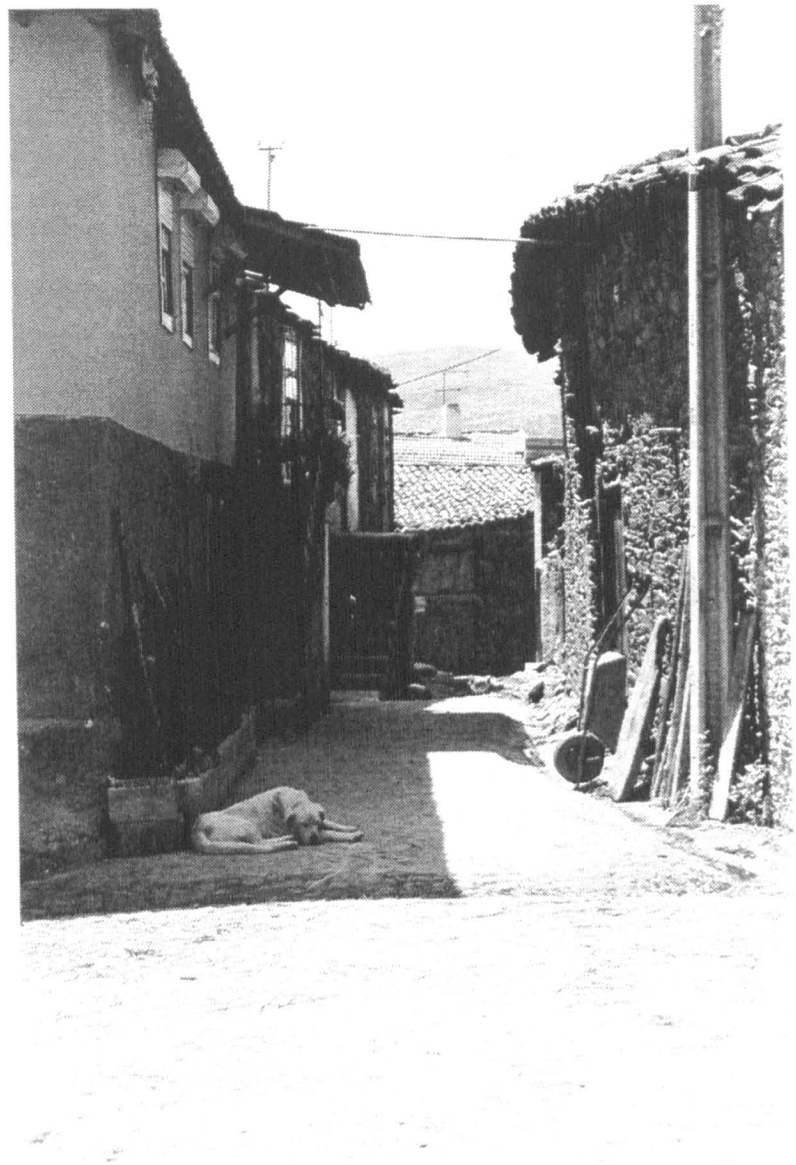

One of the villages in Trás-os-Montes ('behind the hills') northern Portugal.

HIGHER DEGREES OFFICE

LIBRARY AUTHORISATION FORM

STUDENT: John Bridges SERIAL NO: _____

DEGREE: PhD

TITLE OF THESIS: Platinum-Group Elements in the ultrabasic rocks of the Bragança & Morais Massifs, N. Portugal

I confirm that I am willing that my thesis be made available to readers and maybe photocopied, subject to the discretion of the Librarian.

SIGNED: John Bridges DATE: 9-10-92

Abstract

The ultrabasic rocks studied in this thesis are located in the Upper Allochthonous Thrust Complex nappes of the Bragança and Morais massifs, Trás-os-Montes, N. Portugal. They are relicts of residual mantle and cumulates formed at a destructive continental margin. In the Bragança massif, the ultrabasic rocks consist mainly of a harzburgite formation, which is residual mantle. This formation contains lenses of a separate chromitite-bearing dunite formation. The Morais massif assemblage, at an equivalent structural level, is made up of peridotite and gabbroic/troctolitic cumulates.

The chromitite-bearing dunite formation crystallised within small magmatic masses. This chromite crystallisation acted to fractionate the associated Platinum-Group Element (PGE) assemblage. Os, Ir and Ru were incorporated as laurite and irarsite minerals during chromite grain crystallisation, and are located in textural positions from the centres to the margins of the chromite grains. In contrast Pt-bearing arsenides and sulpharsenides started crystallising after the Os, Ir, Ru group, and are only located at the margins of or in between chromite grains. More fractionated assemblages show positive slopes on chondrite normalised whole rock PGE plots. Pd is not directly associated with this fractionation. Instead its mineralisation is associated with that of the base-metal sulphide. Serpentinisation has caused recrystallisation of much original pentlandite to heazlewoodite and magnetite. At the same time Pd-bearing alloys were created, mostly adjacent to sulphide grains with the source of the Pd being in solid solution within the base-metal sulphide.

Several factors suggest that the chromite mineralisation was derived from melts of boninitic affinity. The relatively high Pd/Cu ratios calculated for a silicate melt from which the chromite crystallised are consistent with this. The composition of the chromite grains, having 100Cr/(Cr+Al) ratios clustering around 75, is typical of boninitic magmas. In addition the refractory composition of the harzburgite formation, and the high tenors of Pd within sulphide, show that it was a possible source for such boninitic melts. The chromite mineralisation took place down to depths of 30km within the mantle wedge of a destructive continental margin.

Acknowledgements

This thesis was funded by a European Community Raw Materials Programme Grant. My supervisors were Dr Hazel Prichard and Dr Chris Neary. I would like to thank them for giving encouragement throughout the work. I am also grateful to my supervisors and Professor Ian Gass for commenting on earlier versions of this thesis. In addition, the postmarks on my returned thesis drafts were never lacking in variety: The Grand Hotel Taiwan, Kuwait City, Brazil *etc.*

The Portuguese team: Professor Anthonio Ribeiro, Professor Fernando Barriga, Professor José Munhá, Dr Luisa Ribeiro, Dr Eurico Pereira, Carlos Mereiles, Fernando Marques and Juan Pontes, all of who I have had the pleasure of working with as part of this research programme, have been an invaluable source of knowledge about the Bragança and Morais massifs. In particular I am indebted to Carlos Mereiles for showing me around Bragança as well as giving logistical support. I keep happy memories of field work in Portugal, Shetland and Cornwall with the Portuguese group and Jon Maynard and Richard Lord. I would also like to thank Phil Gravestock for taking me around Cabo Ortegal.

At the O.U. thanks are due to Dr Andy Tindle for microprobe and 'Mac' instruction, Naomi Williams for instruction on the SEM and help in setting it up for quantitative mineral analyses, Dr Pete Webb and John Watson for XRF analyses, Ian Chaplin, Kay Chambers and Brian Ellis for thin sections and John Taylor for cartographic help.

The E.C. Research Programme

The funding for the research presented in this thesis was obtained from an E.C. Raw Materials Programme grant (contract no. MA1M-075-C). This funding was given principally in order to investigate PGE and chromite mineralisation within the Bragança and Morais massifs of northern Portugal. The research was based on collaboration between Portuguese geologists at Lisbon University (Professor Anthonio Ribeiro, Professor Fernando Barriga, Professor José Munhá and Fernando Marques); together with the Serviços Geologicos de Portugal (Dr Luisa Ribeiro, Carlos Mereiles and Dr Eurico Pereira) and British geologists at the Open University (Dr Hazel Prichard, Dr Chris Neary and this author). The research was co-ordinated by Dr Hazel Prichard. As part of this research effort, the Bragança massif has been remapped at a 1:25000 scale by Carlos Mereiles, with special emphasis on the distribution of the disused chromite mines. Dr Eurico Pereira remapped the Morais massif. Detailed structural work on the Bragança massif has been carried out by Fernando Marques as part of a PhD thesis (in preparation) and a completed MSc thesis (Marques 1989). Metamorphic and geochemical studies on a range of mafic lithologies within the Bragança and Morais massifs were undertaken by Professor José Munhá and Dr Luisa Ribeiro. Professor Anthonio Ribeiro and Professor Fernando Barriga co-ordinated the Portuguese research and compiled the Portuguese contribution to the final report. The work at the Open University consists of research into the PGE and chromite mineralisation, detailed mapping of parts of the ultrabasic outcrop and petrographic and geochemical studies of the ultrabasic assemblage carried out by this author, with stream sediment sampling and drill core analyses undertaken by Dr Hazel Prichard. The results of combined Portuguese and British research are presented in a final report for the European Commission (Prichard *et al.* 1991).

Contents

List of figures

Introduction

Chapter 1

Chapter 2

Chapter 3

Chapter 4

Figures

Chapter 5

Chapter 6

Chapter 7

Appendix 2 The Scanning electron microscope

Figures

List of Tables

Introduction

Chapter 1

Chapter 2

Chapter 3

Chapter 4

Chapter 5

Appendix 2

List of plates

Plate numbers refer to relevant chapter sections, except for chapter 4 where the numbers refer to mineral descriptions in table 4.5.1a.

Chapter 1

Chapter 2

Chapter 3

Chapter 4

Chapter 5

Plates

Enclosures

Enclosed in the back cover are maps 1 to 4 and the keys.

Map 1 Derruida 1:10 000 and cross section

Map 2 Vila Verde 1:10 000 and cross section

Map 3 Vinhas (Morais massif) and cross section

Map 4 Braganca massif ultrabasic outline

Preamble and aims of this thesis

Preamble: Platinum-Group Element and Chromite Studies in Mantle Assemblages

The six Platinum-Group Elements (PGE): Os, Ir, Ru, Rh, Pt and Pd have received increasing attention in recent years because they have been shown to provide information of mantle processes involving chromite and sulphide mineralisation. Their generally immobile behaviour during alteration processes and relative abundance in ultrabasic rocks, compared to most other trace elements, makes them suitable for this. A strength in the study of PGE and chromite mineralisation is that the composition of PGE-bearing minerals is related to their textural position within chromite grains. For instance Pt-bearing arsenides and sulpharsenides are present at the margins of or in between chromite grains, whereas Ru-, Os- and Ir-bearing grains are present throughout the chromite grains (Prichard *et al.* 1986). The differing mineralogical assemblages are associated with distinctive chondrite normalised PGE profiles. Thus PGE geochemistry and mineralogy together can give information on fractionation processes with which chromite mineralisation is associated. In this respect the study of PGE geochemistry and mineralogy is of particular use in assemblages derived from supra-subduction zone settings as they are associated with chromite mineralisation.

The PGE exhibit chalcophile behaviour in mantle and crustal-derived melts. Thus in considering the behaviour of sulphide in mantle depletion events the PGE are important geochemical tools. PGE-based studies have provided insights into the relationship between boninitic melts and depleted mantle (Hamlyn and Keays 1986). This link is explored further with relation to the Bragança ultrabasic assemblage in this thesis.

Complimentary to the study of PGE geochemistry and mineralisation is research on the associated chromite. Studies of mantle-derived chromitite and dunite bodies have led to a greater understanding of the processes operating in the mantle above destructive plate margins. It has been shown by previous workers (Dick and Bullen 1984) that chromite grain composition can be related to the environment of formation and broad affinity of the melts from which the chromitite crystallised.

Aims of this thesis

The ultrabasic rocks of the Bragança and Morais Upper Allochthonous Thrust Complex (UATC) have previously received relatively little study. In this thesis the PGE and chromite mineralisation are examined in order to provide insights into the evolution of the ultrabasic assemblage. An aim is to provide a model for the evolution of the ultrabasic assemblage which is consistent with the chromite and PGE mineralisation and geochemistry.

Petrographic and geochemical studies of the enclosing ultrabasic rocks are also made to this end. As part of this overall objective, the type of silicate melt associated with the chromite and PGE mineralisation is proposed. Detailed mapping in selected areas of the Bragança and Morais massifs was carried out to identify lithologies within the ultrabasic assemblage and any variation between Bragança and Morais. The implications of deformation on the petrographic studies are also assessed.

Another aim is to examine the processes of concentration and fractionation of the PGE within the chromite-rich samples and to explore any differences in geochemical and mineralogical trends between the six PGE. A model is proposed which attempts to relate the mineralogical and geochemical trends of the PGE to the crystallisation of chromite and sulphide.

Summary of this thesis

The ultrabasic assemblage is highly tectonised and has a complex structural history. Chapter 1 presents the results of the large scale mapping and structural analysis carried out on parts of the Upper Allochthonous Thrust Complex (UATC) ultrabasic assemblage outcrop in Bragança and Morais. This identified the development of a high strain fabric over much of the ultrabasic outcrop. Only in areas of relatively low strain was it found possible to sample discrete lithologies; in high strain areas there has been mechanical mixing of the different formations. In chapter 2 petrographic and geochemical analyses of the lithologies identified in chapter 1 are presented. The main formation within the ultrabasic assemblage of the Bragança UATC is harzburgite, and within this there are websterite, clinopyroxenite and hornblendite layers, together with a chromitite-bearing dunite formation. In contrast the equivalent assemblage in the Morais massif consists of peridotite with minor troctolite and gabbro. The UATC ultrabasic assemblage in Bragança thus differs from that of Morais and origins as depleted mantle and cumulates respectively, are proposed.

In chapter 3, the textures of the chromite-rich samples and the composition of the chromite grains are considered. The high strain imposed upon the ultrabasic assemblage has caused a recrystallisation of the grains within massive chromitites. There has also been re-equilibration of Mg and Fe compositions between chromite and co-existing olivine during amphibolite grade metamorphism and a remobilisation of some elements at the margins of chromite grains during serpentinisation. Despite this, the 100Cr/(Cr+Al) ratios of the chromite cores can give information about the melts from which the chromite and dunite crystallised. High ratios, clustering around 75 suggest that the melts had a boninitic affinity.

Chapter 4 describes the PGE mineralogy and geochemistry associated with the dunite/chromitite formation. PGE-bearing minerals located within the chromite-rich samples are characterised and probe analyses of some grains presented. The base-metal sulphide has recrystallised to a heazlewoodite and magnetite assemblage during serpentinisation and this breakdown is associated with the creation of Pd-bearing alloys. The Pd is considered previously to have been carried in solid solution within the pentlandite. A fractionation of Pt from the other PGE during chromitite crystallisation is also present; this is believed to be caused by differences in solubility within the silicate melt relating to the conditions of oxygen fugacity. The Pd/Cu ratio of the silicate melt from which the chromite-rich samples crystallised is calculated in order to help characterise the type of melt. The relatively high values of this ratio obtained, due to a high concentration of Pd in relation to sulphide contents, are further evidence for the boninitic affinity of the silicate melt. Pentlandite grains with a relatively high tenor of PGE, are present within the harzburgite formation (chapter 5). This is taken as the explanation for the high Pd/Cu ratios within the melt from which the chromitite-bearing dunite formation was derived. The melt was derived from a source region, similar to the harzburgite formation, which contained a sulphide phase with a high

tenor of Pd relative to sulphide.

In chapter 6 a model for the evolution of the UATC ultrabasic rocks is presented based on the conclusions of the previous chapters. Previous published work: geochemical, radiometric dating, metamorphic and regional studies, are reviewed in order to integrate this model with the existing body of knowledge concerning the UATC. The chromitite mineralisation occurred at a destructive continental margin of Gondwanaland prior to 480-490Ma. The chromitite-bearing dunite formation crystallised from diapirs of olivine-rich, boninitic melt within the harzburgite formation in a supra-subduction zone setting. Pd was enriched within these melts and Pt was fractionated from the other PGE during chromite crystallisation.

Introduction

Bragança and Morais, Northern Portugal: two of the five N.W. Iberian Massifs within the Central-Iberian terrane

The western part of Iberia consists of five terranes (West-Asturia, Cantabria, Central-Iberia, Ossa-Morena and South-Portugal) which each have distinct tectonic, sedimentary, igneous and metamorphic histories. The trend of the five terranes in the Iberian massif is arcuate from E-W to NW-SE towards the NW coast (fig. 1). This is part of the Hercynian orogenic trend, which can be traced into northern France, where there are similar assemblages. Although the Iberian terranes fall within the structural trend of the Hercynian chain and record the geological history of a Devonian/Carboniferous collision episode, they also contain Upper Precambrian and Lower Palaeozoic assemblages that indicate separate rifting and collisional episodes predating the final Devonian/Carboniferous collision. The geological evolution of the Iberian terranes during the Palaeozoic is considered in chapter 6.

Figure 1 Terranes within the European Hercynian Belt during the post-Carboniferous

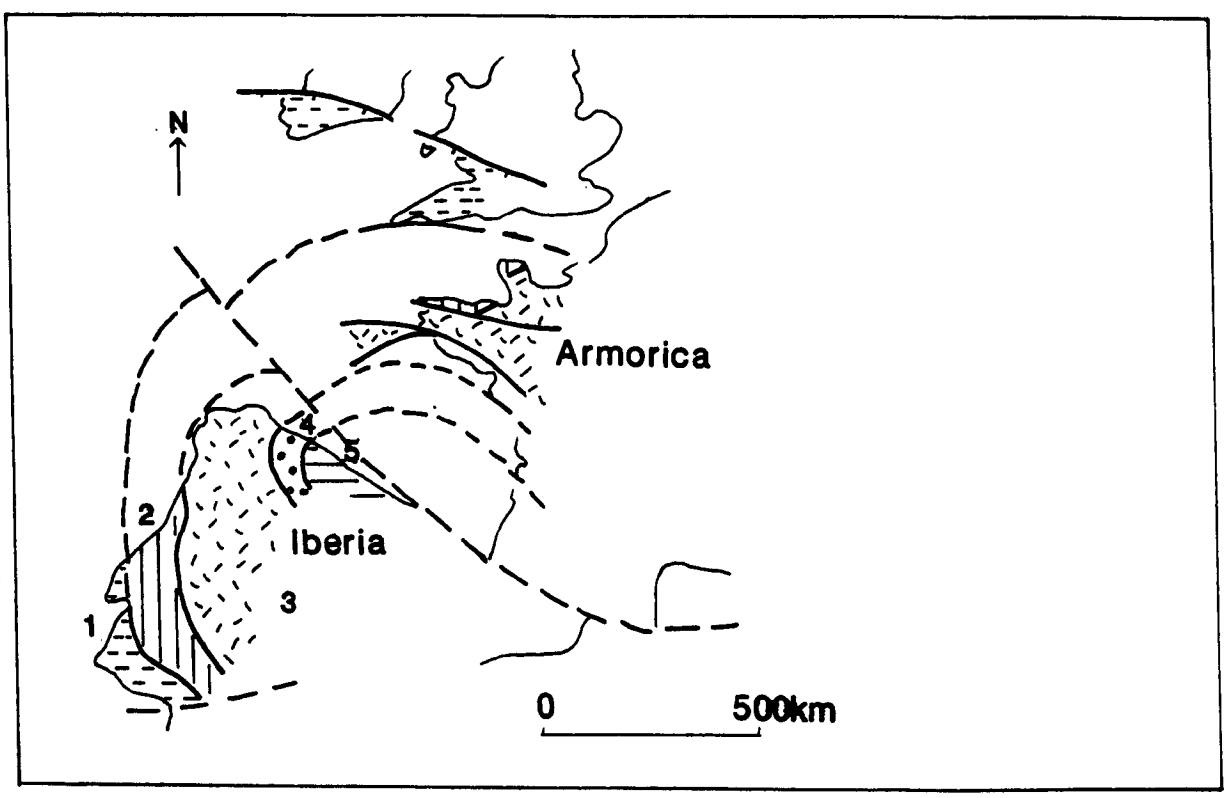

1. South-Portugal Zone, 2. Ossa-Morena Zone, 3. Central-Iberian Zone, 4. West Asturia Zone, 5. Cantabria Zone. The zones (or terranes) within West Iberia are correlated across the Hercynian Belt (shown by the same shading). Dashed and full lines are tectonic divisions between terranes. From Ribeiro *et al.* (1979).

The five N.W. Iberian massifs are located at Cabo Ortegal, Ordenes and Malpica-Tuy in Spain, with Bragança and Morais in Trás-os-Montes, northern Portugal (fig. 2). They are thrust-bounded allochthonous complexes which have been emplaced from the west over the Central-Iberian terrane of the Iberian massif, though the exact provenance of the allochthonous complexes is not known. The five complexes consist of similar assemblages of Palaeozoic ophiolite fragments, Palaeozoic metasediments and interlayered lavas, relict granulites, metasediments with eclogite inclusions and ultrabasic rocks.

Structural succession and lithologies of the Bragança and Morais Massifs

The N.W. Iberian massifs were first recognized as thrust bounded allochthonous bodies by Ries and Shackleton (1971). The transport direction of the nappes was shown by these authors to be towards the NE. Ries and Shackleton (*op. cit.*) also described the similarity of lithologies between the five complexes. Anthonioz (1972) and Ribeiro (1974) made the first detailed descriptions of the Bragança and Morais lithologies and produced geological maps of the surrounding Trás-os-Montes region (figs. 3a,b). Ribeiro (*op. cit.*) suggested that both autochthonous/diapiric and allochthonous models could be applied to Bragança and Morais. Subsequently however, only allochthonous models have been considered for these massifs. Both the Morais and Bragança massifs have the form of basins (fig. 2, cross section) created by late Hercynian folding of underlying thrust planes. NW-SE trending Hercynian structures were shown by both Ribeiro (*op. cit.*) and Anthonioz (*op. cit.*) to have refolded older pre-Hercynian foliation and folds.

Fig 4 summarises the structural succession which has been deduced for the NW Iberian massifs by Ribeiro (1974) and Ribeiro *et al.* (1990a). The lowermost section of the succession is the Parautochthonous Thrust Complex (PATC), which is alternatively named the Peritransmontan complex in Bragança and Morais. It consists of Ordovician to Devonian sediments which are similar to those of the underlying Central Iberian terrane autochthon. Structurally overlying the PATC is the Lower Allochthonous Thrust Complex (LATC) or Centrotransmontan Complex. It consists of per-alkaline rhyolites, tuffs, basic metavolcanites, and sediments. The next section above the LATC is the Ophiolite Thrust Complex (OTC). In Morais the OTC is split by a major E-W trending fault into the Izeda-Remondes Unit of the south and the Morais Unit in the north part of the massif. In the Bragança massif it is occupied by the Soeira Unit. The ophiolite section is most complete in the Morais massif and contains amphibolites, flaser gabbro, dykes in gabbro and ultrabasic rocks. The ultrabasic rocks in the ophiolite complex are younger and have a distinct geological evolution from those of the UATC (Ribeiro *et al.* 1990a). The OTC ultrabasic assemblage contains no significant chromite mineralisation and is generally featureless. Dallmeyer and Gil-Ibarguchi (1990) described these ultrabasic rocks as harzburgite. The harzburgite has been serpentinised in Morais but in Bragança there is a prevalent talc-

carbonate secondary mineralogy. The highest part of the NW Iberian massif structural succession is occupied by the UATC. Chromitite-bearing ultrabasic rocks, which are the main part of the study in this thesis, are located in the UATC of Bragança. Relatively little research has been carried out on the UATC ultrabasic assemblage of Bragança since Cotelo-Neiva (1947). In that work chromitite, pyroxenite and hornblendite-bearing serpentinised peridotite were described for the first time. In more modern work, Ribeiro (1974) described them as metaperidotites which had undergone polycylic deformation. In a published abstract Ribeiro *et al.* (1987) called it garnet-lherzolite. These ultrabasic rocks are infolded and thrust together with granulite and paragneiss formations. The paragneiss contains occasional bodies of eclogite. In the Morais massif ultrabasic rocks and granulites of the UATC are present at Vinhas and Caminho Velho (fig. 3b). Unlike the case of the Bragança massif, there is no chromite mineralisation in these ultrabasic rocks. The ultrabasic outcrop covers approximately 30km^2 in Bragança and 0.5km^2 in Morais. The Morais part of the UATC contains a meta-granitic (Lagoa Gneiss) and sedimentary assemblage (Lagoa Schist) which are thrust over the other lithological groups within the UATC.

Figure 2 The NW Iberian Massifs

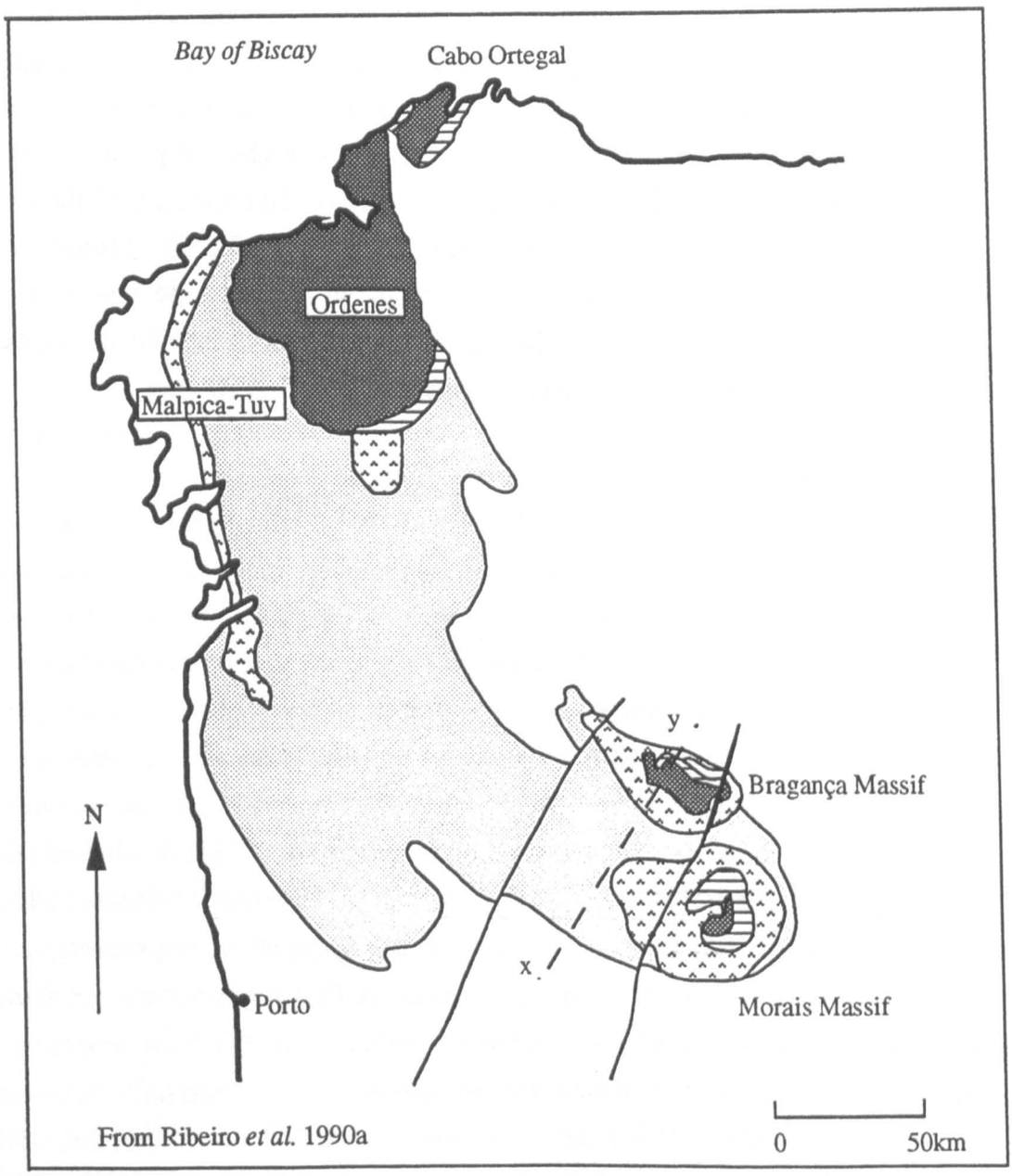

From Ribeiro *et al.* 1990a

The Bragança and Morais massifs are located in NE Portugal with Cabo Ortegal, Ordenes and Malpica-Tuy in N. Spain. The massifs consist of similar assemblages which have been correlated across the five massifs: a lower Parautochthonous Thrust Complex (PATC), succeeded by the Lower Allochthonous Thrust Complex (LATC) then the Ophiolite Thrust Complex (OTC), with the Upper Allochthonous Thrust Complex (UATC) at the top of the structural succession. This entire succession has been thrust over the Central-Iberia terrane of W. Iberia. The associated simplified cross section (X-Y) runs from WSW towards Bragança in the ENE. This shows the basinal shape of the Bragança massif. The Morais massif has a similar basinal shape created by folding of the underlying thrust planes.

Sketch Section X-Y

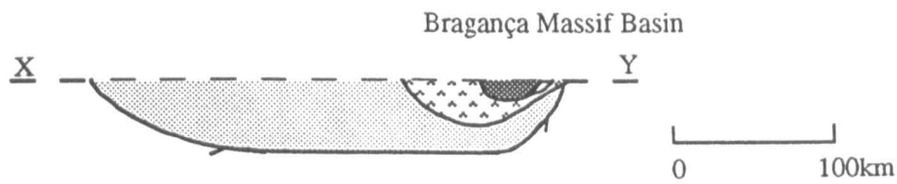

Key to Map and Cross Section

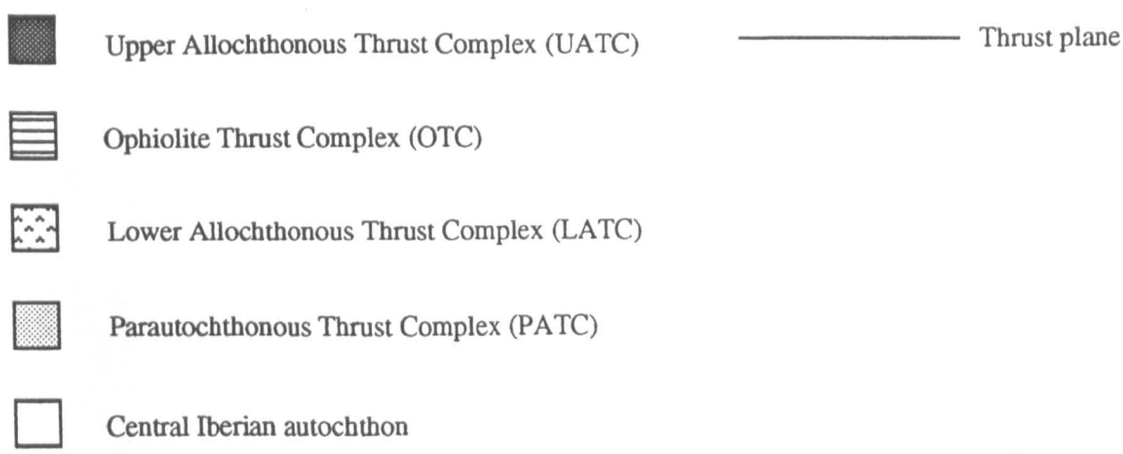

Figure 3a The Bragança Massif

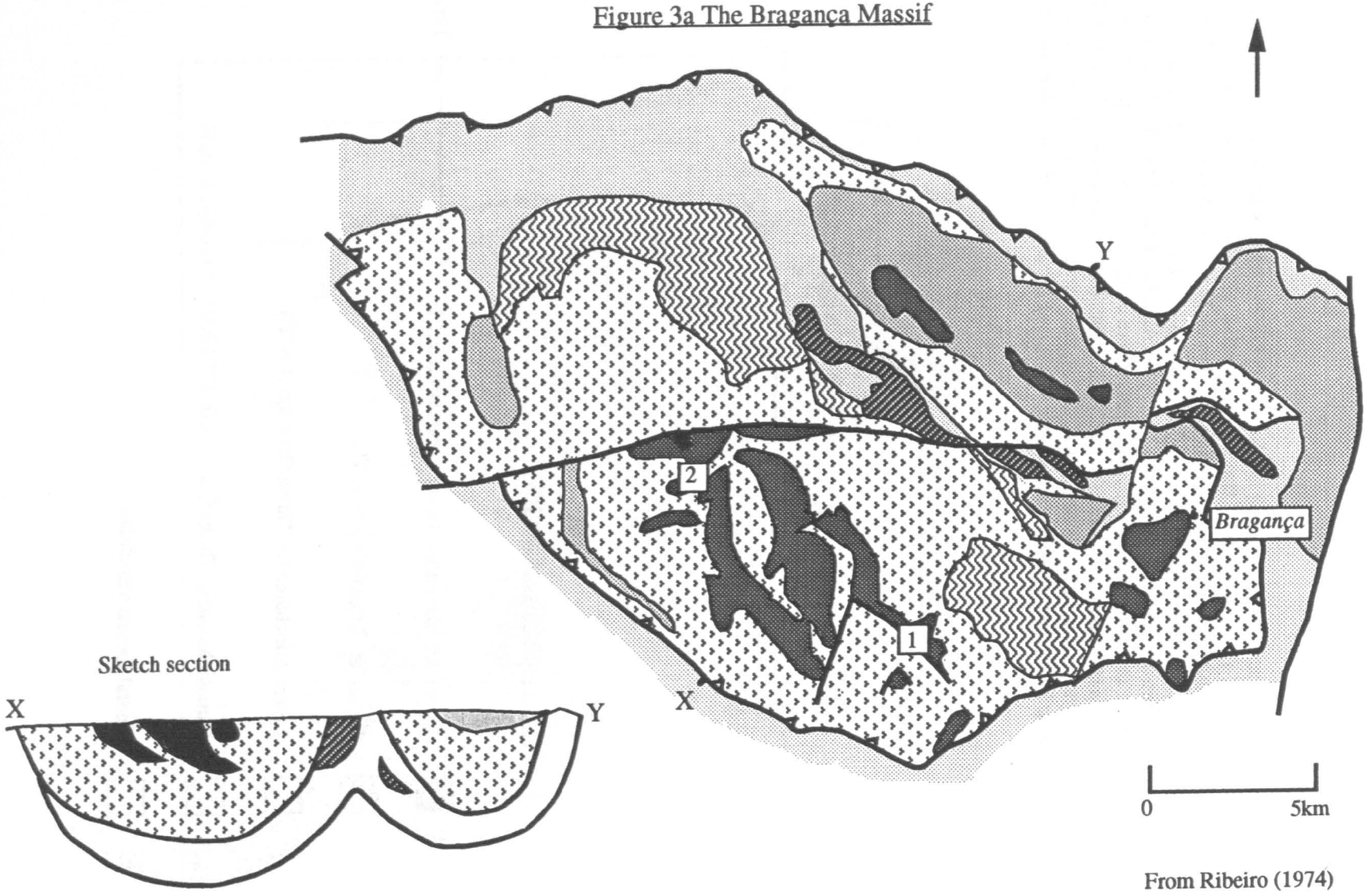

From Ribeiro (1974)

Key to figs. 3a and 3b

- Lagoa Schist
- Lagoa Gneiss
- Ultrabasic assemblage
- Blastomylonitised granulites/gt-pyroxenite
- Paragneiss with occasional eclogite inclusions

Upper Allochthonous Thrust Complex (UATC)

- Amphibolites
- Peridotites, flaser gabbro
- Soeira Greenschist (Bragança)

Ophiolite Thrust Complex (OTC)

- Greenschist/quartz phyllite

Lower Allochthonous Thrust Complex (LATC)

1=Derruida, 2=Vila Verde/Minas de Abicedo, 3=Caminho Velho.
1,2 mapped areas in chapter 1, Vinhas is third mapped area.

Figure 3b The Morais Massif

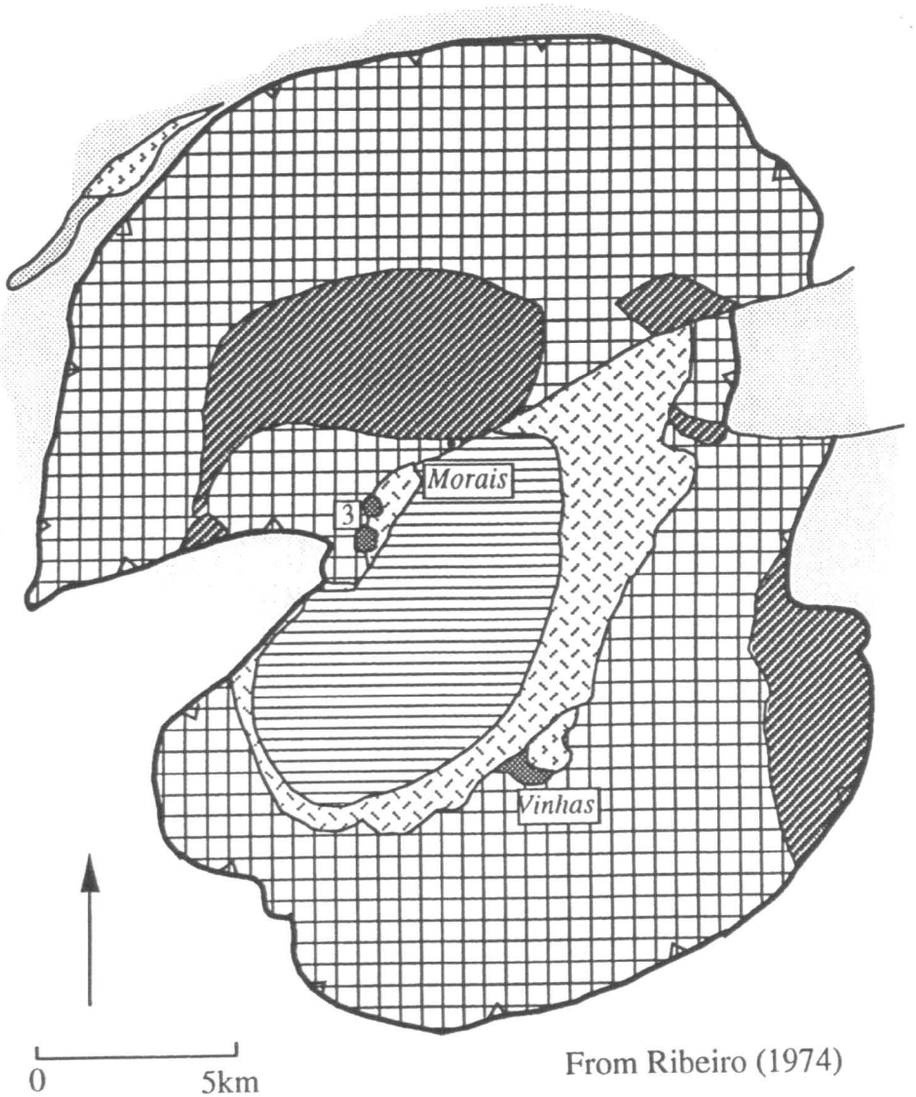

From Ribeiro (1974)

Figure 4 Structural Succession in the Bragança and Morais Massifs

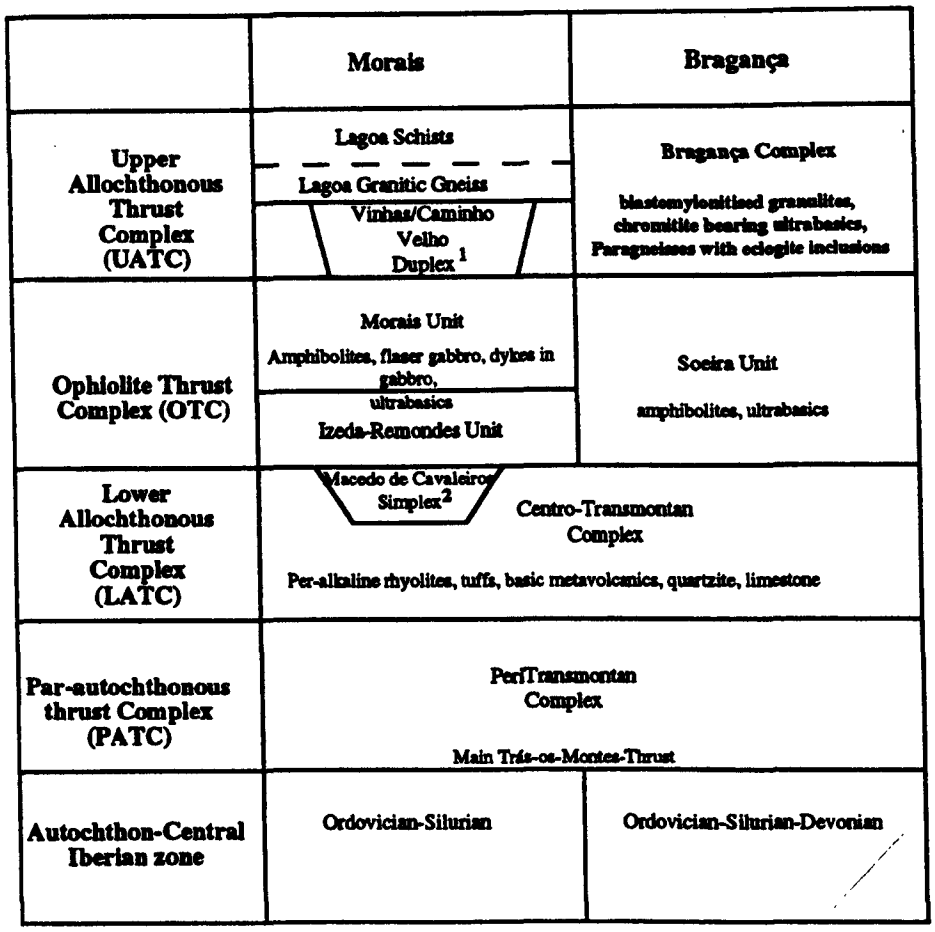

From Ribeiro *et al.* (1990a)

1 Vinhas and Caminho Velho duplex contain blastomylonitised granulites and ultrabasic rocks without chromitite

2 Macedo de Cavaleiros simplex contains UATC assemblages

This figure (from Ribeiro *et al.* 1990a) summarises the structural succession within the Bragança and Morais massifs. There is a stack of four distinct complexes overlying the autochthon. The lower most- the Parautochthonous Thrust Complex contains similar Lower Palaeozoic sediments to those of the autochthon. The Lower Allochthonous Thrust Complex contains per-alkaline rhyolites, tuffs, basic metavolcanics and sediments. Above this is the Ophiolite Thrust Complex which consists of altered ultrabasic rocks, flaser gabbro and relict dykes in gabbro. The complex at the highest structural level is the Upper Allochthonous Thrust Complex. In the Bragança massif this consists of blastomylonitised granulites, paragneisses with eclogite inclusions and the chromite-bearing ultrabasic rocks considered in this thesis. In the Morais massif it contains ultrabasic rocks (at Vinhas and Caminho Velho) which do not have chromite mineralisation and granulites. The highest part of the Upper Allochthonous Thrust Complex is the schist and gneiss formations of Lagoa.

The succession described above, from parautochthon to UATC has been correlated across all five of the complexes and is only locally rearranged by late stage Hercynian thrusting (Ribeiro *et al.* 1990a). Table 1 shows the correlation between different assemblages of the UATC and OTC within the five allochthonous complexes. The distribution of the main structural groups (UATC, OTC, LATC, PATC) is shown on the map in fig. 2. The lower Palaeozoic sedimentary rocks of the Parautochthonous Thrust Complex are similar to those of the underlying autochthon. Apart from this, the lithologies within the complexes bear no direct relation to those of the Central-Iberian autochthon.

Table 1 Lithological assemblages within the Upper Allochthonous and Ophiolite Complexes of the NW Iberian Massifs

Assemblage	Metamorphic and structural history	Age	Interpretation	Massifs Present
1(a) Ultrabasics (b) Chromite mineralisation (c) Pyroxenite layers	Pre-Hercynian foliation. High P. granulite facies peak, later retrogression	500±100ma[1]	Upper continental mantle[4]	1(a)B,M,C.O., Od (b)B (c)B,C.O.
2. Gabbros, Gt-pyroxenites	As for assemblage 1	470-506ma [2]range	Blastomylonitised granulites from lower crust[5]	B,M,C.O., Od.
3. Calkalkaline and alkaline orthogneisses metasediment schists	Pre-Hercynian foliation	Fossils dated at U. Cam. to L. Ord. (525-475ma)[3]	Upper continental or island arc crust[3]	M, M.T., Od.
4. Paragneisses with mafic inclusions	Mafic inclusions up to amphibolite facies	480±5 ma[2]	Metasediments with relict ocean basalt inclusions[3]	B, C.O., M.T., Od.
Ophiolite: Serpentinite, flaser gabbro, relict dykes, pillow lavas	Hercynian deformation, lacking earlier folds; amphibolite facies peak	Post Sil.	Hercynian ophiolite[6]	M, B, C.O., Od.

1. Van Calsteren *et al.* (1979), 2. Peucat *et al.* (1990), 3. Arenas *et al.* (1986), 4. Ribeiro *et al.* (1987), 5. Ribeiro (1974), 6. Ribeiro *et al.* (1990a).

B: Bragança, M: Morais, C.O.: Cabo Ortegal, Od.:Ordenes, M.T. : Malpica-Tuy.

Groups 1 to 4 are part of the Upper Allochthonous Thrust Complex (UATC), which structurally overlies the ophiolite complex.

Age and metamorphism of the NW Iberian Massifs

The UATC has locally reached peaks of granulite and eclogite metamorphism whereas the underlying Palaeozoic ophiolite has only attained a maximum of amphibolite facies. Amphibolitisation and subsequently greenschist facies metamorphism associated with blastomylonitisation and thrusting has strongly retrograded the high grade UATC assemblages. The ultrabasic rocks of the UATC have been serpentinised during tectonic emplacement. The UATC assemblages were named the Polymetamorphic Group by Ribeiro (1974) on the basis of their multi-stage metamorphic and structural history. Assemblages, from what is now considered the Ophiolite Thrust Complex, were grouped as the mono-metamorphic assemblage by Ribeiro (*op cit.*) as they did not contain pre-Hercynian

structures or the high grade granulite metamorphic peak.

The age of the UATC is controversial. Anthonioz (1972), Ribeiro (1974) and Ribeiro *et al.* (1990a) support Precambrian ages for the UATC formations because of the extended time required to create the pre-Hercynian foliations. Recent radiometric dating suggests a Lower Ordovician age for the granulite and eclogite metamorphism (table 1, and discussed further in chapter 6).

Origin of the UATC

Ribeiro *et al.* (1990a) proposed that the assemblages of the UATC could be a section through the continental lithosphere. The blastomylonitised ultrabasic rocks and granulites were considered to be the relict mantle and lower crustal parts of the continental qlithosphere. The Lagoa granitic gneiss and Lagoa schist at Morais were regarded as upper crustal cover. During the Hercynian collision in the Devonian, this group and the Ophiolite Thrust Complex were thrust over the Central-Iberian Zone. This is the only comprehensive model which deals with the UATC development, though there also exists a considerable body of research regarding the metamorphism, ageing and geochemistry of some assemblages within the UATC which is considered futher in chapter 6.

Chapter 1 Field relationships of the UATC ultrabasic assemblage

1.1. Introduction

A total area of 5.75km^2 was mapped in three different parts of the Bragança and Morais massifs. The areas are around Derruida (map 1, appendix 1), Vila Verde to Minas de Abicedo (map 2, appendix 1) in the Bragança massif and Vinhas (map 3, appendix 1) in the Morais massif. On the basis of fieldwork across the UATC, they are regarded here as representative of the UATC ultrabasic assemblage as a whole. The aim of the mapping was to identify separate lithologies within the ultrabasic assemblage and to understand the field relationships between the different lithologies. It was also necessary to assess the implications of the high strain fabric for the petrographic and geochemical study of the samples that were collected. Structural analysis using pi-pole scatter plots of structurally homogenous parts of the mapped areas enables the formation of a model to explain the creation of the planar fabric present in the ultrabasic assemblage to be proposed. The lithologies introduced in this chapter are described in more detail in chapter 2.

25 abandoned chromite mines or chromite exploration trenches are distributed throughout the outcrop of the ultrabasic assemblage (map 4 in appendix 1).

1.2. Previous structural work on the Bragança and Morais UATC

The first detailed descriptions of the structural relationships within the Bragança and Morais massifs were by Anthonioz (1972) and Ribeiro (1974). Both of these authors described pervasive folds with an E-W hinge trend and a later N-S fold hinge trend. Ribeiro (1974) noted that the E-W hinges were part of an isoclinal fold generation and that the N-S trend (with scatter to the NNE-SSW) was associated with subhorizontal folds. Subsequent folding on a NW-SE trend was correlated with the Variscan (Hercynian) trend by both Anthonioz and Ribeiro.

In later more detailed work on the polymetamorphic assemblage within the Vila Boa de Ousilhao synform (fig. 3a in the Introduction chapter), Marques (1989) proposed eight deformation phases. These are listed in table 1.2 and correlated with the work of Anthonioz (1972) and Ribeiro (1974). D2 and D3 correspond to the first E-W and N-S fold hinge trends of the earlier works. These phases were considered to be associated with a penetrative axial plane foliation, blastomylonitisation and amphibolitisation in a non-coaxial strain environment. Thrust contacts within the polymetamorphic rocks were regarded as part of the D3 phase. The difference between D2 (E-W hinges) and D3 (N-S hinges) is in the orientation of structures, their form being similar. Both of these trends showed considerable

scatter, which was attributed by Marques (*op. cit.*) to the probable non cylindrical geometry of folds. D4 was described as open folding on a N-S trend, without associated foliation and the D5 phase corresponded to conjugate shear zones, with shearing to the west. In this work D6 was considered the first Variscan phase. D6 structures were only encountered at the thrust contact above the ophiolitic nappe of Soeira-Nogueira, with a sense of shearing to the south. The synformal structure of the Vila Boa area, where much of the ultrabasic assemblage outcrops, is allocated to a D8 phase in this scheme. This corresponds to the F3 Variscan phase of Ribeiro (1974). The UATC nappe complex in the area around Vila Boa de Ousilhao was subdivided by Marques (*op cit.*) into the Alimonde, Vila Verde, Vale de Cervas, Conlelas and Cabrões nappes. The nappes were described as containing similar assemblages of blastomylonitised granulites and garnet pyroxenites with occasional gabbros. The boundaries of these nappes are shown on map 4 in appendix 1.

As outlined in the introduction chapter, the UATC in Morais consists of the Lagoa mica schists and gneisses and the relict peridotites and mafic granulites of Caminho Velho and Vinhas. The Lagoa formations are effected by a penetrative NNW-SSE lineation (Ribeiro *op. cit.*) which has largely obscured previous foliations.

1.3. Mapped formations and chromite mines in Bragança

The mapped area covers 1.5km^2 around Derruida (map 1) and 2.25km^2 in the area near Vila Verde (map 2). At Derruida, the exposure is best along road cuttings and mine trenches, being limited elsewhere. In the first mapping area, four distinct lithological formations were present within the ultrabasic assemblage: serpentinised harzburgite with visible orthopyroxene, serpentinised dunite with occasional chromite-rich samples, pyroxenite and hornblendite. The largest outcrop area on the Derruida map consists of a variable mixture of these formations and was grouped for mapping purposes as the peridotite formation. A large hornblendite layer was traced along the eastern side of the peridotite outcrop. In the centre of the peridotite outcrop pyroxenite layers predominate over peridotite and this was identified as another formation in mapping the area. To the west and east of the peridotite outcrop in map 1, is a feldspar-bearing amphibolite formation. In places where there is no feldspar, this formation is indistinguishable from the hornblendite layers within the peridotite formation itself. Within the feldspar-bearing amphibolite formation there are two separate north-south trending outcrops of other lithologies. The easterly one has a pargasite-olivine mineralogical assemblage. The westerly outcrop is a garnet-feldspar-mica gneiss. The second map (Vila Verde area) includes the two largest chromite mines in Bragança : Minas de Abicedo and the mine on the Vila Verde side of the Tuela valley. There are good exposures of the ultrabasic assemblage along the valley side and river bank of the Rio Tuela. In the area covered by the second map, only the peridotite, feldspar-bearing amphibolite and hornblendite formations were seen. The peridotite formation in the mapped areas corresponds to the "metaperidotites" and the feldspar-bearing amphibolite formation to

the "blastomylonites" of Anthonioz (1972) and Ribeiro (1974). Ribeiro *et al.* (1987) and subsequently Marques (1989) described these amphibolites as retrograded granulites and garnet pyroxenites. The garnet-feldspar-mica gneiss formation is the paragneiss of Ribeiro (*op. cit.*)

At Derruida and Serralhão (map 1) there are sets of small pits and trenches dug into the hillsides for chromite extraction. There are four trenches at Derruida and five at Serralhão. Small workings or exploration trenches like these are typical of others found across the ultrabasic assemblage (plate 1.3a). The mines at Minas de Abicedo and Vila Verde (map 2) are larger. At Minas de Abicedo there are six pits dug underground into the hillside and other quarried faces and trenches spread over a horizontal distance of 400m. At the Vila Verde mine there are three underground mine entrances (plate 1.3b). At both Minas de Abicedo and Vila Verde, mine entrances exploit prominent near vertical joint sets into the hillsides. At Vila Verde the near vertical joints have an E-W trend and at Minas de Abicedo 140-320. Within the mine shafts the excavation along the strike of foliation in chambers is tens of metres long. At Vila Verde a layer of chromitite or chromite-rich dunite was present in an underground chamber at the end of the entrance shaft. The layer is part of the main foliation, traceable for a few metres and is less than 30cm thick. This layer contains nodular texture chromite.

Table 1.2 Deformation Events in the Bragança and Morais Massifs

	Marques (1989)	Ribeiro (1974)	Anthonioz (1972)	This work
Pre-Hercynian	D1 Inferred recumbent folds			
	D2 E-W trend with scatter, axial planar foliation, blastomylonitisation	F1 Isoclinal folds E-W hinge	E-W trend isoclinal folds	Development of axial planar fabric through progressive folding and boudinage equivalent to D2/D3 of Marques (1989).
	D3 N-S trend with scatter , thrusting, blastomylonitisation	F2 Sub-horizontal folds, N-S hinges, scatter to NNE-SSW.	N-S trend folds.	
	D4 Open folds, subvertical N-S direction.			
	D5 Conjugate shearing to W.			
Hercynian phases	D6 Shearing to S	F3 (=Hercynian F1) Rotation of pre-existing foliation	NW-SE Hercynian trend folds	Predominantly NW-SE open folds in Bragança ultrabasic assemblage, kink folds at Vinhas (Morais)
	D7 Reactivation of D3 thrusts	F4 Upright NW-SE folds (Hercynian F2)		
	D8 Vila Boa de OUsilhao synform, NW-SE trend.	F5 (=Hercynian F3)Upright NW-SE folds, giving basin shapes in Braganca and Morais.		

1.3.1 Lithological contacts and main foliation in the Bragança ultrabasic assemblage

A strong planar fabric was observed across the mapped areas. In the feldspar-bearing amphibolite and the garnet-feldspar-mica gneiss formation, the planar fabric is developed as a foliation defined by mm scale layered segregations of garnet and feldspar. In the peridotite formation it is defined by the cm to m wide pyroxenite and hornblendite layering; in areas devoid of pyroxenite layers this fabric is not well developed. There is a continuous variation from hornblendite and pyroxenite layers which can be traced for tens of metres, as in the case of the hornblendite layer along the western side of the main peridotite outcrop of Derruida, down to pod like layers or clusters a few tens of cm long. The textures across the ultrabasic outcrop illustrate a progressive boudinage and thinning of pyroxenite layers leading to the development of a mylonitic fabric. The term mylonite is used here as a general term for rocks occurring in zones of high deformation containing both cataclastic and recrystallised mineralogy (definition after Hobbs *et al.* 1976). The plates 1.3.1a to 1.3.1e

show this range in rock fabrics from different parts of the Bragança ultrabasic outcrop. Plates 1.3.1a and 1.3.1b show a relatively low strain fabric with pyroxenite forming discrete layers or boudins within the surrounding peridotite formation. Plates 1.3.1c and 1.3.1d show a higher strain mylonitic fabric. In this case the pyroxenite layers have been thinned and boudinaged within the peridotite and a mylonitic mixture of pyroxenite and peridotite is the result. Plate 1.3.1e shows the highest strain fabric where brittle dissaggregation of the lithologies has occurred.

Associated with this progressive deformation is the probable elimination of many fold closures by boudinage and refolding of pre-existing layering. Some fold closures remain in the peridotite and feldspar-bearing amphibolite formations (plates 1.3.1f and 1.3.1g). In both mapped areas different fold generations may be determined on the basis of interlimb angles and axial plane orientation. An early group has interlimb angles of 20-40 degrees across the Vila Verde map area (map 1) and 20-70 degrees in Derruida (map 2). The axial planes of these mainly tight folds have variable orientations varying from recumbent to upright and are generally concordant with the foliation orientation scatters. No marked asymmetry or fold vergences were present. A second set of folds is the series of open to gentle folds typically with 130-150 degree interlimb angles. The axial planes of these folds are near vertical and discordant to the surrounding foliation. This fold generation postdates the set of tight folds.

The contacts between the formations are all tectonic. Thrusts are recognizable in the field as the adjacent rock is fine grained and shows brittle disaggregation. Plate 1.3.1h is an example of a thrust contact concordant with foliation at the eastern margin of the peridotite formation in map 1. Continued movement along thrust zones and the foliation planes has led ultimately to more brittle cataclasis. Shear zones showing brittle cataclasis may be adjacent to thrusts such as at the west contact of the main Derruida peridotite body (map 1). This contact lies at a high angle to the surrounding foliation; the shear zone is between 5 and 30m wide. Plate 1.3.1i shows an example of a vertical shear zone contact between the peridotite formation and the Garnet-feldspar-amphibole-gneiss at the isolated outcrop of peridotite in the south-west corner of map 1. Many other shear zones across the ultrabasic assemblage outcrop are concentrated along the dunite outcrops, which are best exposed in the chromite mines.

Across the ultrabasic outcrop six chromitite bodies were found in-situ. These chromitite bodies are elongated in the orientation of the surrounding dunite. Plates 1.3.1j and 1.3.1k show examples of a folded chromitite layer from Sardoal (GR 3025 5378 map 4) and a chromite-rich layer from the Rio Tuela valley (GR 2980 5395). Chromitite shows evidence of boudinage and necking during the deformation associated with the foliation development; the most massive chromite is affected in this way.

1.3.2 Structural analysis

Axial plane or hinge line orientations of the folds and the trends of stretched chromite grains were measured. Hinge orientations were taken from the upright and symmetrical open folds. Together with foliation orientations these measurements are plotted in lower hemisphere equal area projections in fig. 1.3.2a for map 1 and fig. 1.3.2b and fig. 1.3.2c for map 2. The variation in foliation and fold hinge orientations between different parts of map 2 suggests that it is necessary to subdivide the map into two main areas for stereographic analysis. The first area is in the upper part of the map and extends down to the peridotite contact north of the Rio Tuela/Ribeira de Vila Boa junction. The second part is to the south of this and is bounded at its southern margin by the shear zone contact. Table 1.3.2 shows the calculated mean lineation vector and poles to the calculated best fit great circles for axial plane and foliation measurements in the Derruida and Vila Verde maps.

Table 1.3.2 Structural data for map 1 and map 2

	Derruida (map 1, fig. 1.3.2a)	**Vila Verde (map 2 north, fig. 1.3.2b)**	**Vila Verde (map 2 south, fig. 1.3.2c)**
Foliation	N=46 Cluster distribution around 31/261 r1 2.36, r2 0.62, K 3.81	N=17 Pole 10.7/088 r1 0.61, r2 1.94, k 0.32	N=11 Cluster distribution around 25/130 r1 2.56, r2 2.73, K 0.94
Fold Axial Plane (first fold generation)	N=12 Pole 20.1/325 r1 0.74, r2 2.33, K 0.32	N=2 At edge of foliation pole cluster.	N=3 Two poles lie at margin of cluster, one clearly outside
Fold Hinge (upright folds)	N=8 Mean lineation vector 9.8/328	N=2 Adjacent to foliation girdle pole	
Chromite grain lineation azimuth	N=9 NW-SE trend		

Fold hinges measured from open to gentle late folds and axial planes from the earlier tight folds. 'N' is the number of readings. The foliation and fold axial plane measurements in map 1 show considerable overlap because of the axial planar fabric. The poles to the foliation and axial plane measurements in map 1 are close to the orientation of the hinge line of the upright fold generation, suggesting that the upright folds have caused a reorientation of the earlier fabrics. R1, R2 and K factors calculated using 'Stereo' Mac software (McEachran 1988). Girdle distributions have low K values *eg* <1 and large r2 and small r1 values, cluster distributions the opposite (appendix 8).

For the Derruida (map 1) data the 12 axial plane orientations show a clear girdle distribution (fig. 1.3.2a). The distribution of foliation measurements is more cluster-like, but the overlap between the two data sets is considerable, as a result of the concordance of axial planes and foliation. The mean lineation vector for the Derruida hinge line set is 9.8/328 and the chromite lineation trends show a wide scatter but there is a cluster around 330 when plotted in the N.W. quadrant. There is a notable coincidence between the hinge lines of the open, late folds, chromite lineation trends and the pole to the axial plane best fit great circles, in the NW quadrant. The foliation and axial plane orientations for the north part of the Vila Verde area (fig. 1.3.2b) show reasonable girdle distributions, with poles to calculated best fit great circles at 16.4/085 and 28/108 respectively. The two hinge line

Figure 1.3.2a Map 1 (Derruida) stereoplot

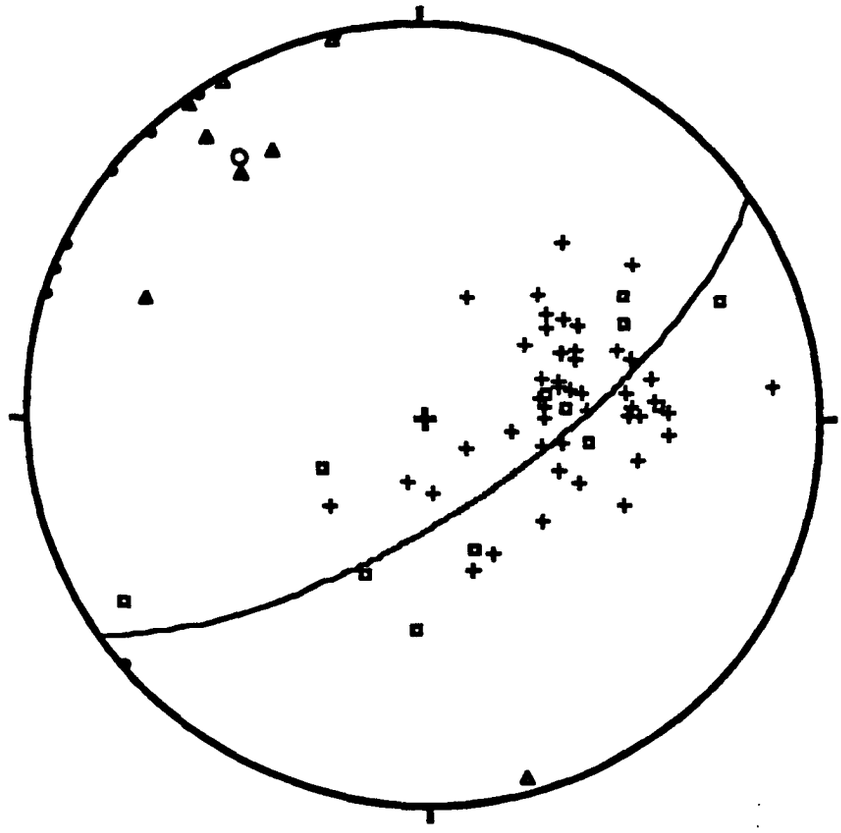

The poles to the axial planes of the first fold generation have a girdle distribution. The best fit great circle through this girdle distribution has a pole at 20.1/325. The distribution of foliation measurements is more cluster like, but there is considerable overlap as a result of the concordance between axial planes and foliation. The mean lineation vector of the hinges of the second fold generation, at 9.8/328, is similar to the orientation of the pole to the first fold generation's great circle. This suggests that the second fold generation has caused a reorientation of the earlier structures.

Key to Stereoplots

- Fold axial plane pole (first fold generation)
- Foliation pole
- Fold hinge lineation (2nd fold generation)
- Pole to best-fit great circle
- Chromite grain azimuth
- Best fit great circle

Figure 1.3.2b Map 2 (Vila Verde north) stereoplot

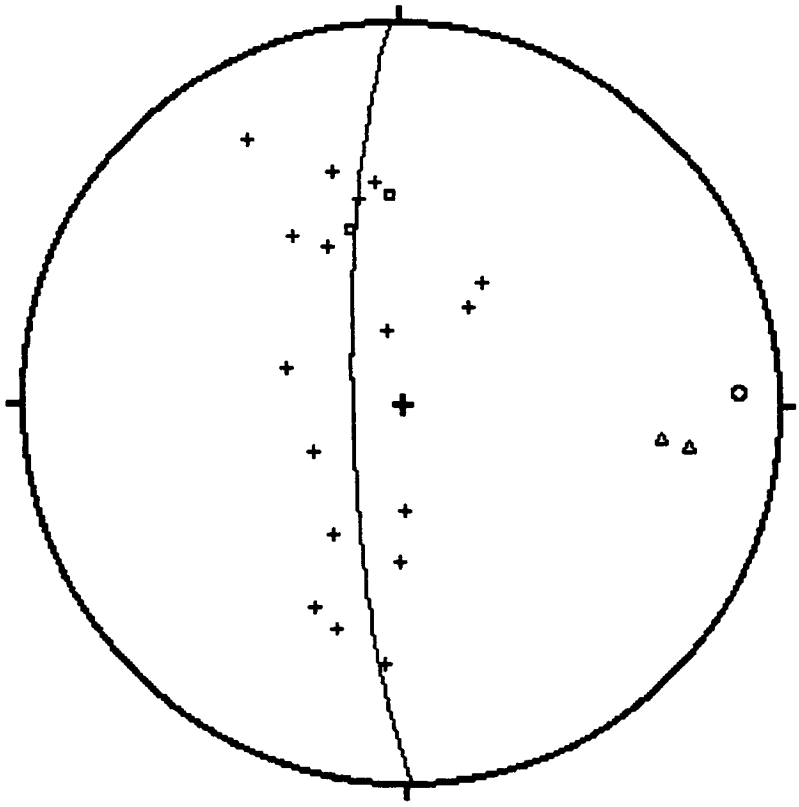

The data for the north part of the Vila Verde area shows a similar structural style to those from the Derruida map. The foliation and axial plane orientations for the north part of the Vila Verde area show reasonable girdle distributions, with poles to the calculated best fit great circles at 16.4/085 and 28/108 respectively. The hinge line measurements of the late fold generation lie close to the foliation girdle poles.

Key to Stereoplots

- ▫ Fold axial plane pole (first fold generation)
- \+ Foliation pole
- ▲ Fold hinge lineation (2nd fold generation)
- ○ Pole to best-fit great circle
- • Chromite grain azimuth
- ⌒ Best fit great circle

Figure 1.3.2c Map 2 (Vila Verde south) stereoplot

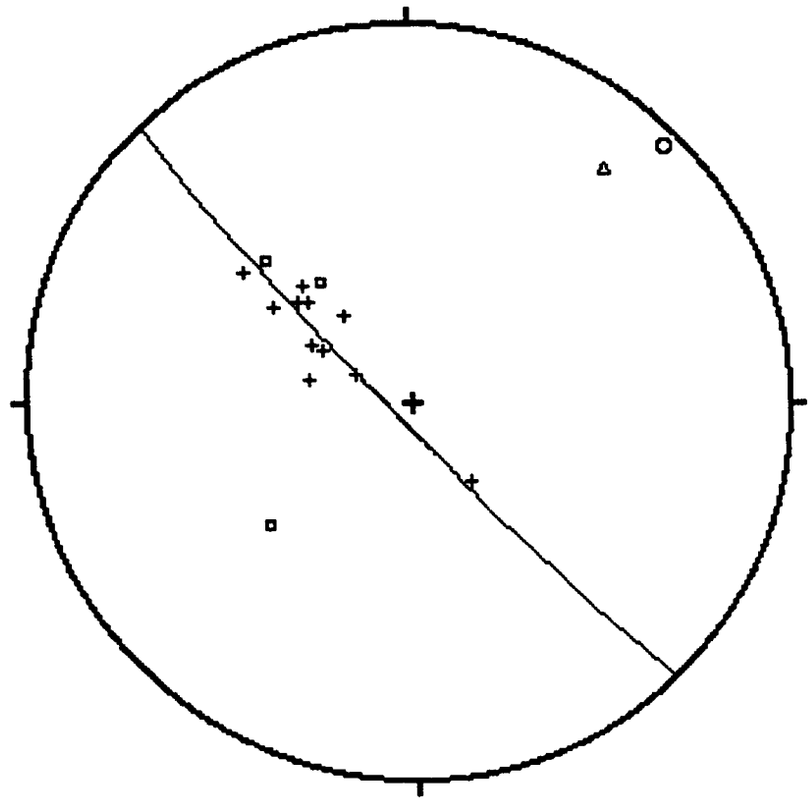

Poles to the foliation from the southern part of the Vila Verde map show a cluster rather than girdle distribution. This cluster is centred around 25/130. Two of the axial plane measurements of the first fold generation, lie at the edge of the cluster whereas one is clearly outside it.

Key to Stereoplots

- Fold axial plane pole (first fold generation)
- Foliation pole
- Fold hinge lineation (2nd fold generation)
- Pole to best-fit great circle
- Chromite grain azimuth
- Best fit great circle

measurements lie close to the foliation girdle pole. The three chromite grain lineation azimuth orientations range from 088 to 111. The data set for the north part of the Vila Verde area (map 2) shows a similar pattern to that from the Derruida area; the poles to the foliation and axial plane best fit circles being close to each other and the fold hinge orientations and chromite grain lineation azimuths, showing a concordant tectonic fabric. Poles to the foliation from the southern part of the Vila Verde map (fig. 1.3.2c) show a cluster rather than girdle distribution. This cluster is centred around 25/130. Two of the axial plane measurement poles lie at the edge of the cluster whereas one is clearly outside it.

The Derruida area (map 1) shows chromite lineations to be of similar trend to the hinges of the open folds, that is north-westerly. This may be a coincidence or it may indicate a direction of extension parallel to the hinge axis of this fold set. At the Minas de Abicedo however a chromite lineation measured of 038 is roughly parallel to the strike of the surrounding foliation. Deformation of chromites leading to a preferred orientation of the grains may result from extension parallel to fold hinges which is at an angle to the main foliation or movement in the plane of the pre-existing foliation.

Plates 1.3a-b, 1.3.1a-k and 1.4.2

Plate 1.3a The largest Derruida mine working (map 1 GR 3042 5357). This example is 20m long, dipping at 20degrees towards the northwest, with a water filled base. The rock, mainly dunite, with one altered pyroxenite layer, has undergone brittle deformation. This type of small working is typical of others across the ultrabasic assemblage outcrop. Tape measure 1m.

Plate 1.3b Vila Verde mine entrances GR2978 5408 (map 2).

Plate 1.3.1a Low Strain Foliation. Laterally continuous pyroxenite layers within the peridotite (harzburgite) formation. Rio Tuela section. Tape measure 1m.

Plate 1.3.1b Intermediate strain foliation. Pyroxenite layers boudinaged within peridotite matrix. Discrete pyroxenite bodies still present. Rio Tuela section.

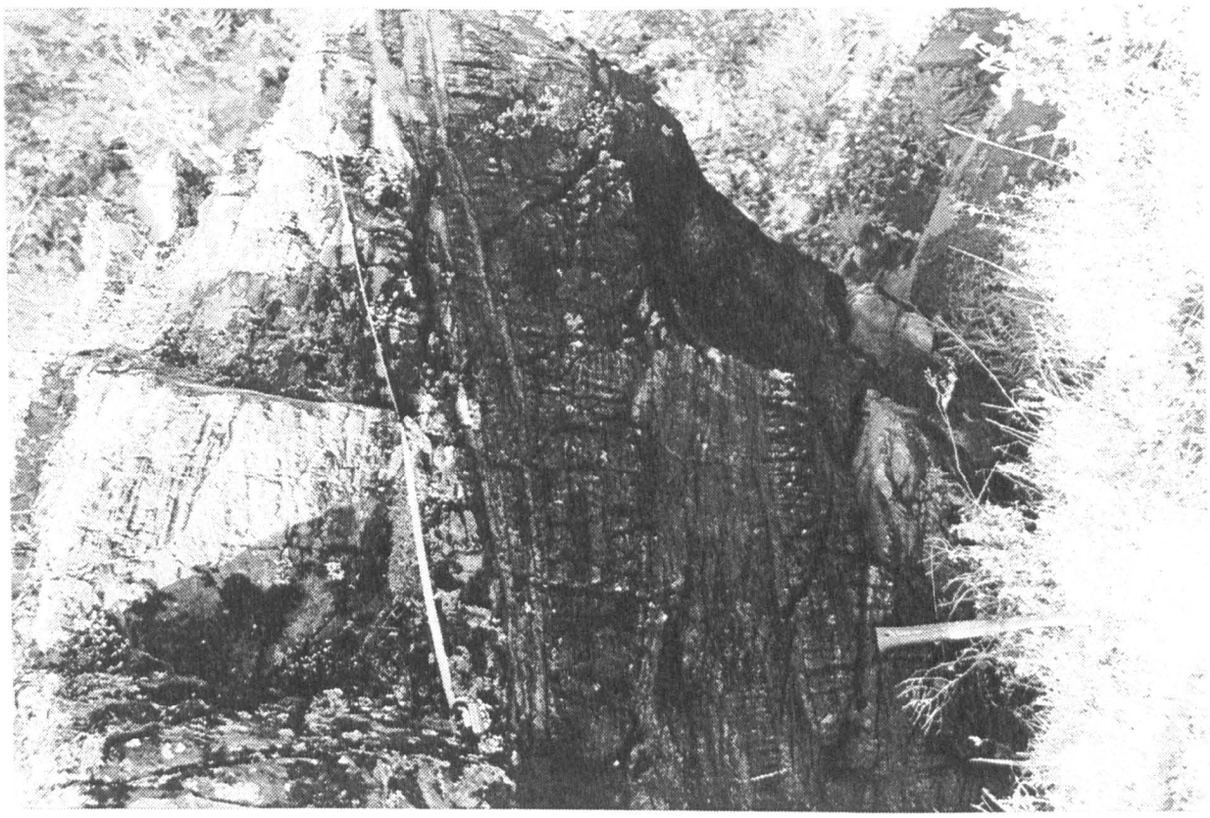

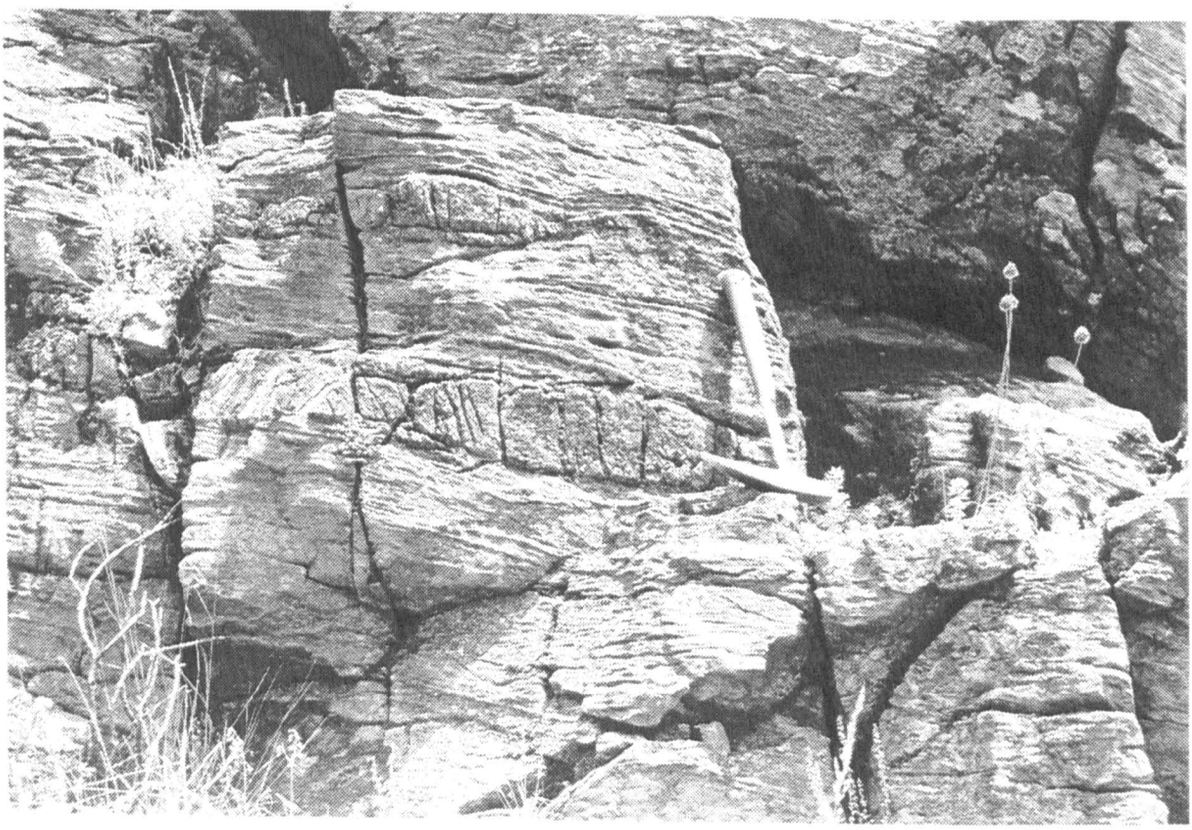

Plate 1.3.1c High strain foliation. Layered mylonitic fabric developing and discrete pyroxenite bodies becoming more rare. Rio Tuela section.

Plate 1.3.1d High strain foliation. Pyroxenite layers have been disaggregated within the peridotite matrix to give an evenly spaced foliation. From Serralhao (map 1). Tape measure 1m.

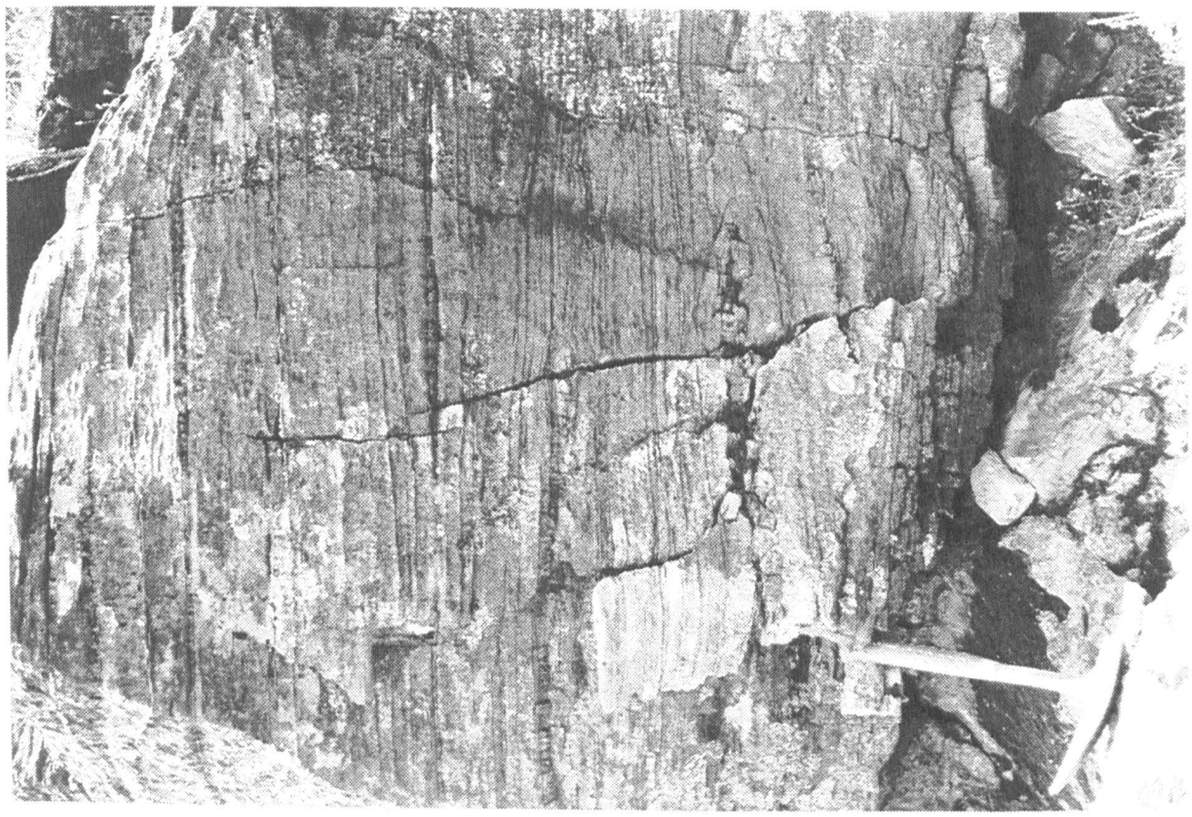

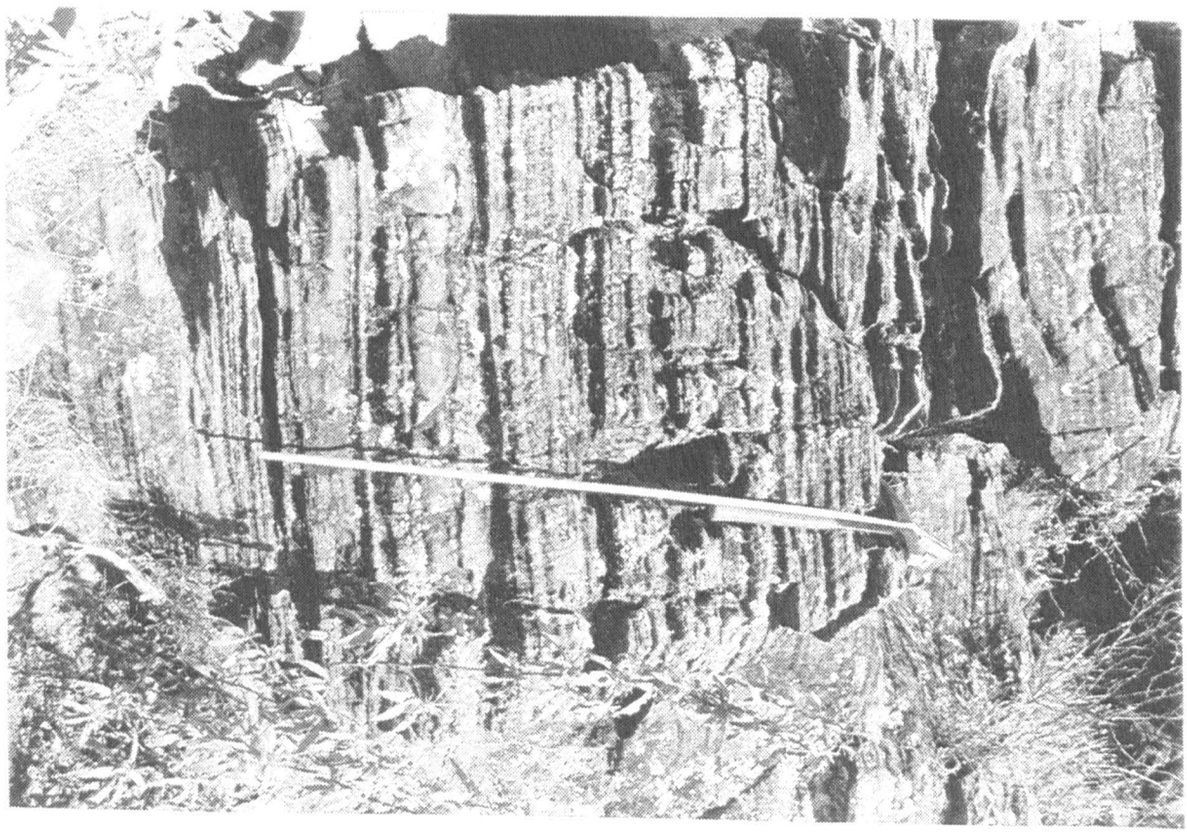

Plate 1.3.1e Highest strain from late movement along foliation postdating ductile deformation shown in plates 1.3.1a-d. Brittle fracturing of pyroxenite and harzburgite layers. Minas de Abicedo GR3985 5394. Tape measure 1m.

Plate 1.3.1f Folded pyroxenite layer within the peridotite formation. The fold has a tight interlimb angle and its axial plane is concordant with the surrounding foliation. Serralhoa GR4045 5365.

Plate 1.3.1g Axial planar fabric within the Garnet-feldspar-amphibole-gneiss. The folds, with tight interlimb angles, are picked out by layers of feldspar. The apparently rootless, intrafolial nature of these folds is characteristic of intensely folded and mylonitised terrains. North bank of Rio Tuela section.

Plate 1.3.1h Thrust contact between peridotite formation above and Garnet-feldspar-amphibole- gneiss below. Hammer pick head is on the contact. Looking west GR3046 5366 (map 1). The gneiss is fine grained adjacent to the contact with brittle disaggregation. The appearance of this thrust contact is typical of others across the ultrabasic outcrop.

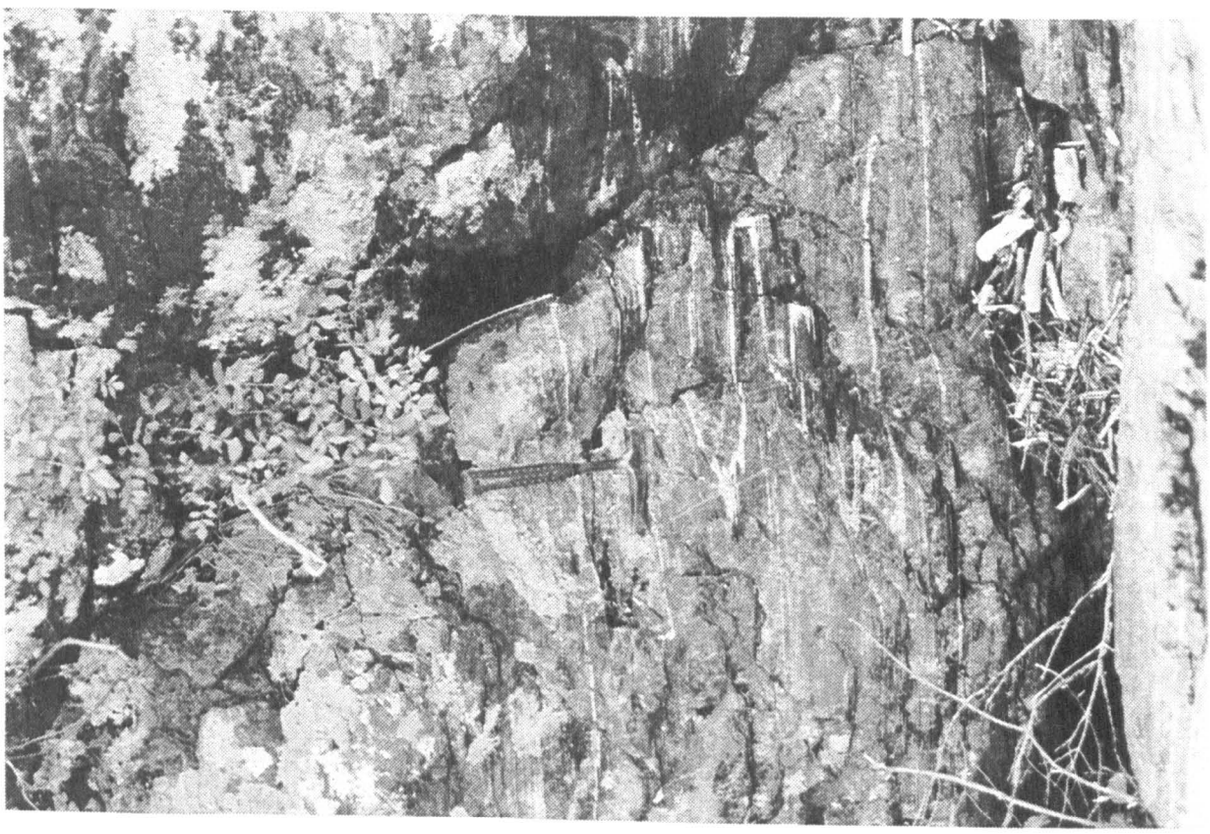

Plate 1.3.1i Example of a vertical brittle shear zone at a dunite and Garnet-feldspar-amphibole-gneiss contact. Looking east, GR3040 5354 (map 1). The mechanically incompetent dunite, to the right of the picture, has undergone the most complete disaggregation. The hammer head lies in the hinge of an upright fold plunging at 25 degrees to the NW, which is also the dunite/gneiss contact.

Plate 1.3.1j Chromitite body of irregular shape within dunite at pick end of hammer. From Sardoal GR3028 5377 .

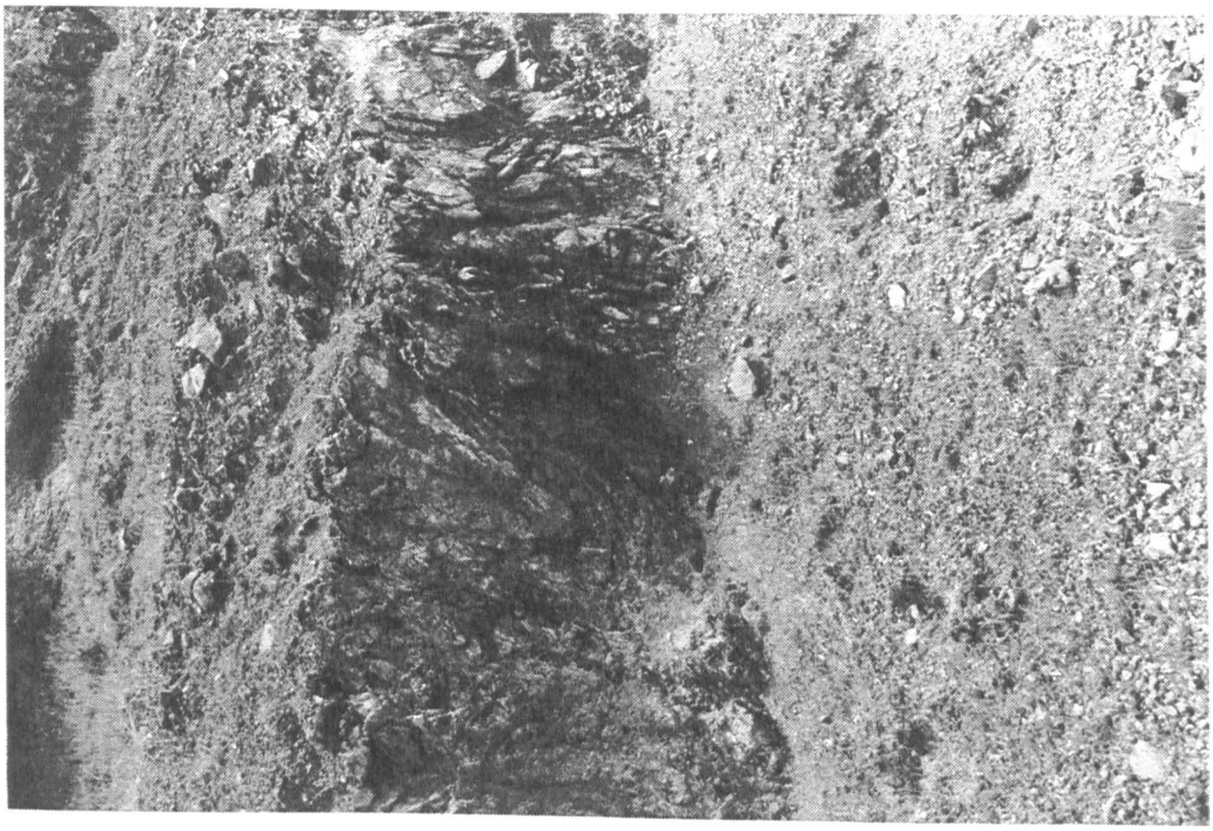

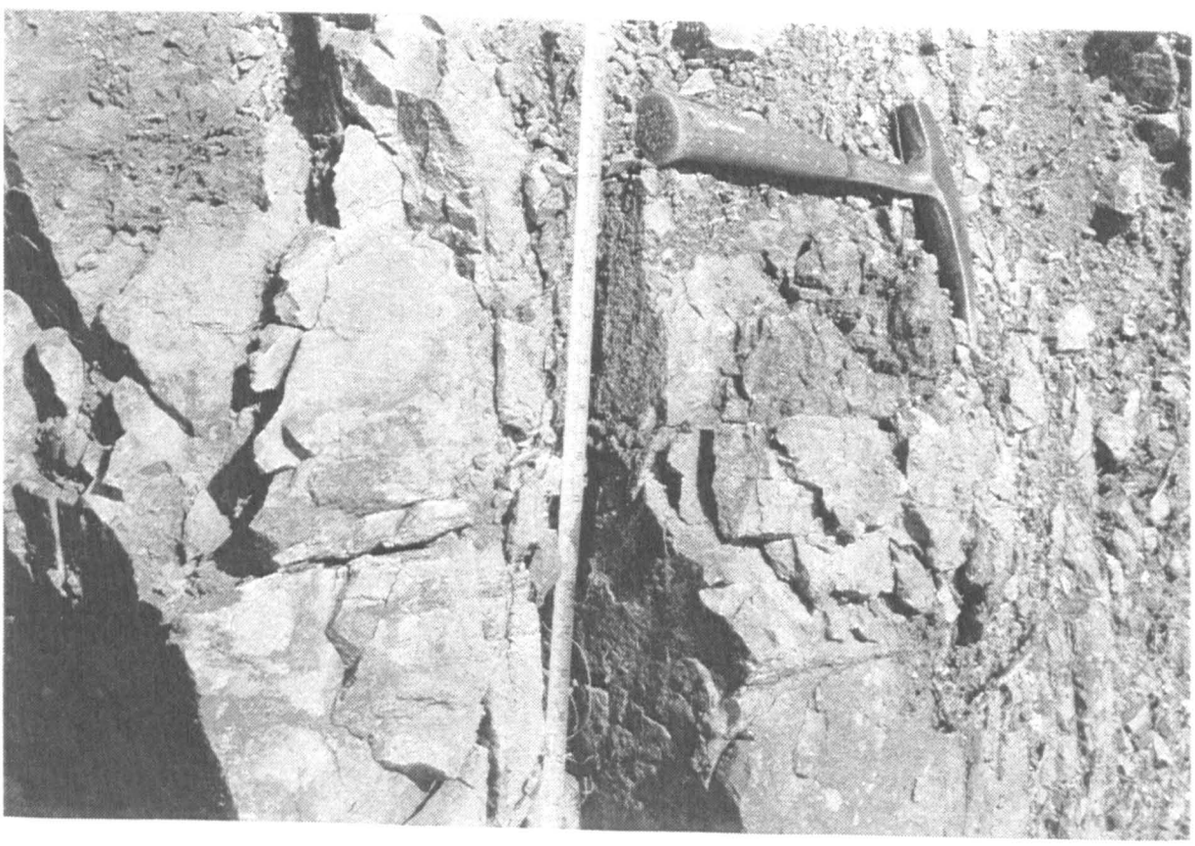

Plate 1.3.1k Chromite-rich layer concordant to surrounding foliation within dunite. From Rio Tuela section.

Plate 1.4.2 Kink folds (below hammer handle), plunging towards NW, within peridotite. These kink folds have largely obliterated any previous foliation . Vinhas GR 3152 4952, map 3.

1.4. Vinhas

1.4.1 Mapped formations

This well exposed area in the Morais massif (map 3) covers about 2km^2 and lies to the west of Vinhas hill along the Rio Sabor valley. Five lithological formations were identified. The largest outcrop is serpentinised ultrabasic rock consisting of relict peridotite. It differs from the equivalent peridotite formation in the Bragança massif (maps 1 and 2) in lacking the distinctive green, pyroxenite layers. The peridotite is bounded to the north by a gt-fel-amph-gneiss formation which is similar to that mapped in the Derruida (map 1) and Vila Verde areas (map 2) of the Bragança massif. The third formation is a granitic augen gneiss and the fourth a mica schist. These two latter formations correspond to the Lagoa gneiss and schist of Ribeiro (1974). The fifth formation is a feldspar-bearing amphibolite without visible garnets, exposed in the southern part of the mapped area. This is the metabasic amphibolite associated with an Upper Palaeozoic ophiolite assemblage (Ophiolitic Thrust Complex) Ribeiro (1974), Ribeiro *et al.* (1990a). The peridotite formation does not have a well developed planar fabric. Although foliation orientations were taken from some massive, blocky layering, a pervasive generation of kink folds has largely obscured any earlier layering. The augen gneiss has massive layering and a rough foliation defined by flattening of feldspar augen. Small kink folds are present at the margins of feldspar augen. The other formations have better developed foliation or schistosity. The best exposed contact between the different formations is that between the granitic augen-gneiss and garnet-bearing amphibolite at GR 3145 4953 (map 3). Here the contact dips at 46/317 and is concordant to the adjacent foliation. At this thrust contact a 2m thick fine-grained mylonitic layer, characterised by a decrease in the number of feldspar augen, is developed.

1.4.2 Structural analysis

A set of 24 foliation orientations together with 25 kink fold hinges and 4 axial plane measurements were taken from across the Vinhas area. This data is plotted on a stereonet (fig. 1.4.2) and summarised in table 1.4.2.

Figure 1.4.2 Map 3 (Vinhas) stereoplot

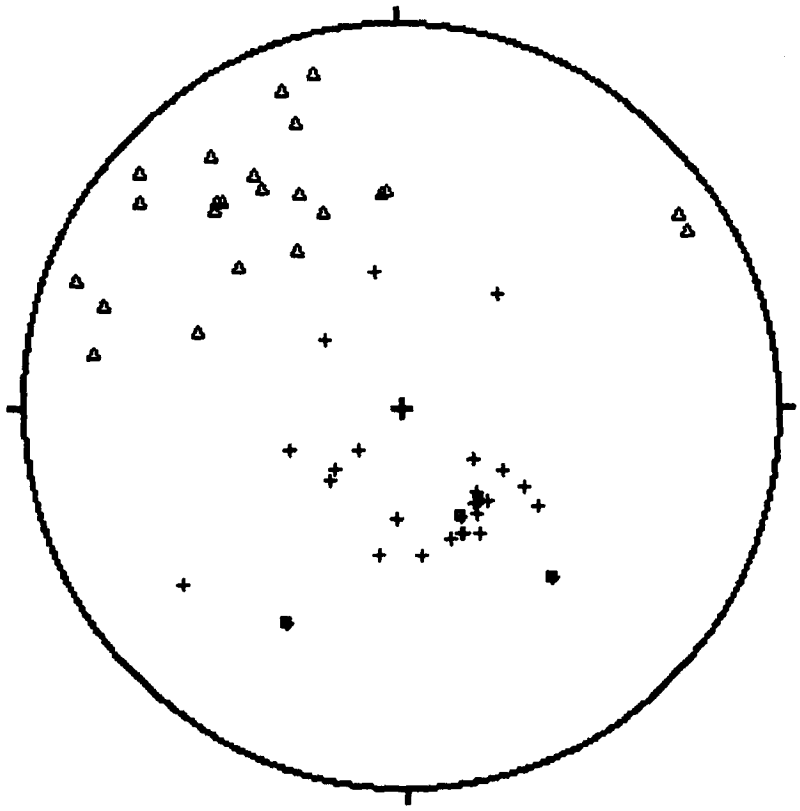

The foliation orientations for Vinhas show a distinct point cluster, without a girdle distribution. The hinges of kink folds show a clustering close to a mean lineation vector of 29.7/322, with two outlying points having north-easterly azimuths. Two axial plane measurements lie within the field of foliation measurements, these were taken from the feldspar-amphibolite formation outcrop (an early axial planar fold generation). The two axial plane poles which lie outside the foliation cluster, having a higher dip, were taken from sets of kink folds within the ultrabasic outcrop. The early folds and foliation have been overprinted by the set of kink folds.

Key to Stereoplots

- ▫ Fold axial plane pole
- \+ Foliation pole
- ▲ Fold hinge lineation (kink folds)
- ○ Pole to best-fit great circle
- • Chromite grain azimuth
- ⌒ Best fit great circle

Table 1.4.2 Vinhas structural data

	Vinhas
Foliation	N=24 cluster in SE quadrant
Axial plane	N=4
Fold hinge	N=25 mean lineation vector 30/322

'N' is the number of readings. The Vinhas ultrabasic rocks do not show the development of an axial planar fabric such as that of map 1. A pervasive linear fabric associated with a set of kink folds is present.

In contrast to Derruida (map 1), the foliation orientations show a distinct point cluster; there is no girdle distribution. The fold hinges show a clustering close to the mean lineation vector of 29.7/322, with two outlying points having north-easterly azimuths. Two axial plane measurements lie within the field of foliation measurements, these were taken from the feldspar-amphibolite formation outcrop. The two axial plane poles which lie outside the foliation cluster, having a higher dip, were taken from sets of kink folds within the ultrabasic outcrop. An early fold generation is found in the feldspar-amphibolite formation. The concordance of axial planar foliation and the tight interlimb angles are reminiscent of the axial planar fabric in the Vila Verde and Derruida areas. This foliation and folding generation is overprinted by the set of kink folds. Plate 1.4.2 shows such folds in an outcrop of the peridotite formation at Vinhas where they are most strongly developed. A change in the orientation of the foliation across the area has enabled an axial trace of a large fold to be drawn (see map and cross section). To the west of the axial trace the foliation mainly dips to the west and north west; to the east of the axial trace it mainly dips towards the north east. The set of fold hinges and two axial planes taken from the ultrabasic outcrop are likely to be associated with the large fold. An upright fold plunging at about 30° towards 322° , that is the mean lineation vector of the fold hinges, is consistent with the outcrop pattern as shown on the map and cross sections. This fold orientation corresponds to that of the F4 Hercynian folds in Trás-os-Montes of Ribeiro (1974).

1.5. Model of structural development

The main Bragança peridotites show no cross-cutting relationships between the pyroxenite/amphibolite layers and the peridotite foliation. Similarly, the dunite and chromitite bodies are concordant with the foliation. Such concordancy is typical of tectonically emplaced peridotite bodies such as the lherzolite massifs of the N.E. Pyrenees (Lorand 1988) and the Ronda peridotite (Obata 1980). Peridotites that have undergone less overall deformation than those in the Bragança area may preserve some cross-cutting relationships. For instance, Lorand (1988) described amphibole-rich and hornblendite veins cutting previous layering in the Lherz and Frechinede peridotites of the N.E. Pyrenees.

In explaining the general concordancy of pyroxenite layering with foliation in peridotites, models based on rotational, noncoaxial strain have been invoked. Nicolas and Jackson (1982) proposed a process of "tectonic transposition" in a rotational strain environment for the creation of concordant mantle-derived pyroxenite dykes. Where rotational, non-coaxial strain models apply, it is assumed that the orientation of the principal directions of strain in the strain ellipsoid have rotated during progressive deformation (fig. 1.5.1) Rotational strain models have also been popular for describing a range of allochthonous terranes of varying lithologies and tectonic grades. Hobbs *et al.* (1976) state that this type of strain is likely to be the most important in allochthonous zones where mylonitisation has occurred and so it is likely to be applicable to the UATC ultrabasic assemblage.

Figure 1.5.1 Simple rotational shear strain ellipse

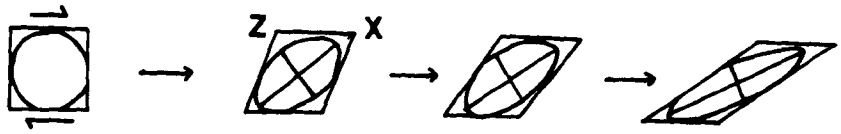

Different lines of material are attached to the principal axes of strain from one increment of deformation to the next. X and Z are the directions of maximum extension and shortening respectively.

If a rotational strain environment is responsible for the progressive deformation during emplacement of mantle assemblages then fold hinges will be rotated out of the plane of the axial surfaces and be eliminated. Layers of competent lithologies such as pyroxenite and chromitite are also boudinaged within the surrounding peridotite and progressively thinned. In this way a lensoid axial planar fabric is developed. This development is shown in plates 1.3.1a-d with the transition towards high strain fabrics within the Bragança ultrabasic assemblage. The creation of this type of axial planar fabric is shown diagramatically in fig. 1.5.2 taken from Hobbs *et al.* (1976). Mylonitisation and cataclastic fracturing of the Bragança ultrabasic assemblage is found in the zones which have undergone the highest strain. During the progressive deformation, dunite has been the least competent lithology, with shearing concentrated along it and chromitite boudinaged within it.

This foliation is not present in the Caminho Velho or Vinhas ultrabasic rocks. This is because the pyroxenite layers which define the planar fabric in Bragança are not present. The pervasive kink folds at Caminho Velho and Vinhas have also masked any previous foliations. The kink folds at Vinhas, with upright axial planes may be of the same generation as the upright gentle folds in the Braganca peridotite. The late, upright fold generation has hinge orientations which are close to the poles of the foliation and axial plane girdles in the Bragança ultrabasic assemblage. This suggests that in places the late folding

has caused a re-orientation of the earlier folds and foliation, giving rise to girdle-like pi-pole scatters of foliation and fold axial planes. This relationship is plausible because the early folds have tight interlimb angles and so nearly parallel limbs. Refolding of early folds with large interlimb angles would cause a wide scatter of the later folds' hinge line orientations. Localised re-orientation of the axial planar fabric by late folding is an additional explanation to that of non-cylindrical geometry for early folds (Marques 1989), in explaining the scattter of fold orientations.

1.6. Conclusions and implications of structural development for petrography and geochemistry

The Bragança ultrabasic assemblage consists of a tectonised mixture of an opx-bearing serpentinised peridotite (harzburgite), pyroxenite layers, hornblendite layers and discontinuous bodies of dunite with occasional chromite mineralisation. The Morais UATC consists of serpentinised peridotite at Vinhas and does not contain the pyroxenite layers or dunite with chromitite bodies of the Bragança ultrabasic assemblage. These lithologies, and those of the Morais UATC outcrop at Caminho Velho, are described in more detail in chapter 2.

There is a variation in fabrics across the outcrop of the Bragança ultrabasic assemblage from relatively low strain areas which contain discrete layers of pyroxenite to higher strain areas where pyroxenite layers have become thinned and disaggregated. A large number of the ultrabasic rock exposures in the Bragança and Morais UATC have a high strain fabric and are frequently mylonitic. This means that the pyroxenite and peridotite lithologies have been mechanically mixed. It is only in relatively low strain zones such as the Tuela valley that discrete pyroxenite and peridotite samples can readily be identified and sampled. In the petrographic analysis of the peridotites a problem arises in deciding whether pyroxenes or amphiboles are derived from a sheared out pyroxenite layer or have crystallised as part of an original peridotite assemblage. This problem is addressed in chapter 2. The effects of the high strain associated with thrusting on the textures of the chromitites, platinum-group minerals and pyroxenites is also described in succeeding chapters.

The creation of the axial planar fabric within the Bragança ultrabasic assemblage, by progressive folding and boudinage, creates a repetition of pyroxenite or chromite-rich layers. The massive chromitite is created through boudinage of chromite-rich layers. Any original igneous stratigraphy or discordant fabrics have been destroyed. The original orientation of podiform chromite deposits within mantle sequences is often discordant to the mantle foliation (Cassard *et al.* 1981). Deposits lying concordantly with the surrounding harzburgite were shown by these authors to have undergone the most strain. The Bragança dunite and chromitite deposits have been orientated, in a rotational high strain regime, into the developing axial planar fabric during tectonic emplacement from the mantle. Folding

associated with Hercynian events, predominantly along a NW-SE trend, postdates this deformation and in places has caused reorientation of the pre-existing folds and foliation.

Figure 1.5.2 Evolution of the Bragança ultrabasic assemblage high strain fabric

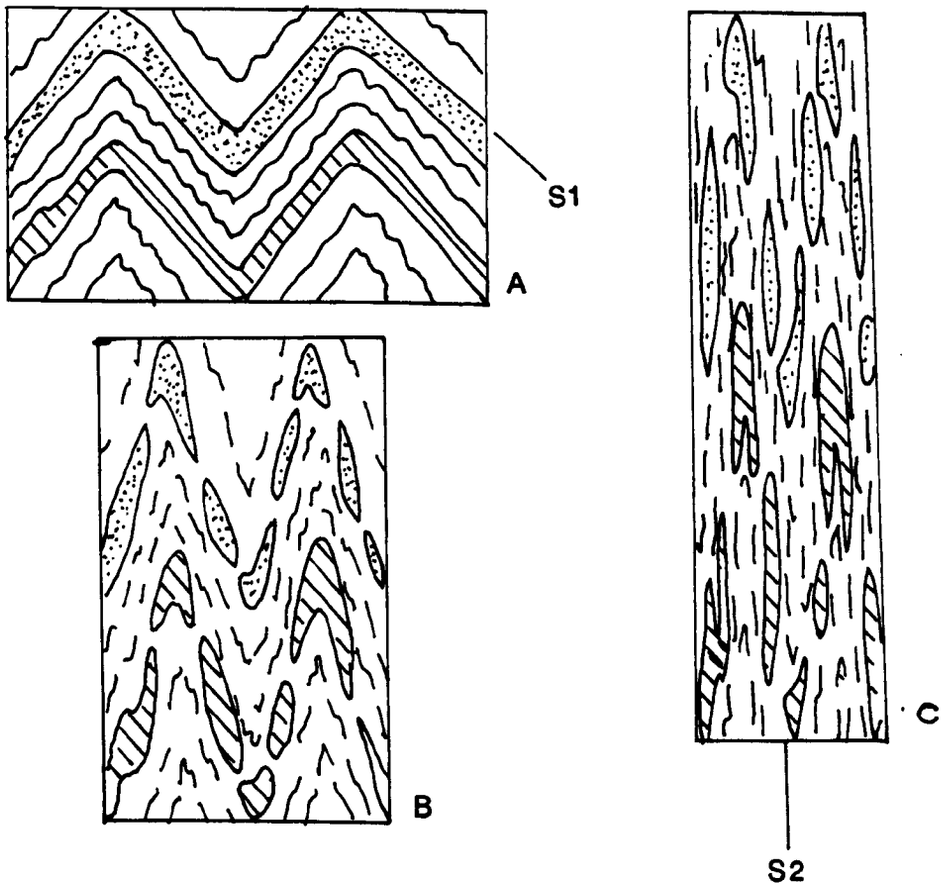

This figure is a diagramatic representation of the development of a high strain fabric such as that present in Bragança. The layers with patterns are competent layers (eg chromitite or pyroxenite) within a less competent peridotite matrix. A. An initial planar fabric S1 has been folded . B. With progressive increments of strain the limbs of the folds are rotated towards parallelism with the axial planes of the folds. The fold hinges start to disaggregate with boudinage. C. An axial planar foliation S2, of different orientation from S1 is developed. Competent layers are thinned and fold hinges are eliminated. From Hobbs *et al.* (1976).

Chapter 2 The petrography and geochemistry of the ultrabasic assemblage

2.1 Introduction

This chapter presents the results of the petrographic, geochemical and microprobe studies on the Bragança and Morais UATC ultrabasic assemblages with the aim of characterising the lithologies introduced in chapter 1. The main peridotite formation of Bragança is shown here to be serpentinised harzburgite. This contains layers of pyroxenite, hornblendite and a separate serpentinised dunite formation which contains occasional chromite mineralisation. The latter dunite with chromitite formation is distinguished by a pale grey colour from the generally more brown harzburgite formation. The dunite/chromitite formation is mainly considered in chapter 3. The Bragança ultrabasic assemblage is shown to have contrasting mineral compositions and geochemistry from the corresponding ultrabasic assemblage at Vinhas and Caminho Velho in the Morais massif.

All samples collected in the Bragança and Morais Massifs (groups Brag1-95 and 1-191BRG) are fully catalogued in appendix 5, together with their sample sites grid reference. A full suite of the different lithologies were collected from across the Upper Allochthonous Thrust Complex of the Bragança and Morais massifs.

2.2 Petrography of the Bragança UATC ultrabasic formations

2.2.1 Harzburgite

In an attempt to describe the primary, pre-serpentinisation rock type in Bragança point counts are presented on thin sections from this formation. As a first approximation it is assumed in this work that the serpentine and magnetite space was previously olivine as there is only limited replacement of pyroxene by serpentine minerals.

Table 2.2.1 Mineral modal abundances in the harzburgite formation

Modal%	191BRG	Brag34	166BRG	Brag87	Brag9	162BRG
Olivine	43.6	50.6	0.1	5.5	18.9	1.90
Orthopyroxene	1.7	8.8	1.6	10.3	0.4	0.0
Amphibole	1.9	2.5	0.2	0.0	0.0	0.0
Serpentine	52.0	32.9	88.1	72.1	72.0	87.1
Magnetite	0.6	5.1	9.9	12.1	7.3	8.9
Chromite	0.2	0.1	0.0	0.0	1.5	2.1

Table 2.2.1 (cont.)

Modal%	133BRG	108BRG	Range
Olivine	0.0	48.0	0.0 - 50.4
Orthopyroxene	5.8	1.9	0.0 - 10.3
Amphibole	0.0	2.6	0.0 - 2.5
Serpentine	82.9	46.5	32.8 - 87.1
Magnetite	9.1	1.0	0.6 - 12.1
Chromite	2.2	0.0	0.0 - 2.2

Based on 1000 point counts for each sample

The ranges of serpentine and magnetite contents of 32.8-87.1 and 0.6-12.1 modal percent of the samples in table 2.2.1 show the high degree of serpentinisation that this formation has undergone. The range in orthopyroxene content of 0.0-10.3 modal percent suggests that these lithologies were dunite to harzburgite before serpentinisation. Scattered amphiboles and chromite grains are minor constituents. This formation is referred to here as harzburgite to avoid confusion with the separate chromitite-bearing dunite formation. The harzburgitic, low orthopyroxene modal composition is characteristic of ultrabasic rocks from depleted mantle assemblages *eg* Nicolas (1986), Crawford *et al.* (1989).

Sections 2.2.1.1 to 2.2.1.5 descibe the distinguishing features of the mineral phases within the harzburgite formation.

2.2.1.1 Olivine

Where serpentinisation and deformation has not obscured pre-existing rock fabrics, three texturally distinct types of olivine grains can be identified. These three types are porphyroclastic, subgrain to neoblast, and grains found rimming orthopyroxene. The first type has relatively large grains, up to 2mm in diameter with irregular outlines. Apart from the ubiquitous serpentine veins which cross-cut and often surround the grains, they do not have mineral inclusions. Undulose extinction is common, sometimes giving a lamellar appearance to the olivine grains as they are rotated in crossed polars. At the margins of these porphyroclasts, or within augen like lenses (plate 2.2.1.1a) smaller olivine grains, less than 0.1mm in diameter are found. These second type grains have straighter edged outlines and commonly grain boundary angles approach 120 degrees. It would be expected that neoblasts of olivine formed as a result of deformation would be strain free. Some grains of this olivine type still have undulose extinction, indicating that there has been incomplete recrystallisation of the larger grains to strain free neoblasts. Instead, intermediate subgrains of olivine are formed. The third and least common type of olivine is associated with orthopyroxene porphyroclasts. Olivine grains with sizes ranging up to 0.1mm are sometimes found at the margins or enclosed within orthopyroxene grains (plate 2.2.1.1b). They can be distinguished optically by their higher birefringence. The olivine also has a less turbid appearance than orthopyroxene and does not contain cleavage or exsolution structures. The olivine is often associated with chromite grains within the orthopyroxene.

2.2.1.2 Orthopyroxene

Orthopyroxene occurs both as porphyroclasts and neoblasts. The porphyroclasts are up to 6mm in diameter with ragged, embayed margins. They usually have a turbid brown colour. The large orthopyroxene grains are often split along kink bands into subgrains, giving a lamellar appearance. The subgrains may have twisted cleavage. Ultimately, in cataclastic deformation, the orthopyroxene grains fragment. Undulose extinction is usual. The porphyroclasts are sometimes surrounded by polygonal shaped neoblasts which are of less than 0.1mm diameter. The neoblasts are strain free, without undulose extinction, having recrystallised from strained subgrains or porphyroclasts as a response to stress. (plate 2.2.1.2a)

Chromite and olivine mineral inclusions are found within large orthopyroxene crystals. The elongated shape and regular orientation of some chromite inclusion clusters suggests an exsolution texture (plate 2.2.1.2b). The size of chromite inclusions varies up to a few tens of microns. Silicate exsolutions are not clearly defined though fine (<10μm width) lamellae parallel to (100) planes in some orthopyroxene grains may be part of an exsolution texture.

2.2.1.3 Amphibole

Amphiboles in the harzburgite formation are identified in thin section by their 120 degree cleavage traces (plate 2.2.1.3). Grain lengths are typically about 0.5mm. They are colourless in thin section and sometimes contain chromite inclusions. In chapter 1 it was shown that the development of a high strain tectonic fabric had led to the formation of a tectonic mix of disaggregated pyroxenite layers and their amphibolitised products within the harzburgite formation. As a result of this, most of the amphiboles present in the harzburgite samples are assumed here to be derived from the thinning and disaggregation of relict pyroxenite layers.

2.2.1.4 Chromite

This opaque phase is readily distinguished in thin section by the characteristic opaque core and reddish-brown colour seen towards thinner grain edges. The main occurrence is as porphyroclastic grains with frequent pull-apart cracks filled with serpentine minerals and in places an elongation parallel to the foliation. Chromite grains located within large orthopyroxene or within a margin of neoblasts surrounding orthopyroxene crystals do not show this deformation.

2.2.1.5 Serpentine

Serpentine occupies up to 87.1 percent (by area) in thin sections examined (table 2.2.1). Samples with high proportions of serpentine also contain the most magnetite. The least serpentinised samples show serpentine veins cross cutting and rimming olivine. Olivine grains may be pseudomorphed completely by single serpentine grains. Around the

pseudomorphs are veins with magnetite along their centres. An apparent fibrous structure is seen in larger veins of this serpentine and in the cross-cutting veins. The pseudomorphs of olivine surrounded by the apparent fibrous serpentine together give a mesh texture characteristic of pervasively serpentinised peridotites. In the most highly serpentinised samples this pseudomorphing, mesh texture is less evident. In these cases serpentine grains are smaller, mainly being less than 30μm in diameter. The magnetite-bearing serpentine veins have an anastomosing pattern enclosing pods of fine grained serpentine. In such samples the orthopyroxene is also seen to be partially replaced by serpentine veins.

Pervasive serpentinisation is associated with the deformation of olivine-bearing rocks. Even in abyssal situations, serpentinised harzburgite samples have high strain foliations and textures produced during tectonic emplacement onto the oceanic floor (Cannat *et al.* 1992). Ocean water may be present during this tectonic associated serpentinisation, as shown by light O^{18}/O^{16} ratios (Evans 1977), but it is not a passive process.

2.2.2 Pyroxenites

Two types of pyroxenite layer are found within the harzburgite formation: orthopyroxene-bearing layers (websterites) and orthopyroxene-free layers (clinopyroxenites). The pyroxenites have been amphibolitised to varying degrees. There is a gradation between clinopyroxenite and its amphibolitised product (hornblendite). Orthopyroxene modal abundances range up to 78.7 modal% and amphiboles 22.9 % in samples examined (table 2.2.2).

The two types of pyroxenite present as layers within the Bragança ultrabasic assemblage are typical of other tectonic slices of relict mantle. Well documented examples are present in the Pyrénean ultrabasic nappes. Spinel-websterite, orthopyroxenite and garnet-pyroxenite layers are present in the Lherz, Frechinéde and Prades massifs of the Pyrénees (Bodinier *et al.* 1987). Rare hornblendite layers, a few mm to 3cm thick, composed of kaersutite amphibole, are also present (Fabries *et al.* 1989). Similarly Cr-rich clinopyroxenite and garnet-pyroxenite layers are present in the Beni-Bousera lherzolite massif of N. Morocco (Pearson *et al.* 1991). The origin of such pyroxenite layers is controversial though most theories have regarded the layers as high pressure crystal segregations formed in relict melt conduits within the lithosphere *eg* Nicolas and Jackson (1982), Bodinier *et al.* (1987). In chapter 5 the layers and smaller disseminations of pyroxenite, or secondary amphiboles derived from them, that are present in Bragança are considered with regard to their base-metal sulphide mineralogy and PGE geochemistry for possible evidence of melt infiltration into the harzburgite formation.

Table 2.2.2 Modal mineral abundances in pyroxenite and hornblendite samples

Modal%	6BRG	55BRG	141BRG	156BRG	35BRG
Clinopyroxene	67.8	39.9	62.6	11.9	3.4
Orthopyroxene	0.0	0.0	9.7	80.1	0.0
Amphibole	12.7	8.0	22.9	7.7	81.2
Chromite	0.2	0.0	0.9	0.2	0.0
Magnetite/opaque	0.3	2.1	1.7	0.0	9.9
Chlorite	18.9	0.0	2.2	0.0	0.0
Apatite and sphene	0.0	0.0	0.0	0.0	2.7
Fine matrix	0.0	50.0	0.0	0.0	0.0
Garnet	0.0	0.0	0.0	0.0	2.8

Samples 6BRG, 55BRG, 141BRG and 156BRG are pyroxenites, 35BRG is hornblendite. Based on 1000 point counts for each sample.

2.2.2.1 Orthopyroxene

The othopyroxene grains are similar to those from the harzburgite formation in size, turbid brown colour and general appearance. Grains often show deformation features, with larger porphyroclasts having twisted cleavage, undulose extinction and the development of subgrains. Fine lamellae of chromite and amphibole along the (100) cleavage orientation are common (plate 2.2.2.1a). Amphibole lamellae are more coarse along kink bands (plate 2.2.2.1b) sometimes having a recognizable typical amphibole outline. This suggests a stress related exsolution texture: the exsolutions have grown largest where the strain has been greatest. During this exsolution phase water must have been present in order to stabilise amphibole rather than clinopyroxene. Amphibole exsolution from pyroxene has been proposed by Prewitt (1980) as a plausible mechanism for the creation of some amphibole lamellae within pyroxene grains. Chromite exsolution is also more abundant, along kink bands (plate 2.2.2.1b).

2.2.2.2 Clinopyroxene

Clinopyroxene has a similar appearance in thin sections of both websterites and clinopyroxenites. It is distinguished from orthopyroxene by higher birefringence colours - second order compared to the first order greys typical of the orthopyroxene. Some of the grains have a lamellar, striped pattern in crossed polars which also serves to distinguish them from orthopyroxene and amphibole (plate 2.2.2.2a). Clinopyroxene grains are sometimes composed of subgrains in a mosaic pattern. Chromite exsolution is often well developed with alignment of grains along (100) and (001) orientations. Other more irregular clusters of chromite inclusions also occur. Silicate (amphibole) exsolution is present along these orientations in some larger grains. These exsolutions are coarser along discrete zones in a similar way to those within the orthopyroxene grains.

2.2.2.3 Amphibole

Amphibole is distinguished from pyroxene in thin section by the lack of strain induced features such as the clinopyroxene lamellae or kink bands. The amphiboles are colourless

and do not show any exsolution features (plate 2.2.2.3). The development of a high strain foliation within the harzburgite formation and the associated disaggregation of pyroxenite layers, described in chapter 1, has left dispersed amphibole grains or clusters of grains in some harzburgite samples. However in some outcrops which have undergone less strain, there are isolated clusters or discontinuous veins, a few cm wide, consisting of amphiboles. There is a gradation in size up to the larger, discrete pyroxenite layers with which they are related in origin. This group of amphiboles has replaced the clinopyroxene associated with the pyroxenite layers.

2.2.2.4 Opaque phases

Ilmenite is present as inclusions in pyroxene and between pyroxene grains in clinopyroxenite. In websterites chromite, with its characteristic reddish brown colour towards grain edges, is present. Chromite grain outlines are rounded except for the small (<50μm) exsolved grains which are more tabular. Sulphide grains rim pyroxenes and more rarely are present as inclusions. Some of these inclusions within pyroxene are located with chromite grains. The sulphide content of the pyroxenites is considered further in chapter 5.

2.2.3 Hornblendite

Throughout the harzburgite formation outcrop there are occasional dark coloured layers of hornblendite. Some of these layers are pegmatoidal, with amphibole grains reaching 15cm in length.

2.2.3.1 Amphiboles

This group of amphiboles is readily distinguished from those present in the harzburgite formation. In thin section the amphiboles are characterised by strong absorption colours and pleochroism. The absorption colours are: γ = very dark green, β = greenish brown, α = green. Cleavage is quite well developed with (110):(1-10) = 57-59°. Larger amphiboles in thin section show irregular extinction and ragged margins. Smaller amphibole neoblasts between the large grains show 120° grain boundaries with straight edged margins. Apatite and spinel inclusions are found within large amphiboles.

2.2.3.2 Clinopyroxene

Clinopyroxene grains show faint green pleochroism with poorly developed cleavage and have second order birefringence colours. Within and at the edges of pyroxene there are sometimes irregular patches of the green amphibole (plate 2.2.3.2). This is an alteration texture, with the amphibole progressively replacing clinopyroxene. In this way the hornblendite layers have been created by the alteration of clinopyroxenite layers but in a different process from that which created the colourless amphiboles present in other pyroxenite thin section samples. This amphibolitisation process is discussed further in section 2.6.2 with regard to the amphibole compositions.

2.2.3.3 Garnet, apatite, sphene, sulphides and magnetite.

Hornblendite samples are rich in apatite and sphene unlike their clinopyroxenite precursors. Accessory minerals together form 15.3 modal % within section of sample 35BRG (table 2.2.2) The majority of this is made up of the opaque phases, sulphide and magnetite which are found rimming amphiboles and less commonly as inclusions within amphibole grains. Apatite grains are clear in plane polarised light and have low order, grey birefringence colours. These grains are present either as inclusions within garnet or amphibole or as small clusters of grains. Sphene grains with characteristic high birefringence and relief are an occasional accessory. Garnets in thin section have a light pink colour, with frequent opaque and amphibole inclusions.

2.3 Petrography of the Morais UATC - Caminho Velho and Vinhas

The main lithology within the Morais UATC ultrabasic assemblage is an amphibole and orthopyroxene-bearing serpentinised peridotite. Because of the high degree of serpentinisation and chloritisation the samples have undergone, the point counts in table 2.3 do not allow for more precise ultrabasic identities to be used *eg* wehrlite or harzburgite. Unlike the Bragança UATC, there are exposures of troctolite and metagabbro at Caminho Velho. The pyroxenite and dark hornblendite layers characteristic of the Bragança ultrabasic assemblage are not present at Vinhas or Caminho Velho.

Table 2.3 Modal mineral abundances in the Morais (Caminho Velho and Vinhas) peridotite samples

	73BRG	184BRG	100BRG	102BRG
Olivine	20.5	36.5	7.3	14.3
Orthopyroxene	9.9	2.0	14.0	0.9
Clinopyroxene	5.0	0.3	0	0
Serp.+chlorite	41.0	47.1	65.7	69.6
Mt/opaque	0.7	1.4	9.2	7.3
Chromite/spinel	5.9	0.9	0.2	0
Amphibole	17.0	11.8	3.7	7.9

Based on 1000 point counts

2.3.1 Peridotite

Olivine grains up to 2mm in diameter are seen in the secondary amphibole-bearing peridotite. Undulose extinction and the development of neoblasts are seen in thin section. Colourless bladed amphibole grains up to 1.5mm long and occasional lenses of orthopyroxene with subgrain structures are present. Some orthopyroxene grains are partially altered to serpentine. The textures of the serpentine matrix are similar to those of the Bragança ultrabasic samples: anastomosing veins of magnetite and serpentine are arranged in lenses around olivine or mosaics of fine grained serpentine plates. The spinel

phase has a green colour in thin section, distinct from the more reddish colour of the chromite grains of the Bragança harzburgite formation.

2.3.2 Troctolite and metagabbro

Within the troctolite (sample 96BRG) from Caminho Velho, plagioclase shows extensive turbid alteration but simple and Carlsbad twinning are still clear. Brown to reddish chromite grains are found at the margins or included within olivine. Orthopyroxene grains with low birefringence and occasional chromite inclusions, are present surrounding and enclosing olivine grains and also as subgrains and neoblasts. In the gabbroic sample (97BRG) feldspar is almost entirely altered to a fine grained white clay. About half of the rock is composed of pale green prismatic amphiboles which appear colourless in thin section. Individual green amphibole grains are visible in hand specimen and this serves to distinguish the formation from the amphibolites of the Ophiolite Thrust Complex (OTC) in the nappes underlying the UATC. This troctolite and metagabbro formation was described as olivine-bearing coronitic gabbro by Ribeiro (1974).

Chapter 2 plates

Plate 2.2.1.1a Lens of olivine and opx neoblasts; part of high strain/mylonitic fabric within a harzburgite sample. At this fine scale (neoblasts <0.1mm) opx and olivine are indistinguishable. Xpl. F.O.V. 3mm.

Plate 2.2.1.1b Large enstatite grain from harzburgite formation with small olivine grain towards central lower margin. Olivine grains along corroded margins of opx grains show a possible alteration texture. Xpl. F.O.V. 0.9mm.

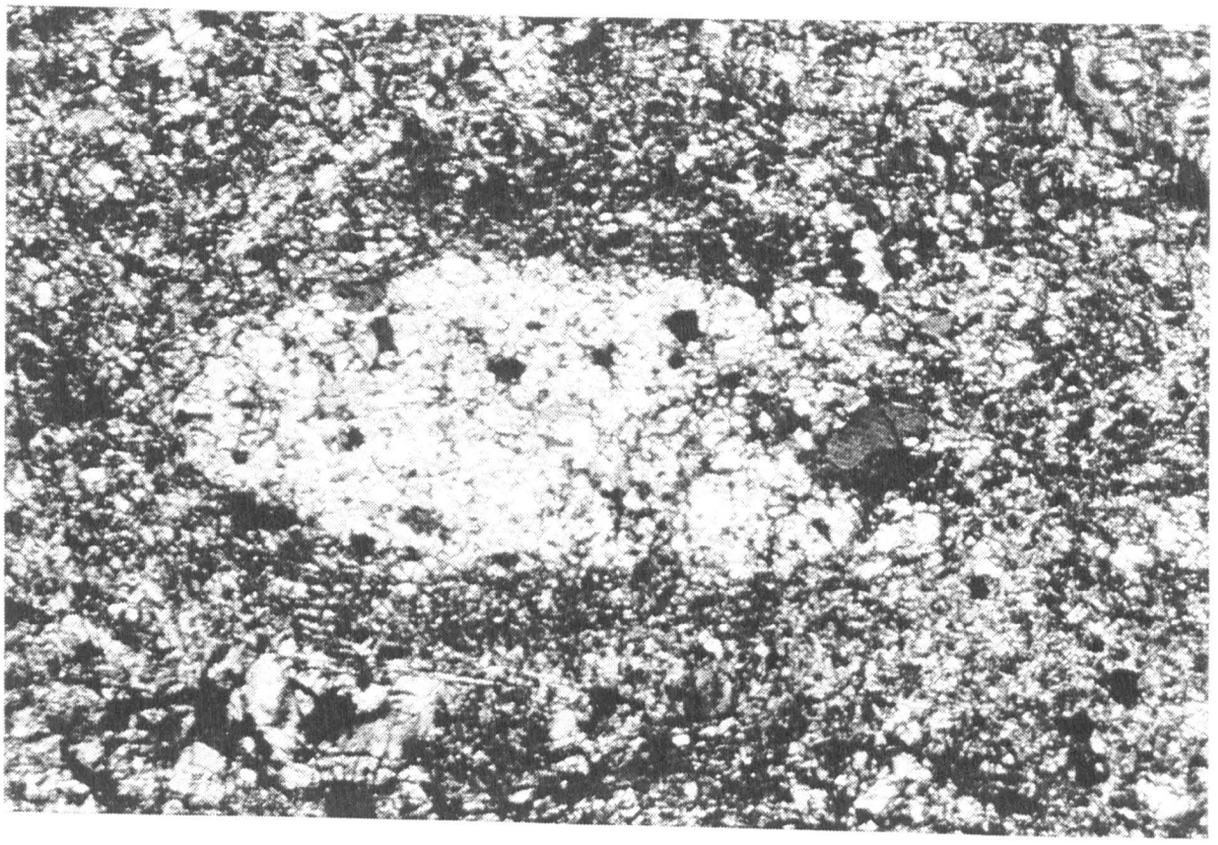

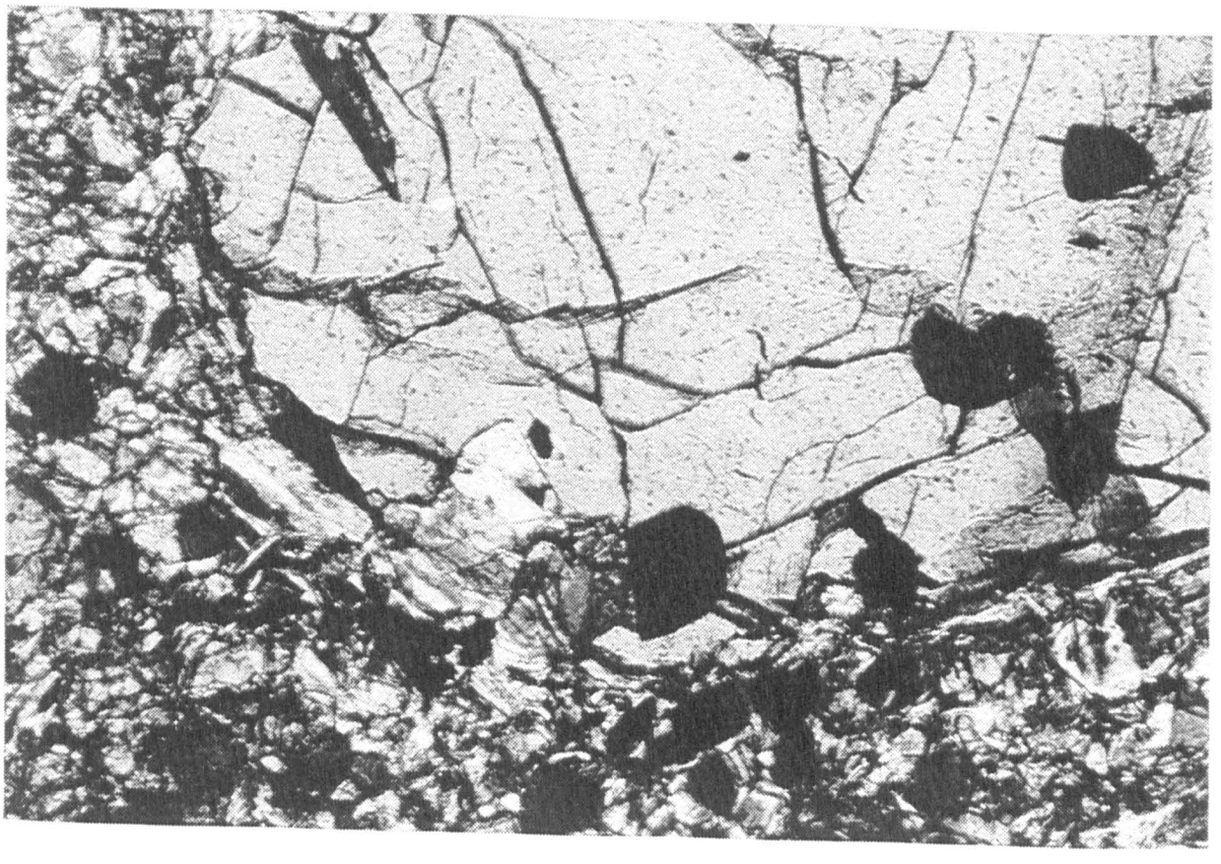

Plate 2.2.1.2 Porphyroclastic texture within harzburgite sample. Enstatite porphyroclast shows partial replacement by serpentine veins and fine subgrain to neoblast development at the margins. Ppl. F.O.V. 3mm.

Plate 2.2.1.3 Dispersed amphiboles showing 120degree cleavage within harzburgite formation sample. Large olivine grains are partially replaced by serpentine veining. Ppl . F.O.V. 3mm.

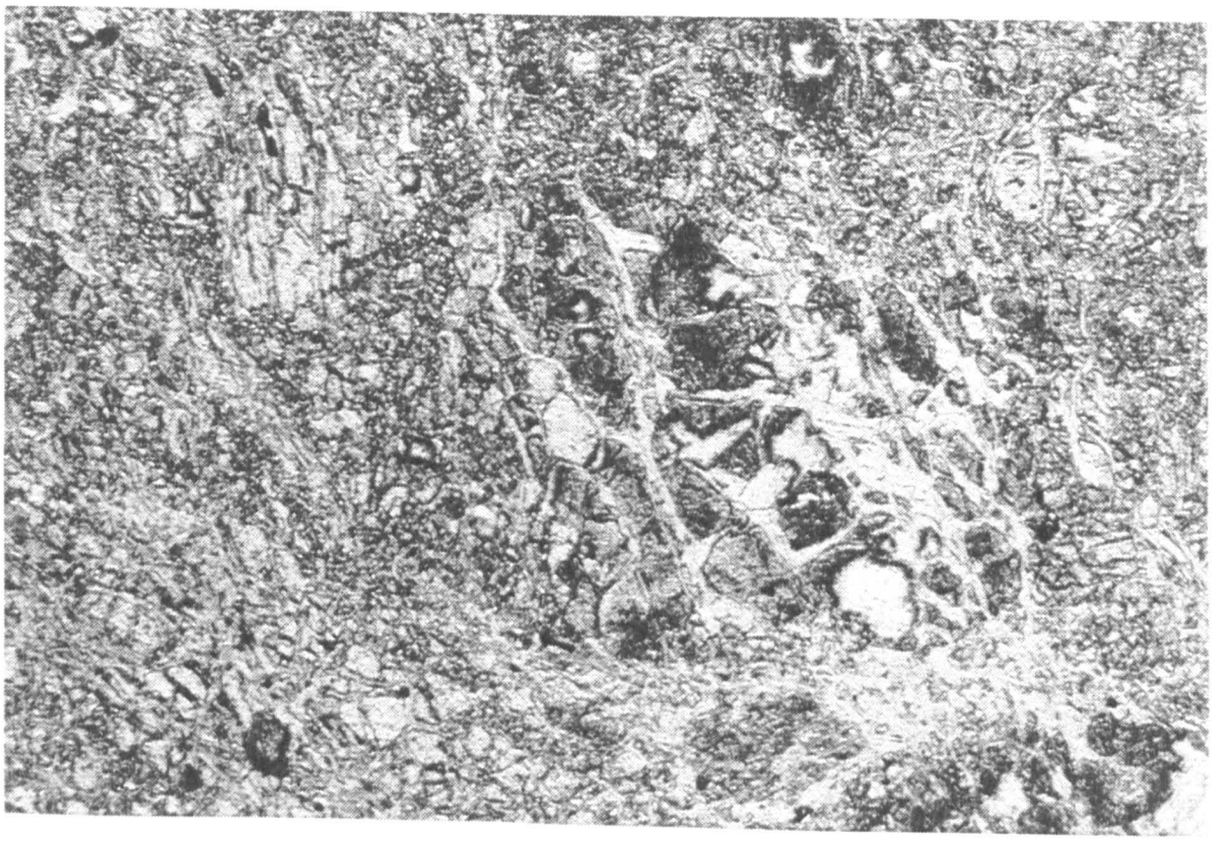

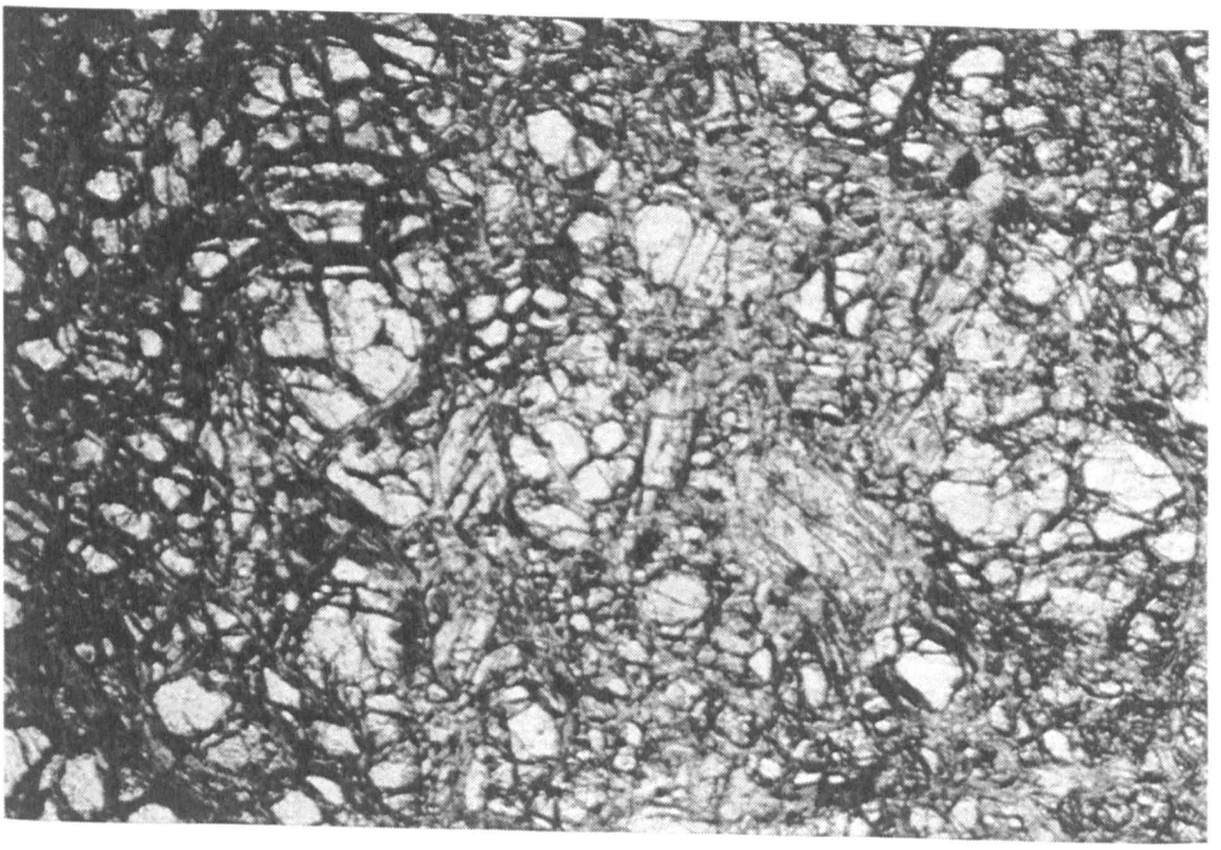

Plate 2.2.1.5 High strain-mylonitic texture in highly serpentinised harzburgite sample. The pseudomorph texture showing replacement of olivines in lower strain samples has disintegrated. Magnetite is present in the centres of cross cutting chrysotile veins. Xpl. F.O.V. 3mm.

Plate 2.2.2.1a Enstatite porphyroclast in websterite with chromite exsolution along (100) orientation. The margins of the opx are subgrain structure to fully recrystallised neoblasts. Ppl. F.O.V. 2mm.

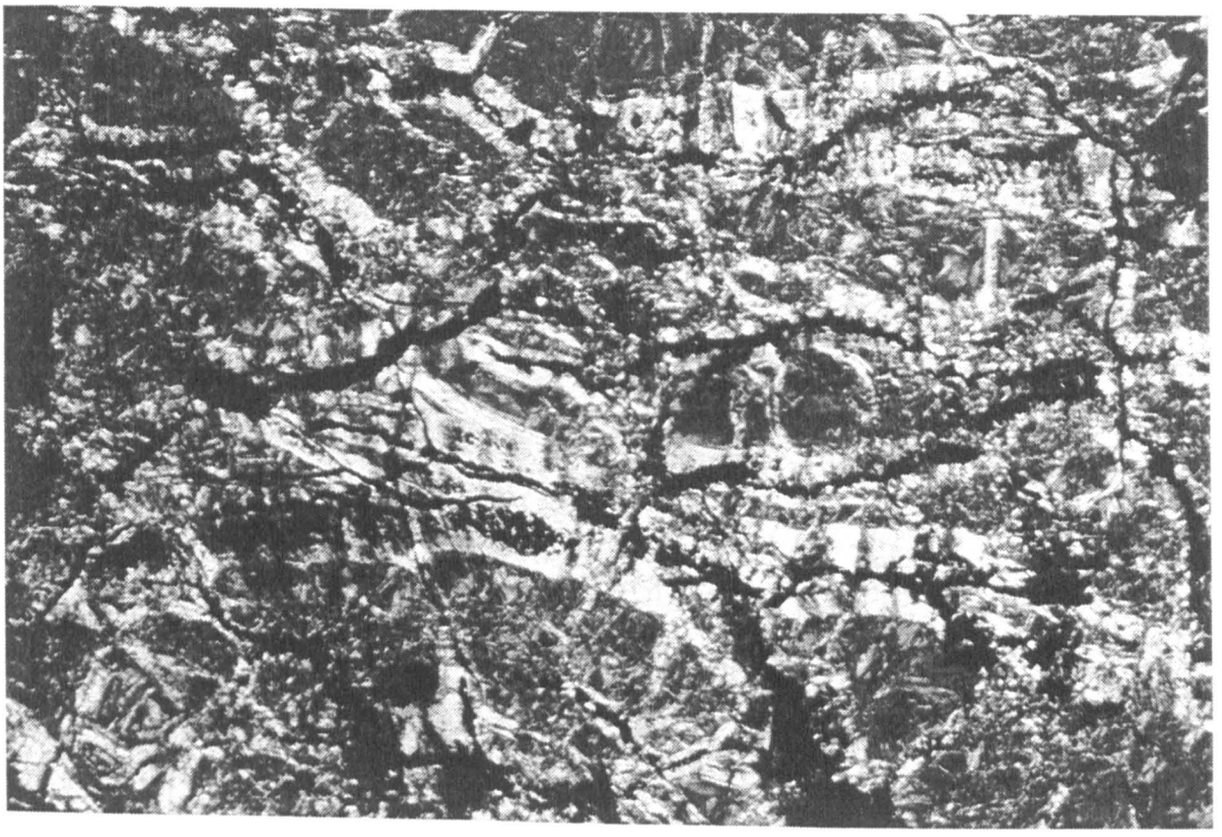

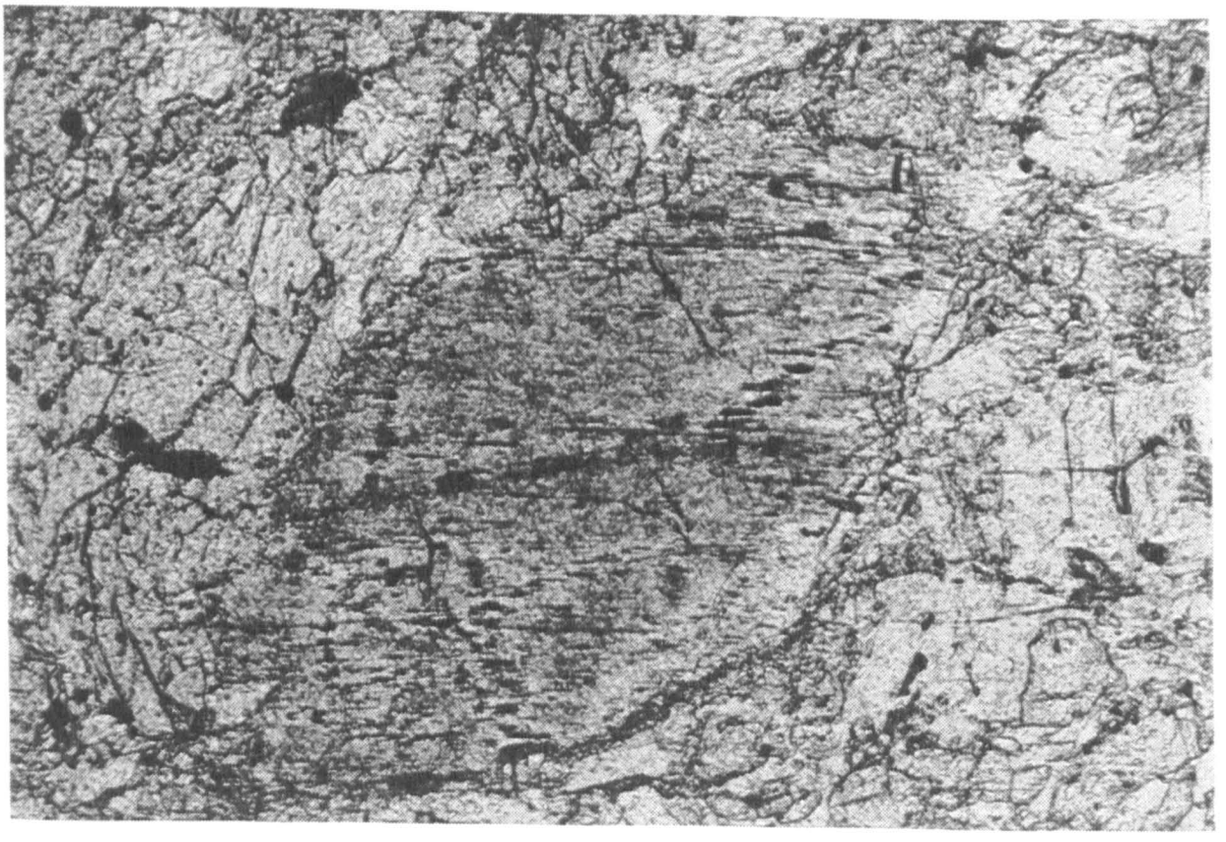

Plate 2.2.2.1b Acicular amphibole exsolutions most coarse along kink band of enstatite from websterite. Xpl. F.O.V. 0.9mm.

Plate 2.2.2.2 Clinopyroxenite containing diopside and tremolite amphibole. The cpx grains show strain lamellae whereas the amphibole grains are mainly strain free. The margins of the cpx and amphiboles are recrystallised to subgrains and neoblasts. Xpl. 3mm.

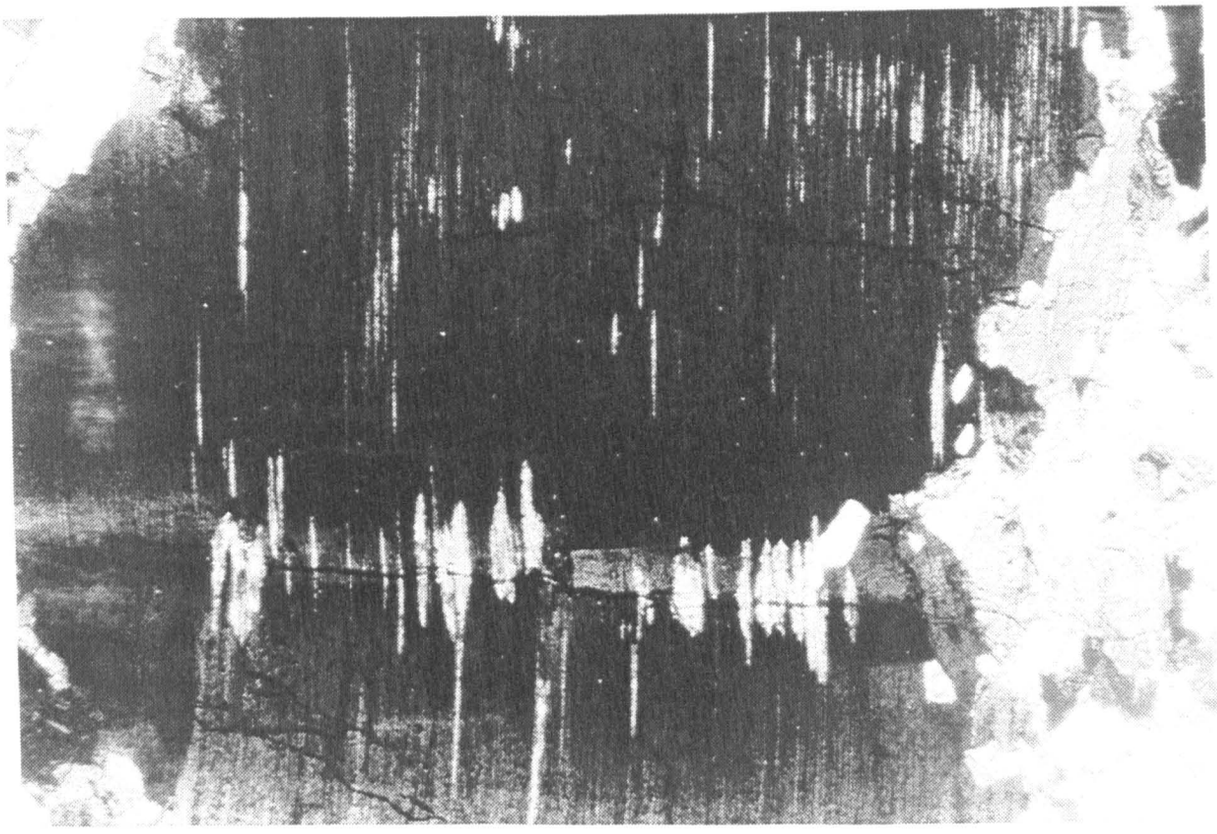

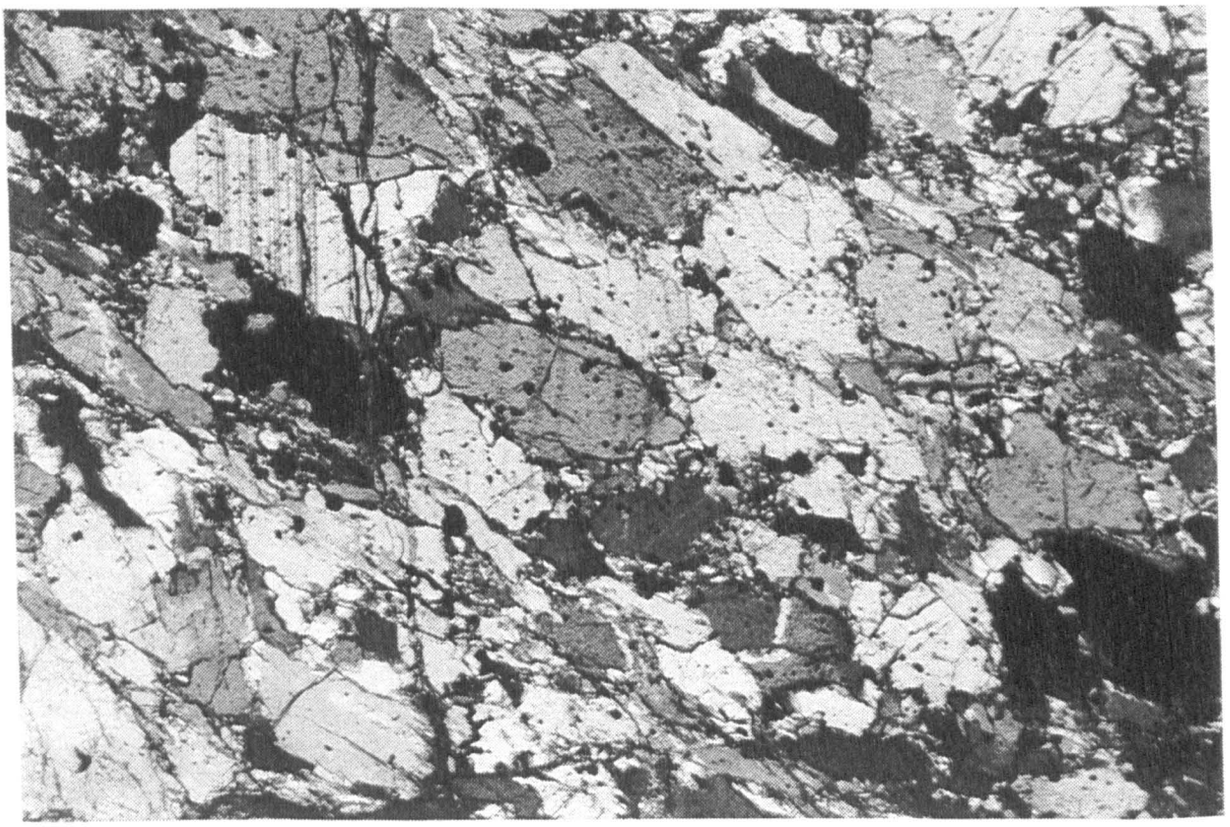

Plate 2.2.2.3 Amphibolitised websterite. Enstatite porphyroclast in the top centre of the photograph shows strain induced kink band and amphibole inclusions. Acicular amphiboles at lower margin of enstatite are strain free showing the syntectonic nature of the amphibolitisation. Xpl. F.O.V. 3mm.

Plate 2.2.3.2 Metasomatic alteration of clinopyroxene grains to ferroan pargasitic hornblende . The large pale cpx grain in the centre of the photograph contains patches of darker ferroan-pargasitic hornblende. The large dark green grain on the right side of the photograph is also amphibole. The margins of the large cpx grain are composed of subgrains created through strain exerted on the grain. Xpl. F.O.V. 2mm.

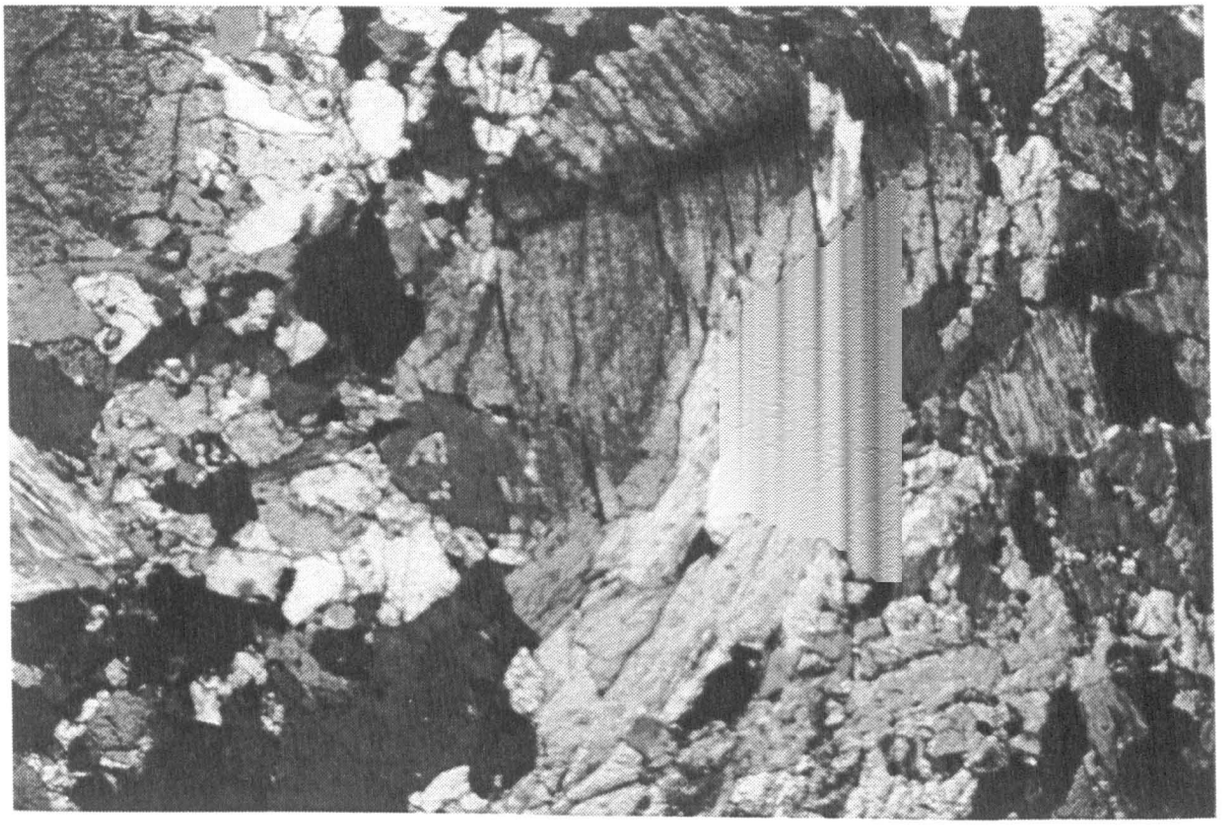

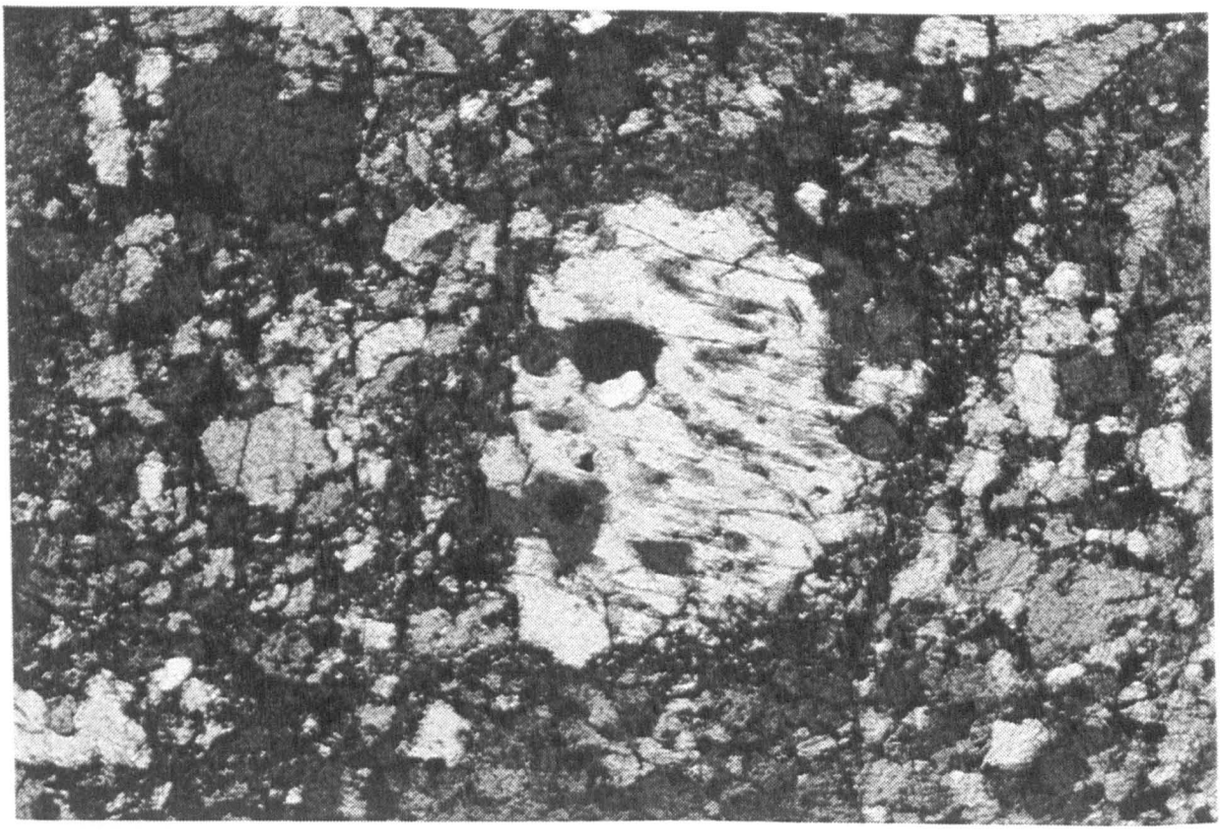

Plate 2.5.1 Enstatite porphyroclast within harzburgite sample showing glide planes along the (100) orientation. Fine recrystallisation along margins of enstatite. Xpl. F.O.V. 2mm.

Plate 2.5.2 Poikilitic texture within troctolite. Opx surrounds olivine grains. Serpentinisation leaves only lenses of olivine in left of photograph. Xpl. F.O.V. 0.9mm.

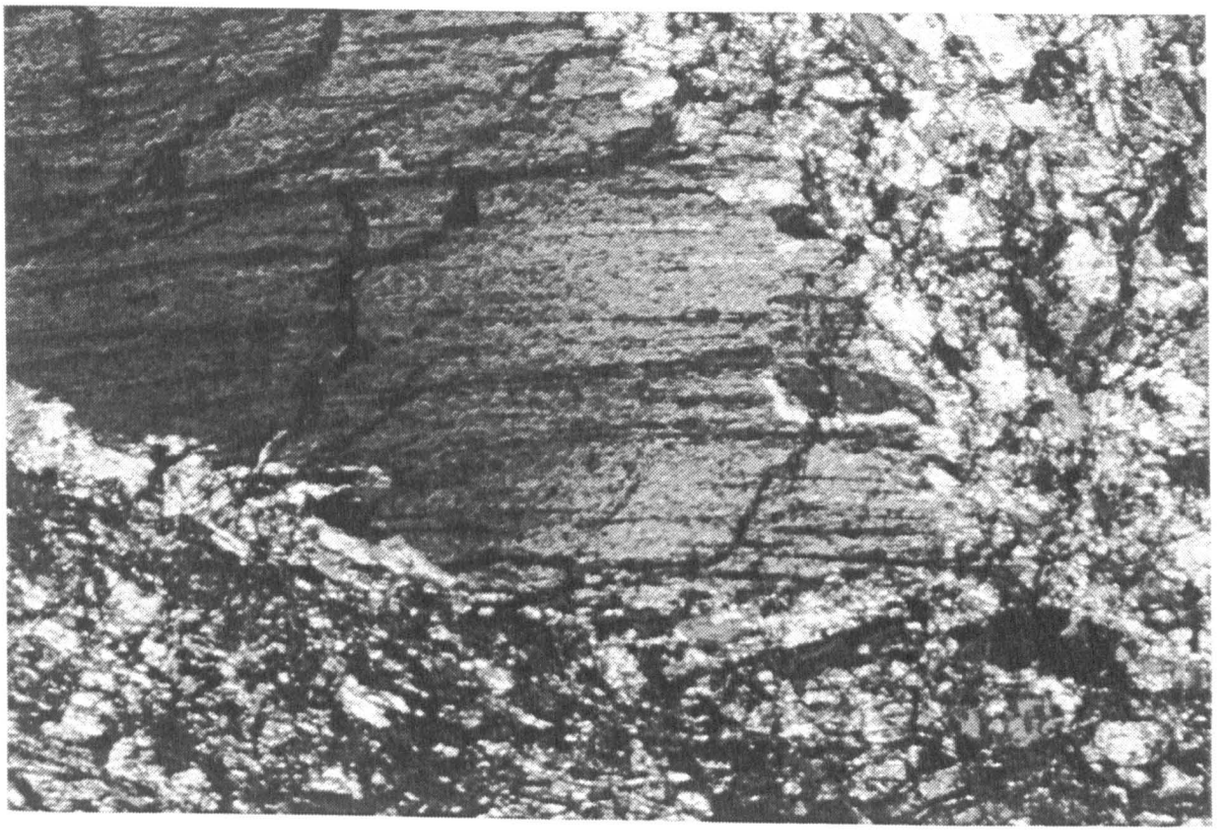

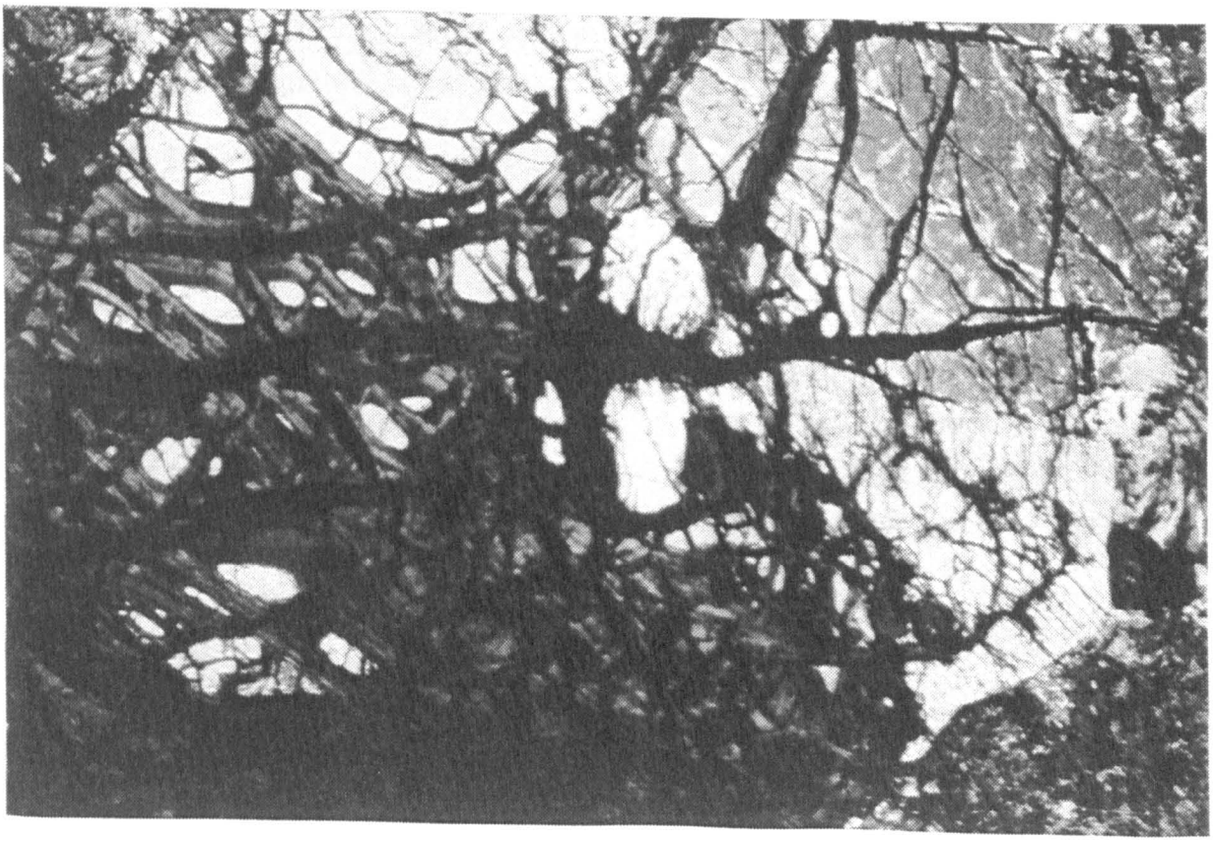

2.4 Other Bragança UATC lithologies

The largest area of outcrop in the Bragança UATC is covered by the garnet-amphibole-feldspar-gneiss noted in chapter 1 (the blastomylonites and amphibolitised granulites of Ribeiro 1974). The garnet-amphibole-mica-gneiss described in the Derruida mapped area is also part of the larger paragneiss formation of Ribeiro (1974) and is not described further here. The pargasite-bearing peridotite is more rare, the only example found being from the Derruida mapped area (map 1).

2.4.1 Garnet-amphibole-feldspar gneiss

In thin section the same dark green, intensely pleochroic amphibole, apatite, garnet and sphene assemblage is present in the gneiss formation as in the hornblendite layers of the ultrabasic assemblage. The difference is the presence of feldspar at most exposures of the gneiss formation, otherwise the two formations appear indistinguishable and may share a common origin.

2.4.2 Pargasite-bearing metaperidotite

In the Derruida map (map 1) this formation was identified as a tectonic slice within the garnet-feldspar-amphibole-gneiss formation. It consists of pargasite, colourless in thin section and olivine. Some of the olivine grains are poikilitically enclosed within the amphiboles, suggesting a relict pre-amphibolitisation igneous texture. This formation appears to be unique and as there is no obvious link with the harzburgite formation.

2.5 Textures

2.5.1 Bragança ultrabasic assemblage

The range in textures and the recrystallisation characteristics of mineral grains seen in thin sections reflect the degree of strain that the samples have undergone. There are no relict igneous textures. The sketches below (fig. 2.5.1a-c) depict the textures arising in samples which have undergone varying degrees of strain in the ultrabasic assemblage rocks.

A

B

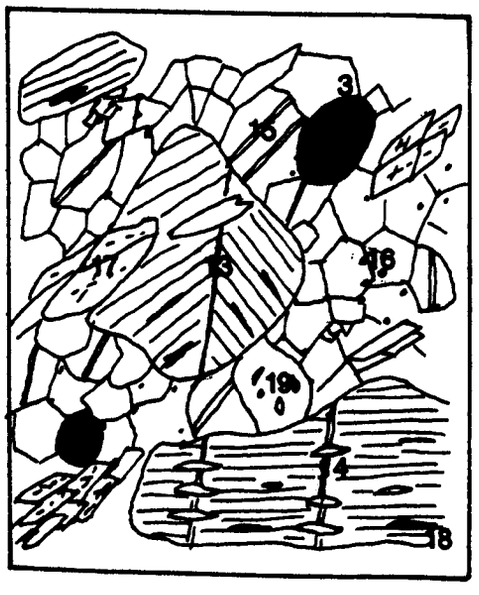

C

Key to figure 2.5.1 on facing page

(A) low strain porphyroclastic fabric in harzburgite (sample 191BRG), (B) high strain mylonitic fabric in harzburgite (sample 166BRG), (C) porphyroclastic fabric in websterite (sample Brag83).

1 Orthopyroxene porphyroclast with slip planes along (100), 2 Olivine grain surrounded and veined by serpentine, 3 Chromite grain, 4 Serpentine mesh texture with magnetite in centre of veins, 5 Recrystallised orthopyroxene neoblasts around orthopyroxene porphyroclast, 6 Lens of olivine and orthopyroxene neoblasts, 7 Twisted orthopyroxene grain, 8 Large fibrous serpentine vein with magnetite along centre, 9 Bastite (orthopyroxene affected by serpentinisation), 10 Fine grained serpentine plates, no mesh texture, 11 Olivine along corroded margin of orthopyroxene, 12 magnetite, 13 Kink band in orthopyroxene, 14 exsolution of amphibole concentrated along kink bands, 15 Deformation lamellae in clinopyroxene, 16 Dusting of chromite grains across websterite, 17 Amphibole, 18 chromite exsolved along (100) plane of orthopyroxene, 19 Blebby exsolution in clinopyroxene.

Relatively low strain textures are marked by coarse olivine grains and lower degrees of serpentinisation. Orthopyroxene has kink bands and subgrains and undulose extinction is common in both olivine and orthopyroxene. This is a porphyroclastic texture (*eg* Basu 1977). Progressively higher degrees of strain are marked by a decrease in grain size accompanying the formation of subgrain structures within pyroxenes and ultimately recrystallised, strain free neoblasts. Large orthopyroxene grains remain even at the highest strain. The serpentine mesh texture, which pseudomorphs olivine grains, is replaced by a more lensoid, sheared serpentine fabric. Brittle fracture of orthopyroxene and chromite grains also occurs creating pull-apart cracks. A progressively more mylonitic fabric is created in the olivine-bearing rock types and the distinctions between lithologies becomes unclear with the development of mylonite zones as relict pyroxenite, dunite and peridotite are mechanically mixed.

The formation of orthopyroxene kink bands along (100) planes is characteristic of slip or translational gliding deformation mechanisms (plate 2.5.1). Slip occurs when there is shear along a crystallographic plane between one part of a mineral grain and another. The polygonisation, annealing textures seen in the development of neoblast mosaics with 120 degree grain boundaries shows that syntectonic recrystallisation of entire mineral grains has also been operative in accomodating strain (Nicolas *et al.* 1971). Exsolution coarsening is also associated with slip mechanisms and the development of kink bands in pyroxenes. With polygonisation of porphyroclastic pyroxenes, exsolved chromite grains are released into the matrix. Pyroxenes within the recrystallised groundmass do not contain chromite exsolutions. As well as chromite grains associated with the polygonisation and breakdown of pyroxenes in the websterites and harzburgite (similar to textures described by Mercier and Nicolas 1975), the presence of olivine grains at embayed edges to some orthopyroxene grains suggests that this olivine may also be a breakdown product.

The strain free nature of amphiboles within the websterites and the coarsening of exsolutions along orthopyroxene kink bands suggests that a syntectonic amphibolitisation took place. Serpentinisation in the ol-bearing ultrabasic rocks is also syn-tectonic as it becomes more pervasive in samples that have textures which indicate that they have undergone a high degree of strain.

The process of serpentinisation is associated with tectonism of ultrabasic rocks in dredged ocean floor ultrabasic samples (Evans 1977, Cannat *et al.* 1992), ophiolites (Prichard 1979) and continental derived, thrust emplaced complexes (Lorand 1989). Therefore the tectonic related serpentinisation of the Bragança harzburgite formation need not imply an oceanic origin. Instead in this thesis, it will be suggested on the basis of a range of mineralogical and geochemical evidence that the ultrabasic formation was created at a continental destructive margin.

2.5.2 Morais UATC

The serpentinisation and pyroxene grain textures are similar to those of the Bragança UATC ultrabasic assemblage, showing features of slip and polygonisation associated with deformation. This suggests that a similar syntectonic amphibolitisation also took place, in which the amphiboles within the peridotite replaced clinopyroxene. Large orthopyroxene porphyroclasts are less frequent, and there is less chromite, compared to Bragança. The important textural feature of the Morais UATC ultrabasic assemblage outcrops occur within the troctolite outcrop at Caminho Velho (plate 2.5.2). The surrounding of olivine grains by pyroxene is reminiscent of a cumulus texture, the olivine being the cumulus phase and the pyroxene the intercumulus phase. This is the only such unambiguous igneous texture found within the UATC ultrabasic assemblage.

2.5.3 Comparisons with mantle-derived textures

Peridotite textures from mantle xenoliths are derived by plastic flow mechanisms, exhibiting kink bands, polygonisation and the development of subgrains. Where the subgrains within pyroxenes exhibit complete recrystallisation and a strain-free nature they are considered neoblasts. These features create the porphyroclastic textures which are most common in mantle xenoliths (Mercier and Nicolas 1975, Basu 1977). They are similar to some of the textures described for the Bragança ultrabasic assemblage in this chapter.

The processes of mylonitisation, amphibolitisation and serpentinisation have acted to overprint any original mantle derived fabric in the ultrabasic samples studied here. The cataclasis of enstatite augen, formation of lensoid clusters of neoblasts, and creation of fine grained polygonal neoblasts in rock groundmass are all a result of the mylonitisation associated with emplacement thrusting. The glide planes shown in enstatite augen of websterites are typical relicts of mantle-derived textures *eg* Basu (*op. cit.*).

2.6 Mineral composition in the Bragança and Morais UATC ultrabasic assemblages

Table 2.6 gives the compositional parameter ranges for olivine, orthopyroxene, clinopyroxene, amphibole, spinel and sheet silicate for different formations within both the Bragança and Morais UATC ultrabasic assemblages. A full set of probe analyses is given in appendix 4. In the following sections the chromite and olivine data is used to calculate temperatures of equilibration between the two phases within the harzburgite and chromitite formations. Aspects of the chromite grain compositions are also used to characterise and distinguish between the Bragança harzburgite formation and the Morais peridotite. In this respect the low range of the $100Mg/(Mg+Fe^{2+})$ ratio and TiO_2 contents in chromite grains from harzburgite formation samples compared to those from the Morais ultrabasic samples are important. Amphibole compositions effected by metasomatic processes are characterised by high alkali and low Si contents. This feature gives information about the creation of the hornblendite layers, their amphibole type having higher alkali and lower Si contents than other secondary amphiboles from the Bragança ultrabasic assemblage.

Table 2.6 Mineral compositions

'N' in the tables below refers to the number of samples for which the range of compositional parameters is given.

Table 2.6.(A). Olivine

	Chromitite/chromite-rich. N=17	Harzburgite formation N=19	Morais UATC N=24
Fo	0.93-0.95	0.91-0.92	0.85-0.92
MnO	0.06-0.11	0.11-0.16	0.14-0.29
NiO	0.26-0.53	0.35-0.45	0.16-0.39

Only those samples for which NiO was analysed are plotted on fig. 2.6.1b

Table 2.6.(B). Orthopyroxene

	Harzburgite N=17	Websterite N=23	Morais UATC N=7
Al_2O_3	0.27-1.86	0.25-1.41	2.91-4.44
$Ca/(Ca+Mg+Fe^{2+})$	0.13-1.12	0.22-2.15	0.56-1.13
$Fe^{2+}/(Ca+Mg+Fe^{2+})$	6.89-14.03	6.63-16.97	7.27-10.25
$Mg/(Ca+Mg+Fe^{2+})$	85.66-92.77	82.57-93.07	88.76-91.78

Table 2.6.(C). Clinopyroxene

	Wollastonite %	Enstatite %	Ferrosilite %
Pyroxenite N=23	47.36-51.00	39.10-49.69	2.96-5.95
Morais UATC N=1	45.13	49.94	4.93

Table 2.6.(D). Amphibole

	Hornblendite N=15	Pyroxenite N=14	Morais UATC N=17	Harzburgite N=7
(Na +K) A	0.57-0.86	0.00-0.29	0.01-0.80	0.02-0.13
Si	6.13-6.36	7.32-7.71	6.12-7.81	6.92-7.75
(Na) B	0.07-0.29	0.02-0.19	0.09-0.30	0.00-0.09
$Mg/(Mg+Fe^{2+})$	0.48-0.70	0.93-1	0.94-1	0.92-1

contains six analyses with apparent $Mg/(Mg+Fe^{2+}) >1$, contains three >1, contains one ratio >1. This is due to the nature of the ferric/ferrous recalculation scheme as outlined in appendix 3. A and B refer to site allocation.

Table 2.6.(E). Spinel

	Harzburgite N=23	Pyroxenite N=15	Morais UATC N=19
100Cr/(Cr+Al)	33.35-56.59	56.62-75.03	15.82-63.20
$100Mg/(Mg+Fe^{2+})$	45.50-81.66	28.17-51.05	19.81-67.96
$100Fe^{3+}/(Cr+Al+Fe^{3+})$	5.96-20.01	5.66-15.96	3.94-24.31
TiO2	0.00-0.20	0.15-0.53	0.05-5.03

Table 2.6.(F). Sheet Silicate

	Serpentine from chromite-rich samples N=9	Chlorite from clinopyroxenite N=4	Chlorite from chromite-rich samples N=12
Fe/(Fe+Mg)	0.03-0.06	0.12	0.02-0.03
Si cation	7.9-8.1	5.7-5.8	5.8-5.9
Cr cation	0-0.06	0.08-0.1	0.34-0.43

Table 2.6.(G). Feldspar

	Troctolite N=5	Gt-Fel-amph-gneiss N=12
Anorthite%	76.9-82.4	22.7-28.8
Orthoclase%	0.06-2.4	0.3-1.8
Albite%	16.2-22.1	68.6-76.8

2.6.1 Chromite and olivine compositions

The compositions of co-existing olivine and accessory spinel in peridotites are interdependent. Continuous re-equilibration of Mg and Fe^{2+} between olivine and spinel at submagmatic temperatures causes the compositions of co-existing olivine and accessory

chromite in peridotites to be interdependent (*eg* Roberts 1986). Geothermometers have been calibrated for olivine-spinel pairs by Roeder *et al.* (1979) and Fabries (1979) on the basis of calculated Mg and Fe^{2+} distribution coefficients. Brown (1982) used these geothermometers on olivine-spinel pairs from the Oman ophiolite harzburgite and obtained sub-magmatic equilibration temperatures between 550 and 825°C. Sack and Ghiorso (1991) presented a model, which was specifically calibrated for relatively low temperature olivine-spinel assemblages in metamorphosed ultrabasic rocks, relating the temperatures of equilibration of Mg and Fe^{2+} to the thermodynamic properties of chromian spinels.

Chromite grain compositions from the harzburgite formation are plotted on fig 2.6.1a. They lie between isotherms of 630 and 500°C. The range of co-existing olivine compositions predicted by this model, about Fo_{90-95}, overlaps the range actually obtained of Fo_{91-92} (table 2.6a). Chromite grain analyses from two samples of the chromite-rich assemblage where olivine analyses have been taken are also plotted on figure 2.6.1a. These give temperatures of 500-550°C and plot at or to the right of the Fo_{95} contour. This is in agreement with the Fo_{93-95} range obtained for olivine compositions in the chromite-rich samples. In chapter 6 the temperature of equilibration for Mg and Fe^{2+} exchange between olivine and chromite is discussed in relation to the metamorphic data available for the N.W. Iberian massifs.

As the ratio of olivine to chromite within the harzburgite formation samples is high, there will be a buffering effect on the olivine composition. The accessory chromite grains will not greatly alter the olivine compositions throughout the assemblage. Conversely the scarce olivine within chromitites will have undergone a greater relative change in composition compared to the more abundant chromite grains. For this reason, despite limited changes in olivine composition due to re-equilibration with accessory chromite, it is considered that the different groupings in olivine grain compositions between the harzburgite formation and Morais UATC peridotite (table 2.6.1a) originated in primary processes during initial crystallisation.

The UATC olivine compositions lie in three main groups when the Fo content is plotted against NiO wt% content figure 2.6.1b. Olivines from Morais UATC samples range from Fo_{85-92}, NiO wt% 0.35-0.45; olivines from the harzburgite formation Fo_{91-92}, NiO wt% 0.21-0.45 and those from chromite-rich samples Fo_{93-95}, NiO wt% 0.26-0.53. Table 2.6.1 summarises olivine Fo contents from different mantle assemblages, stratiform intrusions and chromitites for comparison with this data.

Figure 2.6.1a Temperatures of equilibrium between co-existing olivine and chromite

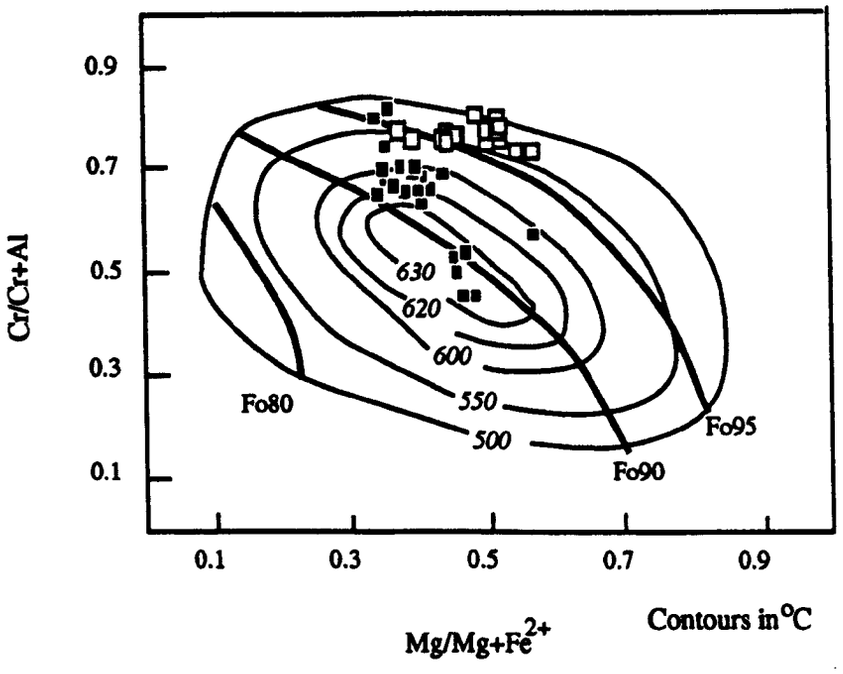

■ Accessory chromite from harzburgite formation

□ Chromite from chromitite samples

This plot of Cr/(Cr+Al) against $Mg/(Mg+Fe^{2+})$ is contoured for the compositions of co-existing olivines from Fo80-95 and the temperature of equilibration of Mg and Fe between the chromite and olivine phases. Chromite from the harzburgite formation records temperatures of 500-630°C and the chromitite samples 500-550°C. From Sack and Ghiorso (1991).

Figure 2.6.1b Olivine NiOwt% v Fo number

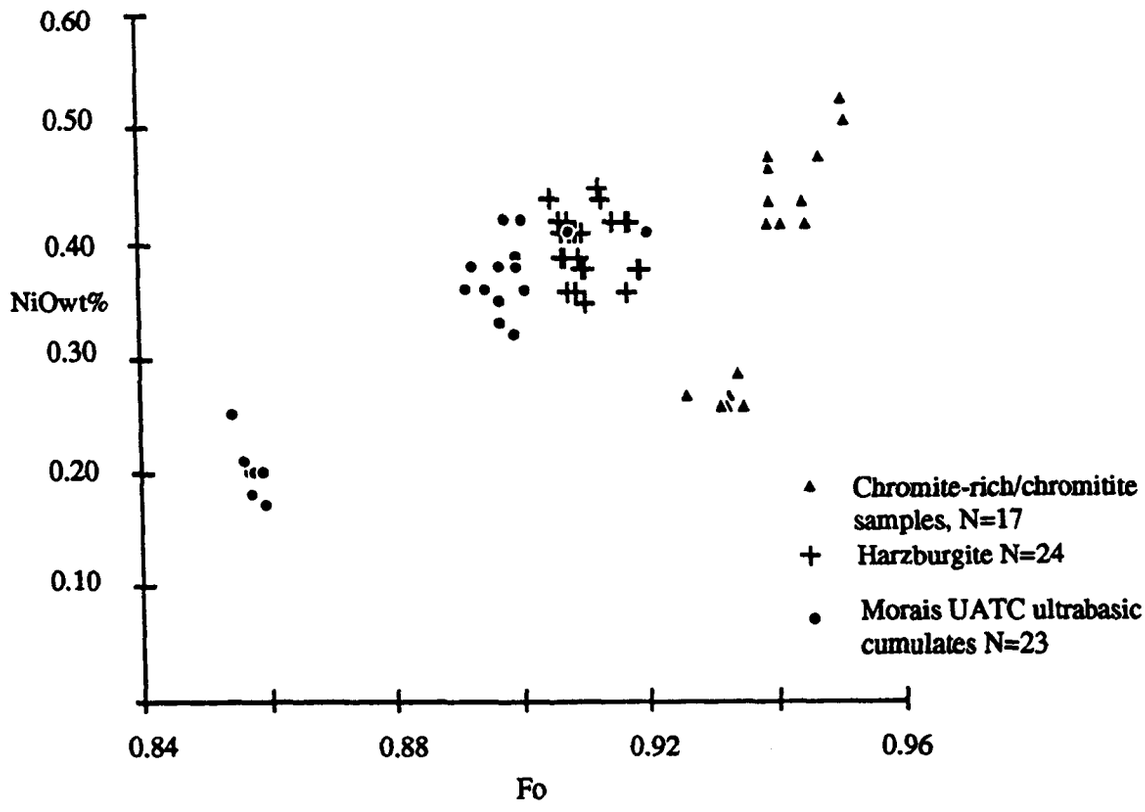

This graph of olivine NiO content versus Fo number shows three groupings: olivines from the harzburgite formation are Fo 91-92 and NiOwt% 0.35-0.45; the chromite-rich samples Fo 93-95 and NiOwt% 0.26-0.53; and the Morais UATC cumulate samples Fo 85-92 and NiOwt% 0.17-0.42. There is a general correlation between NiO and the Fo number, which suggests the different groupings are not solely due to Mg and Fe re-equilibration at submagmatic temperatures but may also have a primary origin.

Table 2.6.1 Olivine Fo compositions of different localities

	Fo number and locality	Reference
Mantle assemblages	89.2-91.7 Semail ophiolite	Brown (1982)
	91.1-94.4 Vourinos	Johan and Augé (1986)
	91.0 mean Tiebaghi	Johan and Augé (*op. cit.*)
	90.5-91.5 compilation of ophiolite mantle peridotites	Boyd (1989)
	88-94 compilation of alpine peridotites	Jackson and Thayer (1972)
	87.8-93.6 compilation of ophiolite, alpine mantle peridotites	Brown (1982)
	88-91 Shetland ophiolite podiform dunite	Gass *et al.* (1982)
	91-92 harzburgite formation	This study
Ultrabasic cumulates	75-94 compilation	Jackson and Thayer (1972)
	85-92 Morais UATC	This study
Chromitites	91.5-96.3 Semail mantle chromitites	Brown (1982)
	96 Shetland ophiolite	Gass *et al.* (1982)
	93-95 Bragança	This study

This table shows the comparison between the olivine compositions from different formations in the Bragança and Morais UATC and Fo compositions from different terrains. The refractory olivine compositions from the harzburgite formation are typical of other depleted mantle assemblages. The very high Fo numbers from the Bragança chromite-rich samples are also typical of accessory olivine within chromitites. In contrast, the lowest Fo numbers obtained (from the Morais UATC) fall within the range expected of ultrabasic cumulates but outside those of refractory mantle

The highly Mg-rich composition of the harzburgite olivines is normal for residual mantle assemblages associated with ophiolite or alpine ultrabasic complexes. The spread of values for Bragança lies within the range for such rocks. The lower end to the Fo range for the Morais UATC assemblage is also compatible with an origin as ultrabasic cumulates. The maximum value of Fo_{95} obtained for the chromite-rich samples is unusually high for olivines in general. Results from the Semail ophiolite Brown (1982), Roberts (1986) and the Shetland ophiolite (Gass *et al.* 1982) see table 2.6.1 above, show however that it is not unprecedented. An enrichment in the Fo content of olivines from within chromitite samples due to Mg and Fe^{2+} partitioning is well established as demonstrated in the previous section.

This control of whole rock composition on accessory spinel composition in peridotites makes the mineral a useful petrogenetic indicator. The range of the 100Cr/(Cr+Al) ratio for chromite grains from the harzburgite formation (33.4-56.6) is typical of alpine peridotites (fig. 2.6.1c). All these analyses lie on or within the field for alpine peridotites. In contrast most of the analyses from the Morais UATC ultrabasic assemblage analyses have a range of $100Mg/(Mg+Fe^{2+})$ ratios (19.8-68.0) more typical of crustal stratiform deposits and some of

the analyses plot outside the alpine field, though the trend between the two clusters of Morais UATC points is parallel to that of the alpine field. The points at the low end of the 100Cr/(Cr+Al) scale are from the troctolite sample 96BRG.

Figure 2.6.1c Accessory chromite grain composition

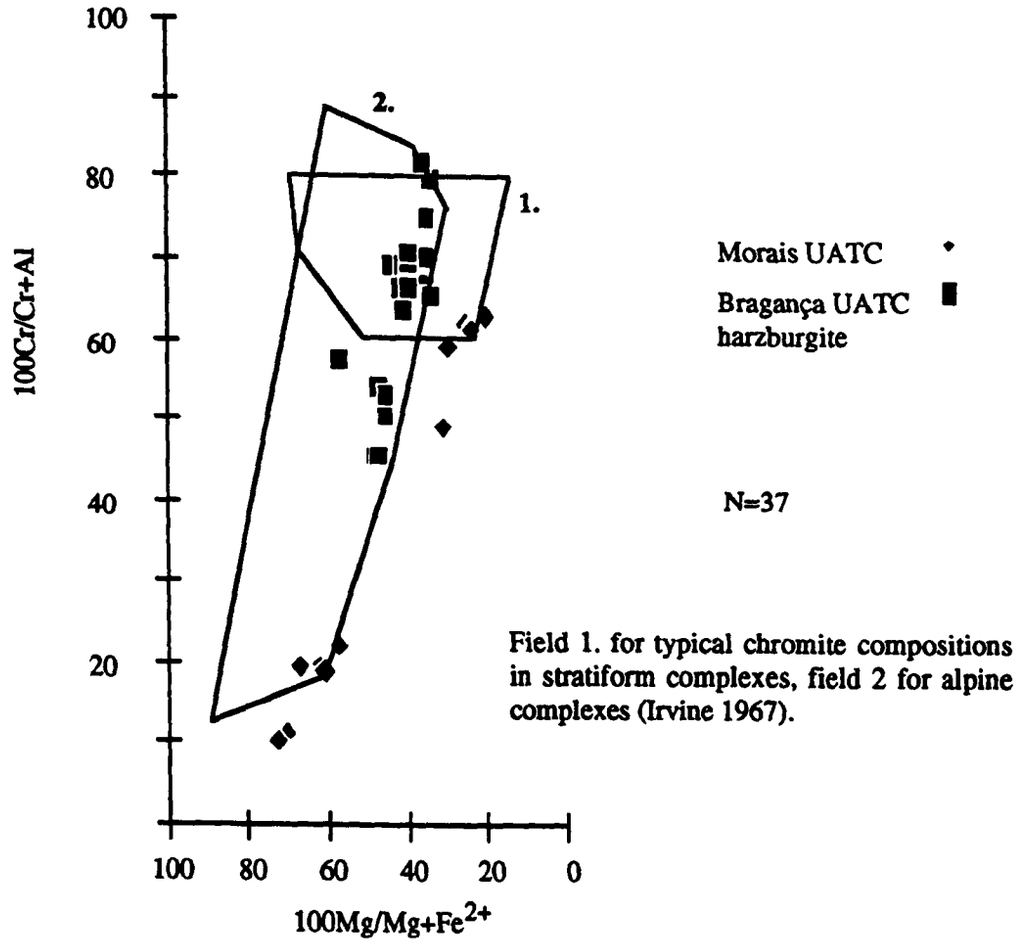

The field for spinels of alpine peridotites shows the characteristic wide range in 100Cr/Cr+Al ratios from 12 to 90 whereas those from stratiform intrusions have greater 100Mg/(Mg+Fe) variability. The accessory chromite grain compositions from the Bragança harzburgite formation all lie within or on the alpine field. The Morais UATC points lie in two clusters, which mainly lie outside the alpine field, having 100Mg/(Mg+Fe) ratios down to lower values than those of the harzburgite formation.

Another method of using chromite grain composition to highlight the differences between the Morais and Bragança sections of the UATC ultrabasic rocks, is to study the

variability of Ti/Fe and Cr/Fe atomic ratios. Neary (1974) and Neary and Brown (1979) used a plot of 100Ti/Fe against Cr/Fe for chromite grain compositions to characterise chromitite deposits. Crustal derived deposits such as chromite from Bushveld, Stillwater or Fiskenaesset layered intrusions show relatively high 100Ti/Fe values and greater variability in this element ratio than chromitites derived from mantle sequences such as Oman or Troodos.

Figure 2.6.1.d 100 x Ti/Fe v Cr/Fe chromite atomic ratios

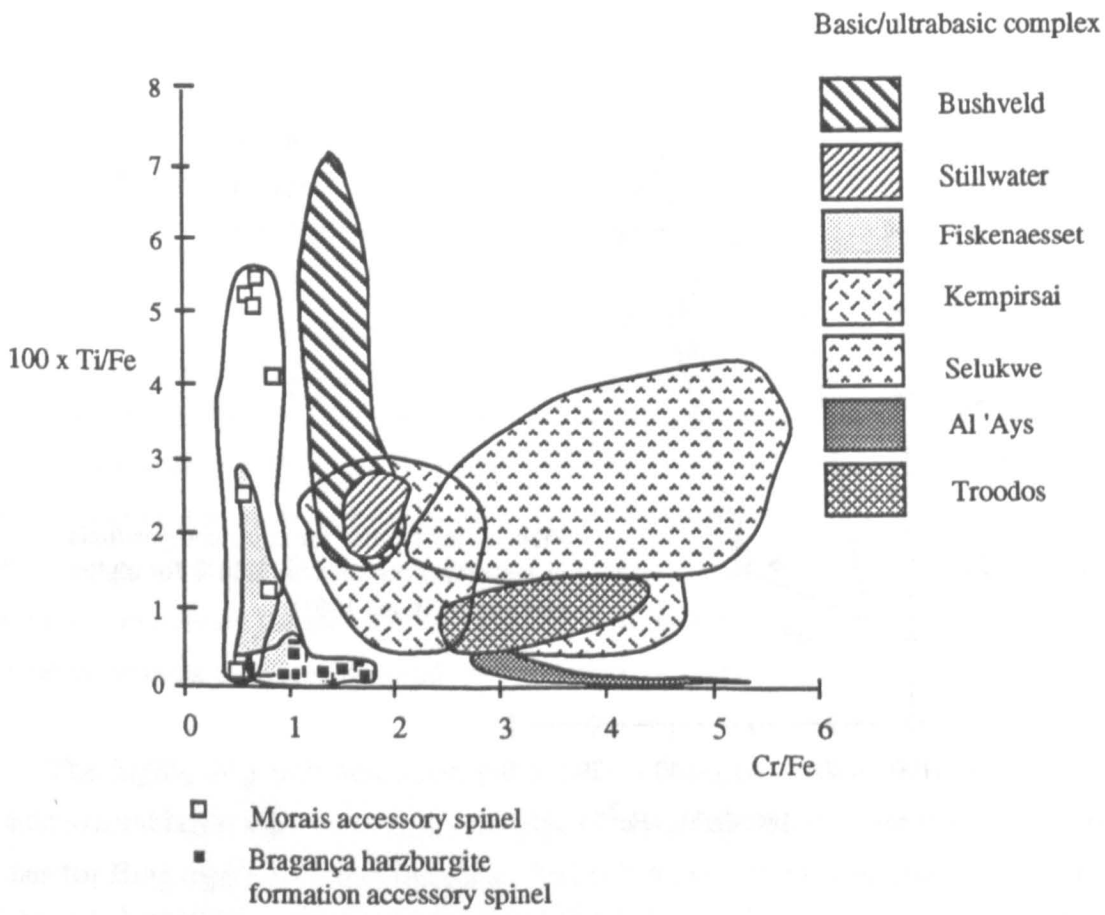

Accessory chromite grain compositions from Morais UATC ultrabasic samples (including troctolite) and the Bragança harzburgite formation are plotted on a 100 x Ti/Fe v Cr/Fe diagram. The diagram has fields from different types of basic/ultrabasic complexes: the mantle sections of ophiolites from Al' Ays and Troodos and crustal derived complexes-the Bushveld, Fiskenaesset and Stillwater. The Selukwe complex of Zimbabwe and the Kempirsai complex of the USSR have characteristics of both podiform and stratiform complexes. The upper sequence of Kempirsai and the crustal, cumulate derived complexes have vertical trends on this graph. The podiform, ophiolitic trend including the Selukwe complex and the lower part of the Kempirsai pluton is near horizontal. The samples from the Morais UATC have greater variability of the 100Ti/Fe ratio than those from the Bragança harzburgite formation giving a vertical compared to horizontal trend. The Morais samples trend is characteristic of crustal derived cumulates whereas those from Bragança are typical of mantle-derived assemblages. From Neary (1974).

Accessory chromite grain compositions from the ultrabasic assemblage in the UATC are plotted on fig. 2.6.1d from Neary (1974). The plot shows two distinct groupings: a vertical trend group with high 100Ti/Fe ratios is present and a low 100Ti/Fe group. The first group is from the Morais UATC, including the troctolite sample from Caminho Velho. The second grouping is from the harzburgite formation of Bragança. These trends are a reflection of the low TiO_2 contents of the latter chromite grains with a range of 0.03 to 0.20wt% and the high TiO_2 contents of the Morais samples. The low TiO_2 contents of grains from the harzburgite formation (lower than the corresponding chromite-rich rocks) together with Cr/(Cr+Al) ratio variability are characteristic of chromite grains from depleted mantle assemblages *eg* Johan and Augé (1986), Brown (1982). In contrast the composition of the Morais UATC grains show more affinities to crustal-derived cumulates.

2.6.2 Amphibole composition

Table 2.6d lists the range of parameters for the amphibole classification scheme of Leake (1978). All the amphiboles analysed have $(Ca+Na)_B$ values greater than 1.34 and Na_B less than 0.67 making them calcic amphiboles. Within this overall group the Bragança UATC rocks show three groupings when plotted with the parameters given in the table 2.6d. The first amphibole group has high Si formula units of 7.32-7.71 and low $(Na+K)_A$ site values 0-0.29. The second distinct group has low Si 6.13-6.36 and high $(Na+K)_A$ 0.57-0.86. The third group lies mainly within the area of the first one, though two analyses plot outside it towards the third group's field.

The first group is amphiboles present within the pyroxenites; in the nomenclature of Leake (1978) this group is tremolite to tremolitic hornblende. The second group is composed of analyses of the dark green, pleochroic amphibole which by the same nomenclature is pargasite to ferroan pargasitic hornblende (this group includes five analyses from a feldspar-bearing gneiss sample 10-BRG). Occasional scattered tremolite amphiboles found within the harzburgite formation comprise the third group. The tremolites found within the pyroxenites and scattered through the harzburgite formation represent an isochemical alteration from diopside (Veblen and Ribbe 1982). This amphibole composition is distinct from that of amphibole grains from mantle peridotite derived by high temperature metasomatic processes. An example of the latter is present in the Ariege lherzolite massif (Pyrénées), where disseminated amphiboles are Ti-pargasite. Such amphiboles are thought to be derived from the percolation of alkali fluids through the mantle (Lorand 1989).

The composition of calcic amphiboles in ultrabasic rocks has been used to demonstrate both prograde metamorphic and metasomatic trends (Veblen and Ribbe 1982). Both trends are marked by greater values of $(Na+K)_A$ site occupancy (appendix 3) and decreasing Si formula unit values. This corresponds to a change from tremolite to pargasite. The amphibole textures described in section 2.2.3, of the dark green pleochroic amphibole replacing clinopyroxene in patches, shows the general retrograde metamorphic origin of the

amphibole occurrence in the ultrabasic UATC rocks. The trend shown in fig. 2.6.2 of a negative correlation between Si and $(Na+K)_A$ in fig. 2.6.2a and a positive trend between $(Na+K)_A$ and Na_B in fig. 2.6.2b demonstrates a metasomatic trend associated with amphibolitisation. The coarse ferroan pargasite amphiboles are most affected by this process.

Figure 2.6.2 Amphibole compositions

Figure 2.6.2a Si v $(Na+K)_A$

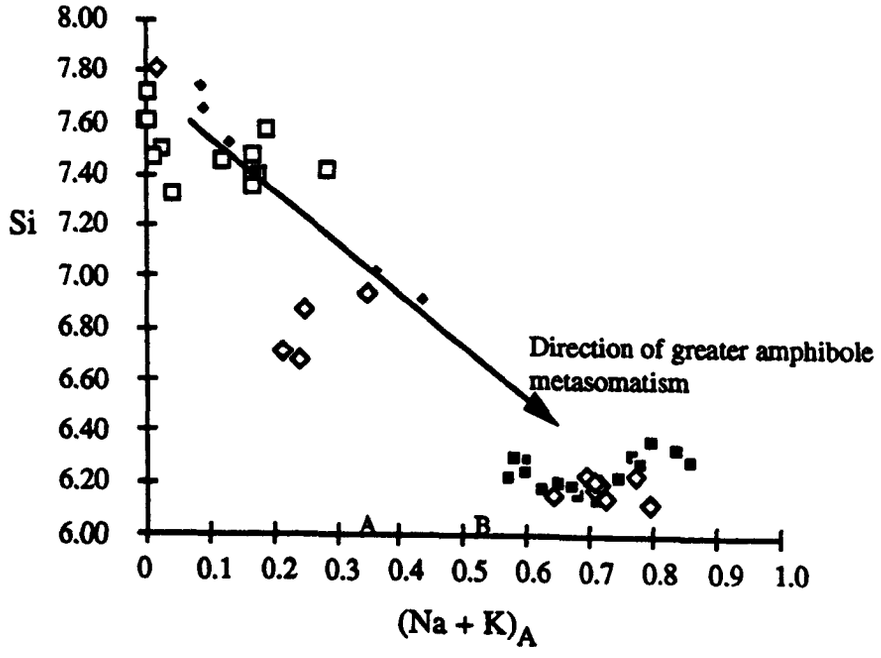

Amphibole analyses from the ultrabasic formations of the Morais and Bragança UATC fall within four compositional groups. Group 1 is from the websterite layers in Bragança (tremolite to tremolitic-hornblende), group 2 is the dark pleochroic amphibole (ferroan pargasitic hornblende) from hornblendite, group 3 is tremolites from the harzburgite formation. Group 4 is from the Morais UATC peridotites and shows a wide range of compositions.

A metasomatic trend is shown in fig.2.6.2b by increasing values of Na in the B amphiboles site and Na+K in the A site. The group 2 amphiboles are most effected by this process, the group 1 amphiboles have been isochemically altered from diopside and do not show the effects of metasomatism. There is a large overlap in composition: Si >6.9, (Na+K) <0.5, Na <0.2 between the amphiboles from group 1 and group 3 (pyroxenites and dunite/harzburgite). This suggests a common origin as isochemically altered diopside.

Figure 2.6.2b Si v Na_B

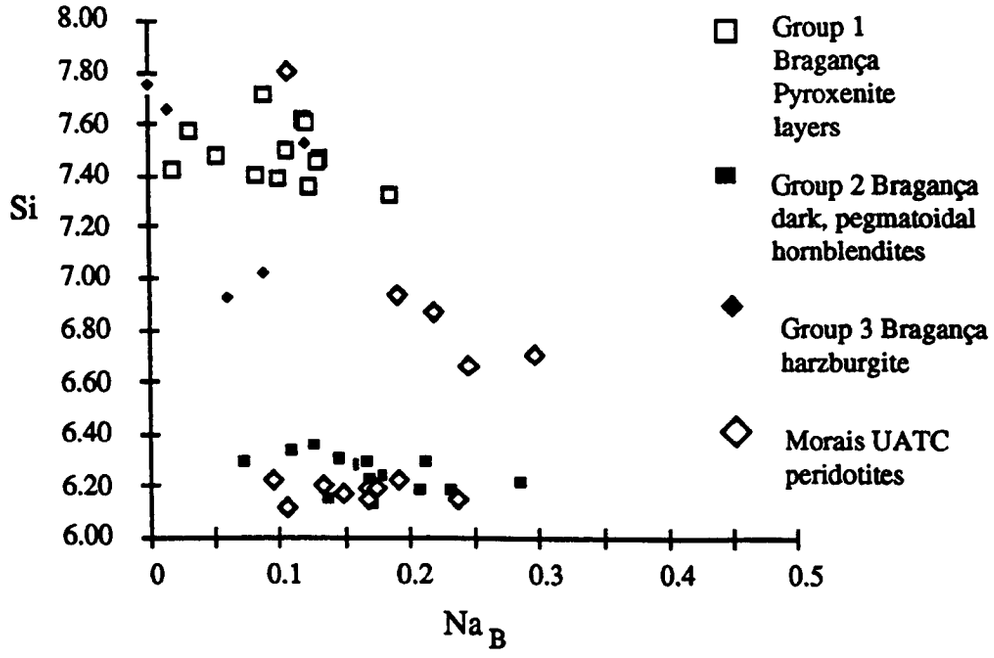

Figure 2.6.2c Na_Bv $(Na+K)_A$

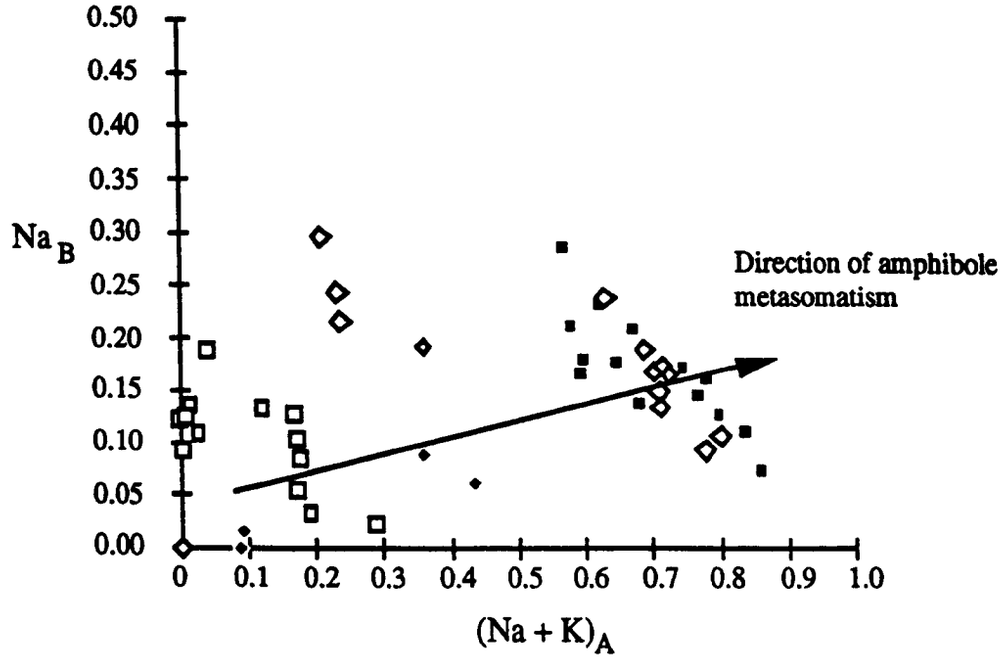

Figure 2.6.3 Clinopyroxene analyses from pyroxenite samples

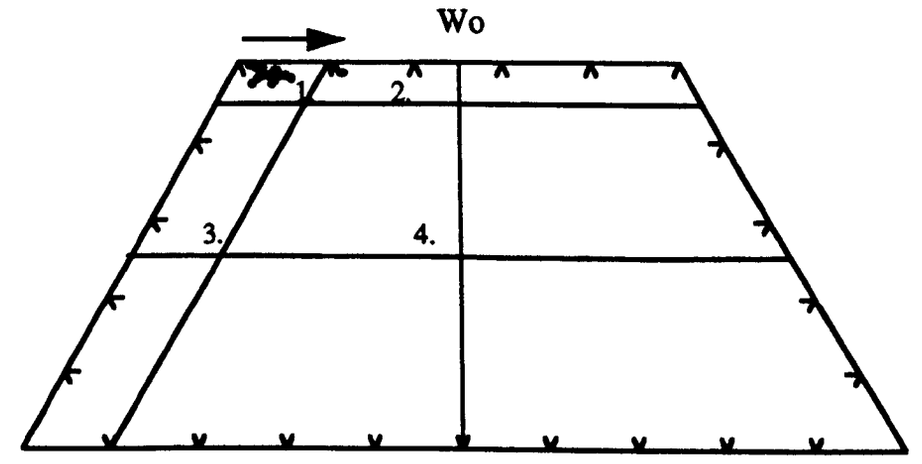

Wo wollastonite end member
En enstatite endmember
Fs ferrosilite end member

N=23

1. Diopside field
2. Salite field
3. Endiopside field
4. Augite field

Diopside alteration trend

Most of the clinopyroxene associated with the pyroxenites have a diopside composition typical of many mantle-derived pyroxenites. Three analyses, from sample 3BRG, plot within the salite field, having greater ferrosilite end member contents. They also contain more Al than the diopside grains. This trend, shown by an arrow on the diagram, is associated with metasomatic amphibolitisation and the creation of hornblendite layers.

Unlike the Bragança samples, those from the Morais UATC do not show close groupings. Instead there is a large range in compositions from tremolite to pargasite, with Si 6.12-7.81 and $(Na+K)_A$ 0.21-0.80. The ferroan pargasitic hornblende grains associated with metasomatism in Braganca are not present however. The compositional variability of the Morais UATC amphiboles may be a result of original igneous variation between different clinopyroxene phases.

2.6.3 Pyroxene

The clinopyroxene analyses were nomalised to 4 cations and used to recalculate wollastonite, enstatite and ferrosilite end members (appendix 3). The clinopyroxene analyses from most of the pyroxenites and one sample from Morais lie close to or within the diopside field (fig. 2.6.3). The analyses from sample 3BRG have more unusual compositions for clinopyroxene in ultrabasic rocks. The three analyses contain higher contents of the ferrosilite end member and higher Al_2O_3 (1.35-2.63wt%) contents than the rest of the clinopyroxene analyses from the pyroxenites. Sample 3BRG is one of the pyroxenite samples which shows the metasomatic alteration to the ferroan pargasitic hornblende (section 2.2.3). In section 2.6.2 on amphibole compositions the metasomatic trend associated with this amphibolitisation was shown to involve increases in the iron contents of mineral grains. These unusual pyroxene compositions are taken to be produced by the metasomatism of diopside, though not having progressed through complete alteration of the entire grains to amphibole. Clinopyroxene Cr_2O_3 contents (less than 0.4wt%) are rather low compared to other mantle-derived clinopyroxene which often have around 1.3wt% Cr_2O_3 (Mercier and Nicolas 1975). The Braganca figure may represent a residue after loss of this element through exsolution of chromite.

The important feature of the orthopyroxene analyses is the difference in Al_2O_3 contents between the Morais UATC analyses and those from the Bragança harzburgite formation. In sample 73BRG from which the Morais analyses were taken, there is a range from 2.91-4.44wt% Al_2O_3 and in the Bragança harzburgite analyses there is a lower range from 0.27-1.86wt% Al_2O_3. This shows the less refractory nature of the Morais UATC samples compared to those of the harzburgite formation. The low $Ca/(Ca+Mg+Fe^{2+})$ and high $Mg/(Ca+Mg+Fe^{2+})$ ratios in orthopyroxene from the ultrabasic samples of the Morais and Bragança samples are typical of enstatite.

2.6.4 Other mineral analyses

The compositions of feldspar from the Caminho Velho troctolite in Morais and those of the garnet-feldspar-amphibole gneiss formation in the UATC are markedly different. Sample Brag96 has plagioclase of labradorite to bytownite composition which is more calcic than the andesine to oligoclase plagioclase of the garnet-feldspar-amphibole-gneiss. The difference in feldspar composition is a reflection of the separate origin of the Caminho Velho

troctolite and the garnet-feldspar-amphibole-gneiss formation. Plagioclase compositions from the Caminho Velho troctolite are given in appendix 3. Apatite grains associated with the ferroan pargasite-sphene metasomatic assemblage have a range of 1.6-3.8wt% F (appendix 3). The Cr-rich chlorite of the dunite/chromitite formation is discussed in chapter 3 and the compositions of the sulphide minerals in the harzburgite formation and websterites are considered in chapter 5.

2.7 Geochemistry of the ultrabasic assemblage

The field mapping and petrographic studies described so far have demonstrated differences between the UATC ultrabasic assemblages of Bragança and Morais. This contrast is explored further in this section. By using whole rock major and trace element compositions of the UATC ultrabasic rocks it is possible to distinguish between those from Morais (Caminho Velho and Vinhas) and Bragança and also to constrain a tectonic setting for the harzburgite formation. Ophiolite complexes provide a valuable basis for comparing with the compositions of the Bragança and Morais ultrabasic samples though as suggested in later parts of this thesis the Braganca and Morais UATC ultrabasic assemblages do not have such an origin themselves.

Figure 2.7a-c Composition of Bragança harzburgite and Morais peridotite formations

Figure 2.7a Al-Ca-Mg triplot

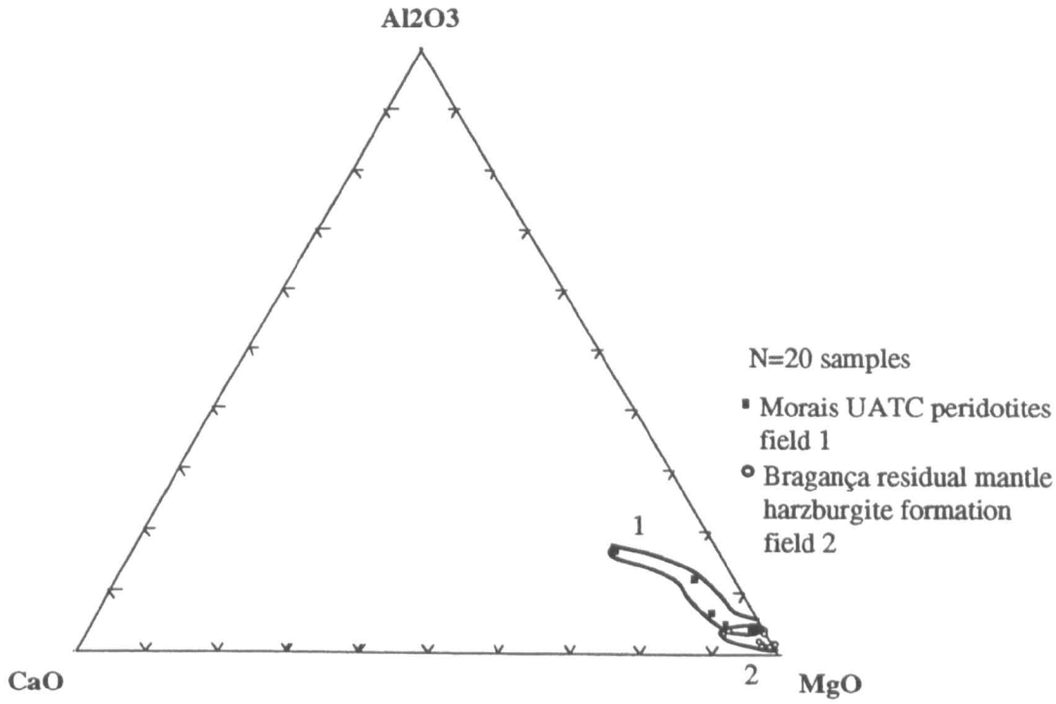

Figure 2.7b Enlarged view around MgO apex of Al-Ca-Mg triplot

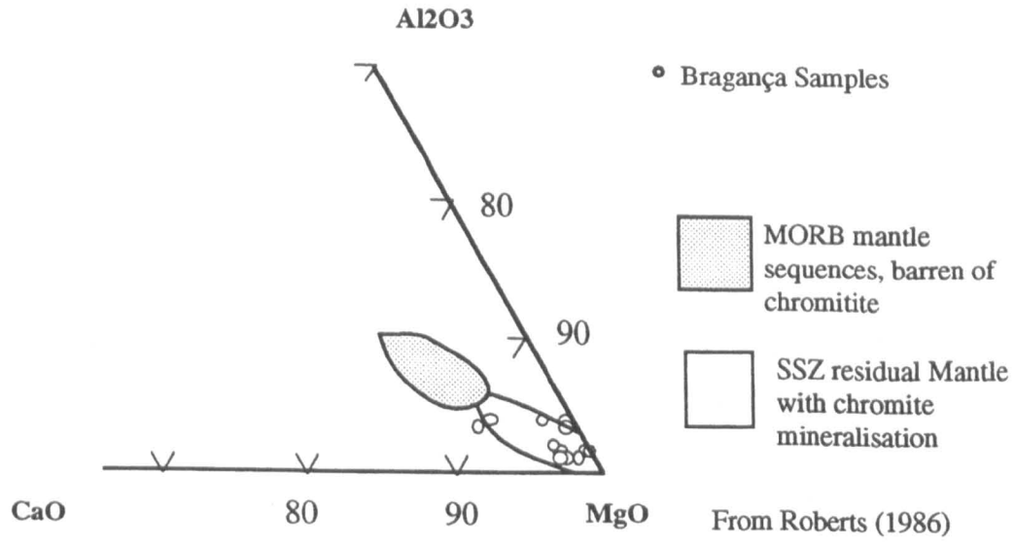

Fig. 2.7b shows the contrasting compositions of the UATC ultrabasic samples from Morais and those from Bragança. The former group have a greater range of CaO and Al_2O_3 contents showing a less refractory composition for most of the samples compared to the other group. Figure 2.7c is an enlarged view of fig. 2.7b around the MgO apex. The compositions of Bragança harzburgite formation samples are plotted on it. The points lie within or close to the field for residual mantle formed in supra-subduction zone settings.

Roberts (1986) devised ternary plots of Ti,Ni,Cr and Al_2O_3,CaO,MgO to characterise residual mantle rocks. The fields drawn are based on a range of ten ophiolite sequences, both mineralised (with chromitite) and barren. The unmineralised ophiolites were considered to be derived from a MOR setting and the mineralised examples from a supra-subduction zone setting. This grouping was supported by the selective enrichment of certain elements *eg* Ba, Sr, K, P, Rb within associated lavas (Pearce *et al.* 1984). The more residual, refractory compositions, those with less Al_2O_3 and CaO, correspond to the ophiolites with chromite mineralisation. An Al-Ca-Mg triplot is also used (fig. 2.7.1a) to discriminate between ultrabasic samples from Bragança and those from Caminho Velho and Vinhas (Morais UATC). The Bragança samples have generally lower CaO and Al_2O_3 contents and plot close to the MgO apex, whereas the Morais samples show a larger spread of CaO and Al_2O_3 contents. The CaO contents must be treated with caution as it is possible that there has been loss of this element from the whole rock during serpentinisation of orthopyroxene, as some of the Morais UATC peridotite orthopyroxene have altered to in patches to serpentine. Table 2.7 shows the marked compositional differences between the Bragança and Morais assemblages. A full list of the major and trace element data is given in appendix 4.

Table 2.7 Compositional Ranges for Braganca and Morais UATC Ultrabasic samples

	SiO_2	TiO_2 (from majors)	Al_2O_3	MgO	CaO
Bragança N=13	37.9-42.9	0.00-0.05	0.50-1.67	35.22-42.5	0.05-2.72
Morais 1 troctolite	39.01	0.09	10.91	25.40	5.91
Morais 6 peridotites	36.13-44.34	0.02-0.37	1.66-7.18	29.11-36.75	0.31-6.00

The Bragança samples are from the harzburgite formation and the Morais samples are peridotite and one troctolite from Caminho Velho.

The second Al-Mg-Ca triplot (fig. 2.7b) shows an expanded view around the MgO apex. The harzburgite formation analyses from Braganca plot within the field of mineralised, residual sequences formed in supra-subduction zone environments. When plotted on the Ti-Ni-Cr ternary discriminant diagram (fig. 2.7c) the Bragança harzburgite analyses also plot within the field associated with SSZ, mineralised mantle sequences. This may be the more reliable discriminant diagram because of possible Ca remobilisation.

Figure 2.7c Ti-Ni-Cr ternary plot of Bragança harzburgite formation samples

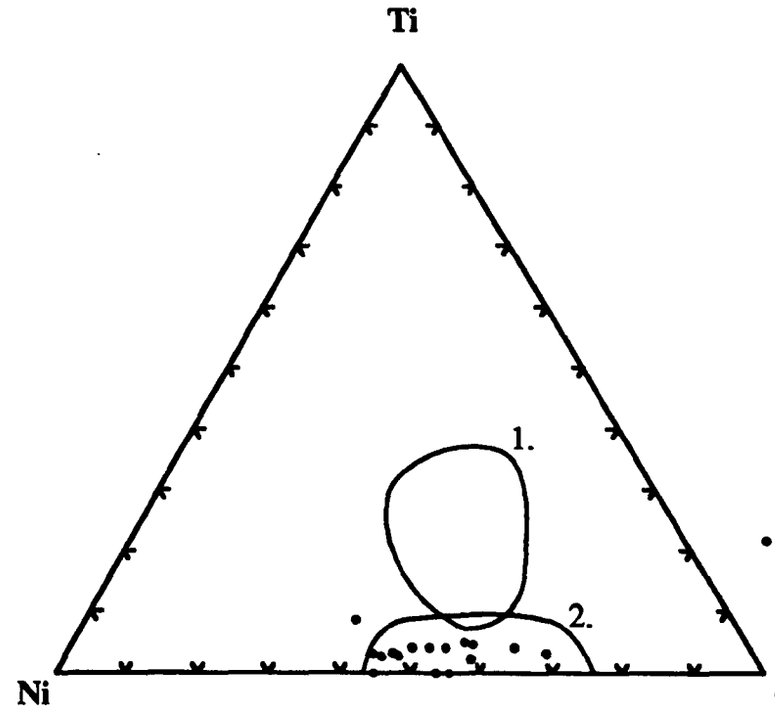

1= Chromitite barren, lherzolite type

2 = Mineralised, harzburgite sequences

• N = 20 Bragança harzburgite formation samples

Plot from Roberts 1986

All but one of the samples from the Bragança harzburgite formation lie within the compositional field of mineralised, harzburgite sequences. They have a more refractory composition than those from lherzolite sequnces.

These compositional differences between the Morais and Bragança UATC ultrabasic assemblages suggest they have differing origins. In a previous section it was proposed, on the basis of chromite grain compositions and petrography, that the Morais samples might represent a cumulate sequence. Evidence to support this idea can be seen by using major element plots. The graphs (fig. 2.7d and e) show the way that a liquid L would evolve if a mineral phase P fractionated from an initial liquid B. The second graph shows the liquid's compositional changes when two mineral phases P and Q crystallise from an initial liquid B. P and Q crystallise in such a proportion that the total extract has composition E. The liquid evolves, in terms of X and Y weight % oxides, perpendicular to the tie line between P and Q mineral phases. A second equally valid interpretation of such trends is that an initial liquid L could have crystals of P and Q added to it in such a proportion as to create an extract of composition E and a magma of composition B. Tie lines between the compositions (from Cox, Bell and Pankhurst 1979) of mineral phases have been constructed on major element plots in fig. 2.7f and g. If the seven Morais UATC samples represent cumulates then they would be expected to show trends relating the rocks to extracts involving olivine, clinopyroxene and orthopyroxene, which are the main mineral phases found within these rocks. The term cumulate is used here to indicate a plutonic rock composed of minerals

rocks. The term cumulate is used here to indicate a plutonic rock composed of minerals precipitated from a melt, whether they have been mechanically separated from a melt by crystal settling or crystallised in-situ by diffusion controlled mechanisms (after Elthon *et al.* 1982).

The data points (not including the two troctolite and metagabbro samples) lie closest to the tie lines between plagioclase and olivine or orthopyroxene and away from those between clinopyroxene and olivine. This suggests that a liquid has evolved perpendicular to the olivine-plagioclase tie line. The major element diagrams are interpreted as showing that the Morais UATC samples are related by derivation from a liquid that has evolved through crystallising olivine and pyroxene but none or lesser amounts of plagioclase. This suggests crystallisation within a magma chamber as opposed to a residual origin such as that envisaged for the harzburgite formation. For comparison with the Morais UATC samples, compositional trends for wehrlite cumulates from the Troodos ophiolite are also shown on some of the graphs, showing similar trends. Murton (1988) interpreted them as resulting from the magmatic accumulation of olivine and pyroxene.

Figure 2.7d-g Major element plots of the Morais UATC peridotites

Figures 2.7d and 2.7e The evolution of cumulate composition shown by major element plots

Fig. 2.7.2d

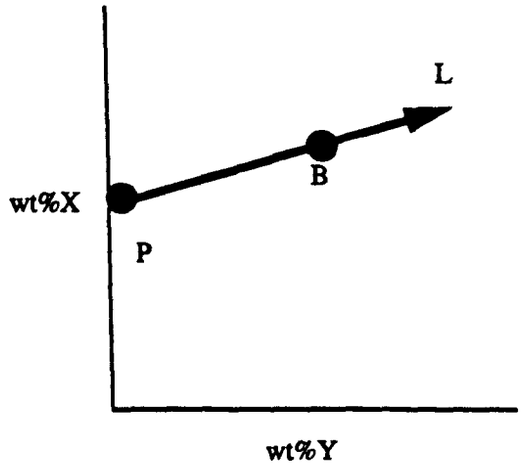

Fig. 2.7.2e

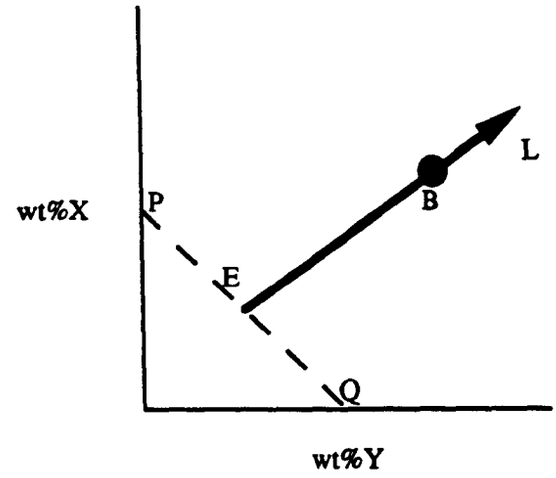

P,Q Mineral Phases
B Magma Composition
E Extract Composition

L Liquid
X,Y wt% oxides

Figure 2.7d shows the way that a liquid L would evolve if a mineral phase P fractionated from an initial liquid of composition B. Figure 2.7e shows the liquid's compositional changes when two mineral phases P and Q crystallise from an initial liquid B. P and Q crystallise in such a proportion that the total extract has composition E. The liquid evolves, in terms of X and Y, perpendicular to the tie line between P and Q mineral phases. A second, equally correct interpretation is that an initial liquid L could have crystals of P and Q added to it in such a proportion as to create an extract of composition E and a magma of composition B. From Cox, Bell and Pankhurst (1979).

Figure 2.7f Al_2O_3 v SiO_2

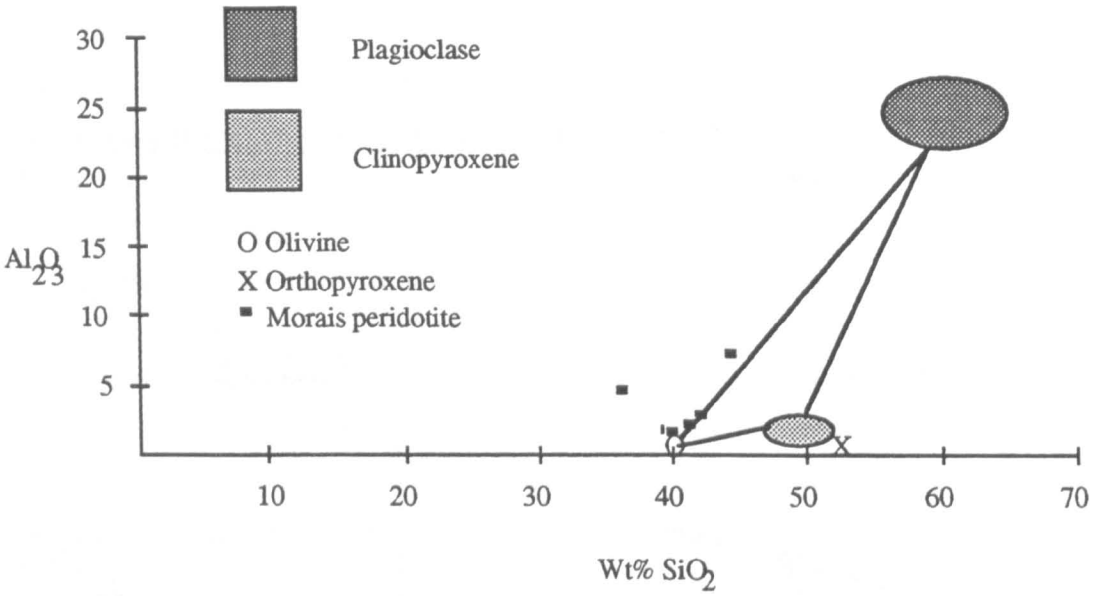

Five of the six Morais UATC peridotite samples lie close to a tie line between olivine and plagioclase compositions suggesting that the samples may be related by crystallisation from a liquid that has evolved through a near perpendicular compositional trend of olivine and orthopyroxene crystallisation.

Figure 2.7g Al_2O_3 v MgO

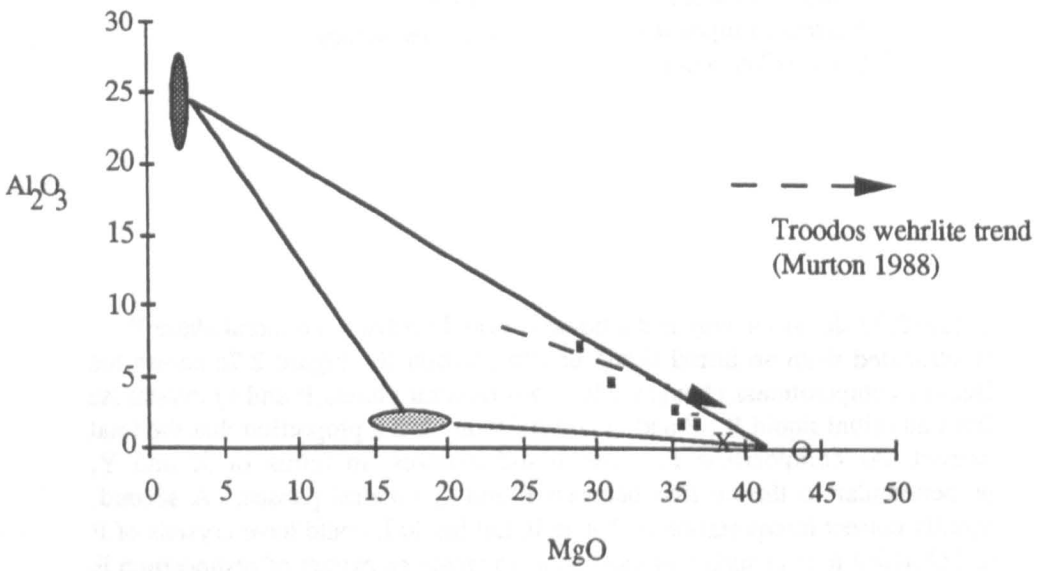

The six peridotite analyses lie close to a tie line joining plagioclase and a mid-point between olivine and orthopyroxene. This is consistent with derivation of the samples from a liquid which has evolved through olivine and orthopyroxene crystallisation The arrow marks the similar trend of wehrlite accumulates from the Troodos massif (Murton 1988).

2.8 Conclusions

The Bragança ultrabasic assemblage mainly consists of a low orthopyroxene harzburgite modal composition formation. This formation contains a separate chromitite-bearing dunite formation which contains no pyroxene. Abundant spinel websterite, clinopyroxenite and hornblendite layers are also present which are similar to those from other mantle assemblages. Relict pyroxenite aggregations range from isolated amphibolitised clusters and small veins, up to large pyroxenite layers. The Morais UATC (Caminho Velho and Vinhas) ultrabasic samples consist of peridotite. At Caminho Velho, troctolite and a metagabbro are also present. All the olivine-bearing ultrabasic samples have been serpentinised to varying degrees.

The Bragança and Morais UATC ultrabasic samples have contrasting whole rock compositions. Most of the samples from Bragança have lower Ti and Al contents than those of Morais. The Bragança ultrabasic sample compositions are typical of residual mantle formed in supra-subduction zone settings. Major element plots of the Morais UATC peridotite samples are consistent with their creation as cumulates. They have similar trends to the major element plots of wehrlitic cumulates from the Troodos ophiolite (Murton 1988). The composition of olivine grains from the harzburgite formation are Mg-rich *eg* olivine Fo_{91-92} and typical of residual mantle assemblages. The Bragança harzburgite formation contains accessory chromite grains with low Ti contents compared to the range of accessory chromite compositions from Morais. The latter chromite compositions are typical of those with a crustal origin from a cumulate sequence, whereas the Bragança ones suggest a residual mantle origin. Chromite grains record temperatures of between 500 and 630°C for re-equilibration of Mg and Fe^{2+} between chromite and the surrounding olivine.

The mineralogical and geochemical data presented in this chapter can give no firm evidence for a genetic link between the Morais and Bragança ultrabasic assemblages *ie* whether the Morais UATC cumulates crystallised from a melt above the Bragança mantle assemblage before tectonic emplacement. The best indication that this relationship might exist is their coexistence at the same structural level within the Morais and Bragança thrust nappe piles (Anthonioz 1972 and Ribeiro 1974). Table 2.8 summarises some of the most important differences between the ultrabasic parts of the UATC assemblages in Morais and Bragança.

The Bragança spinel websterite (enstatite with diopside) and clinopyroxenite (diopside) layers have been variably amphibolitised. A largely isochemical alteration from diopside is suggested by the magnesio-hornblende and tremolite compositions of the amphiboles within these layers (Veblen and Ribbe 1982). A contrasting amphibolitisation style is present in the ferroan pargasite-bearing hornblendite. The higher alkali content, together with the presence of sphene and apatite shows the allochemical nature of this change. The pegmatoidal amphiboles within this formation also attest to the volatile-rich environment present during the change from diopside to ferroan pargasite. The similar

appearance of the feldspar-bearing gneiss formation shows that this metasomatic amphibolitisation affected large parts of the massif. Fluids associated with this metasomatism were apparently concentrated along clinopyroxenite layers creating the hornblendite layers within the ultrabasic assemblage.

Table 2.8 Summary of differences between the Bragança and Morais UATC

Morais: Vinhas and Caminho Velho	**Bragança**
Pervasive kink folds	Axial planar foliation (see chapter 1)
No websterites or clinopyroxenites	Websterite, clinopyroxenite and hornblendite layers
Ultrabasics mainly peridotite with minor troctolite and metagabbro.	Mainly harzburgite formation
No chromitite	Occasional chromitite in dunite bodies
Intercumulus like texture in troctolite.	No recognisable igneous textures
Ultrabasic and troctolite rock compositions MgO 25.4-36.8% Al_2O_3 1.7-10.9%	Ultrabasic rock compositions MgO 35.2-42.5% Al_2O_3 0.5-1.7%.
Spinel 0.05-5.03wt% TiO_2	Spinel 0.0-0.2wt% TiO_2

Apart from the hornblendite layers within the harzburgite formation there is no obvious genetic link between the ultrabasic sequences studied in this chapter and the garnet-feldspar-amphibole-gneiss, retrograded granulite formation. The cumulate sequences at Vinhas and Caminho Velho have a different mineralogical assemblage and style of amphibolitisation from the relict granulites and plagioclase from the Caminho Velho troctolite is more calcic than that from the garnet-feldspar-amphibole-gneiss.

The UATC ultrabasic sequence in Bragança and Morais records a synthrusting retrogressive metamorphism with amphibolitisation and the development of chlorite in pyroxenites and progressive serpentinisation in the dunites, harzburgites and Morais UATC outcrops of peridotite. Mantle derived textures, such as the glide planes of enstatite augen, have been overprinted by a mylonitic fabric which is shown by the cataclasis of pyroxenes and the creation of lensoid clusters of fine olivine neoblasts within the harzburgite formation.

Chapter 3 The chromitite and dunite formation

3.1 Introduction

This chapter presents the results of petrographic and microprobe studies on the chromite-rich samples from the Bragança UATC ultrabasic assemblage. In this study, chromitite has been found at nineteen localities within the Bragança Massif. All but one of these (at the Rio Tuela south valley side) are located at old chromite mines or exploration trenches. The chromitite was taken mainly from old spoil tips, only in a few cases was massive chromitite found in-situ.

In recent years a large body of research has been produced concerning mantle-derived chromitite deposits, especially those from ophiolite complexes. It is this published and unpublished thesis-research on ophiolites which forms an important basis for comparison with the Bragança deposits discussed in this chapter, though as suggested later the rocks at Bragança are not considered to be part of an ophiolite sequence. In general, chromitite mineralisation within dunite is present in both the lower parts of ophiolite cumulate sequences and intramantle podiform bodies. Studies of the best preserved and most complete ophiolitic mantle sequences have shown that podiform bodies of dunite with chromite are mainly concentrated within a few km below the relict petrological Moho, *eg.* Brown (1982) on the Oman ophiolite, Greenbaum (1977) for the Troodos ophiolite, Prichard and Neary (1982) for the Shetland ophiolite and Dickey (1975).

Chromitite is surrounded by envelopes of dunite and chromite-bearing dunite. These in turn are enclosed within harzburgite. Pods of dunite may only contain disseminated chromite grains or they may be mainly composed of chromitite with dunite haloes. Dunite and chromitite bodies within mantle sequences have a large range in sizes. For the Oman, Brown (1982) described dunite veinlets a few cm across and dunite pods, up to 500m long and 50m thick. Quick (1981) described tabular dunite bodies that could be traced for up to 7km within the Trinity (USA) ophiolite mantle peridotites. Smaller, irregular shaped dunite bodies ranging in size from 3.5cm to about 100m were also present. The largest sizes reported, from hundreds to thousands of metres in dimension seem to be exceptional, with most podiform bodies being smaller than this.

The variation in texture found in podiform chromitites is largely dependent on the degree of deformation that they have undergone. Undeformed chromitites preserve textures similar to those found in stratiform intrusions. Laterally continuous chromitite layers, phase and grain size grading, net texture (*ie* interstitial chromite grains surrounding olivines), may be found in both podiform and stratiform chromitites. Nodular chromite is characteristic of podiform chromitites. The term nodular includes a diverse range of textures from well rounded masses of chromite with or without silicate cores, to more irregular clusters of

grains in layers. Nodules are typically a few mm to a few cm in diameter. Greenbaum (1977) described a dendritic texture in and around chromite nodules from Troodos. Skeletal cores to nodular chromite have also been located in New Caledonia (Leblanc 1980). There may be a variety of origins, both primary and tectonic, for nodular textures.

Figure 3.1a Podiform Dunites in Ophiolite Sequences

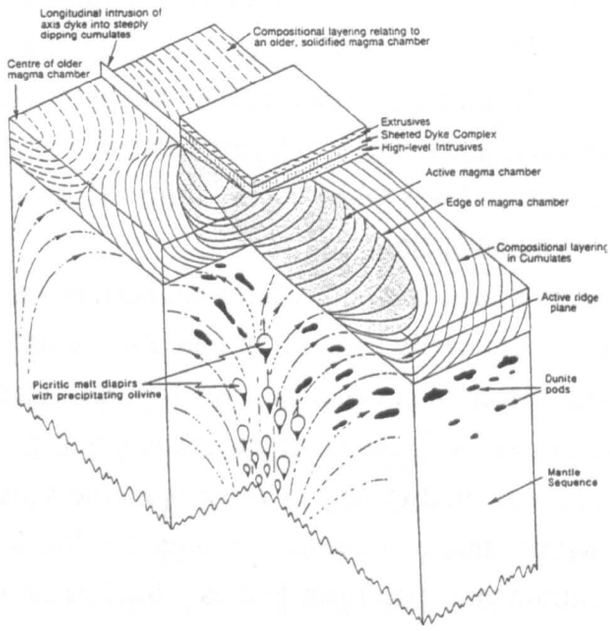

Cartoon diagram depicting a section through the lithosphere associated with oceanic spreading ridge. Within the mantle sequence: solid black patches=dunitic pods; halfblack balloons=rising picritic diapirs; black=precipitating Mg-rich olivine; and thin vertical arrows=melt moving towards the overlying crustal chamber. Chromitite bodies (not shown here) are often present within the podiform dunites. Overlying the mantle section is the crustal plutonic and extrusive series. From Browning (1982).

Where deformation has been intense chromitite layers can be boudinaged and sheared, giving rise to "schlieren structures". Such layers can contain almost pure, coarse grained, anhedral chromite. Brown (1982) noted grains up to 3cm in diameter from Oman chromitites; Gass *et al.* (1982) described grains of 2cm from the Shetland Ophiolite. The coarseness of the chromite grains is a characteristic feature of podiform chromitites as opposed to ones derived from stratiform intrusions which have finer grain sizes (Duke 1983).

Modern theories concerning the creation of podiform dunite and dunite bodies within mantle sequences have centred on either residual or magmatic origins. In an early work, Thayer (1964) reviewed alpine chromitites and noted occasional relict magmatic textures but considered that most of the textures seen: massive chromite aggregates, pull apart cracks and chromitite boudins were linked to the deformation of a crystal mush. Lago *et al.* (1982) proposed that the main part of podiform bodies were relicts of magma conduits within which a melt had circulated, crystallising olivine and chromite. The chromite-poor dunitic margins to such magma conduits could be created by the reaction of a picritic melt with the peridotite

walls by the incongruent melting of opx to olivine and silicate melt (Nicolas 1986). In the absence of water enstatite dissolution does not take place at pressures greater than 2.3kb (Boyd 1964). This suggests that the formation of dunite within the mantle, by enstatite melting, must occur under hydrous conditions.

Other workers have proposed that the creation of residual dunite veins under sub-solidus conditions is initiated by the influx of a fluid phase. In a description of the ultrabasic rocks of Duke Island in S.E. Alaska, which are thought to be cumulates formed in a volcanic arc environment, Irvine (1974) described secondary dunite segregations within olivine-clinopyroxene cumulates. Based on the theoretical work of Bowen and Tuttle (1949) he suggested that their origin could be linked to the removal of Si and other oxides by an externally derived vapour phase channelled through veinlets. The formation of dunite required the removal of Si, Ca, Al and Cr oxides from the clinopyroxene-bearing rocks and the addition of Mg and Fe oxides. Quick (1981), in a description of dunite bodies from the Trinity Peridotite of N. California, described dunite bodies that crosscut other ultrabasic lithologies. It was suggested that these bodies formed by the sub-solidus dissolution of all minerals except olivine and spinel. Part of the evidence for this idea was a trail of spinels through one of the dunite bodies which was parallel to the trend of a pyroxene-bearing dyke that the dunite crosscut.

An essentially residual origin for some dunite bodies, either by melting at the walls of a melt conduit or by the channelling of a fluid phase along veins is widely accepted as an important mechanism in the creation of some dunite bodies *eg* Johan and Augé (1986), Nicolas (1986). However, most models concerning the formation of podiform chromitites and their associated dunite invoke a picritic melt (ascending through mantle) from which chromite and olivine crystallise in small melt conduits *eg* Albrektsten *et al.* (1991), Roberts (1986) or transient magma chambers rising adiabatically within the mantle (Gass 1990). Mantle sequences may preserve both magmatic and residual dunites (Albrektsten *et al. op cit.*). The crystallisation of dunitic bodies is probably facilitated under low pressure, shallow mantle conditions. In such a situation, the field of olivine stability within the basalt tetrahedron increases. An originally picritic melt with a composition near the Ol apex of fig. 3.1b is likely to undergo a period of solely olivine fractionation during ascent through the lithosphere. The creation of the melts responsible for the dunite and chromite mineralisation is considered further in chapter 6.

The composition of chromite grains has been widely used as a discriminant for elucidating partial melting, fractionation and alteration processes affecting mantle sequences. On the basis of chromite grain chemistry, Dick and Bullen (1984) drew distinctions between deposits formed at supra-subduction zone, arc settings and those from MOR settings. In this chapter the effect of low temperature alteration processes on the composition of chromite grains is assessed. From this, what are considered the relict primary compositions are used to suggest an original tectonic setting for the chromite mineralisation.

Figure 3.1b Cpx-Ol-Silica Ternary Phase Diagram

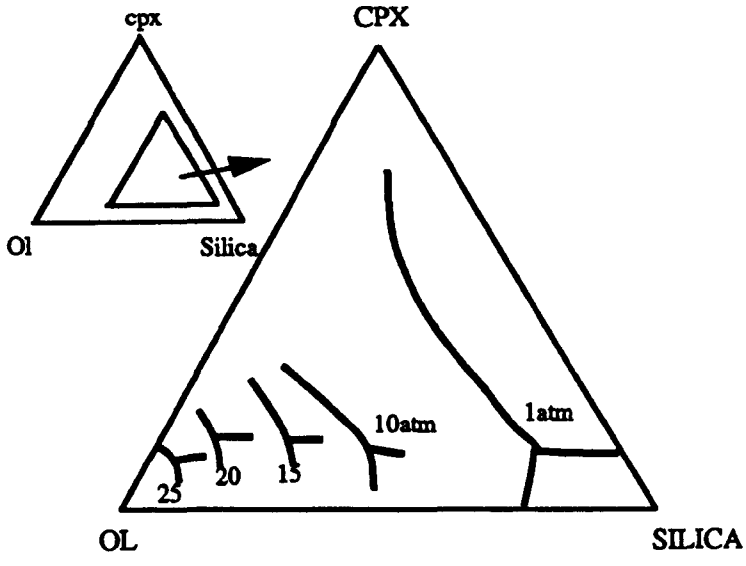

Elthon and Scarfe (1984)

This figure is a section of the basalt tetrahedron diagram projected from anorthite. The stability field of olivine increases with decreasing pressure from 25atm to 1atm. This means that a picritic melt, with an original composition close to the olivine apex, rising through the lithosphere towards low pressure conditions is likely to undergo a period of olivine only fractionation. The phase relations were calculated by calculating the normative compositions of experimentally created melts (Elthon and Scarfe 1984).

3.2 Bragança dunite and chromite-rich sample textures

3.2.1. Chromite-rich layers

Chromite is found within dunite both dispersed, as individual grains, and in discontinuous boudinaged layers. The proportion of chromite in the layers ranges from disseminated grains up to 90 modal%. When exposed in-situ the layers lie concordant with the main tectonic lamination and are less than 15cm thick. Over a few cm along strike in a chromitite layer the proportion of chromite grains can vary from 30 to 90%. Lower grade chromite concentrations are found in thinned or tectonically stretched parts of a layer and the high grade chromitite is found in the thicker parts (plates 3.2.1a-b). A few samples collected show chromitite in isolated, roughly rounded, nodule shapes up to 2cm across (plate 3.2.1c).

In massive chromitite samples, grains vary in maximum length from <0.1mm to 1cm. The smaller grains are generally regularly shaped, commonly having square outlines, with the coarser ones taking more irregular shapes. The coarser chromite grains are found in more massive layers. In chapter 2 it was demonstrated that neoblasts of olivine and orthopyroxene had developed in response to the strain imposed upon the ultrabasic rocks. This process has also effected chromite. The fine textures present are not always clear at the

scale of observation of optical microscopes and SEM photomicrographs are important in this respect. Plate 3.2.1d shows neoblasts of chromite of approximately 10μm diameter within a chromite-rich sample. They have the grain boundary angles approaching 120° which are characteristic of neoblasts. Through recrystallisation, massive aggregates of strain-free neoblasts have been created. A similar texture seen in reflected light is shown in plate 3.2.1e. Granulation and the creation of pull-apart cracks within chromite grains are the final textural overprints and are related to brittle deformation. The margins of chromite grains and areas beside cracks often have a notably lighter grey reflectivity than the main parts of the chromite. This is part of the ferritchromite alteration typical of serpentinised and chloritised chromite-bearing samples (plate 3.2.1e)

3.2.2 Serpentine and chlorite

The serpentinisation fabric is similar to that described for the harzburgite formation in chapter 2. Serpentine shows a mesh like fabric in samples which have undergone relatively low strain, pseudomorphing all but some rare olivine relicts. At higher strain the pseudomorph fabric is destroyed leaving a fine grained serpentine groundmass. In addition to serpentine minerals, chlorite is present as tabular shaped grains within the chromite-rich samples. This chlorite is found adjacent to chromite grains, frequently surrounding them. It shows first order yellow and brown birefringence colours unlike the more monotonous greys of serpentine.

3.2.3 Origin of the Bragança textures and implications

As a result of the high strain fabric present in much of the Bragança UATC ultrabasic assemblage outcrop, it is not easy to distinguish between the dunite associated with chromite mineralisation and the main harzburgite formation. Any residual margins to the dunite associated with chromite or discordant veins of dunite that might originally have been present, cannot be seen. The main bodies of podiform dunite with chromite-rich patches are believed to mark magma conduits in a similar fashion to that envisaged for other mantle assemblages such as the Oman. During tectonic emplacement of the Bragança ultrabasic assemblage any original magmatic textures have been obliterated by the recrystallisation of the chromite in response to the high strain regime. The outline of the platinum-group minerals included within chromite grains has also been changed by this process (chapter 4).

Chapter 3 plates

Plates 3.2.1a-b
These plates show the relationship of boudinage to chromite textures. In the thicker part of the chromitite lens, the chromite grains have a coarse, interlocking texture. In the thinner, necked part of the layer there is a lower proportion of chromite and discrete grains are finer. The creation of massive chromitite is caused by this process of boudinage. Scale ten pence piece. Sample 154BRG.

Plate 3.2.1c
Nodular texture developed in chromite-rich sample (Brag 31). The nodules consist of rounded, massive aggregates of chromite, 2cm across, split by late pull-apart cracks. Scale ten pence piece.

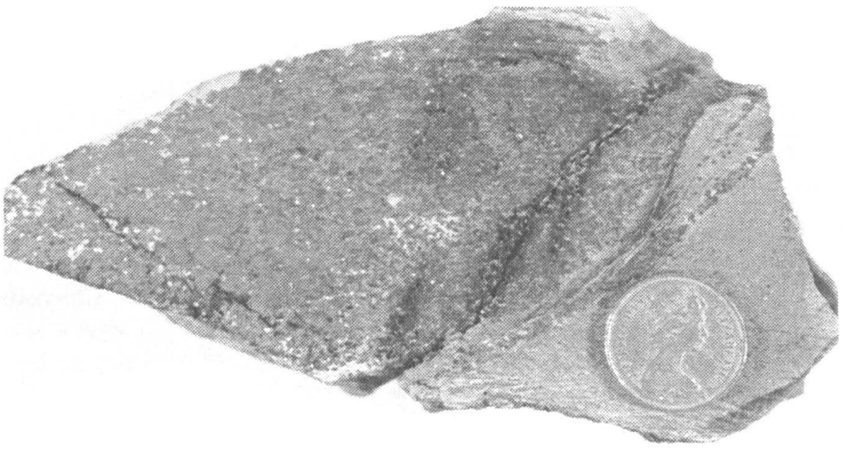

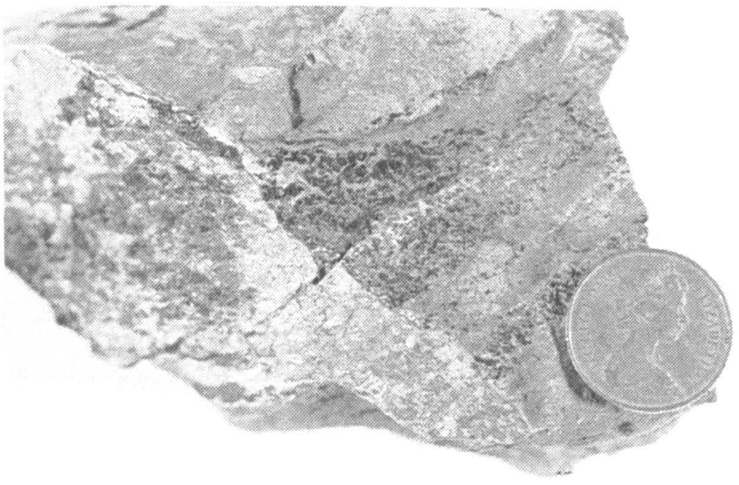

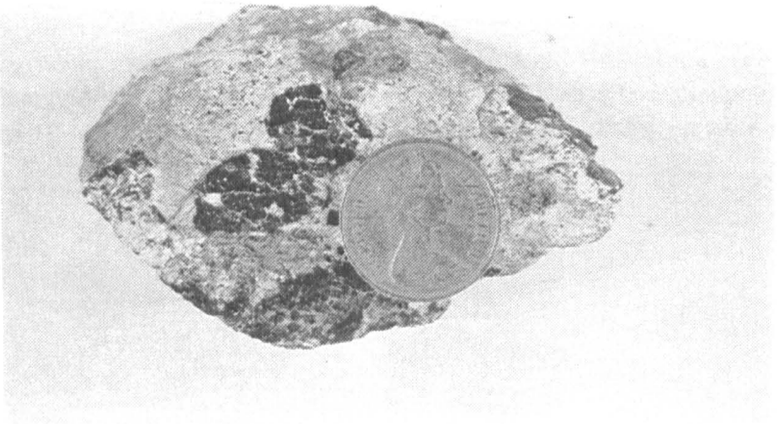

Plate 3.2.1d
This micrograph was taken at high magnification on the SEM. The chromite shows the development of an annealed texture. Chromite neoblasts have polygonal outlines and grain boundaries approaching 120degrees. This recrystallisation has arisen in response to the high strain imposed upon the ultrabasic assemblage. Also included within the field of view is a PGM described in chapter 4. Sample Brag52. Scale on micrograph.

Plate 3.2.1e This plate of a chromitite sample was taken under oil immersion, reflected light. It shows an annealed fabric with polygonal outline neoblasts. Sample Brag76 F.O.V. 1.4mm.

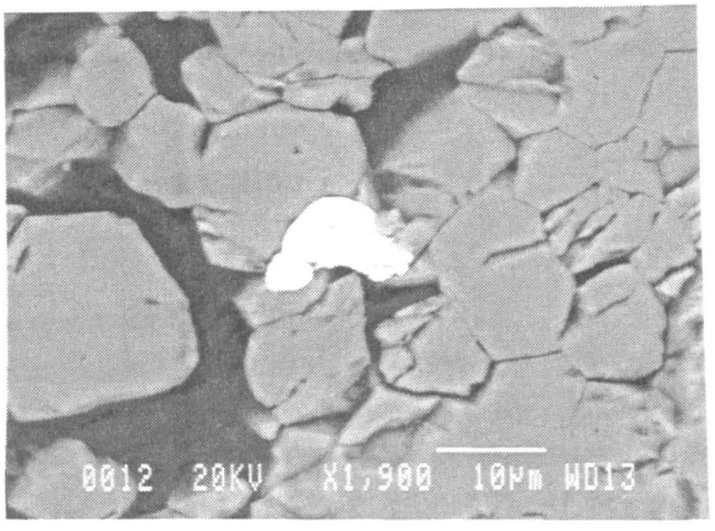
0012 20KV X1,900 10μm WD13

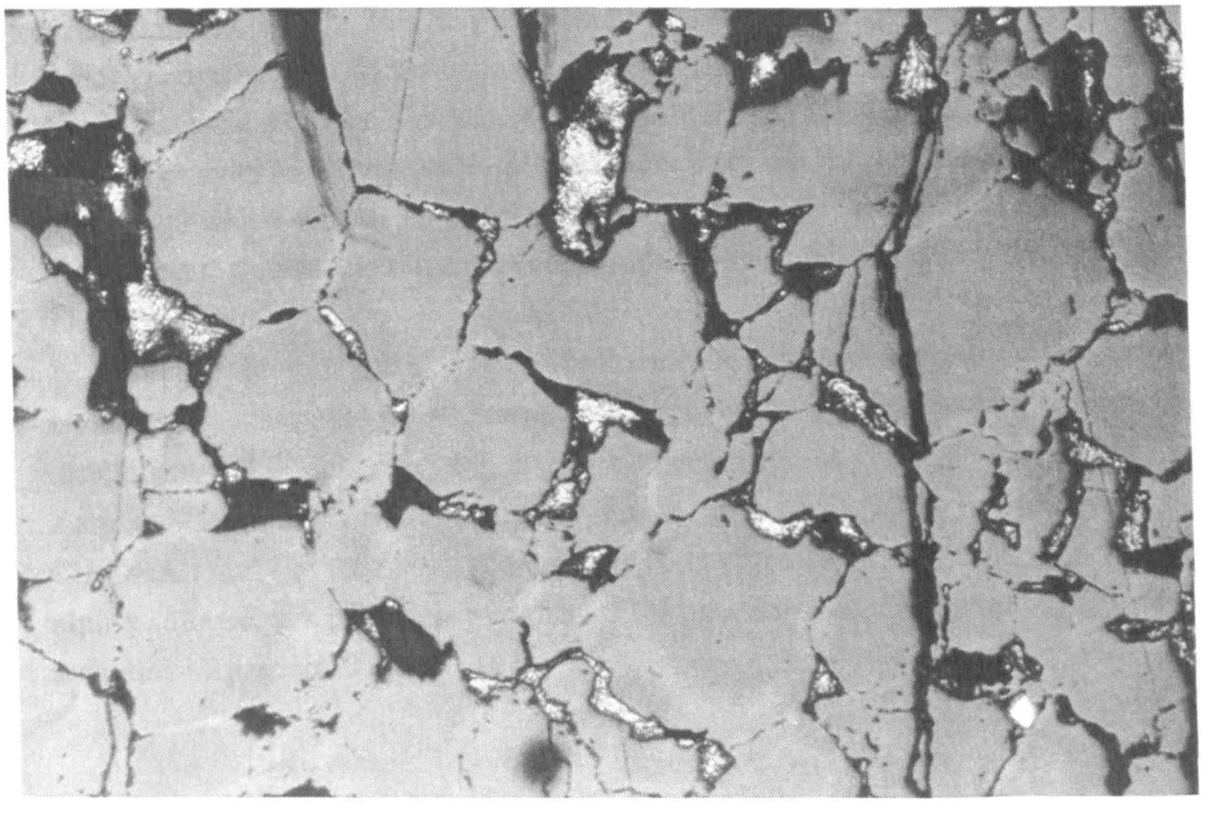

The next section deals with the composition of the chromite grains and other minerals from the chromite-rich samples. A major question to be addressed is whether, in the light of the strain induced recrystallisation of the massive samples, the composition of the chromite grains has been sufficiently preserved to indicate fractionation or partial melting conditions. In order to assess the effects of alteration on chromite composition, several series of probe analyses were taken across individual chromite grains. The results are presented in the next section.

3.3 Mineral composition

3.3.1 Zonation and variation within samples

The plots in figure 3.3.1a-d show the variations in cation contents seen in analyses traversing individual grains as well as between different grains from the same sample. At the margins of some chromite grains, there are decreases in the cation contents of Al and Mg whereas Cr, total Fe, Ti and Mn increase. Out of Cr, Al, Mg and Fe, the greatest relative decrease in the altered zone is shown by Al (up to 43% in fig. 3.3.1d compared to the adjacent analysis) and the greatest relative increase by Fe (up to 54% in fig 3.3.1d compared to the adjacent analysis). Compositional zonation is not found in all chromite grains: the two grains from sample Brag89 (fig. 3.3.1e) show the alteration whereas the example from sample Brag26 does not. This may be caused by local variations in the breadth of the altered zone. Where it has been located by the probe data it is less than 100μm wide. This zonation is not seen using oil immersion lenses. It represents a transitional stage in alteration to the bright reflectivity ferritchromite rims, which were not analysed. The Cr-rich composition of the chlorite which sometimes surrounds them, is used as evidence for Cr remobilisation. The Bragança chlorite and serpentine compositions were tabulated in chapter 2 and are listed fully in appendix 4.

Similar chromite grain compositional zonation has been reported for other ultrabasic assemblages. Chromites from chromitite deposits in Vavdos and Gomati, N. Greece show enrichment in Fe^{3+} and Fe^{2+}, Mn and Ti with reduction of Cr, Mg and Al towards grain margins (Christodolou and Hirst 1985). Similarly Kimball (1990) noted increases in the Cr/(Cr+Al) and $Fe^{2+}/(Fe^{2+}+Mg)$ atomic ratios in chromite grains, from both abyssal and alpine sources, towards their margins. This was attributed to hydrothermal alteration including serpentinisation.

Figure 3.3.1 Compositional zonation of chromite grains

Figure 3.3.1a Sample Brag26

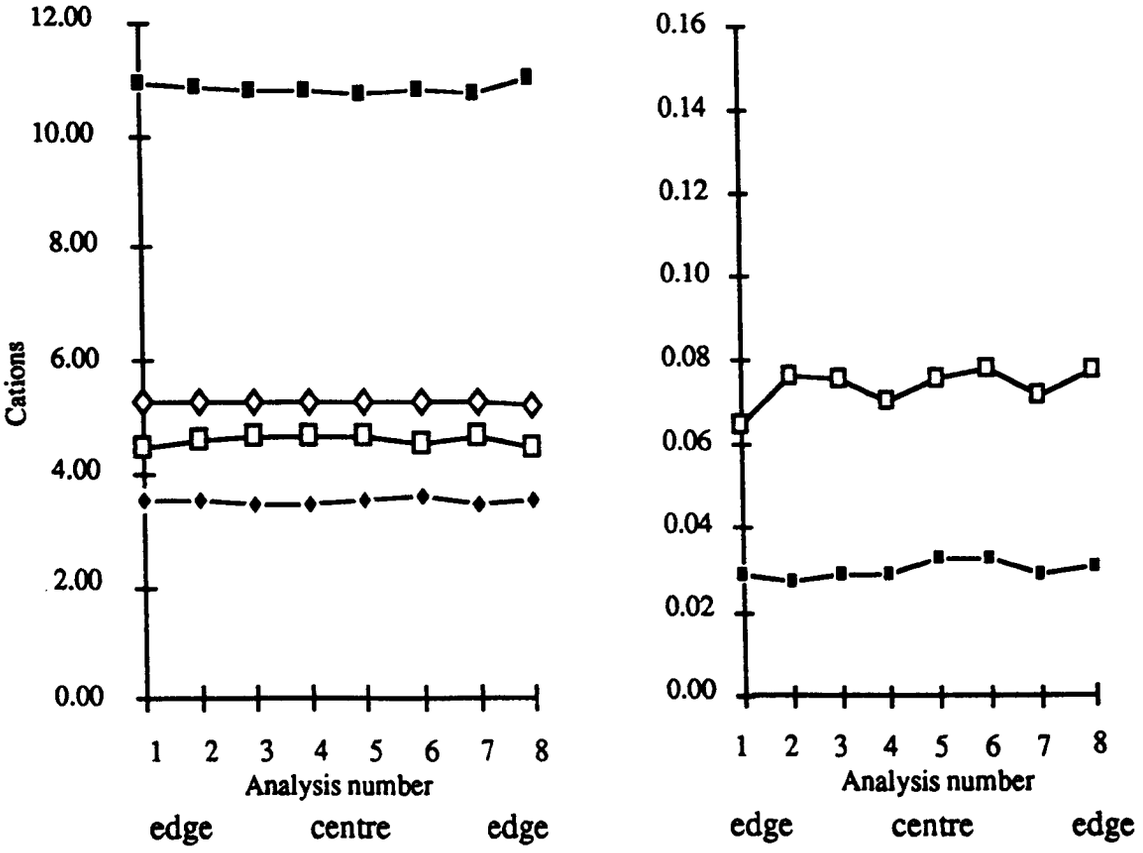

Figure 3.3.1b Sample Brag57

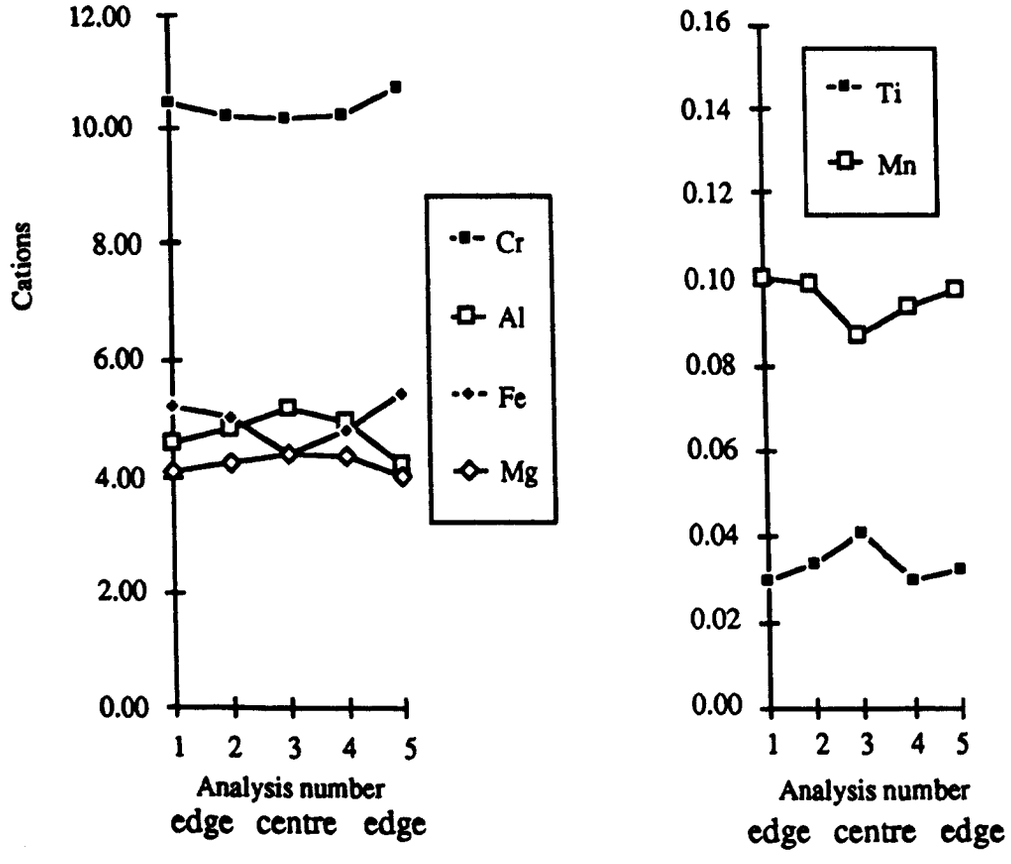

Figure 3.3.1c Sample Brag89 first grain

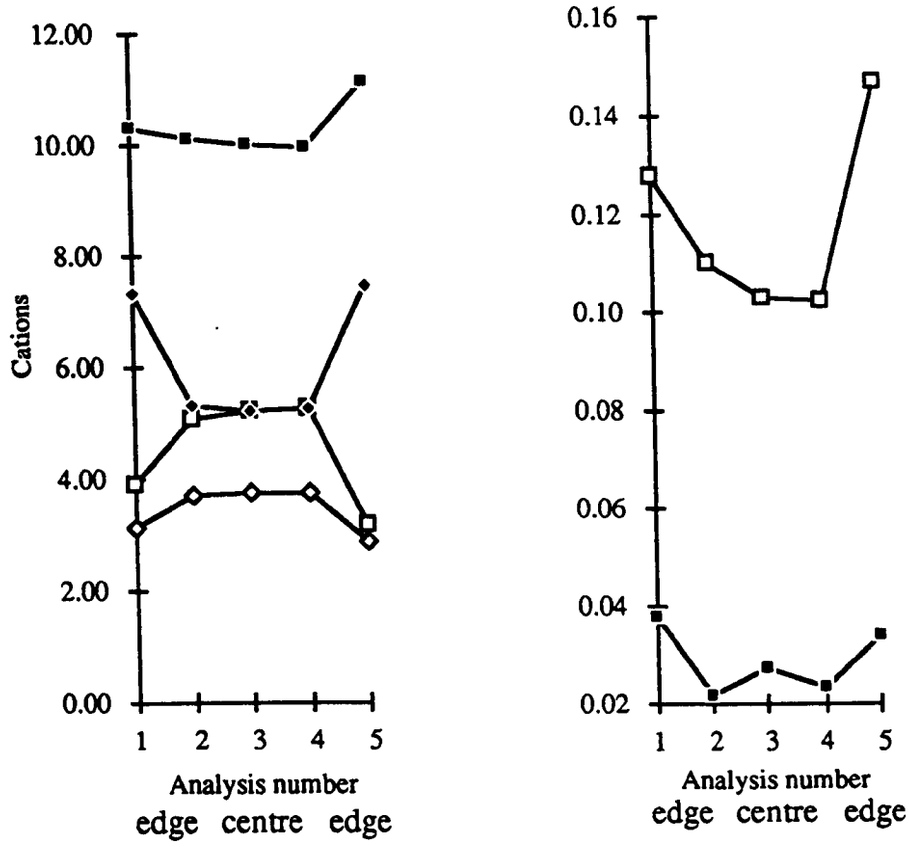

Figure 3.3.1d Sample Brag89 second grain

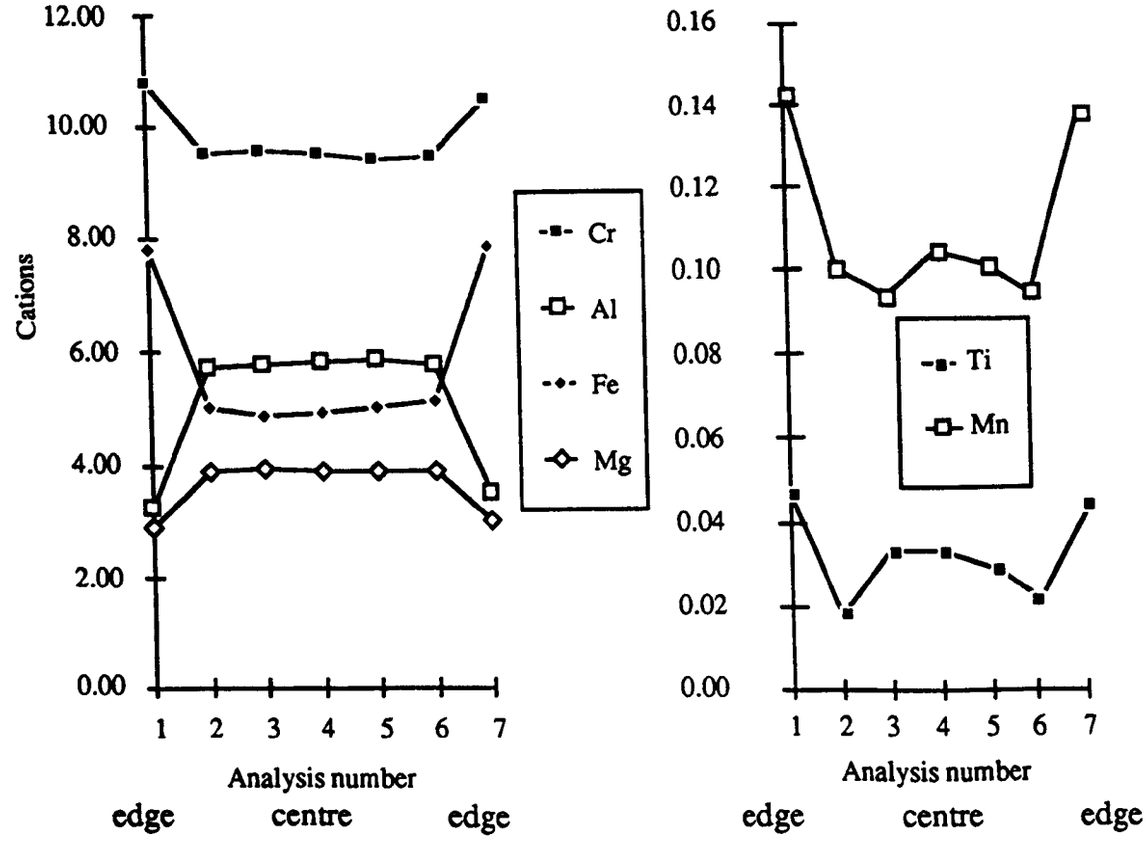

Figure 3.3.1e Brag89 Chromite grain Scan Analyses Sketches

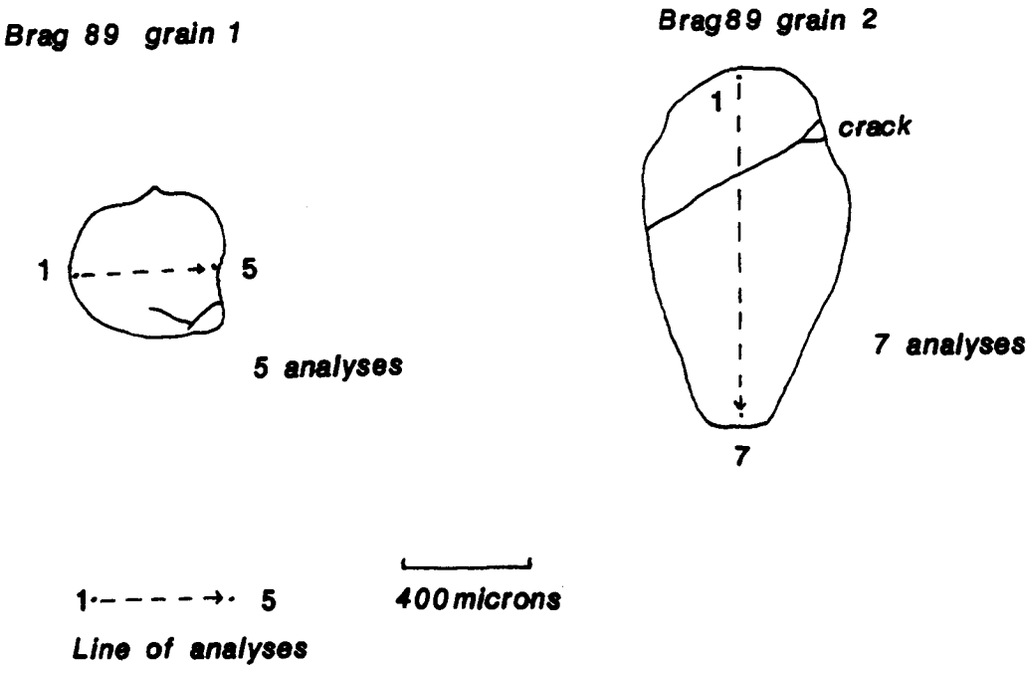

The sketches above are of the two sample Brag89 chromite grains used in the scan analyses. Five analyses were taken at regular intervals across grain 1 and seven across grain 2. The analyses at either end of the scans were taken as close as possible to the grain edge (≤30μm). The width of the altered zone is irregular.

3.3.2 Variation of chromite composition across the Bragança Massif

Table 3.3.2 below summarises the compositional variation of samples taken from across the Bragança Massif. These are analyses taken from the cores of chromite grains not effected by the low temperature alteration characterised in the previous section. In order to determine the variability within one locality, four separate samples from the Derruida locality were analysed: Brag57, Brag56, 8BRG and 12BRG. The Cr_2O_3 range within these samples of 48.08-55.26 (appendix 4) makes up 53% of the total Cr_2O_3 variation as shown in the table below. Thus much of the compositional variation is also present within a single locality. No systematic pattern of compositional variation has been identified across the massif. In contrast Prichard *et al.* (1991) suggest that the chromite occurrences on the west side of the ultrabasic outcrop have higher Cr_2O_3 contents than those on the east side.

Table 3.3.2. Compositional variation of chromite grain core between samples from different localities

	Max.	Min.
% Cr_2O_3	60.0	46.4
% Al_2O_3	19.1	6.9
% TiO_2	0.24	0.09
% FeO	23.3	12.3
% MgO	14.0	7.4
100Cr/(Cr+Al)	85.1	62.4
$100Mg/(Mg+Fe^{2+})$	68.4	35.4
$100Fe^{3+}/(Fe^{3+}+Cr+Al)$	3.32	11.58

224 analyses from 25 polished thin sections made from samples taken from chromite-rich localities across the Bragança UATC ultrabasic outcrop. A full set of analyses and sample numbers is given in appendix 4.

In chapter 2 it was shown that the chromite grains from the chromite-rich samples had undergone Mg and Fe^{2+} partitioning down to temperatures of 500-550°C. The highly forsteritic composition of the olivine grains, compared to others from Bragança and Morais, as described in chapter 2, is also evidence of the Mg/Fe partitioning having taken place, with the olivines being enriched in Mg relative to Fe during cooling. As a result of this the use of $100Mg/(Mg+Fe^{2+})$ ratios in chromites in an attempt to describe melt compositions is probably invalid for samples such as those from Bragança. Cr and Al are unlikely to be effected in the same way as Mg and Fe because there is no other mineral phase at high temperatures with which Cr or Al could partition. The Cr-rich composition of the chlorite shows that this element is remobilised at the lower temperatures associated with greenschist metamorphism. The centres of chromite grains are most likely to preserve original Cr and Al compositions. Chromite grain core analyses are used in the next section to give information about the primary origin of the chromite mineralisation.

3.3.3 Chromite core composition

Much of the possible variation in composition of spinels is shown in the graphs of fig. 3.3.3. Compositional fields for podiform chromitites have been drawn on the fig 3.3.3 graphs and superimposed on the 224 Bragança chromite grain analyses (from the dunite/chromitite formation). The compositional fields are based on the information published for 18 complexes. They are all considered by the respective authors to be associated with ophiolites with some oceanic provenance, apart from the Jijal complex of Pakistan which is thought to be part of an arc complex (Jan and Windley 1990).

Figure 3.3.3 Chromite grain compositions from different geological settings

Fig. 3.3.3a 100Fe3+/(Fe3+Cr+Al) v 100Mg/(Mg+Fe2+)

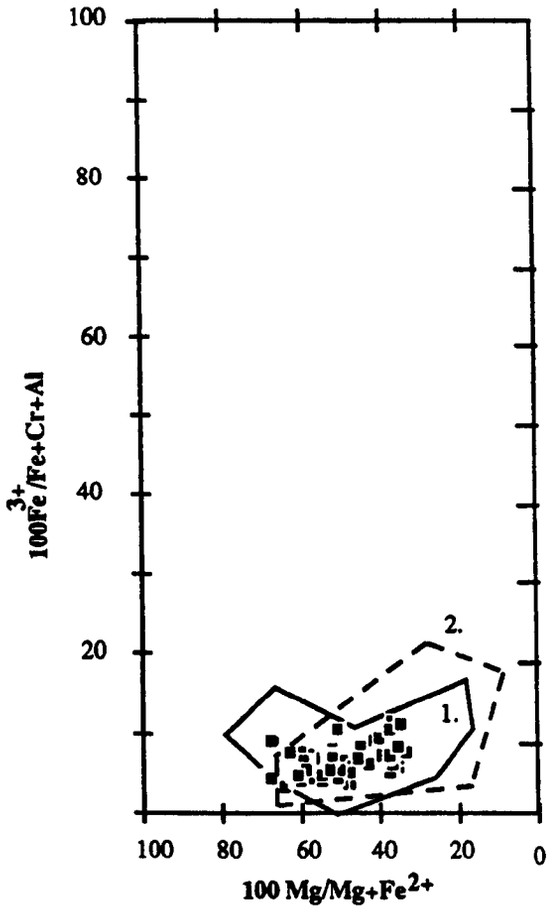

Fig. 3.3.3b Cr/(Cr+Al) v 100Mg/(Mg+Fe2+)

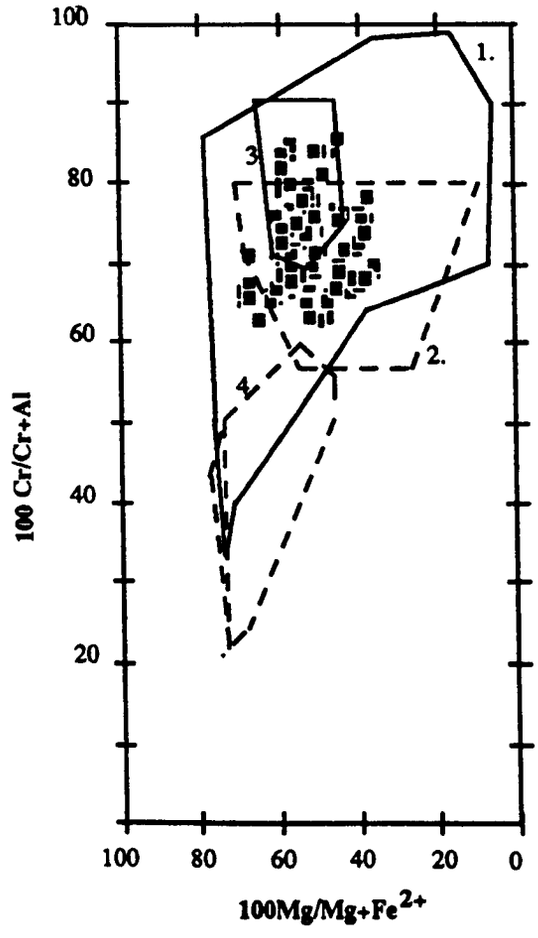

Fig. 3.3.3c Fe3+/Cr/Al triplot

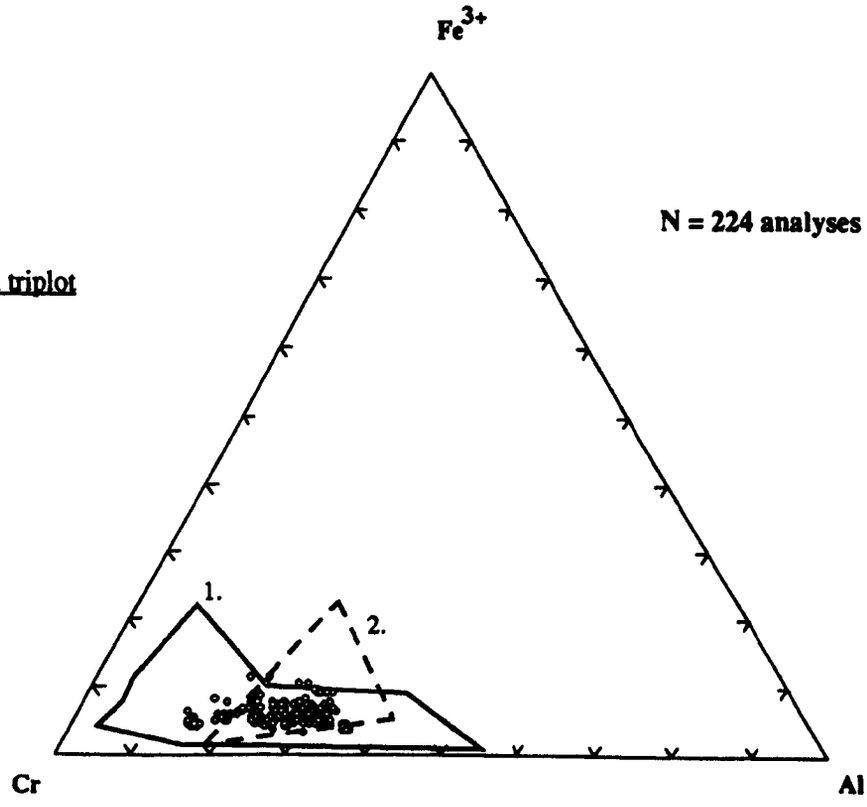

Fields: 1. Podiform Chromitites
2. Stratiform intrusions
3. Boninite lavas
4. MORB
Fields 2 and 4 have dashed outlines for clarity

References: **Field 1.** (a) Brown 1982 Oman;(b) Augé and Roberts 1982 Oman; (c) Jan and Windley 1990 Jijal; (d) Gass *et al.* 1982 Shetland; (e) Christodolou and Hirst 1985 Vavdos and Gomati; (f) Dick and Bullen 1984 Twin Sisters, Troodos; (g) Thalhammer et al. 1990 Kraubath and Hochgrössen (h) Neary 1974 Al 'Ays; (i) Neary and Brown 1979 Al 'Ays; (j) Burgath 1988 Borneo; (k) Leblanc et al. 1980 New Caledonia; (l) Economou and Economou 1986 6 Greek ophiolites.
Field 2. Irvine 1967 Bushveld, Great Dyke, Stillwater, Muskox and Alaskan type intrusions. Duke 1983 (triangular plot) Great Dyke, Bushveld, Bird River, Stillwater.
Field 3. Cameron et al. 1980.
Field 4. Dick and Bullen 1984.

The graphs are three sections through the spinel prism which show much of the possible compositional variation. The podiform chromitite field drawn on the graphs was derived from the 18 localities listed above. The 100Cr/(Cr+Al) ratio is the most useful discriminant between the five tectonic settings. The boninite field plots above 70 and the MORB field below 60. The podiform chromitite field overlaps both of these. The 224 Bragança analyses fall outside those of the MORB field suggesting that the chromite grains' creation were not associated with oceanic generation, as they have too refractory a composition.

As can be seen from figs. 3.3.3a-c there is a large overlap in compositions for a variety of different geological environments. The most useful discriminant is the Cr/(Cr+Al) ratio. The field for podiform chromitites extends from 35 to over 95 on the 100Cr/(Cr+Al) scale. Most of the analyses plot above 50 as shown by the tapering of the field towards lower values. It is apparent that the trend of slightly decreasing 100Mg/(Mg+Fe^{2+}) ratio with increasing 100Cr/(Cr+Al) values seen for accessory chromites from alpine terranes, and (see chapter 2), is preserved. Individual complexes within the overall field do not always show this trend.

The composition of boninite lava spinels (Cameron *et al.*, 1980 and Crawford *et al.* 1989) plots above 70 on the 100Cr/(Cr+Al) scale. This is in a similar position to many podiform chromite analyses. In contrast the field for MORB spinels (Dick and Bullen, 1984) lies between 60 and 20. Table 3.3.3 gives the range of 100Cr/(Cr+Al) ratios for five ophiolite complexes, known to be associated with the creation of ancient oceanic crust, and the Jijal arc complex. The overall range from 45 to 95 in table 3.3.3 covers both the arc related boninite/low Ti lava and MORB fields.

Table 3.3.3 100Cr/(Cr+Al) ratio range of chromite from podiform deposits

	100Cr/(Cr+Al) ratio range of podiform deposits	Authors
Oman	45-83	Brown (1982)
Troodos	41-83	Greenbaum (1977)
Al' Ays	50-95	Neary (1974)
Vavdos and Gomati	45-85	Christodolou and Hirst (1985)
Shetland	55-80	Prichard and Neary (1982)
Jijal arc	67-95	Jan and Windley (1990)
Bragança	62-85	This study

The range of 100Cr/(Cr+Al) ratios for each ophiolite extends to below 60. In contrast the ranges for the Jijal arc complex and Bragança are completely above 60. This suggests that the Bragança chromite composition is not consistent with oceanic lithosphere generation.

Figure 3.3.3d Chromite TiO_2 versus 100Cr/(Cr+Al)

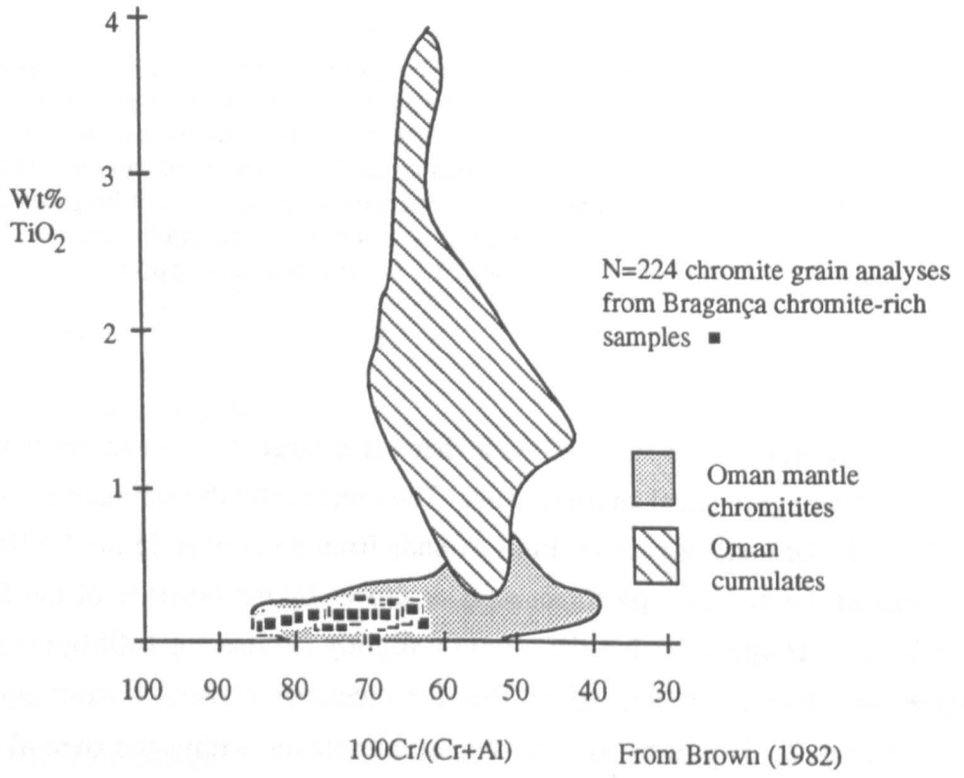

This figure shows the composition of the Bragança chromite-rich sample grains in terms of TiO_2 and the Cr/(Cr+Al) ratio. Superimposed on the analyses are compositional fields from the Oman ophiolite mantle chromitites and cumulates from Brown (1982). The Bragança analyses have low TiO2 contents (less than 0.25wt%) characteristic of podiform chromitites. In contrast the Oman cumulate sequence shows a vertical trend with more TiO_2 enrichment.

The 100Cr/(Cr+Al) values for Braganca all lie above 60, with a cluster around 75 (table 3.3.3 and fig. 3.3.3b). The cluster lies away from most of the abyssal spinel compositions of a MOR setting and does not show the 100Cr/(Cr+Al) ratio range down to the low values associated with the ophiolite complexes given in table 3.3.3.

Chromite grains within podiform chromitites characteristically have low TiO_2 contents *eg* Oman <1wt% (Brown 1982); Troodos <0.23wt% (Greenbaum 1977); Shetland <0.3wt% (Prichard and Neary 1982). There is also little variation in TiO_2 content between chromitites from the same alpine complex. In contrast, chromites from stratiform intrusions may show greater variability and higher contents *eg* Neary (1974), Dickey (1975). Fig. 3.3.3d shows TiO_2 contents plotted against 100Cr/(Cr+Al) for the Bragança samples. Superimposed on this are the compositional fields for Oman mantle chromitite and Oman accessory chromite compositions (from Brown 1982).

3.4 Models to explain primary variation of chromite grain chemistry in podiform settings

3.4.1 Differing degrees of partial melting in mantle source region

In a theoretical approach to partial melting and its effects on chromite composition, Dick and Bullen (1984) modelled the Cr (compatible) and Al (incompatible) values in a residual peridotite after the removal of successive batches of melt. They used a partition coefficient (D) calculated from the ratios of those elements between an average abyssal spinel-peridotite and an abyssal tholeiite basalt which could be derived from it (fig 3.4.1). From this model the authors deduced that 100Cr/(Cr+Al) ratios of chromite grains from mantle chromitite deposits or lavas reflected the total degree of melting that the source material had undergone. Greater values of this ratio are due to derivation from a source that has previously undergone a higher degree of melting compared to chromites with lower ratios. Further evidence for this conclusion was taken by the authors from the differing compositions of spinels in MORB and boninite lava (fig. 3.3.3b).

Leading on from this idea the authors subdivided alpine peridotites into types 1, 2 and 3. Type 1 having spinel 100Cr/(Cr+Al) ratios less than 60, type 3 greater than 60 and type 2 transitional between the two. Type 3 alpine peridotites were thought to represent arc-related rocks, the chromites derived from a source that had already undergone previous melting episodes; with type 1 corresponding to a mid-ocean ridge environment . Type 2 peridotites (in which the Oman and Troodos ophiolites would lie) were considered to mark a transition from MORB to island arc environment. By this model the podiform chromitite field shown in fig 3.3.3b would be a mixture of type 2 and type 3 complexes.

Spinels from boninites have low TiO_2 contents: Cameron *et al.* (1980) published a representative spinel analysis from Troodos boninites of 0.23wt% TiO_2. However this value overlaps with that in a variety of basalts. For instance Dick and Bullen (1984) presented a set of spinel compositions from abyssal basalts, with TiO_2 contents from 0.5wt% down to negligible values. Only the Cr and Al contents of spinels have been shown to be directly related to degrees of partial melting. Chromite Cr/(Cr+Al) ratios vary little with changing pressure between 1 and 10atm, or within normal ranges of oxygen fugacity,

to be directly related to degrees of partial melting. Chromite Cr/(Cr+Al) ratios vary little with changing pressure between 1 and 10atm, or within normal ranges of oxygen fugacity, and instead are mainly dependent on the original composition of the melt (Roeder and Reynolds 1991).

Figure 3.4.1 Batch melting of an abyssal peridotite

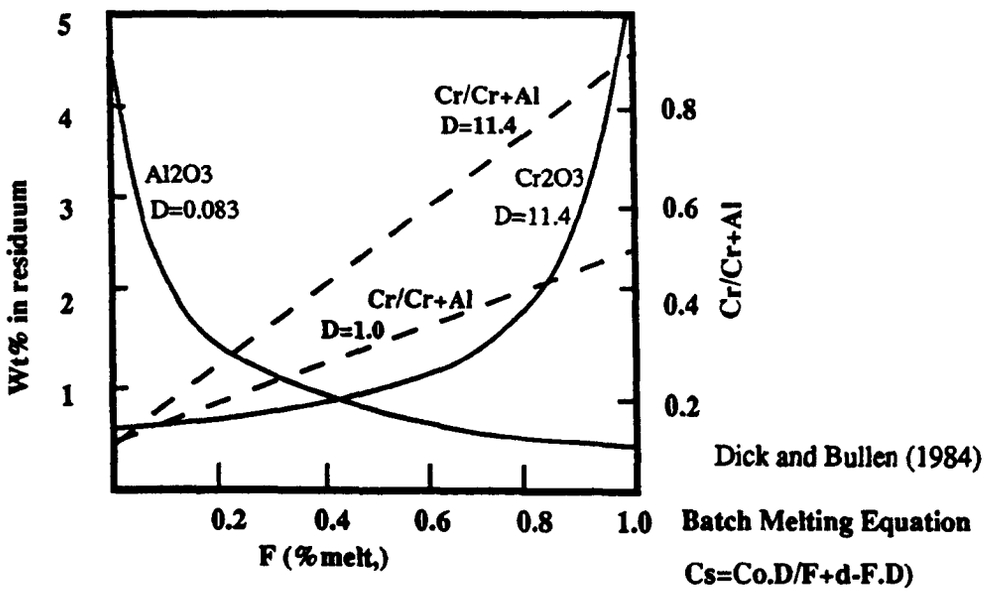

This figure shows the variation of Al2O3, Cr2O3 and Cr/(Cr+Al) within the residue of a melted peridotite using a batch melting model ie melt formed in equilibrium with the residue until it escapes. F is the weight proportion of melt formed. The distribution coefficient D used for Al is 0.083 and those for Cr 11.4 and 1.0. Co and Cs are the original peridotite and melt concentrations respectively. With increasing degrees of partial melt (F) extracted from the peridotite residue the Cr/Cr+Al ratio of the whole rock residue increases for likely D values for Cr of 1.0 and 11.4.

3.4.2 Fractionation

The Oman ophiolite is a well exposed, complete section of oceanic mantle and crust lithosphere; its mantle section is about 7km thick (Augé and Roberts 1982) and a considerable body of research exists on it *eg* Gass (1990), Browning (1982), Brown (1980). For these reasons, the Oman ophiolite offers the best chromitite-bearing mantle sequence with which to compare other less complete sequences in order to recognise any fractionation trends. Trends for the Ti content and the Cr/(Cr+Al) ratio, though not the $Mg/(Mg+Fe^{2+})$ ratio, have been identified by researchers on the Oman ophiolite. Neary and Brown (1979) described an increase in Ti content from about 0.2wt% to 0.4wt% for the

increase in Ti contents from chromite compositions below the petrological Moho to those above, in the Shetland ophiolite.

Brown (1982) noted a general decrease in the Cr/(Cr+Al) ratios of spinels for the chromitite deposits of the Oman ophiolite as they approached the petrological Moho, to values less than 0.6. This trend is not completely regular however (Roberts, 1986): deposits at a similar distance from the Moho in the Oman ophiolite can have differing Cr/(Cr+Al) ratios. Fractionation trends have not been reported from within the mantle sequences of other alpine complexes and it is likely that deformation and the absence of a well preserved mantle stratigraphic sequence, in most complexes such as Bragança, will obscure any fractionation trend.

3.5 Podiform chromitites - a supra subduction zone phenomenon

Pearce *et al.* (1984) reviewed the different tectonic settings of ophiolites in an attempt to identify geochemical components from underlying subduction zones. Ophiolites considered to be of supra-subduction zone (SSZ) origin from their large ionic lithophile enrichment, were characterised by chromitite mineralisation within dunite and harzburgite mantle assemblages. Chromitite was rarely found within ophiolites that have MORB affinity, without an SSZ component. Most podiform chromitites are considered to be part of ophiolite sequences, with an oceanic or arc provenance. However, podiform deposits are also located in massifs which do not contain ophiolite sequences and are not obviously associated with an oceanic setting. The Jijal complex of the Indus suture in Pakistan is one of the best reported examples. Jan and Windley (1990) described the Cretacous chromite-rich lithologies and associated ultrabasic rocks of the Jijal complex. Lithologies include a tectonic melange of peridotites, dunite with chromite-rich layers, pyroxenite and a separate suite of mafic granulites. The dunite contains lenses and layers of chromite-rich rocks from 20 to 70 modal% chromite. Chromite grains from these deposits have 100Cr/(Cr+Al) ratios of between 65 to 95, with a cluster at 80. The TiO_2 content of the spinel is less than 0.34wt%. Jan and Windley (*op cit.*) suggested, largely on the basis of the spinel composition, that the complex represented a suite of ultrabasic cumulates created in an arc setting.

The composition of the chromite grains from the Bragança deposits are similar to those from the Jijal arc complex. They correspond to the composition expected from a supra subduction zone arc environment forming early in the evolution of a destructive plate margin (Dick and Bullen 1984). The low Ti contents are also typical of podiform chromitites. Many ophiolites are thought to have formed in a supra-subduction zone arc situation, but there is no ophiolite stratigraphy in the upper nappes (UATC) of Bragança and Morais with which this assemblage could be correlated. Also all ophiolites whose chromite compositions have been reported, have a range of chrome-spinel 100Cr/(Cr+Al) ratios extending to values below 60 (fig. 3.3.3). Therefore the refractory composition of the chromite grains in the

which this assemblage could be correlated. Also all ophiolites whose chromite compositions have been reported, have a range of chrome-spinel 100Cr/(Cr+Al) ratios extending to values below 60 (fig. 3.3.3). Therefore the refractory composition of the chromite grains in the Bragança deposits, with a clustering of 100Cr/(Cr+Al) ratios around 75 and none below 62, suggests an origin for the relict mantle within a destructive margin, arc setting but not associated with ocean lithosphere (and ophiolite) formation. Chromite grain composition alone is not sufficient to further constrain the tectonic setting of the Bragança chromitites.

3.6 Conclusions

The isolated, tectonically disrupted, lenses of chromite within dunite found in the Bragança harzburgite formation are characteristic of the podiform type of mineralisation found in alpine ultrabasic rocks. The massive and nodular chromitite samples have undergone strain induced recrystallisation as shown by the development of polygonal outline neoblasts. No textures indicating the action of magmatic processes have been observed.

The high temperature partitioning between olivine and chromite is demonstrated by the presence of Mg-rich olivines (up to Fo_{95}) in chromite-rich samples. Low grade metamorphism associated with chloritisation and serpentinisation has caused remobilisation of the chromite's component elements at grain margins. Despite these late chemical changes it is thought that the core Cr, Al and Ti compositions of chromite grains reflect the composition of a primary melt, as there is an absence of silicate minerals such as pyroxene with which these elements could have partitioned at sub-solidus temperatures. The chromite core compositions, have 100Cr/(Cr+Al) ratios that cluster around 75, suggesting crystallisation from a primitive parental melt with boninitic affinities, derived from a depleted mantle source region at a destructive plate margin. The genesis of boninitic melts is considered further in chapter 6. The high 100Cr/(Cr+Al) ratios (all above 60) are not consistent with an ophiolitic type origin associated with ocean crust generation. Similarly high 100Cr/(Cr+Al) ratios have been found in the chromitites of the Jijal island arc complex of Pakistan (Jan and Windley 1990). Despite this the processes that acted in the formation of the Bragança deposits from rising diapirs of picritic melt within the mantle may be similar to those which have operated in suprasubduction zone ophiolites.

Chapter 4 Platinum-Group Element mineralisation within the chromite-rich samples

This chapter presents the results of a study of the Platinum-Group Element (PGE) mineralisation associated with the chromite-rich rocks. The first section is a review of modern research published on PGE mineralisation in podiform chromitites. Geochemical and mineralogical data from Bragança are then presented and interpreted with reference to the review in the succeeding sections and a model to explain concentration and fractionation trends within the chromitites is outlined. The Pd/Cu ratio of the silicate melt from which the chromite-rich rocks were derived is calculated in order to give comparisons with different types of silicate melts.

4.1. Review Of PGE mineralisation in podiform chromitites

Most of the modern research on PGE mineralisation associated with podiform or alpine chromitites has taken place within the last ten years. Interest has mainly been stimulated by a perceived economic potential. Table 4.1 summarises much of the recent published research on PGE geochemistry and mineralogy associated with podiform chromitites. Older studies seem mainly to have been concerned with placer deposits associated with alpine chromitites.

Table 4.1 PGM and PGE analyses of podiform chromitites

Author	Locality	Major PGM	Minor PGM	Whole rock PGE contents (ppb)
Agiorgitis and Wolf (1978).	Nine Greek ophiolites.			1.2 to 1065 Ir
Bacuta *et al.* (1990)	Zambales ophiolite, Philippines.	laurite-$Ru(OsIr)S_2$	Ir-Os-Ru, Pt-Fe, Pt-Pd(-Fe-Cu-Ni) alloys, moncheite-$PtPd(BiTe)_2$.	Pt range 1.0 to 5960, Ir range <20 to 550.
Burgath (1988)	S.E. Kalimantan Borneo.	laurite		
Constantinides *et al.* (1980)	Kokhinorotsos, Troodos Cyprus.	laurite, erlichmanite-OsS_2		

Legendre and Augé (1986)	Ten ophiolites: Tiébaghi and Massif du Sud New Caledonia, Troodos Cyprus, Vourinos Greece, Al Ays Saudi Arabia, Asteroussia Crete, Güleman and Fethyie Turkey, Theken Albania, Chamrousse French Alps.	laurite, ruthenirídosmine-OsIrRu.	iridosmine OsIr, ruthenian osmium OsRu, ruthenosmirid., osmiridium IrOs, erlichmanite OsS_2, xingzhongite IrCuS, osarsite OsAsS, irarsite. Unnamed: $(IrRhRuCuNi)_2S$ Pt-S, PGE-bearing Ni alloy.	
McElduff and Stumpfl (1990)	Troodos	laurite, cooperite-PtS, iridosmine, osmianruthenium Ru-Fe, Ir-Ru-Fe alloys.	Pt-Ir-S, Rh-Ir, Rh-Ir-Ni-Fe-Cu-S.	
Moring *et al.* (1988)	Rattlesnake creek Terrane N. California.	Ru-Fe, Os-Ir-Ru, Pt-Fe, Au-Pd alloys, laurite, irarsite-osarsite-ruarsite - Ir(OsRu)AsS group.		Average of 11 samples Pd 4.3, Pt 271, Rh 23, Ir 999, Ru 1909.
Nilsson (1990)	Osthammeren, Norway.	laurite, osarsite, erlichmanite, irarsite-IrAsS, hollingworthite-RhAsS, platarsite-PtAsS, sperrylite-$PtAs_2$, osmiridium, iridosmine, native Os.	$Pt_2(IrOs)Fe_{0.65}$, Ru-rich platarsite, (IrRh)SbS, IrSbS, $(IrPtPb)S_2$, Pd-Sb.	Up to 2063 total PGE.
Page *et al.* (1982a)	Tiébaghi and Massif du Sud ophiolites New Caledonia			Up to 1461. Pt/Ir 0.04 to 0.32. (average 0.1).
Page *et al.* (1982b)	Semail ophiolite, Oman			Up to 469. Pt/Ir < 0.08 to 0.57.
Page *et al.* (1983)	Voikar-Syninsky ophiolite Urals.			10 chromitite samples up to 85 Ir and 45 Pt. Pt/Ir 0.04 to 0.93.
Page *et al.* (1984)	Guleman-Elazigoph, E. Turkey.			Pt/Ir up to 2.35, av. 0.26.

Page *et al.* (1986)	19 Oregon and California ophiolites.			Up to 9120. Pt/Ir ratios 0.03 to 6.00.
Prichard *et al.* (1987)	Shetland ophiolite	laurite $Ru(IrOs)S_2$, irarsite Ir (Rh)AsS, hollingworthite Rh(IrPt)AsS, sperrylite $PtAs_2$, mertieite/stibiopalladinite Pd-Cu-Sb-As, native osmium Os.	ruthenian pentlandite $FeNi(Ru)_9\ S_8$, potarite PdHg, hongshiite PtCu, genkinite $(PtRhPdNi)_4Sb_3$ geversite $PtSb_2$ Unnamed phases: Os-Ir, Pt-Pd-Cu, Pt-Pd-Au-Cu, Au-Pd, Rh-Sb-S, Ni-Rh-Sb, Ir-Sb-S.	Up to 80 000. Pt/Ir 0.33 to 10.33
Stockman and Hlava (1984)	Josephine Peridotite and Onion Mt. ophiolite, SW Oregon.	laurite, Os-Ir alloy, Ru-(Ir-Os-S) alloy, Pt-(Fe-Cu-Ni-Sb-Ir) alloys.	sperrylite, Ir-Cu-S, Pt-S, Ni-Ir-Cu-Fe-S.	12.9 to 1159 Ir
Talkington and Watkinson (1986)	White Hills peridotite (two samples) Newfoundland, six British Columbia deposits, Vourinos Greece (two samples).			94 to 1985. Pt/Ir < 0.14 to 4.28.
Talkington *et al.* (1984)	White Hills peridotite and Bay of Islands Newfoundland, Troodos Kokkinorotsos.	laurite, erlichmanite.		
Thalhammer *et al.* (1990)	Hochgrössen and Kraubath ophiolite fragments, Austria	laurite, sperrylite, irarsite-hollingworthite-platarsite series (IrRhPt)AsS.	cooperite PtS, platarsite-hollingworthite-ruarsite RuAsS series. Unnamed alloys: Pd-Sb-Pt, Pt-(Os-Ir-Rh-Pd).	36.3 to 2283 Pt/Ir 1.01 to 12.5
This study	Bragança UATC	laurite, irarsite	sperrylite, hollingworthite, potarite, Pt, Pd-alloys, sulphide, antimonide, platarsite.	Up to 11200 Pt/Ir up to 2.61

4.1.1 Geochemistry

A feature of podiform chromitites shown in table 4.1. is the highly variable PGE contents, from tens of ppb up to thousands of ppb, between different pods of chromitite within the same complex. Out of the different complexes listed in table 4.1, the Cliff chromitite body of the Shetland ophiolite has the most enriched values, with up to 80,000ppb quoted for one sample (Prichard *et al.* 1987).

In order to show smooth geochemical and fractionation trends between the PGE, results are frequently chondrite normalised and plotted on graphs in the order Os, Ir, Ru, Rh, Pt, Pd. This is the order of decreasing melting point of the elements. The average C1 chondrite values given in Naldrett and Duke (1980): Os 514ppb, Ir 540ppb, Ru 690ppb, Rh 200ppb, Pt 1020ppb and Pd 545ppb are the only chondrite values to have received wide spread acceptance. Barnes *et al.* (1985) proposed using mantle normalisation as an accurate reflection of the concentrations found within likely igneous source material. Mantle values were calculated from harzburgite and lherzolite outcrops and xenoliths from twenty two localities. The resulting proposed upper mantle averages for the PGE are: Os 4.2ppb, Ir 4.4ppb, Ru 5.6ppb, Rh 1.6ppb, Pt 8.3ppb and Pd 4.4ppb. The chondrite values of Naldrett and Duke (*op. cit.*) are used here as it is considered that mantle source values are not yet well constrained.

Positive chondrite normalised slopes show a more fractionated PGE assemblage than samples with negative slopes. This general relationship is based on surveys of different lithologies *eg* Naldrett *et al.* (1979), Barnes *et al.* (1985), with rocks such as gabbros and norites having steep positive slopes compared with rocks derived from ultramafic magmas such as komatiites which have flatter slopes. Figure 4.1.1 shows the chondrite normalised profiles of different lithologies. The UG2 (Bushveld complex) and Stillwater (Montana USA) stratiform complex chromitite layers show positive slopes towards the Pt-Pd tail. In contrast the field for five podiform chromitite terranes compiled by Page *et al.* (1982b) shows strongly negative, unfractionated slopes. Negative chondrite normalised slopes and associated low (Pt + Pd)/(Ru + Os + Ir) ratios have been thought to be characteristic of podiform chromitites *eg* Page *et al.* (1982a,b ,1984, 1986), Talkington and Watkinson (1986). More recent work however has shown that fractionated PGE assemblages do exist in some podiform chromitite samples (*eg* Prichard *et al.*, 1987, Bacuta *et al.*, 1990). Figure 4.1.1 shows positive slopes from podiform chromitite samples taken from the Zambales ophiolite (Philippines), the Heazlewood complex (Tasmania) and the Cliff locality of the Shetland ophiolite. Table 4.1 uses the Pt/Ir ratio (where data available) to give an indication of the extent of fractionation within podiform chromitites; values range from 0.03 to 12.5. Most chromitite samples in alpine terranes have values in the lower part of this range, showing the unfractionated nature of the associated PGE assemblage.

Figure 4.1.1 PGE chondrite-normalised profiles from different localities

Figure 4.1.1a Stratiform and podiform chromitites

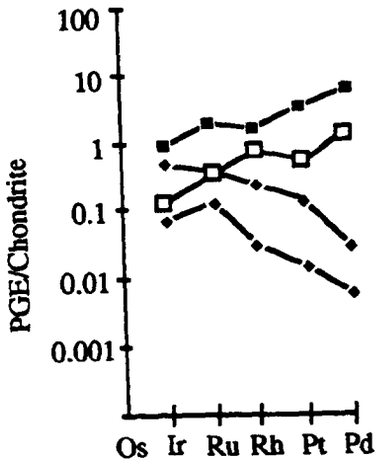

UG2[1]

Stillwater[2]

W. USA podiform deposits range[3]

Figure 4.1.1b Podiform chromitites

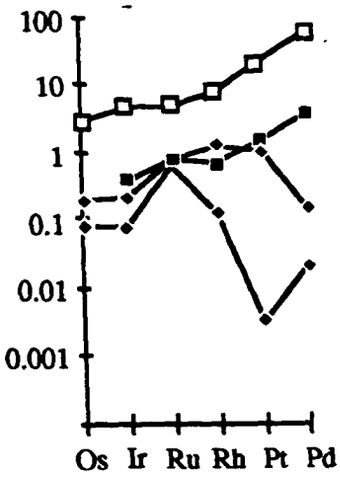

Zambales[4]

Cliff (Shetland ophiolite)[5]

Heazlewood[6]

Figure 4.1.1c Merensky Reef and komatiites

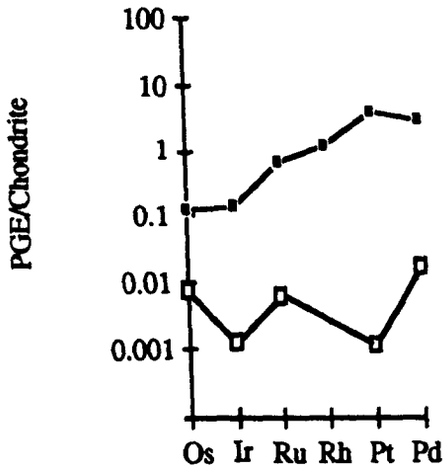

Merensky[7]

Boninite/komatiites[8]

Figure 4.1.1a shows the typical slopes associated with most podiform chromitites (negative, unfractionated) and stratiform chromitites (positive, fractionated). Figure 4.1.1b shows varying chondrite normalised graph trends for podiform chromitites with both negative, unfractionated slopes from Ru to Pt (lower part of the Heazlewood range) and positive, fractionated slopes for Cliff, which is part of the Shetland ophiolite, and Zambales. The lower plot for Heazlewood shows a positive upturn from Pt to Pd. Figure 4.1.1c shows the contrasting patterns for a gabbroic/pyroxenitic rock-Merensky reef of the Bushveld complex and a more flat, unfractionated slope for komatiites.

1. Gain (1985) 2, 7. Barnes *et al.* (1985) 3. Page *et al.* (1986) 4. Bacuta *et al.* (1990) 5. Prichard *et al.* (1987), 6. Peck and Keays (1990), 8. Economou-Eliopoulos and Paraskevopoulos (1989).

4.1.2. Mineralogy

Table 4.1.2. shows the most frequent mineralogical associations of the six PGE found within the podiform chromitites of table 4.1

Table 4.1.2 Most common PGM of podiform chromitites

	Sulphide	Arsenide	Sulpharsenide	Alloys
Os	Erlichmanite OsS_2 (c) Laurite $Ru(OsIr)S_2$ (c)		Osarsite $OsAsS_2$ (m)	Ru-Os-Ir
Ir	Laurite $Ru(OsIr)S_2$		Irarsite IrAsS (c)	Ru-Os-Ir
Ru	Laurite $Ru(OsIr)S_2$		Ruarsite RuAsS (m)	Ru-Os-Ir
Rh			Hollingworthite $Rh(IrPt)AsS_2$ (c)	
Pt		Sperrylite $PtAs_2$ (c)	Platarsite Pt(IrRh)AsS (c)	Pt-Pd-Cu
Pd				Pt-Pd-Cu

The letters in brackets refer to crystal system of the compounds: c cubic, m monoclinic. The PGE form four types of minerals: sulphide, arsenide, sulpharsenide and alloys. Of these minerals, the Os-, Ir-, Ru-bearing disulphide mineral laurite is the most frequently reported.

Os, Ir and Ru are present in disulphides, the Os-Ir-Ru alloy ternary system and in the osarsite-irarsite-ruarsite group. Another association is found between Ir, Rh and Pt in the irarsite-platarsite-hollingworthite group. Pt is also found as as an arsenide - sperrylite. Pd and Pt are present in alloys, combining with other transition elements *eg* Pt-Pd-Cu alloys. Many of these alloys are unnamed. Of these minerals laurite is by far the most common, with irarsite, sperrylite, hollingworthite and alloys also frequently present. More rarely occurring PGM include those containing Bi,Te: moncheite $PtPd(BiTe)_2$, hongshiite PtCu, xingzhongite IrCuS, cooperite PtS and ruthenian pentlandite $(FeNiRu)_9S_8$.

It has been suggested that the PGE might exist in solid solution within chromite. In a geochemical study of some Greek podiform chromitites Agiorgitis and Wolf (1978) presented a correlation between Cr and Os, Ru and Ir. The authors suggested that the PGE substituted for Cr^{3+}. Crocket (1979) in a study of the six PGE's geochemistry such as the similarity of their ionic radii with chromite, stated that the existence of such solid solution could not be ruled out in chromitites. However, the subsequent increased amount of published work on chromitites, including the podiform type summarised in table 4.1, clearly shows that when PGE tenors are high, these elements are present in discrete mineral phases or in solid solution within a sulphide phase.

In addition to the PGM listed in table 4.1.2, Pt and Pd are recognized to lie in solid solution within base-metal sulphide *eg* Bacuta *et al.* (1990). In a report on the experimental results of the variation of PGE solubility with differing sulphide compositions and temperatures Mackovicky *et al.* (1986) found that pyrrhotite could contain up to 11wt% Pd and 2wt% Pt at 900°C, with less at lower temperatures. Pentlandite may contain up to

12.5wt% Pd at 900°C though no Pt at any temperature. Lower solubilities with decreasing temperatures were linked to exsolution of PGE-bearing phases. Recent mineralogical studies *eg* Prichard *et al.* (1987), Thalhammer *et al.* (1990), Bacuta *et al.* (1990) and have shown that the presence of Pt- and Pd- bearing minerals in podiform chromitites is not uncommon though Os-, Ir- and Ru- bearing minerals and in particular laurite are the most frequently seen.

The PGM are usually less than 30μm in diameter. PGM's enclosed within chromite frequently have a hexagonal or polygonal outline. The most commonly occurring PGM are in the cubic system (table 4.1.2) and Legendre and Augé (1986) suggested that the hexagonal outlines were sections through euhedral octahedra. A variation of mineralogy with textural position within chromitites has been noted by several researchers *eg* Legendre and Augé (1986), Prichard and Tarkian (1988) and Thalhammer *et al.* (1990). Pt- and Pd-bearing minerals are usually located within the silicate matrix, between chromite grains, and Ru-, Os- and Ir- bearing minerals enclosed within chromite grains. Prichard and Tarkian (*op. cit.*) suggested that this might represent a primary, igneous fractionation sequence, with the Pt- and Pd-bearing minerals starting to crystallise later than the others.

4.2. Models for PGE fractionation and mineralisation

Models devised to explain the geochemical and mineralogical characteristics of the PGE in igneous rocks (with applications to PGE in podiform chromitites) use the solubility of the PGE within silicate magmas, the role of sulphur droplets as collectors of the PGE, variation of PGE solubility in silicate melts and late remobilisation of the PGE associated with complexing by anions. These models will be discussed in succeeding sections in relation to the new geochemical and mineralogical data from Bragança.

The four main models are:

4.2.1. PGE solubility in silicate melts

Barnes *et al.* (1985) proposed a division of the six PGE into the Palladium-PGE (PPGE) consisting of Rh, Pt and Pd and the Iridium-PGE (IPGE) consisting of Os,Ir and Ru. This division was made on the basis of association *eg* with the IPGE being concentrated in PGM within chromite grains. The authors ascribed this division to different solubilities within silicate melts, the IPGE being less soluble, crystallising first as sulphides and alloys with the more soluble PPGE crystallising later giving rise to a fractionation. Amossé *et al.* (1990) reported experiments designed to compare the variation of Pt and Ir solubility in basic melts with changing fS_2 and fO_2. Their results showed a lower Ir solubility than that of Pt at $\log fO_2$ between -5 and -7 and a higher one at $\log fS_2$ greater than -3.

4.2.2. Sulphide as a PGE collector

The PGE show chalcophile associations in most rocks and because of this sulphide has been invoked as a collector for these elements. All Pt- and Pd-bearing grains, including arsenides and sulpharsenides, in chromitites were considered by Naldrett and Von Gruenewaldt (1989) and Bacuta *et al.* (1990) to be derived initially from a magmatic sulphide liquid. Using this model, based on the work of Campbell and Naldrett (1979), the tenor of Pt and Pd within an immiscible sulphide fraction of a basic melt will be described by a distribution coefficient D of those elements between sulphide and silicate liquids and the mass ratio of silicate to sulphide liquid (R). Greater envisaged values of D and R, up to R=10D, would be expected to increase the scavanging of PGE by this model.

4.2.3. Differing degrees of melting in a mantle source region

Naldrett and Duke (1980) related the slope trends of PGE chondrite normalised graphs to the degree of melting that a mantle source region had undergone. Pt, Pd and Rh (with the lowest melting points) were incorporated into a silicate melt at low degrees of melting whereas Os,Ir and Ru entered a melt only at higher degrees of melting. Thus, Pt- and Pd-enriched rocks, with positive chondrite normalised slopes, were considered to have been derived from lower degrees of mantle melting than rocks depleted in these PGE.

In contrast Hamlyn and Keays (1986) noted that the Pd contents of rocks thought to be derived from second stage mantle melts, such as boninites, were frequently higher than those from first stage melts such as MORB. During a first stage melt extraction, the PGE were believed to be preferentially partitioned into a residual sulphide phase within the mantle. This resulted in a sulphide phase with a high PGE tenor. Subsequent, secondary melts derived from this depleted source contained a high concentration of PGE and relatively little sulphide. This has been related to the presence of major PGE mineralisation in the stratiform complexes of Stillwater and Bushveld, which are thought to have had boninites (or their Precambrian analogues komatiites) as part of their parental melts (Crawford *et al.* 1989).

4.2.4. Remobilisation and complexing of the PGE

Thalhammer *et al.* (1990) presented a mineralogical study of the PGM found within podiform chromitites of the Hochgrössen and Kraubath ultramafic massifs of Austria. Like studies of other podiform chromitites, they noted that the Pt-bearing minerals were found on the edges of chromite grains or in the silicate matrix. These sulphide, arsenide and sulpharsenide Pt- and Pd-bearing minerals were considered to have formed from the alteration of primary sulphides within chromite rims or the silicate matrix at the same time as serpentinisation of the complexes. Economou and Naldrett (1984) came to a similar conclusion on PGE mineralisation within the Eretria podiform chromitites of Greece.

Recent research concerning the thermodynamics of solubility and remobilisation of the

PGE under hydrothermal conditions has concentrated on the role of HS^-, Cl^- and OH^- - bearing complexes (Wood 1987, Mountain and Wood 1988). Mountain and Wood (*op. cit.*) and Wood and Mountain (1992) showed that Cl^- and OH^- complexing would only be important under acidic and oxidising conditions. In contrast, serpentinisation is characterised by reducing conditions and so Cl^- and OH^- complexing can be ruled out as a way of remobilising the PGE during this type of alteration. The complexing and remobilisation of PGE by the HS^- ligand during serpentinisation remains a possibility.

4.3. Previous work On the PGE content and mineralogy of the Bragança chromitites

The first mention of the presence of PGM within chromitite samples from the Bragança Massif was by Cotelo Neiva (1945, 1947). In order to confirm these results, Jedwab *et al.* (1989) published the results of a preliminary mineralogical study of samples taken from three localities in the Bragança Massif: Minas de Abicedo, Carrazedo and Valongo (the Conlelas locality in this thesis). The presence of laurites, irarsites, sperrylite, potarite and a variety of Pt- and Pd- bearing unnamed alloys was noted within chromite-rich samples and silicate. In addition sobolevskite (PdBi) , froodite ($PdBi_2$) and atheneite $(PdHgPt)_3As$ grains were found. The mineral species were identified by examining x-ray spectra without quantitative analyses. This chapter extends the knowledge of the Bragança PGM and base-metal sulphide textures, compositions and genesis.

4.4. Bragança PGE and chalcophile geochemistry

4.4.1. PGE, As, Ni and Cu whole rock values

A complete set of the different PGE analysis batches, together with a brief discussion of the results of standards and blank analyses is given in appendices 3,7. In order to have a consistent data set all the analyses used in this chapter are from the same batch. An exception is sample Brag57 which was analysed in an earlier batch but is included because it clearly shows the highest degree of PGE enrichment. There is a range of sum PGE (∑PGE) from 24ppb in sample Brag70 to 11.2ppm in sample Brag57. Most of the values are towards the lower end of this scale; the whole rock value of 11.2ppm for sample Brag57 is unusually high for podiform chromitites. Only samples from the Cliff locality of the Shetland ophiolite (table 4.1) are higher (Prichard *et al.* 1987). Before discussing the PGE/chondrite ratio patterns it is necessary to determine what effect variations in modal % chromite between the samples have on PGE values. The highest ∑PGE tenors are in massive chromitites though other such chromitites *eg* sample 39BRG have low values (table 4.4.1). Of the six PGE, Ru is the most abundant element in thirteen samples, Pt in five, Pd in one and Pt and Ru equal highest in one sample. The samples with Pt most abundant are

all massive chromitites.

Table 4.4.1. PGE, Ni, Cu concentrations for Bragança chromite-rich samples

	Brag39	**Brag51**	**Brag56**	**Brag64**	**Brag70**	**Brag73**	**Brag76**
Locality	Pena de Velhos	Serralhoa	Demuida	Leutiscais	W. Leutiscais	N. Leutiscais	Conlelas
%Chrom.	60	55	50	25-50	50	50	30
Os ppb	34	18	28	70	4	28	46
Ir ppb	32	14	26	56	2	26	42
Ru ppb	72	62	38	140	12	54	185
Rh ppb	10	5	3	36	2	5	8
Pt ppb	20	4	2	86	2	8	6
Pd ppb	44	4	4	180	2	8	14
Ni ppm	1608	3503	2646	9778	2932	2643	
Cu ppm	87	0	16	1793	0	22	
Pt/Ir	0.63	0.29	0.08	1.54	1.00	0.31	0.14
Pt/ (RuOsIr)	0.14	0.04	0.02	0.32	0.11	0.07	0.02
Pd/Ir	1.38	0.29	0.15	3.21	1.00	0.31	0.33
Sample	**39BRG**	**45BRG**	**47BRG**	**55BRG**	**130BRG**	**134BRG**	
Locality	Vila Verde	Campos	N. Campos	Samil	Alimonde	Serralhoa	
%Chrom.	80	75	25-50	50	50-75	65	
Os ppb	18	78	20	38	20	34	
Ir ppb	18	118	12	32	20	32	
Ru ppb	58	225	40	86	66	60	
Rh ppb	7	45	3	6	6	5	
Pt ppb	8	155	4	2	4	2	
Pd ppb	2	90	6	4	2	2	
Ni ppm	1865	2057	3147	1700	1157	1815	
Cu ppm	0	26	13	0	0	107	
Pt/Ir	0.44	1.31	0.33	0.06	0.20	0.06	
Pt/ (RuOsIr)	0.09	0.37	0.06	0.01	0.04	0.02	
Pd/Ir	0.11	0.76	0.50	0.13	0.10	0.06	
Sample	**145BRG**	**152BRG**	**154BRG**	**155BRG**	**142BRG**		**BRAG57**
Locality	Cabeço Pedrosa	Cabeço Paixao	R. Tuela/ Abicedo	R. Tuela/ Abicedo	Cabeço Pedrosa		Demuida
%Chrom.	75	50	70	65	80-90		80
Os ppb	370	40	56	50	960		675
Ir ppb	400	70	135	130	1350		1550
Ru ppb	740	100	145	125	1500		1150
Rh ppb	125	18	118	135	240		605
Pt ppb	740	16	250	235	1650		4050
Pd ppb	116	8	43	22	260		3150
Ni ppm	915	1159	569	847	755		1384
Cu ppm	0	45	0	0	0		0
Pt/Ir	1.85	0.23	1.85	1.81	1.22		2.61
Pt/ (RuOsIr)	0.49	0.08	0.74	0.77	0.43		1.75
Pd/Ir	0.29	0.11	0.32	0.17	0.19		2.03

Both the Pt/Ir and Pt/(Os+Ir+Ru) ratios give similar trends between the samples showing that either can be used as an index of fractionation. Pt/Ir values range from 0.06 (least fractionated) for samples 134-BRG and 55-BRG up to 2.61 for sample Brag57 (the most fractionated). The average is 0.74. All but one of the samples (Brag64) with ratios above this average have 50% modal chromite or more. The exception is sample Brag64. The Pt/Ir ratios for the Braganca chromitites lie within the range of values for other podiform chromitites shown in table 4.1. The range of Pd/Ir ratios is 0.06, for sample 134BRG, to 3.21 for Brag64. All the samples with Pd/Ir ratios greater than 1 are massive chromitites except for sample Brag64.

Analyses for As showed that apart from samples Brag64 (26ppm), Brag70 (7ppm) and 47BRG (6ppm) all the chromite-rich samples had levels below detection limit. Values for Ni range from 569ppm for 154BRG to 9778ppm for Brag64. Cu contents range from below detection limit for twelve of the samples analysed up to 1793ppm for Brag64.

4.4.2 Correlations between the PGE

Table 4.4.2. Table of Pearson's 'r' correlation coefficients between the PGE and Ni, Cu

	Os	Ir	Ru	Rh	Pt	Pd	Ni	Cu
Os	-							
Ir	0.99	-						
Ru	0.99	0.98	-					
Rh	0.82	0.85	0.84	-				
Pt	0.98	0.98	0.98	0.90	-			
Pd	0.82	0.80	0.82	0.73	0.78	-		
Ni	-0.14	-0.18	-0.10	-0.18	-0.17	0.07	-	
Cu	-0.24	-0.24	-0.24	-0.24	-0.23	0.38	(0.90)†	-

N=18 chromite-rich and chromitite samples for PGE correlations and N=17 for coefficients with Cu or Ni. Correlation coefficient 'r' calculated as in Cheeney (1983). † This figure for the correlation between Ni and Cu is regarded here as unreliable, owing to one outlying data point distorting the calculation. The other calculations show smooth data ranges and therefore give more reliable indications of correlations.

All of the PGE correlate significantly and positively with each other at the 99% confidence level. The only element to show positive correlations with Ni and Cu is Pd, though they are not significant correlations at the 99% or 95% levels of confidence. Pd and Rh show the weakest correlations with the other PGE.

4.4.3 Chondrite normalised graphs of chromite-rich samples

The graphs are divided into those of samples with >50% chromite (fig.4.4.3a-d) and those ≤50% (fig.4.4.3e-g). In the high chromite group there is one clear positive, fractionated profile, for sample Brag57 fig. 4.4.3(a). Fig 4.4.3(b) shows flat patterns to moderately negative patterns and figs. 4.4.3(c) and (d) have strongly, unfractionated negative profiles from Ru to Pt. Sample 155BRG (fig 4.4.3b) shows a positive slope to Rh and then negative to Pd. In the strongly negative slopes Pd shows an upturn from Pt in fig

4.3.5(d), disrupting the profiles.

The lower modal percent chromite rocks show similar patterns. Figs 4.4.3(e) and (f) samples having markedly negative slopes with positive upturns between Pt and Pd. In fig. 4.4.3(g) sample Brag64 (base-metal sulphide enriched) shows a different flat profile, with a strong upturn between Pt and Pd.

4.4.4 Fractionation of the PGE

Most of the samples show unfractionated PGE assemblages, with low Pt/Ir and Pt/(Os+Ir+Ru) ratios and flat to negative slopes from Ru to Pt on the chondrite normalised graphs. Sample Brag57 as well as being the most enriched sample, also contains the most fractionated assemblage, as shown by the high Pt/Ir ratio and positive sloped graph. However sample 142BRG , with a negative slope shown in fig. 4.3.5b, has a higher ΣOsIrRu (3810ppb) than Brag57 (3375ppb) suggesting that there is no direct relationship between degree of fractionation and the tenor of PGE. The nature of the PGE association is partly shown in the shapes of the chondrite normalised graphs. There is a clear distinction, or change in trend, between Os,Ir,Ru and Rh,Pt,Pd on many of the graph plots. Pd, with the weakest correlation (table 4.4.2) to the other PGE, does not lie on smooth trends with the other five PGE for most of the samples. This element seems to be distinct from the main fractionation trend for the other five PGE, suggesting different concentration processes. The comparisons between higher and lower modal % chromite-bearing whole rock samples, suggests that the massive chromitites are more likely to contain a fractionated PGE assemblage. So, in comparing whole rock analyses between samples and different localities, this effect needs to be borne in mind.

Figure 4.4.3a-d Chondrite normalised PGE plots of samples with >50% chromite

Figure 4.4.3a

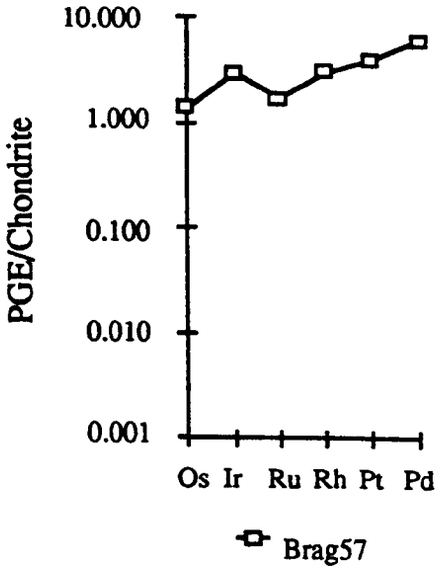

Figure 4.4.3b

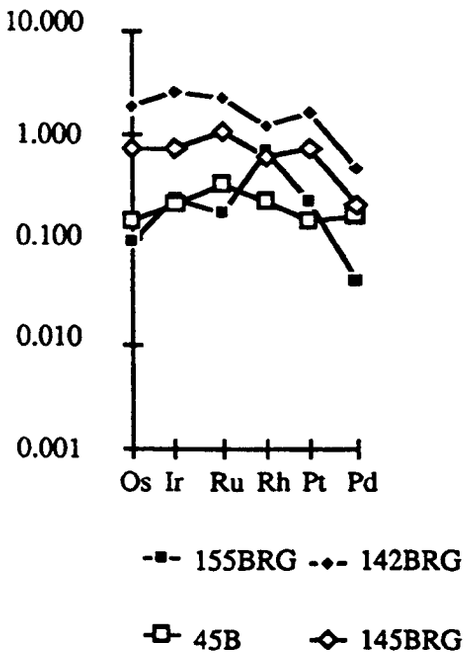

Figure 4.4.3c

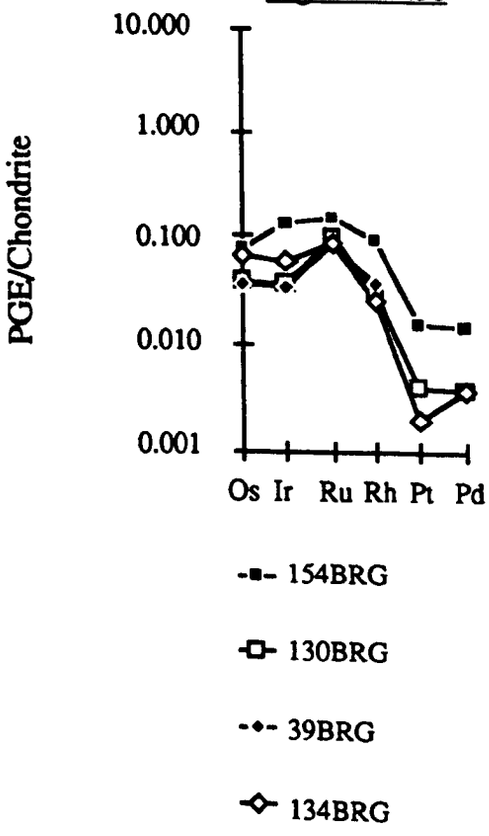

Figure 4.4.3d

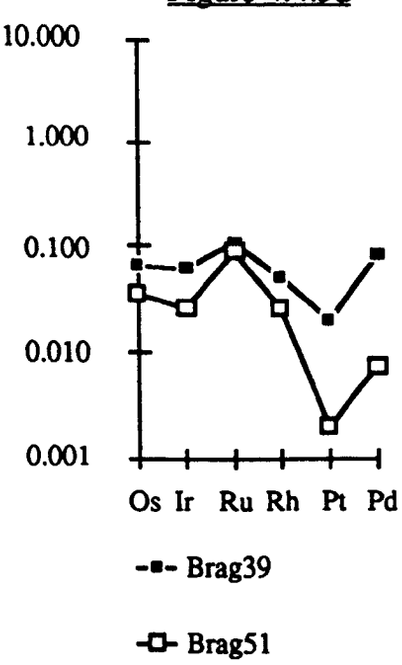

Figure 4.4.3e-g Chondrite normalised PGE plots of samples with ≤50% chromite

Figure 4.4.3e

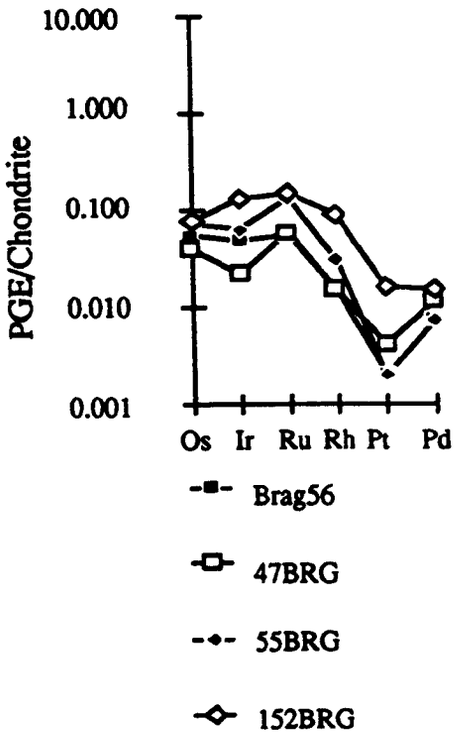

Figure 4.4.3f

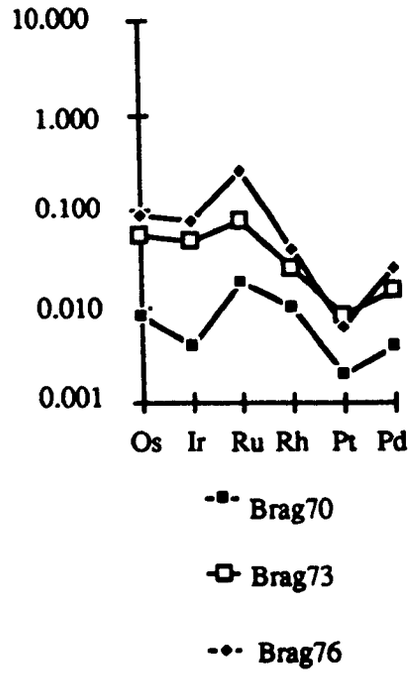

Figure 4.4.3g

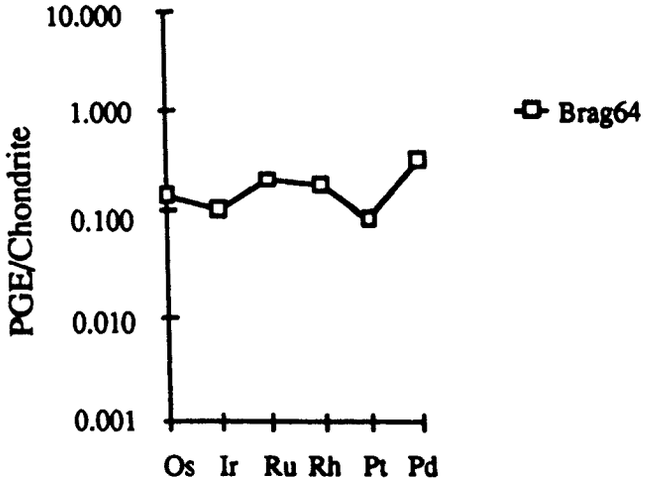

The graphs are divided into those of samples with >50% chromite (fig. 4.4.3a-d) and those ≤50% chromite(fig. 4.4.3e-g). In the high chromite group there is one clearly positive slope, for sample Brag57 (fig. 4.4.3a). Fig. 4.4.3b shows flat to moderately negative patterns and figures 4.4.3c-d have strongly negative slopes from Ru to Pt. Sample 155BRG (fig. 4.4.3b shows a positive slope to Rh and then negative to Pd. In the strongly negative slopes Pd shows an upturn from Pt in fig. 4.4.3d, disrupting the profiles. The lower modal% chromite group show similar patterns. Figure 4.4.3e-f samples having markedly negative slopes with positive upturns between Pt and Pd. In fig. 4.4.3g, sample Brag64 shows a different, flat profile, with a strong upturn between Pt andPd.

4.5. Mineralogy

4.5.1 Platinum Group Minerals

Quantitative analyses on laurites, base-metal sulphide and some irarsites were successfully carried out on an SEM. Details of the procedure are given in appendix 2. In some cases (*eg* potarite PdHg and sperrylite $PtAs_2$) the mineral species can be characterised by qualitative examination of the X-ray spectra as there are no other known minerals with these combination of elements.

The PGM found in this study are irregularly distributed between samples, most having none or only one or two grains; though in one polished thin section (Brag57) twenty eight PGM were identified. The PGM are mainly located within chromite grains or at their margins; six are located entirely within the serpentine matrix. They have sizes ranging from 1μm to 45μm. Of these grains ten are seen, in the plane of the polished thin section, to be composite, with separate mineral sub-grains. Grain (and sub-grain) outlines are mostly hexagonal, rounded rectangular or octahedral (*eg* plates 1,7) except at the edges of chromites or in the serpentine matrix where they are generally more irregular (plate 10). Table 4.5.1 lists the different mineral species, their textural location, relative abundances, sizes and shapes.

Table 4.5.1 PGM mineralogy

Locality	Sample no.	No. of grains	Hexag., rectang. or polygono utline	Textural setting	Size μm	Mineral/ composition
Abicedo	HPP3	1	√	Chromite	15	laurite
Sardoal	HPP4B	1	√	Chromite near edge		Composite laurite and Ir-Rh-As-S
Sardoal	Brag78	2(I)		Chromite edge	35	Composite laurite and Ir-Rh-As-S
		(II)	√	Small chromite grain (5)	4	laurite
Carrazedo	HPP6A	2(I)		Chromite near edge on small crack	10	Ir-As-S
		(II)		Chromite near edge	2	Ir-Rh-As-S
Carrascale	HPP2	1	√	On crack within chromite	30	laurite with Ru-(Ir?)-Mn around edge
Derruida Hill	Brag57	28(I)	√	Chromite, near edge (7)	25	laurite , S loss towards an edge
		(II)	√	Chromite, near edge beside I (7)	10	Ir-As-S
		(III)		Chromite edge	13	Composite Pt-As,Ir-(Rh)-As-S,Rh-(Ir-Pt)-As-S
		(IV)	√	Chromite	8	laurite
		(V)	√	Chromite	13	laurite
		(VI)		Si crack in chromite	15	Ir-(Rh)-As-S

		(VII)	√	Chromite beside hz	5	laurite
		(VIII)	√	Chromite towards edge	10	laurite
		(IX)	√	Chromite edge	15	Ir-(Rh)-As-S
		(X)		Chromite	5	Ir-(Rh)-As-S
		(XI)	√	Chromite beside Si inclusion,near edge	5	Ir-(Rh)-As-S
		(XII)		Inclusion in hz in chromite (15, 20)	5	PdHg
		(XIII)		Chromite edge (11)	45	Composite Ir-As-S,with Ru-Os-S and Ru-(Ir) alloy around edge
		(XIV)	√	Chromite (1, 19)	35	Composite laurite,Ir-(Rh)-As-S, pn
		(XV)	√	Chromite near edge	20	Composite hz and laurite
		(XVI)	√	Chromite	3	laurite
		(XVII)		Chromite edge (9, 10)	15	laurite S loss towards edge
		(XVIII)	√	Chromite edge	10	Ir-As-S
		(XIX)	√	Chromite on crack (6)	15	laurite
		(XX)		Edge of Hz/Mg grain (16)	10	Pt-Pd-Cu-(S)
		(XXI)	√	Chromite	20	Composite, two laurite grains with silicate inclusion
		(XXII)		Serpentine between chromite grains (14)	20	Pt-Fe-Cu alloy
		(XXIII)		In serpentine adjacent to (XX111) (14)	15	Pt-Ir alloy with trace Rh,S
		(XXIV)		In serpentine	1	Pd-Sb
		(XXV)		Serpentine	4	Pt-Cu-Fe alloy
		(XXVI)		Serpentine	1.5	Pt-Pd
		(XXVII)		Serpentine, chromite edge	15	laurite
		(XXVIII)		Serpentine (13)		Pt(Rh)AsS
	Brag64	1	√	Edge of pentlandite (on edge of chromite) (17)	6	Pd-S
Alimonde	Brag 79	2(I)	√	Chromite	10	Composite laurite and Ir-As-S
		(II)			15	laurite
Leutiscais	Brag76	1		Between chromite grains (3)	30	laurite
Leutiscais	Brag70	1	√	Chromite (8)	5	laurite
Serralhoa	Brag52	7(I)	√	Chromite (4)	3	laurite
		(II)		Between chromites (12)	10	Composite Pt-As and Ir-Rh-Pt-As-S
		(III)		Chromite	8	Composite laurite and Rh-(Ir)-As-S
		(IV)	√	Chromite	3	Composite Fe-Ni-S and laurite
		(V)	√		2	laurite
		(VI)	√	Chromite (2)		Composite laurite, pn and silicate
		(VII)		Serpentine	2.5	Rh-As-S
Demuida	12-BRG	2(I)	√	Chromite	8	laurite
		(II)	√	Chromite	5	laurite
		Total 60				

Table 4.5.1 continued. A total of 49 single and composite grains were located, giving a total of 60 distinct PGM grains. All were located within chromite-rich samples. Of the total number of PGM, 31 are laurite $Ru(OsIr)S_2$; 15 irarsite Ir(Rh)AsS; 2 sperrylite $PtAs_2$; 3 Pt-Rh-bearing irarsite/hollingworthite/platarsite series Ir(RhPt)AsS; 8 Pd-, Pt-bearing alloys, sulphide, antimonide, potarite-PdHg; and 1 hollingworthite RhAsS. Most of the PGM are located within chromite, though all the Pt-As-bearing grains are located at the margins of chromite grains.

hz: heazelwoodite, pn: pentlandite The number in brackets in the texture column refers to the plate number. Roman numerals refer to a SEM probe analysis (tables 4.5.1.1, 4.5.1.2).

Out of the PGM listed in table 4.5.1, three mineralogical groups were identified:

4.5.1.1. Ru, Os, Ir, S minerals

Table 4.5.1.1 Laurite composition

Wt%	Brag57 XIX	XIV	XXVII	I	VII	XXI	XXI	Brag76	12BRG I
Os	14.5	20.7	22.7	19.5	8.7	22.6	21.5	10.1	19.0
Ir	2.9	6.8	5.1	5.9	2	7	6.6	5.8	9.3
Ru	42.9	36.4	39.7	38.1	50.5	37.9	38.1	47.9	39.3
S	36.8	33.9	35.2	33.8	36.3	35.1	33.3	36.7	36.4
Total	97.1	97.7	102.7	97.3	97.5	102.6	99.6	100.6	104.1
Atom. %									
Os	4.6	7	7.3	6.6	2.7	7.3	7.2	3.1	6.0
Ir	0.9	2.3	1.6	2.0	0.6	2.2	2.2	1.8	2.9
Ru	25.5	23.1	24	24.1	29.6	23.1	24.1	27.8	23.3
S	69.0	67.7	67.1	67.4	67.1	67.4	66.5	67.3	67.9

Analyses obtained on a SEM calibrated for quantitative analysis (appendix 2). Seven analyses were obtained on separate grains from the PGE-enriched sample Brag57, one from 12BRG and one from sample Brag76. Roman numerals refer to mineral description in table 4.5.1.

Laurite ($Ru[OsIr]S_2$) is the most frequent of all the PGM seen in this study being found throughout the chromite grains and at their edges. All laurites have at least traces of Os and Ir. The range of composition for the 9 laurite grains suitable for quantitative analysis is: Os 2.7-7.3, Ir 0.6-2.9 and Ru 23.1-29.6 atomic% (table 4.5.1.1). These analyses are plotted on the ternary plot fig. (4.5.1). The laurite grains have a range of compositions typical of podiform chromitites as shown by the compositional range from Legendre and Augé (1986) and Tarkian and Prichard (1987). Some of the samples have low Ir contents compared to most grains from other podiform deposits and plot at the low Ir side of the compositional range field. Most of the variation in composition of the Bragança samples is present within one polished section: Brag57.

Figure 4.5.1 Laurite composition triangle

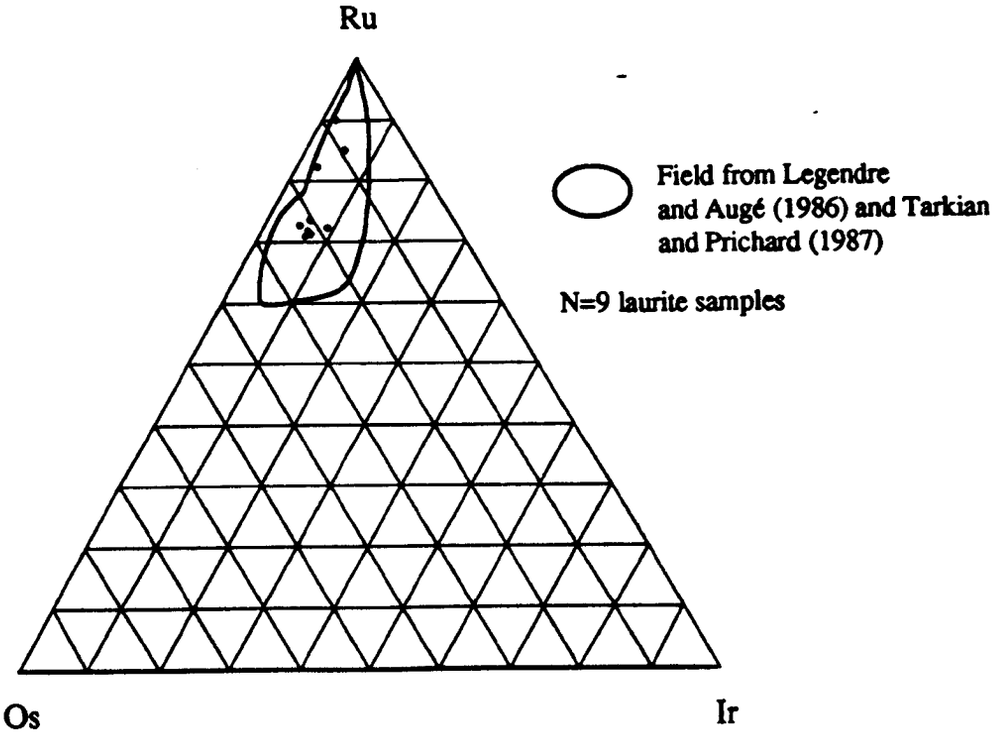

The compositional triangle shows the proportions of Ru, Os and Ir within the laurite samples analysed. Superimposed on this is the field for laurite composition in podiform chromitites taken from Legendre and Augé (1986) and the Shetland ophiolite (Tarkian and Prichard 1987). Three of the samples plot at the low Ir side of the superimposed field.

4.5.1.2. Ir, Rh, Pt, As, S minerals

Table 4.5.1.2 Irarsite composition

Brag57	II	XIII
S	11.1	11.6
As	21.5	23.9
Ir	65.1	61.9
Total	97.7	97.4
Atomic%		
S	35.6	36.0
As	29.5	31.9
Ir	34.9	32.2

Two analyses of irarsite grains from sample Brag57. Roman numerals in first row refer to mineral description in table 4.5.1

Minerals in the irarsite/hollingworthite/platarsite (IrAsS-RhAsS-PtAsS) series are found in the edges and at the centre of chromites, though notably the only Pt-bearing grains are seen at the edge of chromites or within the serpentine matrix (plate 13). Two sperrylite

grains ($PtAs_2$) were found in composite grains with minerals of the irarsite/hollingworthite/platarsite series, again at the margin of chromite grains (plate 12).

4.5.1.3 Pd, Pt minerals

The other PGM groups described above are collectively identifiable by their bright white reflectance in oil-immersion reflected light. The Pt-Pd group of minerals has a darker grey reflectance not readily identifiable in thin section, instead they are located using back-scattered images on the scanning electron microscope where they appear brightly. The Pt,Pd group of alloys, sulphides, one potarite PdHg and one antimonide are present in the serpentine matrix and with the base-metal sulphide. Alloys located are: Pt-Pd, Pt-Fe-Cu, Pt-Pd-Cu, Pt-Ir and Pd-Sb. The alloy grains range in size up to 20μm in length, though the narrow width prohibits quantitative analysis. The Pt-Pd-Cu alloy forms a rim to a heazlewoodite-magnetite composite grain in sample Brag57 (plate16). A 5μm long potarite grain PdHg (plates 20,15) was located within another heazlewoodite-magnetite grain of the same sample. In sample Brag64 a 5μm Pd-S acicular grain is present along one edge of a pentlandite (plate 17). An association of some of the Pd-bearing minerals with the base-metal sulphide phase is apparent. The PGE-enriched sample Brag57 contains the other alloys described above: Pt-Pd, Pt-Fe-Cu (plate 14), Pt-Ir (plate 14), Pd-Sb. These are not adjacent to pentlandite or heazlewoodite but are present within the serpentine matrix between chromite grains. The Pt-Ir alloy X-ray spectrum also showed small Rh and S peaks .

4.5.2 Base-metal sulphide

Base-metal sulphide (BMS) is present in variable though scarce amounts, occurring both within chromite grains and in the silicate matrix. The grain outlines are similar to those of the PGM, with commonly hexagonal or rectangular outlines for grains enclosed within chromite grains and more irregular, embayed outlines to those grains within the silicate matrix. The sulphides are pentlandite $(FeNi)_9S_8$ and heazlewoodite Ni_3S_2 (fig. 4.5.2). Both are commonly found with magnetite in polished section. Magnetite replaces pentlandite along grain margins (plates 9, 15, 20).

Table 4.5.2 Pentlandite and heazlewoodite analyses

Wt%	Brag57						Brag2	Brag64		
	hz	hz	hz	hz	hz	pn	pn	hz	pn	pn
S	28.6	28.8	28.7	26.4	27.8	34.8	34.5	25.8	32.8	34.5
Fe	-	2.4	1.3	1.2	-	37.8	27.0	2.8	29.4	29.8
Ni	69.4	68.4	69.6	70.6	70.6	31.6	36.0	66.5	35.9	33.2
Total	98.0	99.6	99.6	99.7	98.4	104.2	97.5	95.9	98.2	97.5
Cr				1.5				0.9		
Atomic%										
S	43.0	42.7	42.5	39.6	41.8	47.2	49.6	40.1	47.3	49.5
Fe	0.0	2.0	1.1	1.0	0.0	29.4	22.2	2.5	22.7	24.6
Ni	57.0	55.3	56.3	58.0	58.2	23.4	28.2	56.5	28.1	26.0
Cr				1.4				0.9		
(Fe+Ni)/S	1.3	1.3	1.4	1.5	1.4	1.1	1.0	1.5	1.1	1.0

Minerals hz: heazlewoodite, pn: pentlandite. Cr was included in some analyses due to excitation of co-existing chromite, it is not part of the actual mineral composition. The analyses were obtained on a SEM calibrated for quantitative analysis (appendix 2).

The range of pentlandite Ni contents: 23.4 - 28.1 atomic% (table 4.5.2) lies mainly within the range of 24 - 30 atomic% typical for pentlandite-heazlewoodite assemblages (Misra and Fleet 1973). Pentlandite-heazlewoodite-magnetite is a sulphide assemblage associated with serpentinisation. Serpentinisation of ultrabasic rocks is characterised by very low S fugacities of -25 to -33 $\log fS_2$. This is shown in figure 4.5.2 taken from Eckstrand (1975).

4.5.3. Mineralogy and textures

There is no consistent sequence of mineralisation between the laurites and irarsites. Sometimes irarsite is seen to have grown at the edge of laurite (plate 11) and in other examples (plate 14) the irarsite is surrounded by laurites. Pentlandite, when adjacent to the PGM, appears to rim them (plate 12) suggesting that its crystallisation locally follows that of the laurite and irarsite, although pentlandite is found throughout the chromite grains. The Pt-bearing PGM all lie at the margins of chromite grains, unlike the laurites and irarsites which occur throughout the chromite grains. Although the number of PGM located is not great, their textural location suggests a fractionation of the PGE. Pt has been separated by some process from the mineralisation of Ru-, Ir- and Os-bearing laurites and irarsites. These textural relationships are depicted graphically in figure 4.5.3a. Similar fractionation of Pt within chromitites has been described as late hydrothermal (Thalhammer *et al.* 1990) or primary igneous (Prichard *et al.* 1986).

Group 1 Ru-, Os-, Ir-, S-bearing minerals

Plate 1
Composite grain of laurite, pentlandite and irarsite. The irarsite is enclosed by pentlandite. The composite grain has a roughly eight-sided to rounded outline and is entirely enclosed within chromite. The PGM outline is created by strain-induced annealing. scale dashes 10μm. Sample Brag57(XIV)

Plate 2
Composite grain of laurite, pentlandite and silicate. All are enclosed within chromite grain. Sample Brag52(VI).

Plate 3
Laurite located on silicate crack at the margin of a chromite grain. Rounded, rectangular outline. Scale dashes 10μm. Sample Brag76.

Plate 4
Laurite located within chromite grain, towards its margins. Rectangular to rounded polygonal outline. Sample Brag52(I).

Plate 5
Laurite fully enclosed within chromite. Scale dashes 1μm. Sample Brag78(II).

Plate 6
Two PGM within the field of view, irarsite to right at edge of chromite grain and laurite, with rounded outline, on left of photo. Ferritchromit alteration at margins of the chromite shows up as lighter patches. Sample Brag57(XIX).

Key to plate annotations
C chromite, Pn pentlandite, Hz heazlewoodite, M magnetite, Se serpentine, Fe ferritchromit, L laurite, I irarsite, Sp sperrylite, P platarsite, Po potarite. Sample numbers and roman numerals refer to table 4.5.1. Scales are shown on the plates.

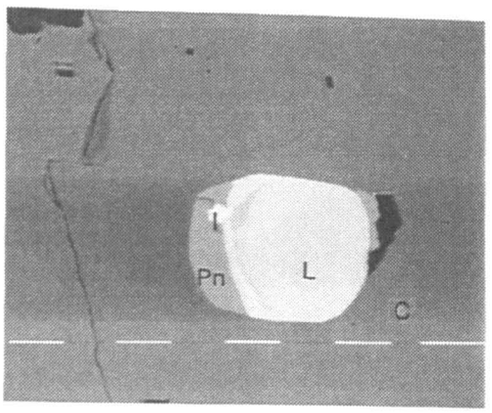
L
Pn
L
C

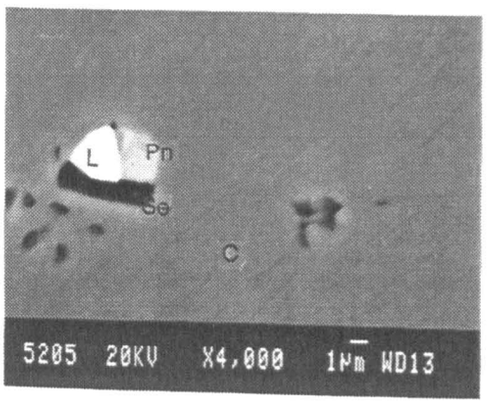
L
Pn
Se
C
5205 20KV X4,000 1µm WD13

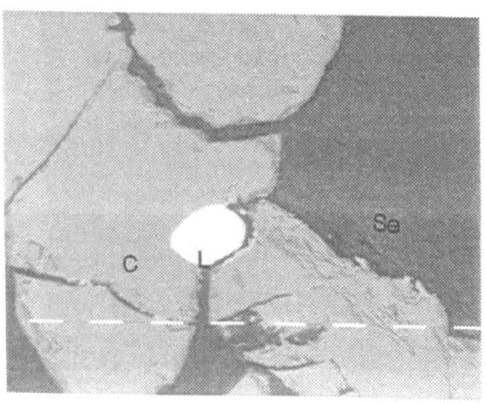
Se
C
L

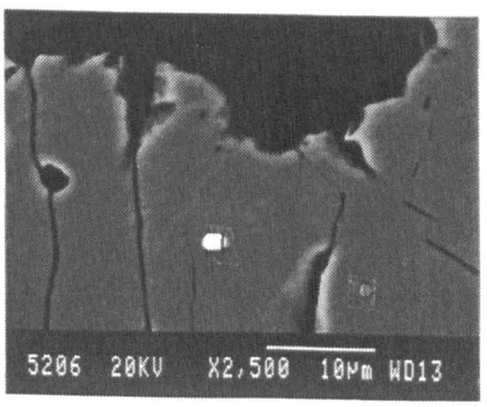
5206 20KV X2,500 10µm WD13

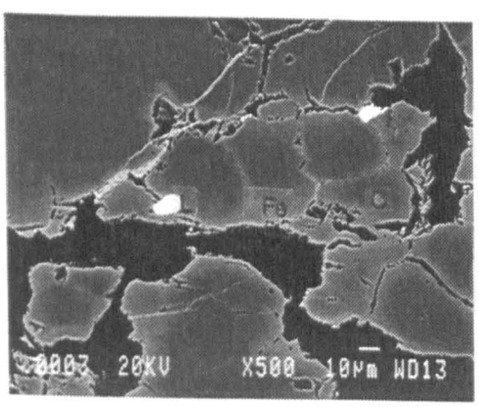
Fe
0007 20KV X500 10µm WD13

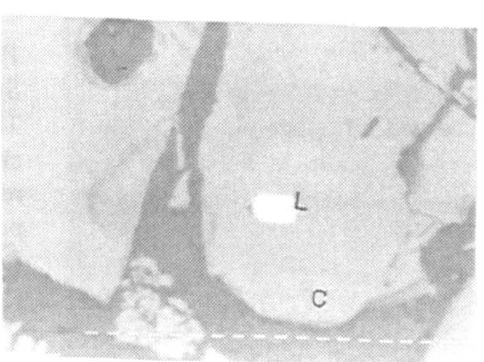
L
C

Plate 7.
Laurite grain with an irarsite grain at one edge. Both have sub-hexagonal outlines created through annealing within chromite. Scale dashes 1μm. Sample Brag57(I,II).

Plate 8
Low magnification view of laurite enclosed within chromite. Sample Brag70.

Plate 9
Heazlewoodite on left of plate and laurite to right at chromite/serpentine contact. The laurite is shown in higher magnification in plate 10. Sample Brag57(XVIII).

Plate 10
Enlarged view of laurite grain in plate 9. Ragged appearance is due to S-loss associated with serpentinisation. Sample Brag57(XVII).

Group 2 Pt-, Ir-, Rh-, As-, S-bearing minerals

Plate 11
Composite irarsite and laurite grain. The laurite grains partially surround the irarsite. The composite grain is located at a chromite/silicate boundary. Scale dashes 10μm. Sample Brag57(XIII).

Plate 12
Sperrylite with platarsite at its margin. The composite grain is located between chromite grains. The chromite shows recrystallisation and the formation of polygonal neoblasts. Sample Brag52(II).

Key to plate annotations
C chromite, Pn pentlandite, Hz heazlewoodite, M magnetite, Se serpentine, Fc ferritchromite, L laurite, I irarsite, Sp sperrylite, P platarsite series, Po potarite. Sample numbers and roman numerals refer to table 4.5.1.

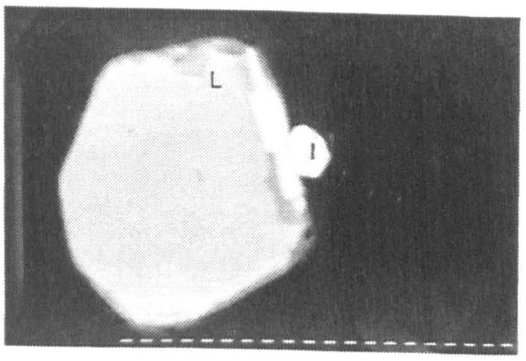
L
I

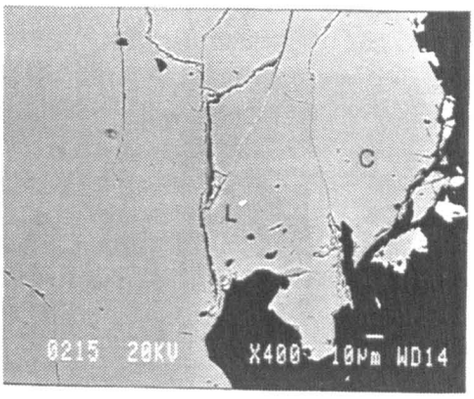
C
L
0215 20KV X400 10µm WD14

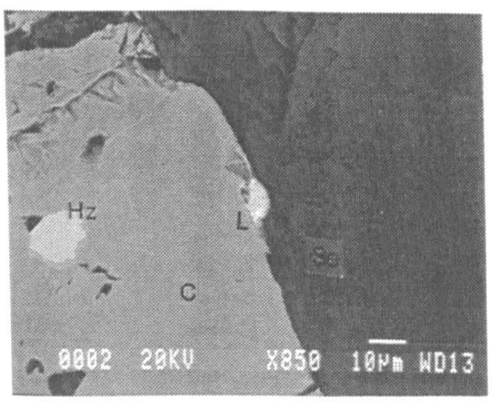
Hz
L
C
0002 20KV X850 10µm WD13

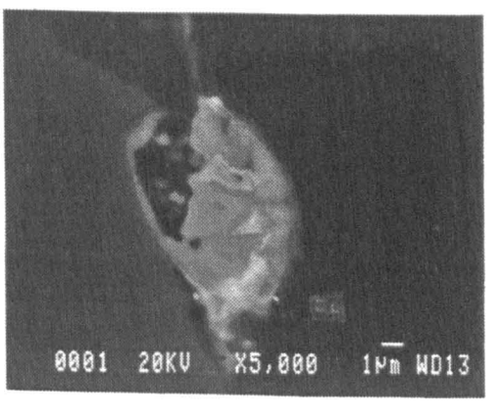
0001 20KV X5,000 1µm WD13


I
L
L
C

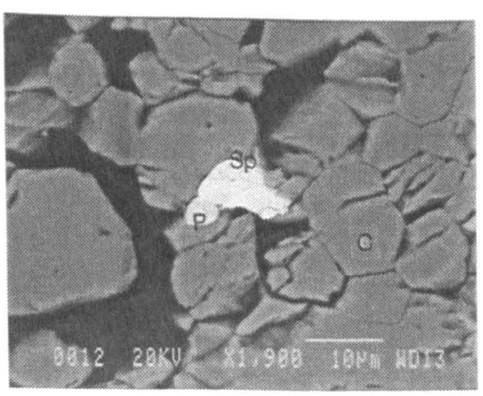
Sp
P
C
0012 20KV X1,900 10µm WD13

Plate 13
Pt(Rh)AsS within serpentine at margin of a chromite grain. The ragged uneven appearance is due to alteration during serpentinisation. The central dark patch within the PGM is serpentine. Sample Brag57(XXVIII).

Plate14
Two alloys within serpentine matrix: Pt-Fe-Cu at top and Pt-Ir at bottom. The Pt-Ir alloy contains weak peaks of Rh and S. This suggests that the alloys are the remnants of of a platarsite that has altered in-situ during serpentinisation. Sample Brag57(XXII, XXIII).

Group 3 Pd-bearing minerals and secondary assemblage

Plate 15
Altered sulphide grain located within chromite which consists of heazlewoodite and magnetite. At the lower end of the sulphide is a potarite grain. The potarite has crystallised during the breakdown of an original pentlandite caused by serpentinisation. Sample Brag57(XII).

Plate 16
Heazelwoodite/magnetite grain located within chromite. This is an alteration assemblage, replacing pentlandite, typical of serpentinised rocks. At the lower left margin of the sulphide is a Pt-Pd-Cu alloy. Its association with the heazelwoodite/magnetite grain suggests that it too was created during serpentinisation. Sample Brag57(XX).

Plate 17
Pentlandite on the left of the plate has a Pd-S needle-like grain at its lower margin with serpentine. A band of magnetite separates the pentlandite from chromite. Sample Brag64.

Key to plate annotations
C chromite, Pn pentlandite, Hz heazlewoodite, M magnetite, Se serpentine, Fc ferritchromite, L laurite, I irarsite, Sp sperrylite, P platarsite series, Po potarite. Sample numbers and roman numerals refer to table 4.5.1.

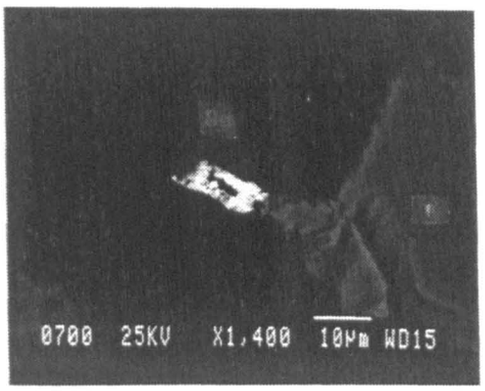
0700 25KV X1,400 10µm WD15

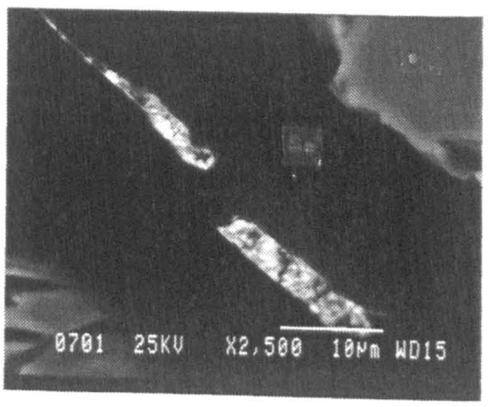
0701 25KV X2,500 10µm WD15

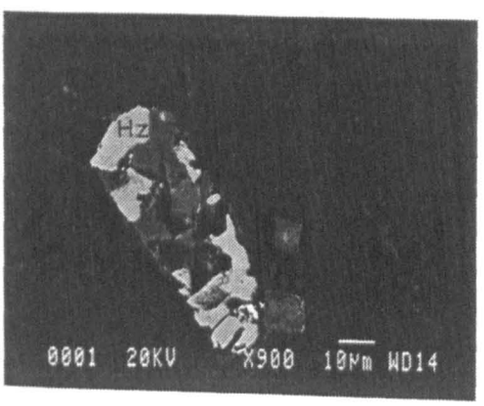
Hz
0001 20KV X900 10µm WD14

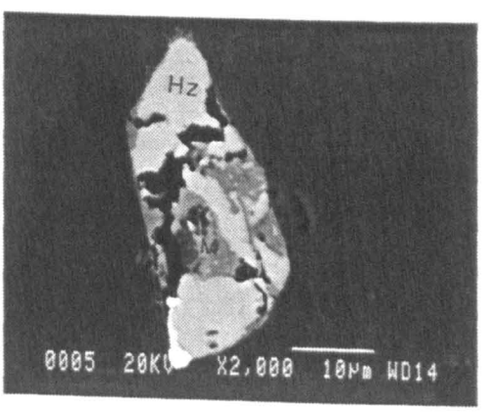
Hz
M
0005 20KV X2,000 10µm WD14

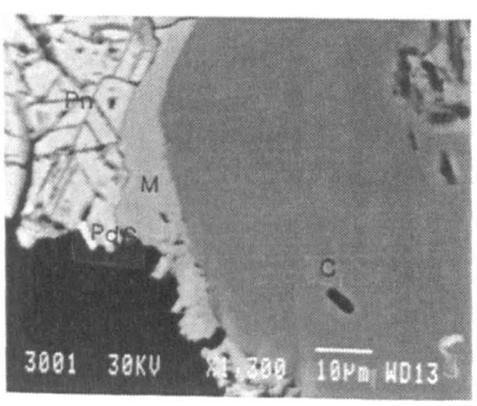
Pm
M
Pd
C
3001 30KV 10µm WD13

Dot mapping

Plate 18
X-ray map of composite grain in plate 11. The images show up the concentrations of the different elements. The laurite grains are picked out by the concentrations of Os, S and Ru whereas the irarsite is marked by Ir and As concentrations. The apparent Os concentration within the irarsite is an artifact of the Os-L and Ir-L line overlap.

Plate 19
X-ray map of composite grain shown in plate 1. The laurite shows up as a concentration of Ru, S and Os. The pentlandite which partially rims the laurite shows up as a concentration of Ni.

Key to plate annotations
C chromite, Pn pentlandite, Hz heazlewoodite, M magnetite, Se serpentine, Fc ferritchromite, L laurite, I irarsite, Sp sperrylite, P platarsite series, Po potarite.

Ru
S
Ir
Os
Ni
As
PAGE= 1 X= 256 Y= 12

Ru
Os
Ir
S
As
PAGE= 1 X= 256 Y= 12

Plate 20
X-ray map of an altered sulphide grain (plate 15) containing potarite. Magnetite shows up as a bright Fe patch and the heazlewoodite as S and Ni concentrations. The potarite grain shows up as a bright patch in the Pd section.

Plate 21
X-ray map of the Pt-Fe-Cu alloy in plate 14.

Key to plate annotations
C chromite, Pn pentlandite, Hz heazlewoodite, M magnetite, Se serpentine, Fc ferritchromite, L laurite, I irarsite, Sp sperrylite, P platarsite series, Po potarite.

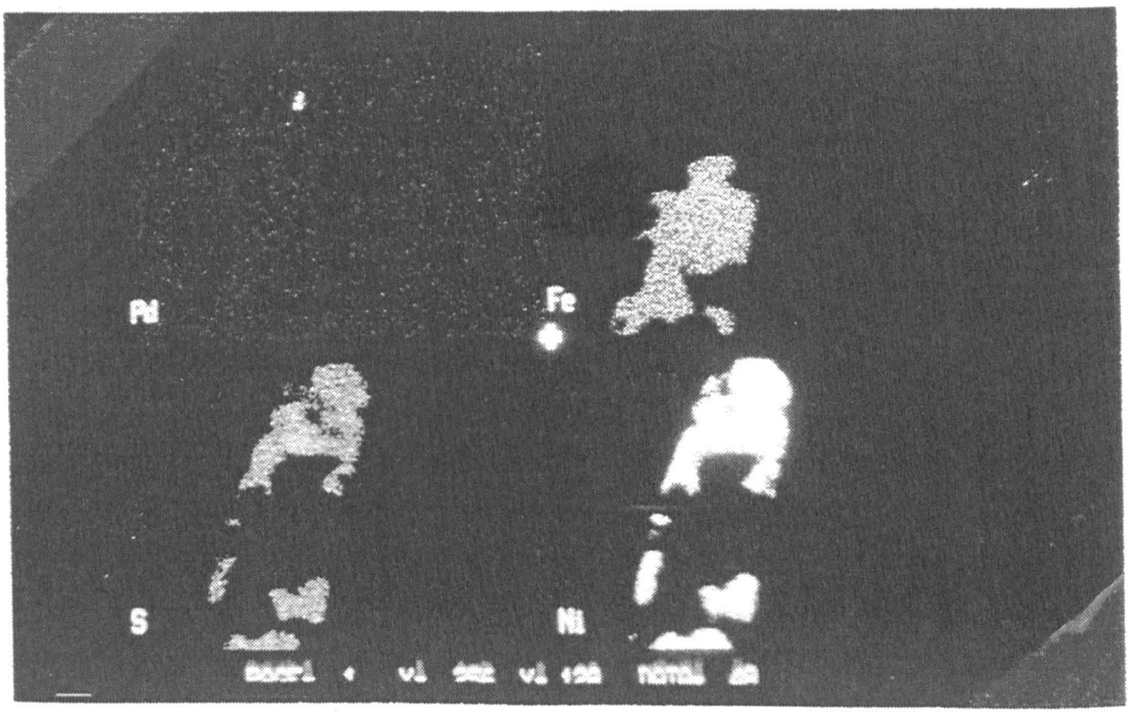
Pd
Fe
S
Ni

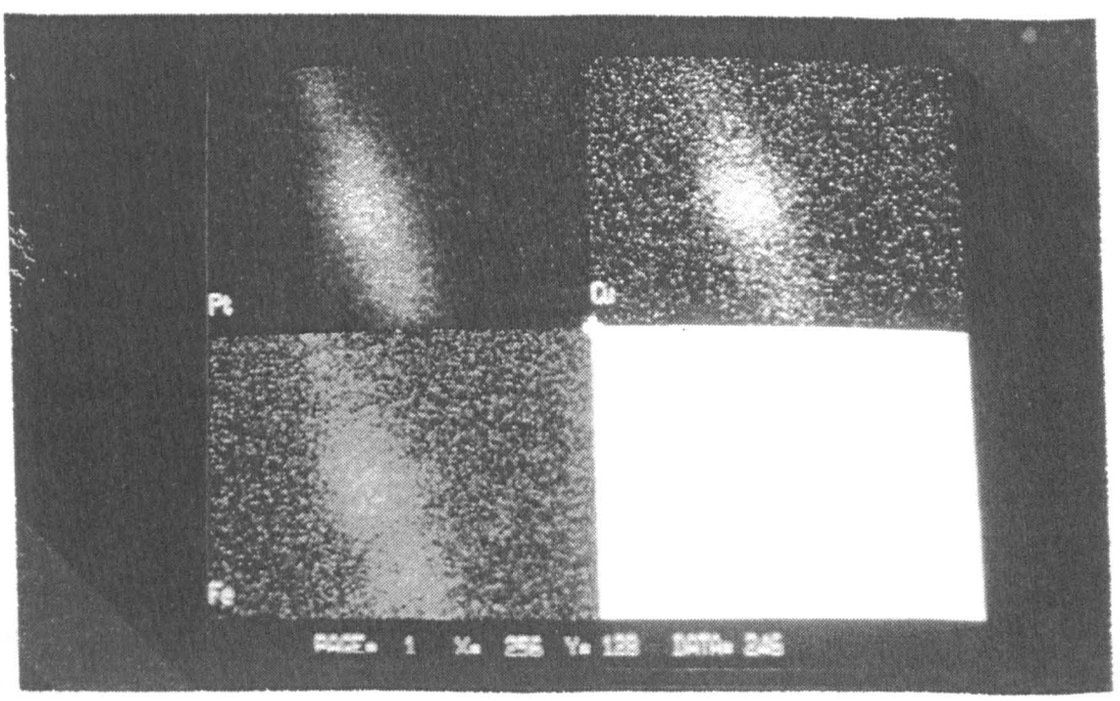
Pt
Cu
Fe

Figure 4.5.2 fS_2 v fO_2 sulphide assemblages

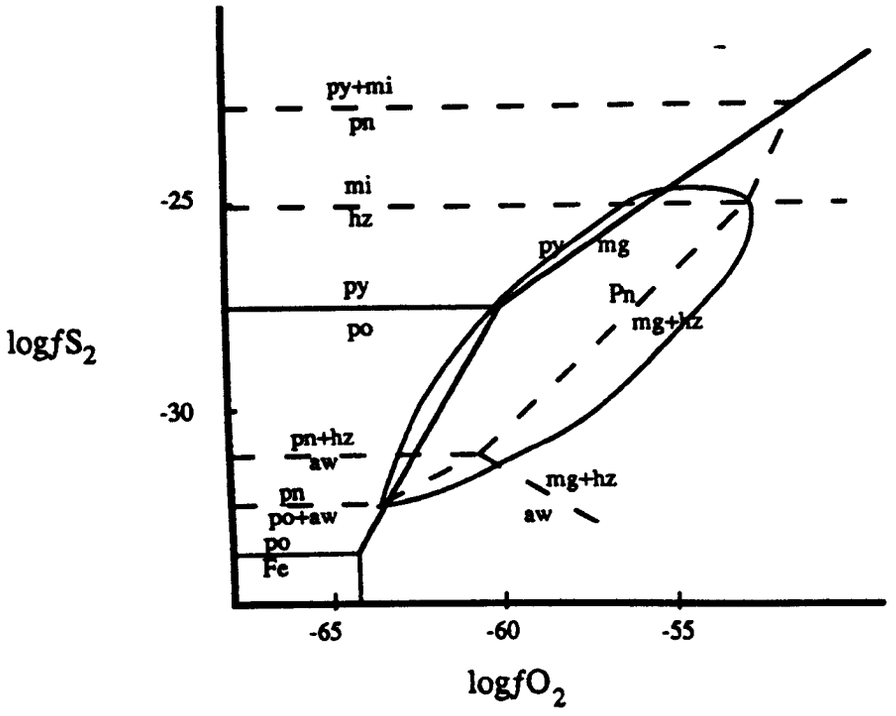

Pyrite(py), Millerite(mi),
Pentlandite(pn),
heazlewoodite(hz), pyrrhotite(po),
awaruite(aw), magnetite(mg)

Serpentinisation field

From Eckstrand (1975)

This diagram shows the stability fields of Fe-Ni-sulphides varying with fS_2 and fO_2 at 127°C. Superimposed on this is the field of mineral assemblages found with the serpentinisation type of alteration of ultrabasic rocks (from Eckstrand 1975). The most important assemblage associated with serpentinisation is pentlandite, heazlewoodite and magnetite, which are the minerals found in the Bragança chromite-rich samples.

In chapters 2 and 3 it was proposed that the mineralogical fabric of the silicates and chromite-rich samples had been determined by the high strain which the ultrabasic assemblage had undergone due to the thrusting of the complex. The polygonal, annealed textures taken on by the chromite grains suggest that processes of recovery (Hobbs *et al.* 1976) may have taken place. This is a process whereby dislocations in the crystallographic structure of strained mineral grains begin to be eliminated. To minimise surface tension

energies, mineral grains undergoing recovery processes tend to take on outlines which have the least surface area relative to their volumes. In an isotropic mineralogical structure the individual grains approach octahedral shapes (Hobbs *et al. op. cit.*), though in phases where a particular crystallographic form is strongly developed this ideal shape is not attained (such as with platy mica morphology). It has been proposed that such a strain induced phenomenen causes the reshaping of sulphide inclusions with pyroxene crystals of mantle-derived pyroxenite layers (Lorand 1989a). Lorand described this as a process of 'spheroidization' whereby irregularly shaped sulphide inclusions may approach a circular or regularly faceted outline in response to the deformation which the pyroxenite layers had undergone.

The PGM inclusions within the chromite grains of the Bragança samples may not have escaped the effects of the imposed strain. The PGM and their surrounding chromite grains could have reacted to the strain by taking on an orientation which minimises the grain boundary tension between them. The hexagonal outlines of the PGM inclusions suggest sections through octahedra. This is consistent with the cubic system, to which the major PGM phases belong. The PGM outlines are generally euhedral in appearance and could be considered to be primary mineralogical outlines derived through crystallisation from a melt as proposed by Legendre and Augé (1986). An alternative proposition is that the polygonal PGM outlines are the products of the annealing which took place within the chromite-rich samples in response to deformation in a similar way to that described for the sulphide inclusions of pyroxenite layers by Lorand (1989a). The latter proposition is favoured here because as suggested in chapter 3, it is thought that the chromite-rich layers have an annealed texture and so the PGM inclusions may have similarly recrystallised outlines. However there is no definitive evidence for this in the Bragança samples and the possibility remains that the polygonal outlines of many of the PGM are a primary magmatic feature.

The Pt-Pd group of minerals has different textural relationships from those of the other groups. It is associated either with base-metal sulphide or located within the serpentine between chromite grains. The polygonal outlines of the laurites and irarsites are also not developed. The grain outlines within the silicate are either irregular or have lath shapes, similar to the surrounding serpentine grains. The grains within the serpentine matrix or at chromite margins have a more patchy surface when seen in secondary or backscattered images. The pentlandite-heazlewoodite-magnetite base-metal sulphide assemblage (plates 15, 16) is characteristic of the serpentinisation-type alteration of ultrabasic rocks (Eckstrand 1975). The potarite (PdHg), Pd-S and some of the Pd-bearing alloys are associated with this assemblage, showing that these minerals also have a serpentinisation related paragenesis, formed during reduction of the pre-existing pentlandite dominated sulphide assemblage under conditions of low S fugacity.

Figure 4.5.3a PGM textural relationships

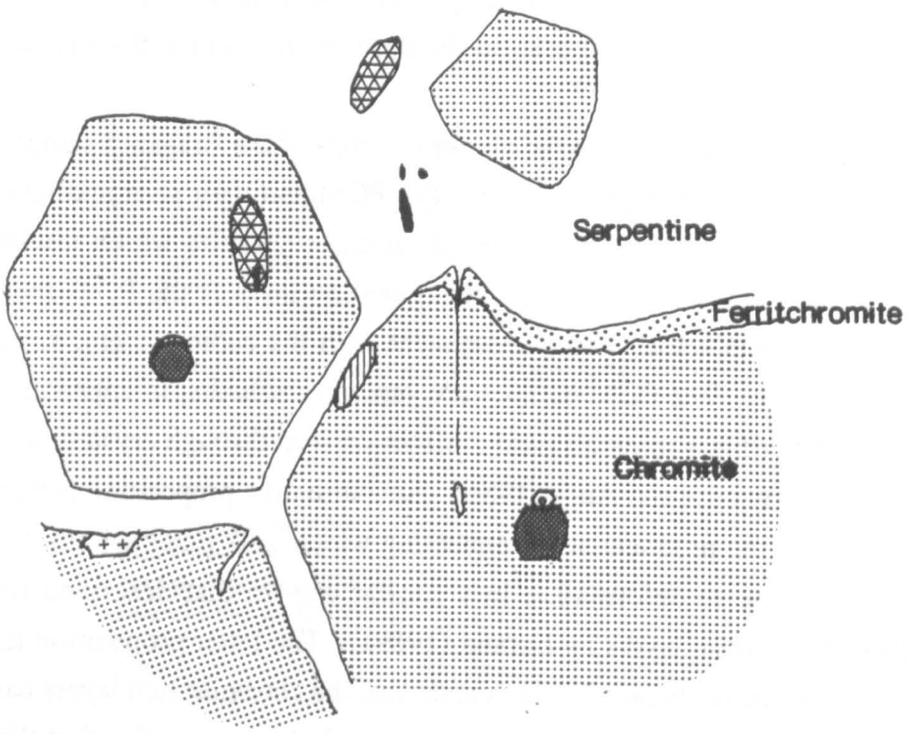

Not to scale.

Ru-, Os-, Ir-bearing laurites

Pt-Pd alloys

Pt-bearing arsenides and sulpharsenides

Fe-Ni-S: pentlandite, heazlewoodite, magnetite

Ir-bearing irarsites

Altered PGM at chromite margin having S-loss

This figure is a diagramatic representation of the textural relationships between PGM, the Fe-Ni-S assemblage and chromite within the Bragança samples. Ru-, Os-, Ir-bearing minerals are found throughout the chromite grains whereas the Pt-, As-bearing PGM are only found at the margins of chromite grains, or within the silicate matrix. The Fe-Ni-S assemblage (pentlandite, heazlewoodite, magnetite) is present throughout the chromite grains and the silicate matrix. Pd-bearing grains are found at the margins of the Fe-Ni-S grains and within the silicate. The Pd-bearing grains are Pt-, Cu- bearing alloys, Pd-S, PdHg, Pd-Sb. Most of the PGM included within the chromite grains have polygonal outlines and are frequently part of composite grains.

Figure 4.5.3b Stability fields of PGM with varying temperature and fS_2

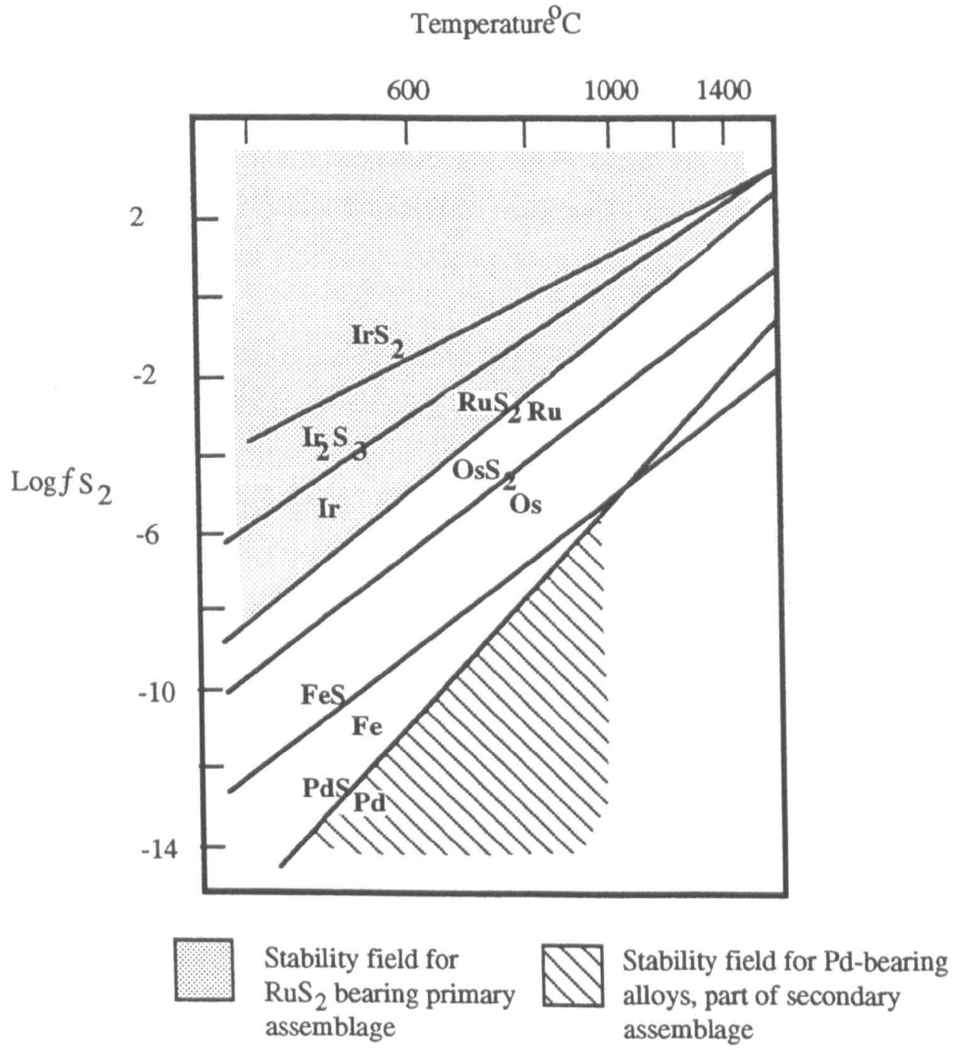

This figure shows the stability fields of PGE-bearing metals and S-bearing phases varying with temperature and fS_2. At the fS_2 where Pd-bearing alloys are stable (sloping lines on the figure), the RuS_2 laurites of the Bragança primary assemblage will not be stable (dotted area). The Pd-bearing alloys are associated with low fS_2 conditions present during serpentinisation. From Keays and Campbell (1981).

Figure 4.5.3b shows stability fields for PGE phases as a function of temperature and fS_2. At the fS_2 conditions where native Pd and Pd-bearing alloys are stable, RuS_2 (laurite) is not. Laurite is part of the primary assemblage, whereas the Pd-bearing alloys are secondary.

Comparison between figs 4.5.2 and 4.5.3b shows that at the sulphur fugacities associated with serpentinisation ie $<-25\log fS_2$, laurites and irarsites will not be stable. Native PGE and alloys are the stable PGE-bearing phases under these conditions. Laurites, which have been most exposed to the serpentinisation conditions at the margins of chromite grains show an uneven ragged surface under secondary electron image examination, which may be associated with S-loss. Similarly, the platarsite in plate 13 has a ragged, irregular appearance, suggesting S and As loss. The presence of trace amounts of Rh and S, indicated by small peaks on the X-ray spectrum of the Pt-Ir alloy in sample Brag57 (plate 14) suggests that this grain may be the alteration product (due to a loss of As and S) of a Rh-bearing platarsite.

The changes in PGE mineralogy associated with serpentinisation can be characterised as the creation of alloys associated with S (and As) loss. It is possible that the presence of alloys within the silicate matrix of sample Brag57 may indicate small scale localised remobilisation of Pt and Pd but the bulk of the minerals have been altered in-situ. Thus in contrast to Thalhammer *et al.* (1990), and in agreement with Prichard and Tarkian (1988), the zonation and fractionation of Pt-bearing arsenides and sulpharsenides towards the edges of chromite grains is regarded here as being essentially a primary igneous, not hydrothermal, feature.

4.6 Mineralogical and geochemical trends

The high correlations between the five PGE Os, Ir, Ru, Rh, Pt and the weaker correlations between these elements and Pd (table 4.4.2) are reflected in the mineralogical groupings. Ru, Os, Ir occur together in laurites and Ir, Rh, Pt are found together in the irarsite/hollingworthite/platarsite series. In contrast Pd is mainly associated with the base-metal sulphides. The mineralogical groups are typical of those from other podiform chromitites as summarised in table 4.1. The fractionation between Os,Ir,Ru and Pt suggested by sample Brag57's positive chondrite-normalised plot in fig 4.4.3 and its correspondingly high Pt/Ir ratio, is borne out by the textural location of the PGM. In samples Brag57 and Brag52 the Pt-bearing primary PGM are located at the edges of chromite grains. Pd appears to be distinct from the fractionation trend for the other five PGE. The chondrite normalised graphs show a change in fractionation trends from Pt to Pd. Original Pd enrichment is linked to the amount of base-metal sulphide present *eg* sample Brag64, with Pd being the most abundant PGE, has the highest amount of base-metal sulphide of all the samples. This is clear from visual observation of polished sections. Mackovicky *et al.* (1986) presented the results of experiments on the solubility of the PGE within sulphide-bearing systems at various temperatures. At 500°C pentlandite was reported to be able to dissolve up to 12.5wt% Pd. Pentlandite retained its Pd to 300°C. If the Pd-bearing grains in this study are derived from the adjacent relict pentlandites then the release of Pd may occur with the start of the decomposition of some pentlandite to heazlewoodite and magnetite. Possible limited remobilisation within hand specimens associated with alloy formation indicates that the change in slope at the Pd tails may be due to the greater mobility of this element during serpentinisation. It seems likely that the Pd was originally incorporated from the melt into the base-metal sulphide phase during the chromite crystallisation. The lack of a significant correlation between Pd and Cu in table 4.4.2 may be due to the limited remobilisation of these elements during serpentinisation. Probably there has also been some S loss from the whole rock during serpentinisation; this is evidenced by the magnetite partially replacing pentlandite. The S contents will not have changed much, there is no evidence to suggest that these rocks had a much greater amount of base-metal sulphide at a previous stage.

It is clear that the chromitite crystallisation acts to fractionate the PGE whilst the Pd fractionation is more directly linked to that of the sulphide phase. The following three sections concern the collection of Pd and Cu by a sulphide liquid, possible concentrations of these elements within a parental silicate melt and the effects of varying fO_2 on the mineralisation of the PGE. In this way a model to explain the concentration and fractionation of the PGE is outlined.

4.7. Collection of PGE and base metals from a silicate liquid by a sulphide phase

4.7.1 Pd/Cu ratios

Pd/Cu ratios vary between different types of silicate melts; for instance boninites have higher Pd and lower Cu contents than MORB. The whole rock Pd/Cu ratio is the same as that of the sulphide fraction of an igneous rock (Campbell and Naldrett 1979). By using published Pd and Cu concentrations within different silicate melt types and plausible distribution coefficients, a range of approximate Pd/Cu ratios may be calculated for the sulphide fraction which would crystallise from the different silicate melts. These theoretical ratios are then compared with the actual maximum Pd/Cu value for the Bragança chromite-rich samples in order to constrain the type of silicate melt from which the chromitites have been derived.

In order to explain the partitioning of chalcophile elements such as Pd and Cu into the sulphide fraction of melts, Campbell and Naldrett (1979) showed that the mass ratio of silicate to sulphide liquid (R) and the distribution coefficient of an element between sulphide and silicate liquids D^s_{Pd} affected the composition of the crystallising sulphide phase.

They derived the formulae:

$$D_i^s = \frac{Y_i}{X_i} \qquad \text{and} \quad Y_i = \frac{X_{i(0)} D_i^s (R + 1)}{R + D_i^s}$$

Where $X_{i(0)}$ is the initial concentration of element i in the silicate liquid, X_i is the final concentration of (i) in the silicate liquid and Y_i is the concentration of (i) in the sulphide liquid, R is the ratio of silicate to sulphide liquid and D_i^s is the distribution coefficient for an element i between sulphide and silicate liquids.

R values cannot be constrained for the Bragança chromitites, but using the simple distribution coefficient equation for Pd and Cu can still allow an approximation for initial silicate concentrations to be made. Low R values *eg* R=D would decrease both the Pd and Cu contents within the sulphide fraction but the resultant Pd/Cu ratio would remain similar. Thus the effects of the R value can be ignored for the purpose of calculating a Pd/Cu ratio.

The values of distribution coefficients for chalcophile elements between silicate and sulphide liquid have been shown to vary as a function of melt composition (Francis 1990), temperature and oxygen fugacity (Crocket *et al.* 1991). A recent experimental estimate of D^s_{Pd} for MORB liquids is 10 000 (Peach *et al.* 1989). In separate experiments Crocket *et al.* (*op. cit.*) derived a range of D^s_{Pd} values from 700 to 100 000 for MORB liquids. The highest

value was obtained for a run at 1200°C under wustite-magnetite oxygen fugacity conditions and low Ni content in the sulphide; the lowest value was obtained with the same oxygen buffer at 1300°C but with a higher initial Ni content. A separate estimate of 10 000 for D^s_{Cu} was made for the UG2 chromitites of the Bushveld complex based on the composition of sulphides (Sharpe 1982). Naldrett and Duke (1980) used an estimate of 1500 D^s_{Pd} for magmatic sulphide ores. Francis (1990) showed that D^s_{Cu} values were five times higher in a fractionated tholeite (D^s_{Cu} =1006) compared to komatiitic melts (D^s_{Cu} =178). The author suggested that this was due to a higher oxygen content in Fe-S-O liquids associated with MORB.

It is clear from the above brief account that any estimation of D^s_{Cu} and D^s_{Pd} for the Bragança chromite-rich rocks must be uncertain. If D^s_{Pd} values decrease from MORB to komatiitic melts in an analagous way to Cu then the upper estimate of 100 000 (Crocket *et al. op. cit.*) is too high, as the melts from which the chromite-rich samples were derived, are thought to have boninitic affinities (chapter 3) more analagous to picritic komatiitic melts than fractionated tholeites. In the following calculations a high value of 10 000 and a low value of 1500 for D^s_{Pd} are used. The komatiitic melt value for D^s_{Cu} of 178 is used.

A Pd/Cu ratio may only be calculated for some Bragança samples because Cu values are below detection limits in other cases. The range obtained was $1.9x10^{-5}$ to $4.9x10^{-3}$ (table 4.7.1). This figure probably represents a lower part of the true range; for several samples have relatively high Pd contents, whereas Cu is still below the limits of detection.

Table 4.7.1a The range of Pd/Cu ratio values for chromitite and sulphide ore occurrences in different complexes.

Pd/Cu range	Example	Reference
$1.2x10^{-5}$- $1.8x10^{-3}$	Heazelwood complex chromitites	Peck and Keays (1990)
$8.6x10^{-5}$- $4.7x10^{-3}$	Oman chromitites	Page (1982a)
$8.8x10^{-3}$- 0.01	Bushveld chromitites	Von Gruenewaldt *et al.* (1986)
$6.4x10^{-6}$- $3.2x10^{-4}$	Bushveld critical zone sulphide ores	Naldrett *et al.* (1986)
$2.0x10^{-5}$- 0.115	Great Dyke sulphide ores	Wilson and Tredoux (1990)
$1.9x10^{-5}$- $4.9x10^{-3}$	Bragança	This study

The range of Pd/Cu ratios for Bragança are similar to those for other podiform chromitites suggesting similar processes of concentration for Pd and Cu from silicate melts into a sulphide phase.

The maximum figure of $4.9x10^{-3}$ for the Bragança samples can now be compared with the range of initial silicate melt concentrations needed to create such a ratio as follows. Pd/Cu ratios are calculated for D=10 000 with Pd and 178 for Cu in table 4.7.1b and 1500 for Pd in table 4.7.1c. Initial melt concentrations of 2ppb, 10ppb and 38ppb are used for Pd, 70ppm and 20ppm for Cu. The 20ppm Cu figure and 38ppb Pd content are extreme values for silicate melts, only associated with boninite affinity lavas (table 4.7.2). The

range of Y_{Pd} and Y_{Cu} values are then used (table 4.7.1d) to calculate a theoretical range of Pd/Cu ratios for sulphide phases derived from different types of silicate melts.

Table 4.7.1b Calculated Pd and Cu concentrations within a sulphide phase for varying initial silicate melt concentrations and D^s_{Pd}=10 000, D^s_{Cu}=178

X_{Pd}	Y_{Pd}	X_{Cu}	Y_{Cu}
38ppb	380ppm	20ppm	3560ppm
10ppb	100ppm	70ppm	12460ppm
2ppb	20ppm		

Pd $Y_i = D_i^s X_i$ For D=10 000, Cu $Y_i = D_i^s X_i$ D=178

Table 4.7.1c Calculated Pd concentration within sulphide phase for varying initial silicate melt concentrations and D=1500

X_{Pd}	Y_{Pd}
38ppb	57ppm
10ppb	15ppm
2ppb	3ppm

Pd $Y_i = D_i^s X_i$ For D=1500

Using these Y_{Cu} and Y_{Pd} values, calculated for differing initial silicate melt concentrations and distribution coefficients, a range of Pd/Cu ratios is calculated in table 4.7.1d.

Table 4.7.1d Calculated Pd/Cu ratios for range of Y_{Cu} and Y_{Pd} values (ppm)

	Y_{Cu}=3560	Y_{Cu}=12460
Y_{Pd}=380	0.11	0.03
Y_{Pd}=100	0.03	$8x10^{-3}$
Y_{Pd}=20	$6x10^{-3}$	$2x10^{-3}$
Y_{Pd}=57	0.02	$5x10^{-3}$
Y_{Pd}=15	$4x10^{-3}$	$1x10^{-3}$
Y_{Pd}=3	$8x10^{-4}$	$2x10^{-4}$

The results in the tables 4.7.1b-d show that the circumstances which generate Pd/Cu ratios equal to or greater than those of the maximum Bragança value of $4.9x10^{-3}$ are a low initial Cu content, high initial Pd contents and 10 000 for D^s_{Pd} within a silicate melt. For instance with D^s_{Pd} of 10 000 and an initial Pd silicate melt concentration of 2ppb (which is equivalent to Y_{Pd} of 20ppm) 20ppm Cu (equivalent to 3560ppm Y_{Cu}) is necessary to create a Pd/Cu ratio greater than that of $4.9x10^{-3}$.within a sulphide bearing rock which has crystallised from that melt The types of silicate melt compatible with such Pd and Cu concentrations are discussed in the next section.

4.7.2 Pd and Cu silicate melt contents

The Pd/Cu ratios for some of the Bragança chromitites suggest either or both an

enrichment in Pd, above 10ppb and a depletion in Cu, to 20ppm within a melt from which the sulphide fraction was derived. The initial silicate melt concentration of Pd may have been high, equal to or above 10ppb in some areas of crystallisation. Boninite lavas and komatiites show similarities to this level of enrichment. Similarly such melts typically show low Cu contents, with an average of 20ppm compared to that of the 72ppm average for MORB (Hamlyn *et al.* 1985).

Normal whole rock Pd abundances in silicate melts are in a range up to 30ppb (Naldrett and Duke 1980). Enrichment in Pd, though in variable amounts, is characteristic of boninites (table 4.7.2). The Archean equivalents of boninites (komatiites) also have high levels, with an average whole rock value of 10ppb (Naldrett and Duke, 1980). Continental flood basalts show lesser though still relatively high levels with up to 8.3ppb for the Karoo and Deccan provinces. Boninites and komatiites are widely accepted to have been derived from a mantle source that has undergone a high degree of melt extraction *eg* Cameron *et al.* (1980), Crawford *et al.* (1989).

Table 4.7.2 Pd contents in different silicate melt associations

Rock Type	Pd ppb Cu ppm	Reference
MORB	<0.1 to 6.29ppb; Cu 72ppm average	Hertogen *et al.* (1980); Hamlyn *et al.* (1985)
MORB	0.7ppb average	Crocket (1979)
Karoo and Deccan flood basalts	8.3ppb average	Crocket (1981)
Cont. Flood Basalts	6ppb average	Crocket (1979)
Low Ti lavas and boninites	0.6 to 38ppb; Cu 20ppm average	Hamlyn *et al.* (1985)
Komatiites	10ppb	Naldrett and Duke (1980)

Table 4.8 shows the enrichment in Pd of liquids derived from a high degree of mantle melting (boninites and komatiites) compared to first stage melts (MORB and flood basalts). Cu values show the reverse relationship, with depletion in boninites compared to MORB.

Hamlyn and Keays (1986) proposed a model to explain the enrichment of Pd in rocks presumed to be derived from second stage melts such as boninites. First stage melts like MORB or continental flood basalts were noted as sulphur saturated. The residual mantle created through this melt extraction was envisaged as being depleted in S and Cu. The authors proposed that an accessory sulphide phase remained within the depleted mantle, into which the PGE partitioned. The residual sulphide phase would be characterised by a high PGE and low Cu tenor; further melting of this mantle source resulting in magmas with a high PGE concentration. Hamlyn and Keays (*op. cit.*) proposed that the Bushveld complex (*eg* see UG2 chromitites in table 4.7.1a) had been created from two parental melts - anorthositic and boninitic - in order to explain the high PGE tenors of Bushveld ores.

If the parental melts to the Bragança chromitites were enriched in Pd in order to produce the relatively high Pd/Cu ratios of some samples, then a possible explanation for this is provided by the Hamlyn and Keays (1986) model. The melt from which the

chromitites crystallised may have been derived from a depleted mantle source region containing sulphides with a high PGE tenor. In chapter 5 the validity of this model is discussed further in the light of the sulphide and PGE mineralisation within the harzburgite formation.

4.8. Fractionation of Pt from Ir

In sections 4.4. and 4.5 it was shown that the Os, Ir, Ru group had been fractionated from the Pt-bearing arsenides and sulpharsenides within the chromite-rich samples. This section proposes a way in which this process can be related to the crystallisation of the chromite-rich samples.

Amossé *et al.* (1990) reported the results of experimental work carried out on the solubility of Pt and Ir within a basaltic silicate melt at 1400°C. Pt and Ir metal samples were heated around a pellet of the basaltic composition powder. S- and O-bearing gases were passed over the heated mixture to control the fugacities. The solubility was measured as the final concentration of Pt and Ir within the quenched basaltic melt. Some of the results are shown in fig. 4.8a. At a range of oxygen fugacities from $\log_{10}^{-7}$ to $\log_{10}^{-5}$ the solubility of Pt was reported to fall from 2900ppb Pd in the silicate melt down to about 100ppb. The Ir solubility decreased from 300ppb towards zero at oxygen fugacities greater than $\log_{10}^{-5}$. The relative trends in solubility change are expected to stay similar at different temperatures.

In order to show the effects of increased fO_2 on the PGE mineralisation of the Bragança samples, it is neccessary to calculate the fO_2 range present during their crystallisation. Experimental work on basic and ultrabasic melts (Murck and Campbell 1986) has enabled the Fe^{3+} content of chromite grains to be related to the fO_2 present at their formation. It is likely to be of most use in massive chromitites, where the effects of re-equilibration with the silicate phase will be minimised. Using the range of $100Fe^{3+}/(Fe^{3+}+Cr+Al)$ ratios of 3.32 -11.58 for the Bragança samples (chapter 3 table 3.3.2) gives an fO_2 range of $\log_{10}^{-7.5}$ to $\log_{10}^{-5}$ at 1400°C and $\log_{10}^{-7}$ to $\log_{10}^{-10}$ at 1250°C (fig. 4.8b). Under these conditions (fig. 4.8a) Pt has a much higher solubility than Ir although both solubilities decrease markedly at lower oxygen fugacities.

Figure 4.8a PGE solubility in silicate melts

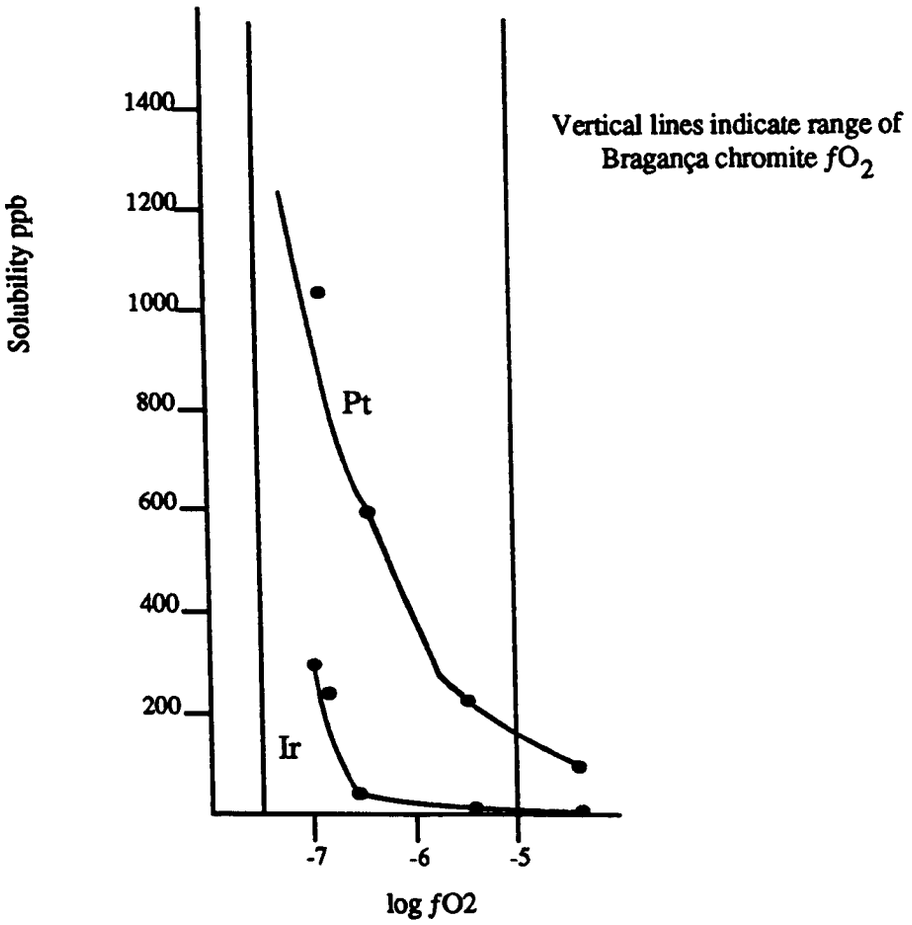

From Amossé *et.al.* 1990

This figure shows the variation in solubility of Pt and Ir with varying fO_2 Pt has a higher solubility within the basaltic melt than Ir. With increasing fO_2, the solubilities of both Pt and Ir decrease, but Pt retains some solubility whereas the solubility of Ir becomes negligible. This is an explanation for the fractionation of Pt from the other PGE; Pt retains a relatively high solubility during the fO_2 conditions under which the chromite crystallised (between the vertical lines on the figure) and thus is incorporated into minerals later than the other PGE. Calculation of chromite fO_2 values demonstrated in fig. 4.8b.

Figure 4.8b Variation of oxygen fugacity with chromite composition

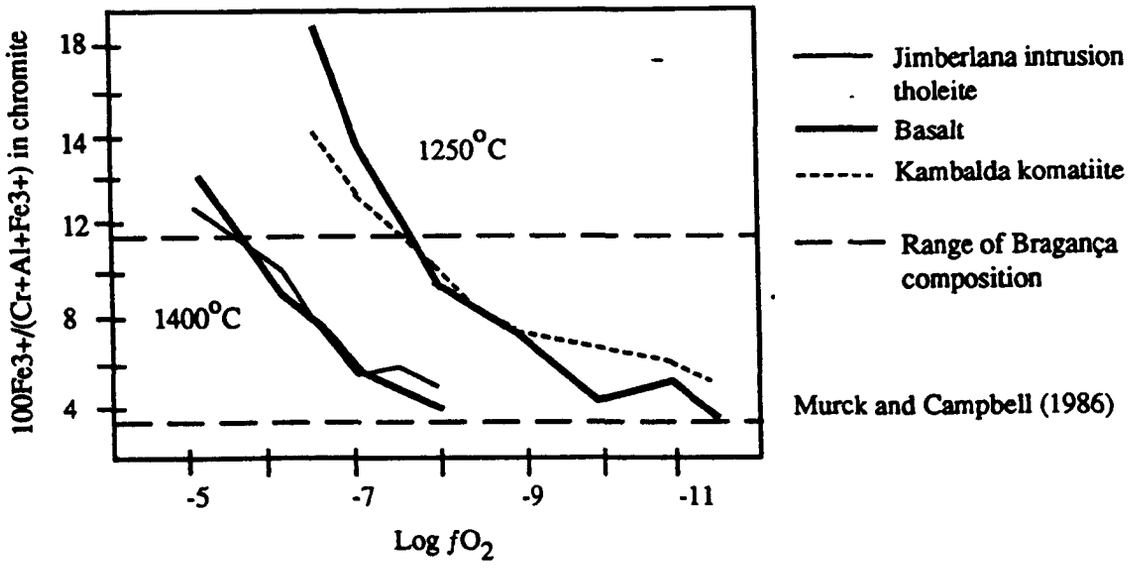

Chromite grain composition (the Fe3+/(Cr+Al+Fe3+) ratio) is related to the conditions of fO_2 under which the chromite crystallised. Greater concentrations of ferric iron occur with increasing fO_2. The Bragança chromite compositional range for this ratio is between 3.32 and 11.58 (table 3.3.2). At 1400°C this gives an logfO_2 range of -7.5 to -5 and at 1250°C -7 to -10. The experiments were based on analyses of chromite grains derived from ultrabasic and basic melts under controlled fO_2 conditions. Murck and Campbell (1986).

The following oxidised species were proposed, from consideration of available thermodynamic data, to be the most stable species in basic melts at 1600K by Wood (1987): OsO_4, IrO_3, RuO_3, RuO_3, PtO_2. In the same publication, Wood also suggested that the volatility of these species was dependent on the conditions of fO_2.

Using the oxidised species at 1600K of Wood (*op. cit.*) the following partition formulae can be proposed:

$$OsO_4 \leftrightarrow Os_{(o)} + 2O_2 \qquad RhO_2 \leftrightarrow Rh_{(o)} + O_2$$

$$IrO_3 \leftrightarrow Ir_{(o)} + \tfrac{3}{2}O_2 \qquad PtO_2 \leftrightarrow Pt_{(o)} + O_2$$

$$RuO_3 \leftrightarrow Ru_{(o)} + \tfrac{3}{2}O_2$$

(o) species dissolved in silicate melt

The O-bearing compounds represent species with relatively low solubility (Wood, *op. cit.*) from which solid phases, alloys and sulphides, will crystallise. With increasing oxygen partial pressure, the position of equilibrium in the equations above will move to the left. The effect will be relatively greater for Os, Ir, Ru than for Rh, Pt, as the latter two elements combine with less oxygen. Amossé *et al.* (1990) used the same argument, though with

different oxidised species, to explain their experimental result of dropping PGE solubility with increased oxygen fugacity.

The primary fractionation of the PGE described in sections 4.4. and 4.5 for the Bragança samples can be explained by this model. The more insoluble Os, Ir, Ru start forming PGM at an early point or before the chromite grain's crystallisation, whilst Rh and Pt can stay dissolved within the melt for longer so starting to form minerals later.

4.9. Model of PGE mineralisation and conclusions

The PGE are grouped on the basis of mineralogy into a Ru, Os, Ir group, an Ir, Rh, Pt group and a Pd, Pt group. Ru, Os, Ir are found together in laurites $Ru(OsIr)S_2$ and Ir, Rh, Pt are found in the irarsite/hollingworthite/platarsite series minerals Ir(RhPt)AsS and sperrylite $PtAs_2$. Pd-bearing minerals have been found as Pd-S, and Pd-Hg (potarite) associated with pentlandites or heazlewoodite and in one case a Pt-Pd-Cu alloy. Other Pd and Pt-bearing alloys are located in the serpentine matrix of sample Brag57. Sample Brag57 is unusually enriched in PGE, with a total of 11.2ppm.

In terms of the PGE groups the six elements are fractionated during chromite crystallisation in the order the Ru, Os, Ir group first followed by the Ir, Rh, Pt group. This fractionation is evidenced by positive chondrite normalised slopes for some of the samples and the presence of Pt-As bearing minerals at the edge of chromite grains. The other PGM are found throughout the chromite grains. An element of bias is present in the sampling as the massive chromitites seem more likely to have positive fractionation trends than samples with less chromite in them.

Alteration of the samples during serpentinisation has led to the breakdown of pentlandite to heazlewoodite and magnetite in some sulphide grains. This sulphide assemblage is associated with Pt- and Pd-bearing alloys which were formed under reducing conditions and low sulphur fugacities. Limited remobilisation of Cu, Pt and Pd, originally associated with pentlandite, may have occurred at this stage as shown by the presence of Pt- and Pd-bearing alloys within the serpentine matrix of sample Brag57 but the alteration is essentially in-situ. The laurite and irarsite dominated PGM mineralogy of the Braganca chromitites is typical of podiform chromitites. The fractionation for much of the Pt described for some other chromitites is confirmed in this study. Pd was not part of this fractionation trend and instead was incorporated into pentlandite during its crystallisation.

The Pd/Cu ratio calculated for the parental silicate melt of the chromite-rich samples suggest a high tenor of Pd relative to base-metal sulphide for at least some of the samples. The low Cu and relatively high Pd contents thought to be present in the original silicate melt are characteristic of secondary melts, notably boninites. This provides further evidence to support the conclusions of chapter 3, based on chromite composition, that the parental melt to the dunite/chromitite formation had boninitic affinities.

In order to explain the fractionation of the other five PGE it is suggested that a model

based on the work of Amossé *et al.* (1990) relating the effects of fO_2 to the solubility of the PGE within silicate melts is applicable. At the $\log fO_2$ likely during the formation of the chromitite (-7.5 to -5) the solubility of the PGE decrease. Ru, Os, Ir are relatively less soluble than Pt and this may explain the observed fractionation in some of the samples as Pt is likely to be incorporated in minerals after Ru, Os, Ir.

Chapter 5 PGE in silicate lithologies

This chapter deals with the PGE contents and sulphide mineralogy of the silicate lithologies within the ultrabasic assemblage of the Bragança UATC. A question arising is whether the sulphide phase present in the harzburgite has the same, residual origin as the silicate minerals or is due to a later introduction of sulphide. A number of workers have postulated the existence of a PGE-enriched residual sulphide phase within depleted mantle (Mitchell and Keays 1981, Hamlyn *et al.*1985). The authors proposed that instead of being incorporated into a first silicate melt with much of the sulphur, PGE were preferentially scavanged by the relatively small amount of sulphide that remained within the mantle during further partial melting. Secondary melts, such as boninites, into which more of the remaining sulphide was incorporated, would have a high PGE content relative to sulphide. This theory was described in chapter 4 with regard to the possible boninitic affinity of melts from which the PGE-bearing chromitite was derived. In this chapter the validity of the theory in understanding the PGE geochemistry of the Bragança residual assemblage is considered. In chapter 4 the Pd/Cu ratio was used to indicate the concentration of PGE relative to the amount of sulphide for different types of silicate melt. In this chapter Pd/Cu ratios are used to give an indication of the tenor of PGE within sulphide, in addition to using whole rock S abundances to calculate the concentration of Pd within the sulphide phase.

5.1 The PGE contents of the harzburgite and pyroxenite formations

The six samples of the harzburgite formation from Bragança show a range of total ΣPGE contents from 32 to 78ppb (table 5.1a). This shows the relatively low levels of PGE in comparison to the chromite-rich samples described in chapter 4. Pd/Ir ratios from 0.7 to 4 largely overlap the range in the chromite-rich samples (chapter 4) of 0.06-3.21 and Pd/Cu ratios range from $7.3x10^{-4}$ to $>2x10^{-3}$. The chondrite-normalised PGE trends (fig. 5.1a) have a trough at Ir and a peak at Ru similar to some of the patterns found associated with the chromite mineralisation. All but one of the harzburgite samples also have a peak at Pd, giving an overall positive slope to the graphs. In chapter 4 such trends were explained by the presence of fractionated PGE-bearing assemblages or base-metal sulphide control on Pt, Pd geochemistry. As no fractionated PGM assemblage was identified in the harzburgite samples this suggests sulphide control on the Pt,Pd geochemistry of the harzburgite formation.

Figure 5.1 PGE Chondrite normalised graphs for pyroxenites and the harzburgite formation

Figure 5.1a. Harzburgite formation

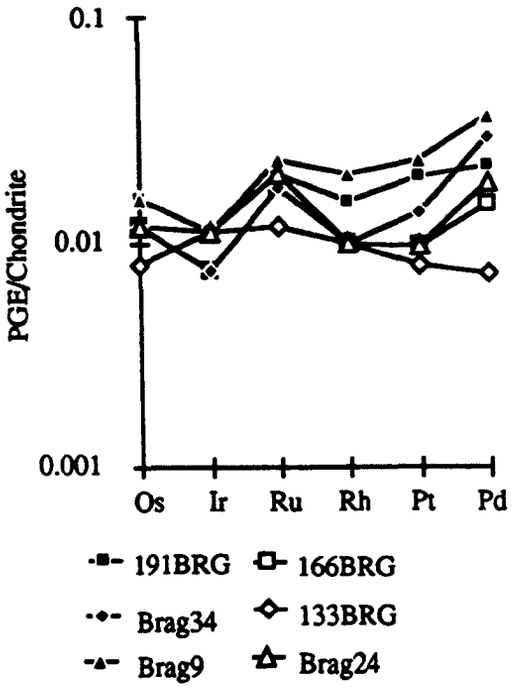

Figure 5.1b.Pyroxenites

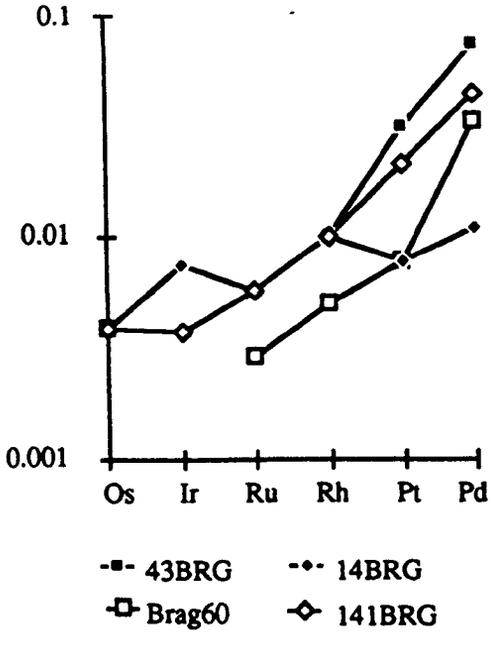

Figure 5.1c Bay of Islands residual mantle

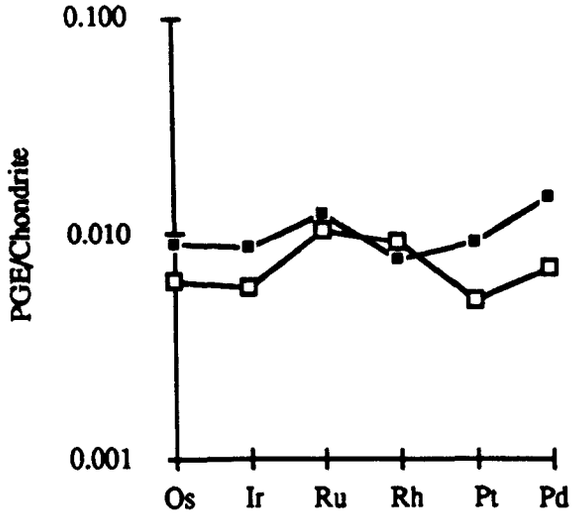

From Edwards (1990)

Figure 5.1a shows the chondrite normalised PGE profiles of 6 harzburgite formation samples. Five of the samples display a peak at Ru, reminiscent of the chromite-associated PGE mineralisation described in chapter 4. The broadly positive slopes at the Pt, Pd tails also suggest a sulphide control on mineralisation. Fig. 5.1b shows the chondrite normalised PGE profiles of 4 pyroxenite samples. The steeply positive slopes towards Pd are a result of the sulphide enrichment of these samples. Os and Ir contents are below detection limits for sample Brag60; this extreme depletion shows the lack of chromite-associated PGE mineralisation in the pyroxenites. Figure 5.1c shows the profiles of two samples of residual mantle from the Bay of Islands ophiolite (Edwards 1990). These have peaks at Ru and Pd suggesting both accessory chromite and sulphide controls on the PGE mineralisation.

The S content data available is only approximate (appendix 7). Despite this, it is possible to calculate a conservative estimate for the tenor of Pd within sulphide. This has been done by taking a likely upper limit for the S content of the sample based on the analytical limitations (twice the analysed value-see appendix 7) and using it to calculate an equivalent whole rock pentlandite content. The factor by which this calculated pentlandite content is multiplied to create 100% pentlandite is multiplied by the whole rock Pd content. The resultant product is an estimation of the concentration of Pd within the sulphide phase. The calculated estimates for the Pd tenor of samples 133BRG, Brag24 and Brag9 are 2ppm, 2ppm and 9ppm, all to the nearest 1ppm. These values are considered in the next section. The approximate S concentrations for these samples are 210ppm, 500ppm and 220ppm respectively. In contrast, pyroxenite sample 141BRG shows more sulphide enrichment, with an approximate value of 2230ppm S.

The four pyroxenite (websterite) samples have PGE contents (ppb) ranging from 26 to 76 and Pt+Pd totals ranging from 14 - 72. Two of these samples contain no detected Ir, the other samples have Pd/Ir ratios of 1.5 and 12. The pyroxenites have an enrichment of Pt+Pd over the other PGE, greater than most of the harzburgite samples. This is demonstrated by the chondrite-normalised graphs in fig. 5.1b which have steeply positive trends, giving the Pt,Pd relative enrichment associated with base-metal sulphide controlled PGE mineralisation (chapter 4). Pd/Cu ratios range from $6.3x10^{-5}$ to $8.6x10^{-4}$ for the pyroxenite samples. This range is lower than that for the harzburgite samples showing that despite the greater enrichment of Pt and Pd within the pyroxenite samples, compared to the harzburgite formation, the tenor of PGE relative to the amount of sulphide is lower. Two samples (1BRG and 20BRG) in which there is a mixture of harzburgite and pyroxenite have lower PGE contents of 26 and 36ppb. Pd/Ir ratios are 1.0 and 1.3.

Table 5.1a PGE Contents of harzburgite and pyroxenite (ppb)

	Pyrox.					Harz.	
	43BRG	Brag60	14BRG	141BRG	Range	191BRG	166BRG
Os	2	2	2	2	2	8	6
Ir	nd	nd	4	2	nd-4	6	4
Ru	nd	2	4	4	nd-4	14	12
Rh	2	1	2	2	1-2	3	2
Pt	32	8	8	22	8-32	20	10
Pd	40	18	6	24	6-40	12	8
Pd/Ir	-	-	1.5	12	12->12	2	2
Pt/Ir	-	-	2	11	11->11	3.3	2.5
ΣPGE	76	31	26	56	26-76	63	42
Cu (ppm)	330	21	84	378	21-378	<10	11
Pd/Cu	$1.2x10^{-4}$	$8.6x10^{-4}$	$7.1x10^{-5}$	$6.3x10^{-5}$	$6.3x10^{-5}$ $8.6x10^{-4}$	>$1.2x10^{-3}$	$7.3x10^{-4}$

Table 5.1a continued

						Pyroxenite Mix	
	133BRG	Brag9	Brag24	Brag34	Range	20BRG	1BRG
Os	4	8	6	6	4-8	4	4
Ir	6	6	6	4	4-6	6	4
Ru	8	16	14	12	8-16	8	8
Rh	2	4	2	2	2-4	2	2
Pt	8	24	10	14	10-24	8	4
Pd	4	20	10	16	8-20	8	4
Pd/Ir	0.7	3.3	1.7	4	0.7-4	1.3	1
Pt/Ir	1.3	4	1.7	3.5	2.5-4	1.3	1
ΣPGE	32	78	48	54	32-78	36	26
Cu (ppm)	16	<10	12	-		<10	<10
Pd/Cu	2.5x10-4	>2x10-3	8.3x10-4	-		>8x10-4	>8x10-4

Table 5.1b PGE Contents of other mantle peridotites and pyroxenite (ppb)

	Mantle Pyroxenite					**Mantle peridotite**	
Locality	Ariege[1]				Range	Bay of Islands[2]	
Os	<3	<3	<3	<3	<3	4.61	3.16
Ir	2.1	15	1.1	1.8	1.1-15	4.76	3.13
Ru	<5	16	<5	<5	<5-16	8.75	7.23
Rh	1	35	1	2	1-35	1.53	1.84
Pt	18	150	<5	6	<5-150	9.54	5.19
Pd	9	319	<5	11	<5-319	8.16	3.87
Pd/Ir	4.3	21.3	<4.5	6.1	<4.5-21.3	1.7	1.3
Pt/Ir	8.6	10	<4.5	3.3	<4.5-10	2.0	1.7
ΣPGE	30.1	535	2.1	20.8	2.1-535	37.4	24.4
Cu (ppm)							
Pd/Cu							

Table 5.1b continued

		Review[4]	
	Ivrea Verbano		Range
Os			3.16-4.61
Ir			3.13-4.76
Ru			7.23-8.75
Rh	<0.4-2.8		<0.4-2.8
Pt	1.8-22	2.1-10	1.8-22
Pd	0.5-13.5	0.29-9.5	0.29-9.5
Pd/Ir			-
Pt/Ir			-
ΣPGE			-
Cu	6.8-28.5		
Pd/Cu	$2.6x10^{-4}$ $3.2x10^{-4}$		

nd =not detected, 1=Lorand (1988), 2=Edwards (1990), 3= average of 23 samples in Garuti *et al.* (1984), 4=review in Barnes *et al.* (1985).

The Pt and Pd contents of the samples from the Bragança harzburgite formation are similar to those from other complexes (table 5.1b). One of the Pt values and two of the Pd values are greater than the range given in the table above. The Pd/Cu ratios of the harzburgite samples are similar to those of the Ivrea-Verbano samples (table 5.1). Mitchell and Keays (1981) presented the results of Pd analyses performed on spinel and garnet lherzolite nodules. These nodules were considered by the authors to be the residua following basaltic melt extraction from a fertile mantle source. The samples had a range of 0.3ppb to 8.8ppb Pd and a high tenor (up to 15.8ppm) when recalculated to the concentration within sulphide. By comparison, this figure and those calculated for the three Bragança samples, are higher than 11 of the 16 magmatic sulphide ore occurrences mentioned in Naldrett and Duke (1980). Pd/Cu ratios for spinel and garnet nodules range from $1.6x10^{-4}$ to $3.5x10^{-3}$ (Mitchell and Keays *op. cit.*). This range shows the high Pd tenor present within mantle residua. Similarly the Bragança harzburgite samples, the Pd/Cu ratios of which overlap this range, have a high tenor of Pd within sulphide.

5.2 Origin of the Pt,Pd mineralisation within the residual mantle assemblage

If by analogy with the Pt and Pd base-metal sulphide associated mineralogy of the dunite/chromitite formation discussed in the previous chapter, it is assumed that Pt and Pd are associated with the relict base-metal sulphide within the harzburgite formation, then the

question of the origin of the Pt,Pd mineralisation rests on the genesis of the sulphide phase.

5.2.1 Sulphide minerals in the harzburgite and pyroxenite formations

A very scarce sulphide phase has been located in four of the harzburgite samples. No more than six recognizable sulphide grains have been found in any polished section. The sulphide that is present is invariably rimmed and partially replaced by magnetite. Grains are no more than a few tens of microns across (plate 5.2.1a). Only pentlandite has been located, unlike the sulphide mineralisation in the chromite-rich samples where heazlewoodite was present as well. No Cu-bearing phases have been identified.

The range of S and Ni atomic percentages for the pentlandite grains (45.5 - 48.6 S, 22.9 - 30.7 Ni) in table 5.2.1a lie within those of the pentlandites described in chapter 4. The range of Ni contents for the pentlandite grains in the harzburgite formation is characteristic of pentlandite-heazlewoodite assemblages in serpentinised ultrabasic rocks (Misra and Fleet 1973). The pentlandite and magnetite assemblage is similar to that described for the chromite-rich samples in the previous chapter and is a serpentinisation related assemblage. The pentlandite and magnetite clusters represent relicts of pentlandite predating the serpentinisation overprint.

Table 5.2.1a Pentlandite analyses from the harzburgite formation

	166BRG		191BRG			Brag34		
Wt%								
S	34.2	33.7	31.7	33.6	33.4	32.0	32.2	31.6
Fe	25.0	25.6	33.3	33.6	34.0	31.8	27.8	33.3
Ni	39.4	38.8	31.2	31.1	28.8	32.4	35.9	30.5
Total	98.7	98.1	96.2	98.4	96.2	96.2	95.9	95.4
Atomic %								
S	48.8	48.4	46.8	48.1	48.6	47.1	47.5	46.8
Fe	20.5	21.1	28.1	27.6	28.5	26.8	23.5	28.4
Ni	30.7	30.4	25.1	24.3	22.9	26.0	29.0	24.8
(Fe+Ni) /S	1.0	1.1	1.1	1.1	1.1	1.1	1.1	1.1

Table 5.2.1 continued

	Brag9		Range
Wt%			
S	31.5	32.1	31.5-34.2
Fe	28.9	28.3	25.0-34.0
Ni	35.6	34.6	30.5-39.4
Total	96.0	95.1	95.1-98.7
Atomic %			
S	46.7	47.8	46.7-48.8
Fe	24.6	24.1	20.5-28.5
Ni	28.8	28.1	22.9-30.7
(Fe+Ni)/S	1.1	1.1	

These analyses were taken on sulphide grains within samples of the harzburgite formation. The sulphides are situated in serpentine and show alteration to magnetite along edges. Analyses performed on SEM (appendix 2).

There are two possible origins for this sulphide. Either it represents a residual phase which remained within the mantle, like olivine, whilst other mineral phases were preferentially incorporated into melts or it has been introduced in some way. The latter explanation may in turn be due either to an early melt infiltration of an already depleted mantle or else be a late hydrothermal remobilisation associated with serpentinisation.

The hydrothermal remobilisation of the sulphide phase is discounted here. As was shown for the sulphides found with the chromite-rich lithologies (chapter 4) the change in mineralogy which accompanies serpentinisation occurs essentially 'in-situ' and isochemically with apparently little if any actual movement of most sulphide and associated PGE. The other process of sulphide introduction, by a form of melt infiltration, can be assessed for the Bragança samples. The only plausible source for an infiltrating melt lies with the pyroxenite layers. It was suggested in chapter 2 that the similarity in amphibole compositions between those of the harzburgite formation and those from the amphibolitised pyroxenite layers might point to a common origin. A mechanism of melt impregnation by which pyroxene might crystallise in peridotites as diffuse disseminations rather than in discrete layers was proposed by Nicolas and Dupuy (1984). Harzburgites were enriched in clinopyroxene and feldspar, creating lherzolites, wehrlite and troctolite. Edwards (1990) proposed that disseminations of pyroxene within the Bay of Islands ophiolite harzburgite resulted when the melt pressure was not great enough to fracture the peridotite to form pyroxenite dykes. Pyroxenite layers and small relict aggregates within the Bragança harzburgite formation may be associated with the passage of a silicate melt through the mantle sequence. Edwards (*op. cit.*) used this model to explain Pt and Pd enrichments, within the Bay of Islands harzburgite (fig. 5.1c),at similar or lower level than those of the Bragança samples. Pt and Pd were considered to be associated with arsenide platinum-group mineral inclusions within the harzburgite's pyroxenes; such minerals having been

Chapter 5 Plates

Plate 5.2.1a
Pentlandite (pn) and magnetite (mg) composite grain within harzburgite sample 166BRG. F.O.V. 0.25mm. Oil immersion. This is a typical grain from the harzburgite formation.

Plate 5.2.1b
Chalcopyrite (Cp) and pyrrhotite (po) composite grains in between cpx within websterite sample 141BRG. F.O.V. 0.25mm. Oil immersion.

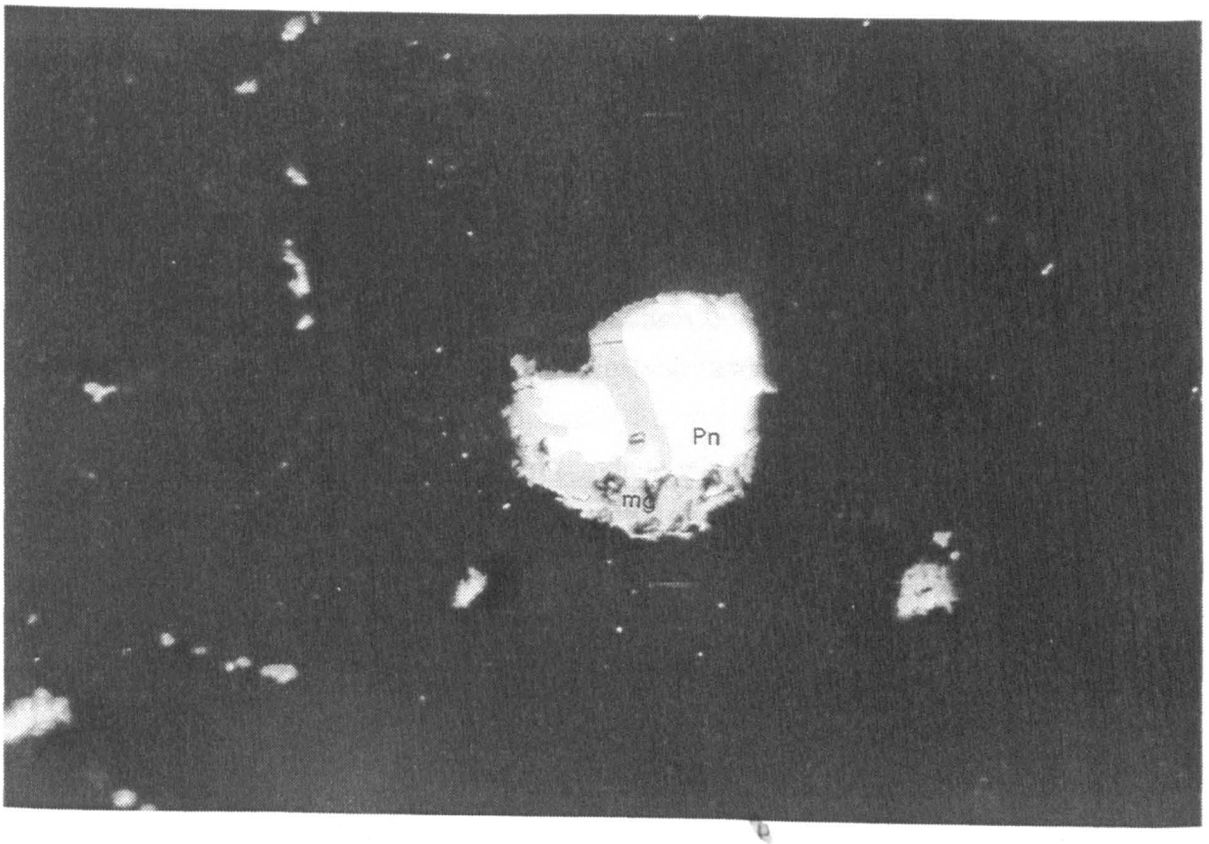
Pn
mg

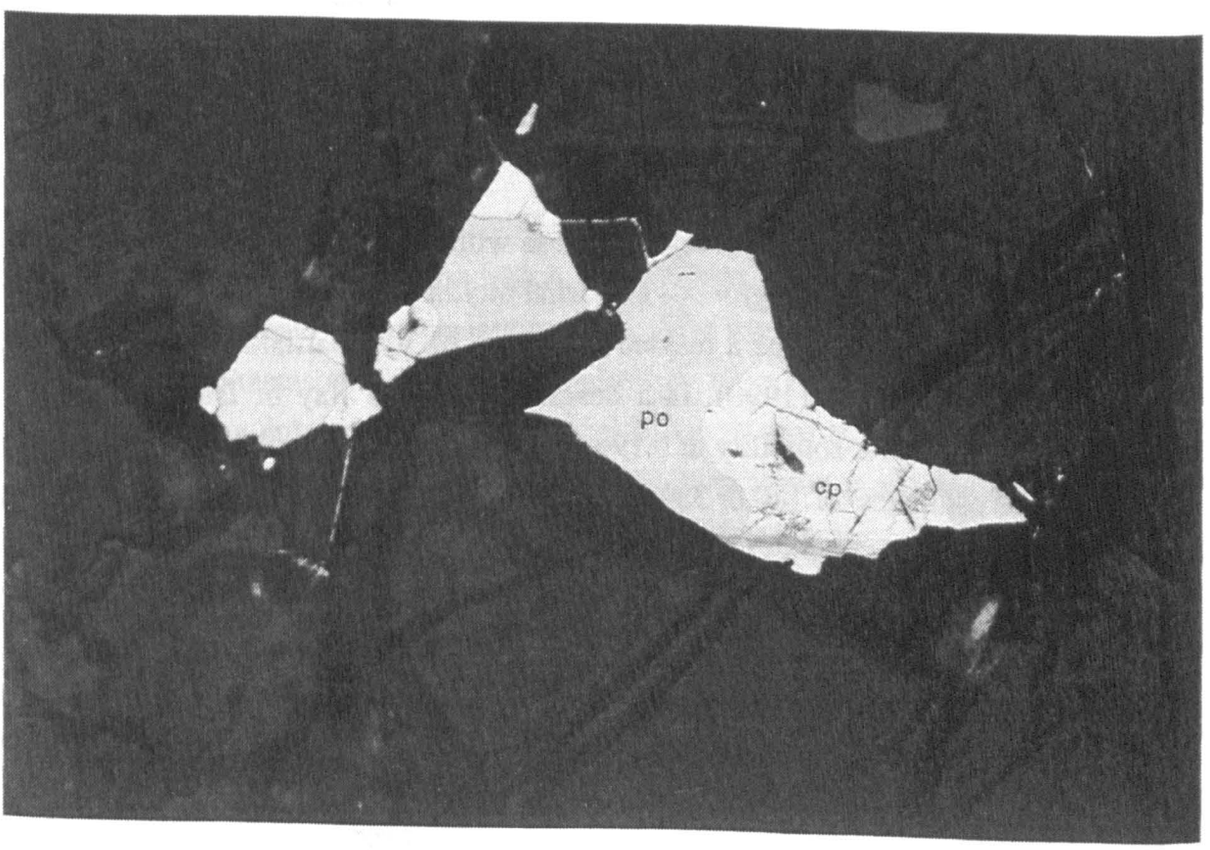
po
cp

identified within the pyroxenite layers. This latter model can be readily assessed for the Bragança assemblage. Bragança pyroxenite contains a sulphide assemblage which has not been affected by the serpentinisation overprint (table 5.2.1b). Pentlandite, chalcopyrite and pyrrhotite are present in composite grains (plate 5.2.1b). These minerals are distinct from the harzburgite formation sulphide minerals in being Cu-rich; the harzburgite sulphide assemblage is not likely to have been derived from pyroxenite. On this basis a model whereby the Pt and Pd contents of the harzburgite formation is controlled by a pyroxenite derived component is rejected. The remaining, favoured, origin for the sulphide is as a residual phase which has survived mantle depletion.

Table 5.2.1b Pyrrhotite and chalcopyrite analyses from Bragança pyroxenite

	141BRG po	cp	po	po
Wt%				
S	36.4	34.8	36.3	37.1
Fe	62.9	30.2	61.7	64.4
Cu	-	33.0	-	-
Total	99.3	98.0	98.0	101.5
Atomic %				
S	50.2	50.6	50.6	50.1
Fe	49.8	25.2	49.4	49.9
Cu	-	24.2	-	-

Po pyrrhotite, cp chalcopyrite. Sulphide minerals are more abundant in pyroxenite than the other Bragança lithologies and unlike the harzburgite formation, contain chalcopyrite and pyrrhotite. Analyses performed on an SEM (appendix 2).

5.2.2 Residual sulphide phase

The plausibility of a residual sulphide phase within depleted mantle sequences has been disputed on the theoretical grounds of partial melting. Mantle harzburgite has been considered by many authors to be a residue of around 20-30% partial melting of a fertile lherzolite source. Edwards (1990), in a description of the Bay of Islands ophiolite, estimated that for a sulphur solubility of 0.19wt% and initial mantle sulphur content (based on mantle nodule estimates) of 140 or 320ppm then 7-17% partial melting of a fertile mantle would remove all sulphur. The sulphide which was present within the mantle sequence was attributed to serpentinisation of the silicate phases. This argument, however, does not account for the solubility of sulphide phases which will differ from those of sulphur. Another objection that has been proposed to the interpretation of sulphides as residual is that Cu-Fe-Ni-sulphide is generally considered a low melting point phase eg <1100°C within the spinel lherzolite field pressures and temperatures (Fabries *et al.* 1989).

Despite these theoretically-based objections sulphide assemblages from other depleted mantle relicts have been described as residual. Harzburgite from the Oman ophiolite has been considered to contain sulphide phases of both metasomatic and residual origin (Lorand 1988). The former sulphides are closely associated with what were thought to be impregnation derived pyroxenes and feldspar. The residual phase consists mainly of pentlandite and chalcopyrite, with alteration to secondary serpentinisation related assemblages, and is not associated with the impregnation phases. A similar pentlandite and chalcopyrite assemblage was found in the Ivrea-Verbano mantle peridotites of the Italian Alps (Garuti *et al.* 1984). These sulphides also showed alteration to secondary sulphides including heazlewoodite.

The existence of a PGE-enriched sulphide phase within depleted mantle has been postulated by Hamlyn *et al.* (1985) and Hamlyn and Keays (1986). The presence of sulphide with relatively high Pd/Cu ratios and tenors of Pd within sulphide, not associated with any obvious silicate impregnations or metasomatism, within the Bragança harzburgite formation supports this theory. Melts derived from the Bragança harzburgite formation would be expected to have a high concentration of Pd in relation to sulphide content, reflecting the source composition. As shown in chapter 4, the primitive melts from which the dunite/chromitite formation crystallised had high Pd/Cu ratios reflecting a high tenor of Pd relative to base-metal sulphide. This suggests a genetic link between the residual mantle harzburgite formation and the dunite/chromitite formation: the melts from which the latter formation crystallised were derived from the harzburgite formation.

5.3 Conclusions

Scarce pentlandite grains within the harzburgite samples are the relicts of a phase residual after partial melting depletion events. This interpretation is preferred over that of an origin through metasomatic impregnation because there is no mineralogical association with the Cu-bearing sulphides of the pyroxenite layers, and their associated amphibolitised disseminations, which are the only obvious candidates for silicate impregnation of the harzburgite. Pd/Cu ratios give an indication of the tenor of Pd relative to sulphide. Harzburgite samples have a higher range of the Pd/Cu ratio than the pyroxenite samples, despite the latter being more PGE-enriched. This relationship is also shown by the concentration of Pd within sulphide. The Bragança harzburgite samples have relatively high Pd/Cu ratios, similar to other mantle-derived samples

The proposal of Hamlyn *et al.* (1985) and Mitchell and Keays (1981) that a PGE-enriched sulphide phase is retained within depleted mantle that has undergone previous melting events is supported in this study. Melts derived from the Bragança harzburgite formation would be expected to have a high PGE tenor relative to sulphide content and so a high Pd/Cu ratio. In chapter 4 it was suggested that the melts from which the chromite-rich

samples crystallised were enriched in Pd relative to sulphide. This could be explained by derivation of these melts from the Bragança residual assemblage which contained a PGE-rich sulphide phase. In contrast the pyroxenites have been derived from a source region with more abundant Cu. This suggests an unknown, less depleted source, not genetically related to the harzburgite and dunite/chromitite formations.

Chapter 6 A model for the origin of the Bragança and Morais UATC ultrabasic rocks

6.1 The story so far

In the preceeding chapters the ultrabasic assemblage of the Upper Allochthonous Thrust Complex (UATC) has been identified as residual mantle in Bragança and crustal cumulates at Morais, formed at a continental destructive margin. The assemblage in Bragança is mainly composed of a formation of serpentinised peridotite with a harzburgite modal composition. Distinct layers of a separate chromitite-bearing dunite formation are found within the ultrabasic assemblage, which are relict magmatic conduits within which melt was drained from the residual mantle. In contrast to this, the assemblage at an equivalent structural level within the Morais massif consists of peridotitic cumulates with occasional bodies of gabbro and troctolite.

The inferred high Pd/Cu ratios of the melts associated with the Bragança dunite/chromitite bodies suggests that they are related to boninite-type melts. Further discussion of boninite melts is given later in this chapter. High 100Cr/(Cr+Al) ratios of the chromite grain cores are also consistent with this melt composition. The highly residual nature of the main formation within the ultrabasic assemblage of the UATC and the broadly boninitic affinity of the PGE and chromite mineralisation suggests creation in a fluid-rich, supra subduction zone setting. In order to outline a model for the UATC ultrabasic assemblage's geological development based on the information in the previous chapters, the complex tectonic, lithological and geochronological features of the Iberian Massif are now discussed.

6.2 The Iberian Massif and NW Iberian allochthonous complexes

6.2.1 Palaeozoic tectonic and sedimentary evolution

Plate reconstuctions for the Lower Palaeozoic based on paleomagnetic data have envisaged Gondwanaland (Africa and S. America), Laurentia (N. America), Baltica and Armorica (S. Europe including most of Iberia) continental masses (Scotese *et al.* 1979). These were separated by oceans which subsequently closed during Palaeozoic orogenic cycles. In more detail, and based on sedimentary and faunal evidence, Robardet *et al.* (1990) envisage the existence of separate microplates to the north of Gondwanaland during the Lower Devonian (fig. 6.2.1a). These microplates are now represented by the Iberian terranes.

Figure 6.2.1a Paleogeographical reconstruction for the early Devonian

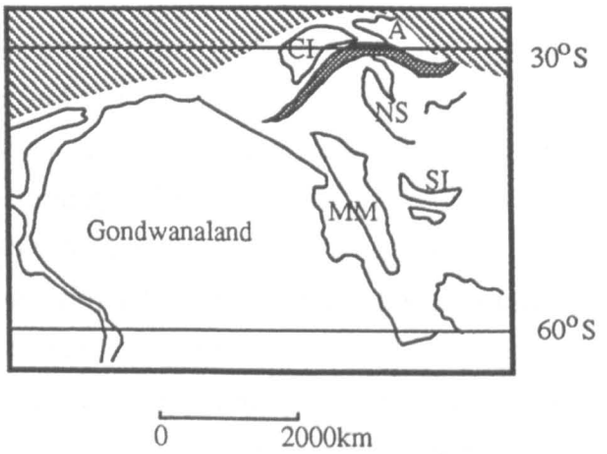

This paleogeographical reconstruction is based upon the sedimentary and faunal differences within SW Europe during the Lower Devonian (from Robardet *et al.* 1990). It shows the separation by a suture zone between the Central Iberian and South Iberian terranes (the South Portuguese and Ossa Morena zones). The South Iberian terranes have Gondwanaland/Moroccan affinities whereas the Central Iberia terranes have affinities to Armorica.
A: Armorica, CI: Central Iberian terrane, NS: Northern Spain, SI: South Iberian terrane, MM: Moroccan Meseta.

Rheic Ocean

South Armorican Ocean suture

During the Lower Palaeozoic, significant faunal and lithological differences emerged, between the Central Iberian Zone to the north and the Ossa Morena and South Portuguese zones to the south, separated by what is now the Badajoz-Cordoba Shear Zone (figs. 6.2.1b,c). Major rifting commenced in the Cambrian. The Cambrian sediments contain platform facies at the margin of a central axial trough within the Central Iberian Zone. Synsedimentary thrusting occurred around the margins directed towards the basin centre (Ribeiro *et al.* 1990b). In the south of the Ossa Morena zone, alkaline and tholeitic magmatism of this age is preserved. This together with the presence of an ophiolite complex on the margin with the South Portuguese zone (fig. 6.2.1c) was taken to indicate the axis of

Figure 6.2.1b Palaeozoic succession in the Central Iberian and Ossa Morena zones

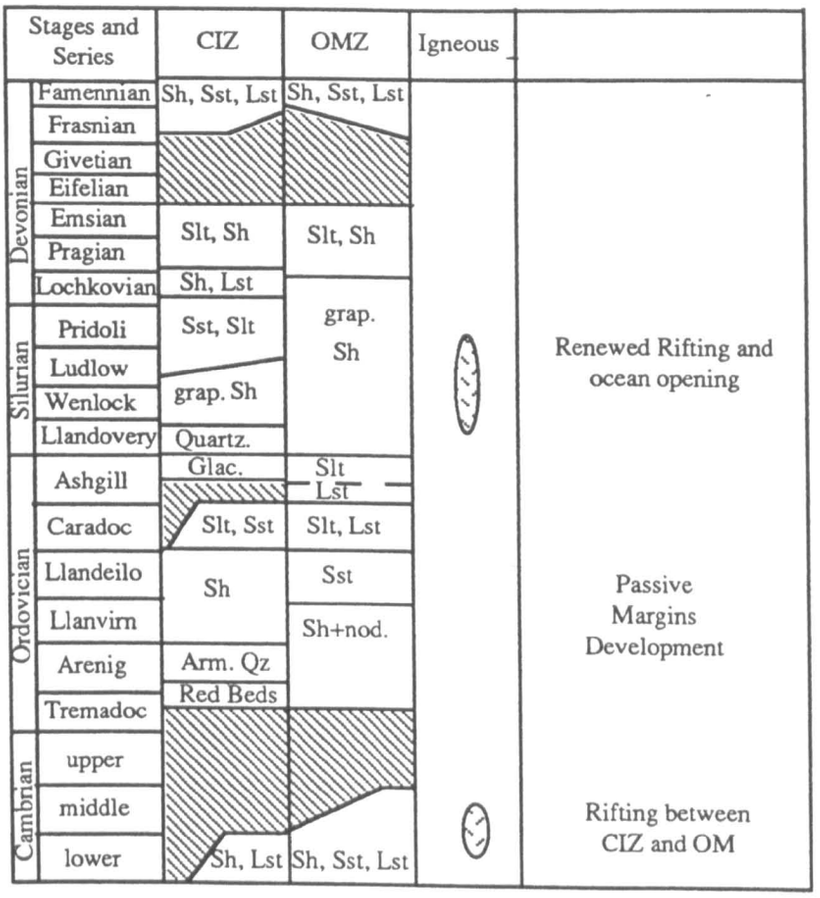

Rift related magmatism

Sh: shale, Sst: sandstone, Slt: siltstone, Lst; limestone,

Glac: glacial derived sediments, grap: graptolites, nod: nodular, Arm qz. : Armorican quartzite, Quartz: quartzite.

Stratigraphic Gap

CIZ:Central Iberian Zone OMZ: Ossa-Morena zone

The Palaeozoic succession in the Iberian terranes shows the development of marked faunal and lithological differences between the Central Iberian zone and the Ossa Morena zones after a period of rifting within the Cambrian. The Ordovician successions of the Central Iberian and Ossa Morena zones show the development of passive margins. The Central Iberian zone contains the Armorican Quartzite which has south european affinities. In the Silurian this diversity is increased, with significant diferences in graptolite faunas; those of the Ossa Morena zone have Moroccan/Gondwanaland affinities whereas those of the Central Iberian zone are southern european. A renewed sequence of rifting occurs in the Silurian. This is associated with the creation of oceanic domains emplaced during the Hercynian collision as ophiolites in the Bragança and Morais massifs.

Based on Robardet and Guitiérrez Marco (1990)

maximum extension during the Cambrian by Queseda (1991). The rift-related Cambrian succession is succeeded unconformably by sediments deposited during the Arenig transgression. In the Central Iberian zone a succession of dark silts, shales and the 5 to 300m thick Armorican quartzite, formed on a passive margin. The Central Iberian Zone, Lower Ordovician succession is similar to that of the Armorican massif of northern France but differs from that in the Ossa Morena zone, where the Armorican quartzite is absent. On this basis and on differences in faunas, Robardet and Guitiérrez Marco (1990) assigned the Ossa Morena zone to a different faunal domain from the Central Iberian zone and Armorican Massif. Silurian sedimentation in Iberia is characterised by graptolite-bearing black shales. The Ossa Morena Silurian succession is distinguished from zones north of the Badajoz Cordoba shear zone by being a more euxinic shale assemblage and lacking sandstone formations. There are also significant differences in graptolite faunas (Robardet and Guitiérrez Marco *op. cit.*). Faunal provincialism and lithological diversity, developed during the Lower Palaeozoic, is well represented in the Devonian sediments. Lower Devonian rocks in the Ossa Morena zone have a dominant shale facies whereas the Central Iberian region has more terrigenous deposits. Brachiopods of the Ossa Morena zone have Moroccan affinities but the Central Iberian zone shows faunal affinities to the Armorican Massif (Robardet and Guitiérrez Marco *op. cit.*).

Sediments of Ordovician to Silurian age, similar to those in the autochthonous series are present in the Lower Allochthonous Thrust Complex of the N.W. Iberian massifs. Lithologies include chert-bearing quartz phyllites and limestone lenses (Ribeiro *et al.* 1990a) as well as volcanic rocks. Within the allochthonous complexes an igneous assemblage of alkaline basalts, peralkaline rhyolites and transitional MORB lavas is present, interbedded with clastic Silurian sediments (Ribeiro *et al.* 1985). This volcanism was attributed by Ribeiro *et al.* (1990b) to the development of an oceanic rift system along the Badajoz Cordoba shear zone (fig. 6.2.1b,c) in Silurian times.

Palaeomagnetic work on Portuguese rocks from either side of this shear zone indicates a 15 degree latitude separation in late Devonian times (Perroud *et al.* 1985). The southern part - the Ossa Morena and South Portuguese zones - were closer to Gondwanaland than the north (Central Iberian zone) which was assembled as part of the Armorican plate. This palaeomagnetic evidence together with the faunal domains shows that the Badajoz-Cordoba Shear Zone is a relict suture which separated the Ossa Morena zone with Gondwanaland/Moroccan faunal affinities and the Central Iberian Zone with southern European, Armorican affinities. This suture is a possible location of the oceanic domain that opened in the Cambrian between Gondwanaland (or a northern Moroccan fragment separate from the main Gondwanaland mass) and N. Iberia/Armorica. The Badajoz-Cordoba Shear Zone had a complex history which may have included different rifting and oceanic closures within the Lower Palaeozoic, as indicated by the separate Silurian rift related assemblage, also believed to have originated there and now present in the allochthons of the N.W. Iberian massifs.

Figure 6.2.1c The Iberian terranes and five NW Iberian allochthonous complexes

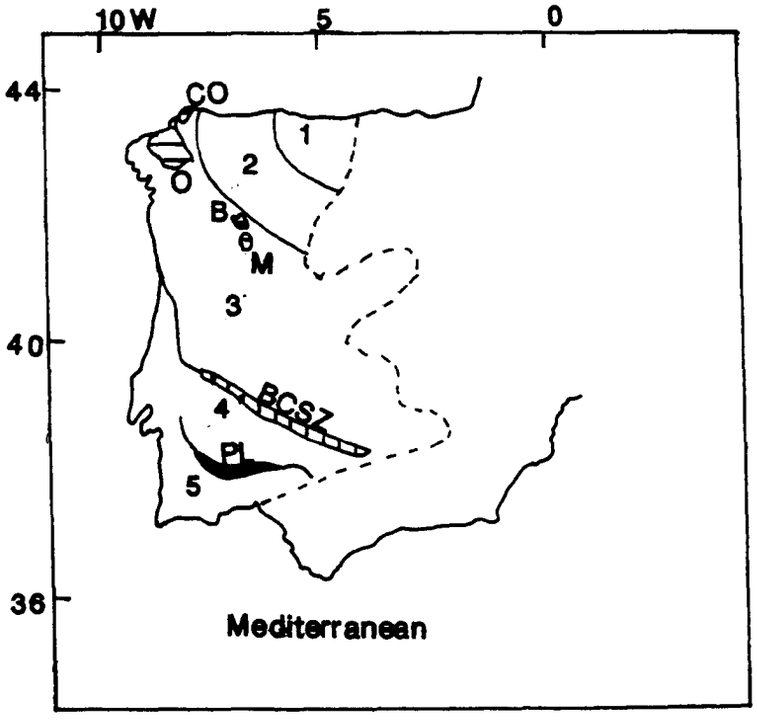

1. Cantabrian terrane, 2. West Asturian terrane, 3. Central Iberian terrane, 4. Ossa Morena terrane, 5. South Portuguese terrane. Allochthonous complexes: CO Cabo Ortegal, O Ordenes, B Bragança, M Morais. PL Pulo Lobo Ophiolite Zone, BCSZ Badajoz Cordoba Shear Zone. The rocks to the east of the dotted line are associated with the alpine orogenic cycle. The BCSZ marks a major separation between terranes to the north which have south European, Armorican affinities and those to the south which have sedimentary similarities to Gondwanaland,/Moroccan provinces. From Robardet and Gutierrez Marco (1990).

Final closure of a palaeozoic ocean between Armorica and Gondwanaland followed on an approximately W/SW to E/NE trend. This is associated with the Hercynian (Variscan) orogenic cycle. It culminated in continent-continent collision during late Devonian to Carboniferous times and the deposition of syn-orogenic turbidites in Central Iberian Zone basins. Ophiolite assemblages were obducted from the west onto the Central Iberian Zone and are now present within the Lower Allochthonous Thrust Complex of the N.W. Iberian massifs. By Late Devonian to Carboniferous times faunal differences between the terranes had been lost, marking their amalgamation as Iberia. The major granite magmatism seen in the Central Iberian zone and other terranes also originates from the latter part of the Hercynian orogenic cycle. Progressive deformation led to the tightening and arcuation of the

Ibero-Armorican arc giving its present U-shape profile (thesis introduction fig. 1).

Possible source regions for the ophiolite complexes of the N.W. Iberian massifs are the Badajoz-Cordoba Shear zone (though no ophiolites have been identified here) and the Polo do Lobo ophiolite zone between the South Portuguese and Ossa Morena terranes. However the origin of the UATC assemblage with harzburgite and granulites remains problematical, there being no obvious high grade metamorphic source outcrops with which it could be correlated. No evidence has been preserved within the Iberian autochthon for a destructive plate margin during the Lower Palaeozoic with which the chromite mineralisation of the UATC could be associated. What has been demonstrated by the regional geological studies summarised in this chapter, is that its emplacement is associated with obduction from the W/SW towards the E/NE of the ophiolite complexes over the Central Iberian Zone. Ribeiro *et al.* 1990b suggest that a possible western continental source region is the South Portuguese zone, perhaps in rocks now no longer exposed because of the Upper Palaeozoic cover.

In order to provide further information regarding the development of the Bragança and Morais, the next sections present the current state of knowledge of geochemistry, metamorphism and dating about these complexes.

6.2.2 Geochemistry of UATC granulites and eclogites

Eclogite and granulite samples from Cabo Ortegal and to a lesser extent Ordenes have been analysed geochemically by previous workers. Within the high grade assemblage, a clear distinction is present between granulites and eclogites in their REE profiles. Mafic granulites are characterised by LREE relative enrichment, having negative chondrite normalised slopes (Drury 1980, Van Calsteren 1978, Peucat *et al.* 1990). In contrast the eclogites show consistent LREE depletion and broadly positive chondrite normalised slopes (Bernard-Griffiths *et al.* 1985, Peucat *et al. op. cit.*). Bernard-Griffiths *et al.* (*op. cit.*) interpreted the eclogite LREE depletion as being the result of MORB magmatism at a constructive plate margin. On the basis of relative LREE enrichment (La/Sm = 3.25) and quartz normative compositions, Van Calsteren (*op. cit.*) proposed that the mafic granulites had continental tholeitic affinities. With similar results Peucat *et al.* (*op. cit.*) suggested that they were also compatible with an origin in a continental margin, arc setting. The latter interpretation is favoured here because it is consistent with creation above a destructive plate margin.

εNd values of +11.5 to +12.4, for various initial ages, obtained on eclogite samples fall within the range of modern MORB (Bernard-Griffiths *et al. op. cit.*). Peucat *et al.* (*op. cit.*) presented initial εNd ratios (for 480ma) of +1 to +10.2 for Ordennes and Ortegal mafic granulite samples. This greater spread of granulite results compared to the eclogites was interpreted as being due to an interaction between a mantle source of varying degrees of depletion and continental crust: such mixing occurring in an arc or intracontinental environment.

Eclogite geochemical analyses have pointed conclusively towards an oceanic origin. The origin of the granulites is more obscure but has to involve a continental provenance.

6.2.3 Metamorphism

Three main metamorphic episodes have been identified in the N.W. Iberian allochthonous massifs. The first is a prograde metamorphism up to a granulite and eclogite peak. The second phase gave rise to prograde amphibolite facies and locally eclogite facies metamorphism, this is in part coincident with retrogradation of the first cycle in other areas. A third metamorphic episode is seen within the lower nappes of the allochthonous complexes and ranges from greenschist facies in Galicia to a blueschist peak in Portugal.

Mafic granulite and eclogite asemblages from Ortegal have similar mineral assemblages: the granulite assemblage is characterised by clinopyroxene + pyralmandine + quartz + sodic plagioclase. ± hornblende.; eclogite has omphacitic pyroxene (Jad > 30%) replacing plagioclase. In describing these assemblages (Den Tex *et al.* 1972) also suggested that corroded staurolite relicts included within kyanite grains of eclogites demonstrated the prograde nature towards higher pressure of the eclogite metamorphism. Eclogites from Bragança are similar, with a peak pressure assemblage of garnet + clinopyroxene + jadeite (40 - 45%) + kyanite ± hornblende ± zoisite (Munhá and Ribeiro 1986). Mafic granulites from Bragança, described by Anthonioz (1972), have the general assemblage diopside + garnet + plagioclase + quartz + hornblende + rutile + ilmenite + calcite. Within the Bragança granulite assemblage recognizable original igneous enclaves of gabbros (*eg* Cabroes village) and garnet-pyroxenite layers (Alimonde village) are found (Anthonioz *op. cit.*).

In the massifs' high grade mafic assemblages the amphibolitisation stage is a strongly retrogressive metamorphism. Granulites developed abundant secondary hornblende and sphene, apatite and mica appear. In the Bragança UATC assemblages this amphibolitisation is associated with the blastomylonitisation phase (Munhá and Ribeiro 1986). Amphibolitised rocks can pass gradually into less retrograded granulites or eclogites (Gil Ibarguchi and Arenas 1990). Some parts of the massifs underwent prograde metamorphism up to amphibolite facies at about the same time. This phase is best developed in parts of the ophiolite units as at Morais, with the development of hornblende + plagioclase + epidote + garnet assemblages (Ribeiro 1974).

The previous metamorphic episodes are retrogressed in the third, greenschist facies phase, with the development of chlorite, actinolite, quartz and mica-bearing assemblages in mafic rocks. This is associated with localised mylonitisation and thrusting (Gil Ibarguchi and Arenas *op. cit.*). However in some parts of the Ortegal and Ordenes ophiolitic units and the lowest structural levels of the thrust piles above the autochthon this is the peak metamorphic phase. In Portugal the same phase of metamorphism reached a higher pressure facies. In lavas and volcaniclastic layers within the Silurian assemblage of the Lower Allochthonous Thrust Complex domain a mineralogical assemblage of glaucophane or crossite + epidote + phengite + chlorite has been described and allocated to blueschist

metamorphism (Munhá *et al.* 1984).

Pressure and temperature calculations for the NW Iberian massifs are plotted on fig. 6.2.3. The eclogite metamorphism is characterised by a high pressure gradient. Pressure and temperature estimates for the peak metamorphism of the Braganca eclogites are 18-20kb, 570-630°C followed by decompression to 16-17kb, 850-900°C (Munhá and Ribeiro 1986). These authors attributed such a low geothermal gradient to the rapid subduction of oceanic crust. Gil Ibarguchi and Arenas (1990) estimated >17kbar, 790°C peak for the massifs' eclogites.

The granulites are a lower pressure assemblage. Munhá and Ribeiro (1986) estimated pressure and temperature peaks of 11-12kb, 800-850°C for Bragança granulites. Bragança garnet pyroxenites were believed by Munhá (1986) to be mafic cumulates equilibrated in the upper part of the mantle at 10-12kb, 760-900°C. Gil Ibarguchi and Arenas (*op cit.*) estimated that the granulite equilibriation took place at 13.5kbar, >790°C for the Iberian massifs. The peak pressure of the amphibolite to eclogite metamorphic phase was >14kbar, 600°C for mafic eclogites from Malpica-Tuy (Gil Ibarguchi and Arenas *op. cit.*). Arenas *et al.* (1986) proposed 4-6kbar, 550°C peak for the retrogressive amphibolitisation. Bragança eclogites and granulites underwent a retrogressive amphibolitisation and blastomylonitisation together; at 4-8kb, 500-700°C (Munhá and Ribeiro *op. cit.*).

Blueschist metamorphism within the Lower Allochthonous Thrust Complex had a pressure maximum of 6kb, 400°C, followed by decompression to 3kb, 420°C (Munhá *et al.* 1984). Low geothermal gradients with peak temperatures following later in a cycle than peak pressures in blueschist facies metamorphism are associated with crustal thickening in nappe piles during continent collision events The contemporary greenschist metamorphic assemblage was created under a lower pressure gradient at 2.5-3.5kb, 375-425°C (Gil Ibarguchi *et al. op. cit.*).

In chapter 2 a blocking temperature range for the re-equilibration of Mg and Fe^{2+} between chromite cores and olivine grains of 500 to 630°C was calculated. This falls within the range of 500 to 700°C (4-8kb) at which blastomylonitisation and amphibolitisation of the UATC nappes occurred (Munhá and Ribeiro 1986). The alteration of chromite grain rim compositions and growth of Cr-bearing chlorite demonstrated in chapter 3 must postdate this phase and may be associated with final greenschist facies metamorphism. Any separate metamorphism of the harzburgite formation within the Bragança UATC ultrabasic assemblage prior to the mylonitisation and amphibolitisation phase is not recorded due to the intense nature of the retrogression.

Figure 6.2.3 Chromite Mg/Fe re-equilibration temperature in relation to the PT development of the NW Iberian Massifs

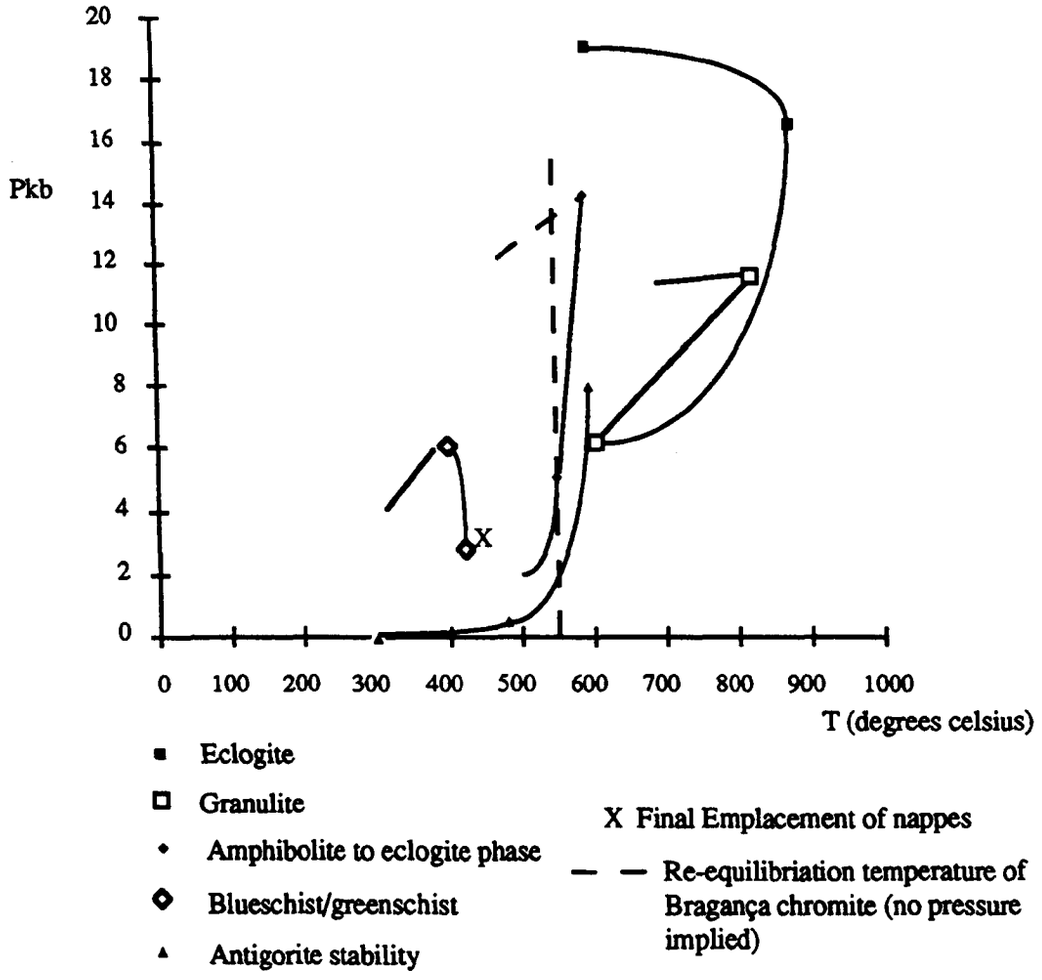

References: eclogite-Munhá and Ribeiro (1986); granulites-Munhá and Ribeiro (*op. cit.*); amphibolite-Gil Ibarguchi and Arenas (1990), Arenas *et al.* (1986); greenschist/blueschist-Munhá *et al.* (1984), Gil Ibarguchi *et al* .(*op. cit.*) .

Figure 6.2.3 shows the clockwise metamorphic paths of the different metamorphic phases within the NW Iberian massifs, compiled from various references. The main metamorphic episodes are eclogite, granulite, amphibolite (with an eclogite peak) and greenschist to blueschist. The eclogite (peak 18-20kb 570-630C Munhá and Ribeiro 1986) and granulite (peak 10-12kb, 760-900C Munhá and Ribeiro *op. cit.*) phases of metamorphism are retrogressed together in the third amphibolite phase. This is coincident with thrusting of nappes. In places the amphibolite phase is prograde and reaches an eclogite peak. The greenschist metamorphism coincides with the final emplacement of the nappes during the Hercynian orogeny; in Portugal this phase reaches a blueschist peak (6kb 550C, Munhá *et al.* 1984).
Also plotted are the stability curves for antigorite and a vertical line through the temperature (500-630C) at which the chromite and olivine compositional equilibration took place. The latter temperature coincides with the amphibolitisation of the high grade rocks. This may also have been close to the beginning of serpentinisation.

6.2.4 Dating of the UATC

6.2.4.1 Radiometric ages

Radiometric dating of the massifs' lithologies gives consistently Palaeozoic ages. A K/Ar date of 900±30Ma obtained on an eclogite specimen from Cabo Ortegal (Vogel and Abdel-Minem 1971) has been discounted by later work. Fig. 6.2.4.1 shows the ranges of metamorphic ages obtained from different units within the massifs; four age groups may be distinguished. The oldest age group, shown by U/Pb dating which has not been reset by subsequent retrogradation, clusters around 480-490Ma - L. Ordovician (*eg* Peucat *et al.* 1990). This corresponds to the high grade eclogitic and granulitic peak metamorphism. There remains the possibility of magmatic precursors to the eclogites predating this age. The second grouping occurs at about 420Ma (M. Silurian) which Peucat *et al.* (*op. cit.*) associated with the prograde amphibolite to eclogite phase of metamorphism. Dallmeyer and Gil Ibarguchi (1990) showed $^{36}Ar/^{40}Ar$ versus $^{39}Ar/^{40}Ar$ ratios which gave ages of 384±5.2 and 392.4±7.3Ma ages for amphibole concentrates from metabasic and ultrabasic rocks of the lower (Remondes - Izeda) and upper units (Monte de Morais - Talhinhas) respectively of the Morais ophiolite complex. These dates form part of the third age group at about 390Ma (Early to Mid Devonian) associated with amphibolitisation. A clustering of 21 K-Ar dates at this age for the mafic and ultrabasic rocks of Cabo Ortegal (Van Calsteren *et al.* 1979) marks the amphibolitisation related to Hercynian thrust emplacement. The greenschist-blueschist metamorphic episode, related to the continuing thrusting and mylonitisation within the massifs, is shown by dates around 350Ma. These dates have been determined by Rb-Sr dating on micas (Peucat *et al. op. cit.*) and mafic granulite whole rocks (Van Calsteren *et al. op. cit.*).

Figure 6.2.4.1 Radiometric age groups of the metamorphic phases

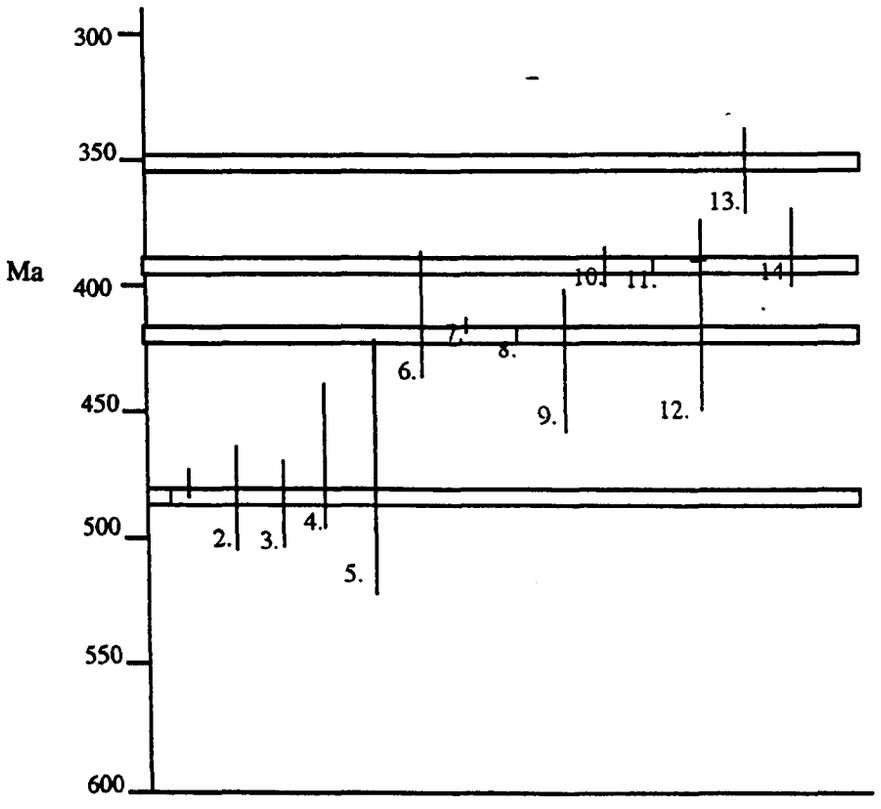

The vertical lines on the figure are the total age ranges, including error bars given in the references. There are four main age groups: 480-490Ma, 420Ma, 390Ma and 350Ma. These groupings are shown by the horizontal bars. The dash on line 12 represents a cluster of data points. The first grouping corresponds to the eclogite and granulite facies metamorphisms; the second and third to the amphibolite/eclogite facies phase and the fourth to the greenschist metamorphism.

1. Eclogites from Ortegal (480±5ma U-Pb) 2. Granulites from Ortegal (two samples 482±7 497+11/-13ma U-Pb) 3. Granulites from Ordenes (489+17/-19ma U-Pd) 4. Orthogneisses from Malpica Tuy (466±30ma) 5. Volcanics from Macedo de Cavaleiros (473±49ma Rb-Sr) 6. Mellid orthogneisses from Ordenes 409±24 Rb-Sr) 7. Ortegal banded gneiss metasediment? (417+3/-2ma U-Pb) 8. Ortegal Chimpara gneiss metasediment 422±4ma U-Pb). 9 Morais ophiolite (upper part 431±27.3ma Ar/Ar 10. Morais ophiolite (lower part 397±4ma Ar/Ar) 11 Ortegal garnet pyroxenite granulite (392±4ma U-Pb) 12 Ortegal Range of 21 mineral dates clustering around 390ma (K-Ar, Rb-Sr) 13 Ortegal granulites (354±17ma Rb-Sr) 14 Ortegal Amphibole separates from diffrent formations (370-397.5 range Ar/Ar).

1, 2, 3, 7, 8, 11, 14 from Peucat *et al.* (1990); 4, 6, 12, 13 Van Calsteren *et al.* (1979); 5 Ribeiro *et al.* (1985); 9,10 Dallmeyer and Gil Ibarguchi (1990).

6.2.4.2 Dating from fossils and field relations

Before much radiometric dating was available for the high grade assemblages of the N.W. Iberian Massifs, Ries and Shackleton (1971), Anthonioz (1972) and Ribeiro (1974) believed them to be of Precambrian age. Evidence for Precambrian ages in the upper nappes of the N.W. Iberian massifs (the granulites, eclogites ultrabasics, Lagoa formations) was put forward on the basis of observed field relations within the Morais massif by Ribeiro *et al.* 1990a), that can be summarised as follows. The Lagoa metasediment schist has previously been dated with fossil acritarchs at Lower Ordovician to Upper Cambrian (Arenas *et al.* 1986). The Lagoa gneiss, interpreted as the sediment's granitic basement, contains an occasional tectonite fabric thought to predate that of the schists. This implies that a foliation existed in the gneisses before the sediment's deposition. On the basis of this apparent time gap a Precambrian age was assigned to the Lagoa Gneisses. The Lagoa Gneiss is believed by Ribeiro *et al.* (*op cit.*) to be the upper part of a section through the lithosphere preserved within the UATC, lower parts of which are the mafic granulites and chromitite-bearing peridotites. Thus a Precambrian age was allocated for the high grade assemblage, including the ultrabasic rocks. On the basis of the radiometric dating summarised previously, it seems clear that a 480-490ma event associated with granulite and eclogite facies metamorphism occurred which the field relations above cannot account for. A Precambrian age for the granulite assemblage now seems unlikely. Despite this there remains a possibility of pre-480-490Ma ages, for some parts of the UATC assemblage such as magmatic protoliths to the eclogites and the chromitite-bearing formation.

6.2.5 Geological setting of the UATC ultrabasic assemblage

From the above accounts of chronological, geochemical, structural and petrographic research into the Iberian terranes and the allochthonous massifs a number of matters in the evolution of the UATC ultrabasic rocks can be more precisely defined. At 480-490ma parts of the UATC assemblages underwent a high grade metamorphic episode associated with a continent-continent collision. MORB protolith rocks, emplaced by subduction deep (as much as 60km) into the lithosphere of a continental destructive margin underwent eclogite facies metamorphism. The destructive plate margin may have been located in a western continental unit that was linked to Gondwanaland or Morrocan terranes, separated by an oceanic domain from the Central Iberian/Armorican land mass to the east. Magmatism within the lithosphere at this time gave rise to the mafic granulite assemblage. Subsequent amphibolitisation related to thrust emplacement, over the ophiolite assemblages and Lower Allochthonous Thrust Complex and across the Central Iberian Zone, occurred at 390ma. Prior to this there is no direct evidence linking the UATC assemblage to the rest of the Iberian terranes orogenic evolution. The ultrabasic rocks have a common metamorphic history with the granulites and eclogites at least from 390ma onwards when

amphibolitisation occurred.

Two possibilities for the location of the 480-490ma destructive continental margin are the Badajoz-Cordoba relict suture or between the South Portuguese and Ossa-Morena zones. In either case, it was associated with the Gondwanaland and Moroccan affinity terranes rather than the Central-Iberian/Armorican side. Ophiolite assemblages of this age have not been preserved; the Silurian and Devonian rift and ophiolite assemblages found in the lower nappes of the N.W. Iberian massifs are fragments from a later oceanic formation event probably sited along the Badajoz-Cordoba shear zone.

In chapters 3 and 4 it was proposed that the dunite and chromitite bodies had crystallised from olivine-rich melts of boninitic affinity. The following section outlines how this may be related to a destructive plate margin.

6.2.6 Melts of boninitic affinity

Boninite magmas have high SiO_2, >53%, $Mg^{2+}/(Mg^{2+}+Fe^{2+})$ ratios >0.6 and enrichment in certain elements including LILE and Pd. They are thought to be derived from the hydrous, shallow melting (<50km depth) of an already depleted mantle (Crawford *et al.* 1989). Boninite melt derived rocks are found in four main tectonic settings: fore-arc *eg* Marianas; destructive continental margins *eg* Baja Mexico, Setouchi SW Japan; intra-ocean and back arcs preserved in ophiolites *eg* the Troodos Upper Pillow Lavas and the ultramafic portions of Precambrian layered intrusions *eg* Bushveld and Stillwater. The association of boninites with the early extensional stages of subduction, or immediate post-subduction, rather than the later high pressure continental collisions is shown by their presence in back-arc oceanic crust. The term boninite covers a wide range of other, older terms including "low-Ti ophiolitic basalts", "high-Mg andesites", "magnesian quartz tholeites" and "komatiitic basalts". The boninite suite has been subdivided into high and low Ca groups by Crawford *et al.* (*op. cit.*). High Ca boninites have SiO_2 <56%, CaO/Al_2O_3 >0.75 and chromite grain Cr/(Cr+Al) ratios of 0.65-0.85. An example of such magmas is the Troodos Upper Pillow Lavas. Low Ca boninites have SiO_2 <56%, CaO/Al_2O_3 0.5-0.75 and chromite grain Cr/(Cr+Al) ratios of up to 0.98. The low-Ca group includes samples from Setouchi SW Japan, Baja Mexico, the Cape Vogel islands and the Bonin islands. Many boninite suites have olivine of Fo >88, NiO >0.4wt%, and together with chromite Cr/(Cr+Al) ratios of up to 0.98, these refractory compositions suggest that some boninites are candidates for primary melts, formed in equilibrium with residual mantle (Umino and Kushiro 1989). In this regard, experimental evidence has shown that at about a 35% degree of melting of a pyrolite under water-saturated conditions, at 1200°C and 10kbar, a melt with boninitic characteristics (54% SiO2, 14% MgO, $Mg/Mg+Fe^{2+}$ ratio of 0.73) is created (Green 1976). In contrast however, Saunders *et al.* (1987) suggested that Cenozoic lavas of boninitic affinity from Baja, Mexico had been created from the reaction of a melt derived from subducted oceanic lithosphere with the overlying mantle wedge.

A melt to be associated with the Bragança dunite bodies must have both picritic (*ie*

olivine-rich) and boninitic affinities. Experimental work (Umino and Kushiro 1989) on the melting relations of a boninite sample (CH414) from the Bonin Islands has shown the presence of an olivine + liquid field around 8-10kb and 1150^{0}C-1160^{0}C (fig. 6.2.6a) under water-saturated conditions. This sample has the characteristics of low-Ca boninites, with CaO/Al_2O_3 ratios <0.75 (Crawford *et al.* 1989). This experimental evidence shows that the formation of dunite bodies from rising primary boninitic melts within the hydrated mantle is feasible.

Figure 6.2.6a Melting relationships of low-Ca boninite

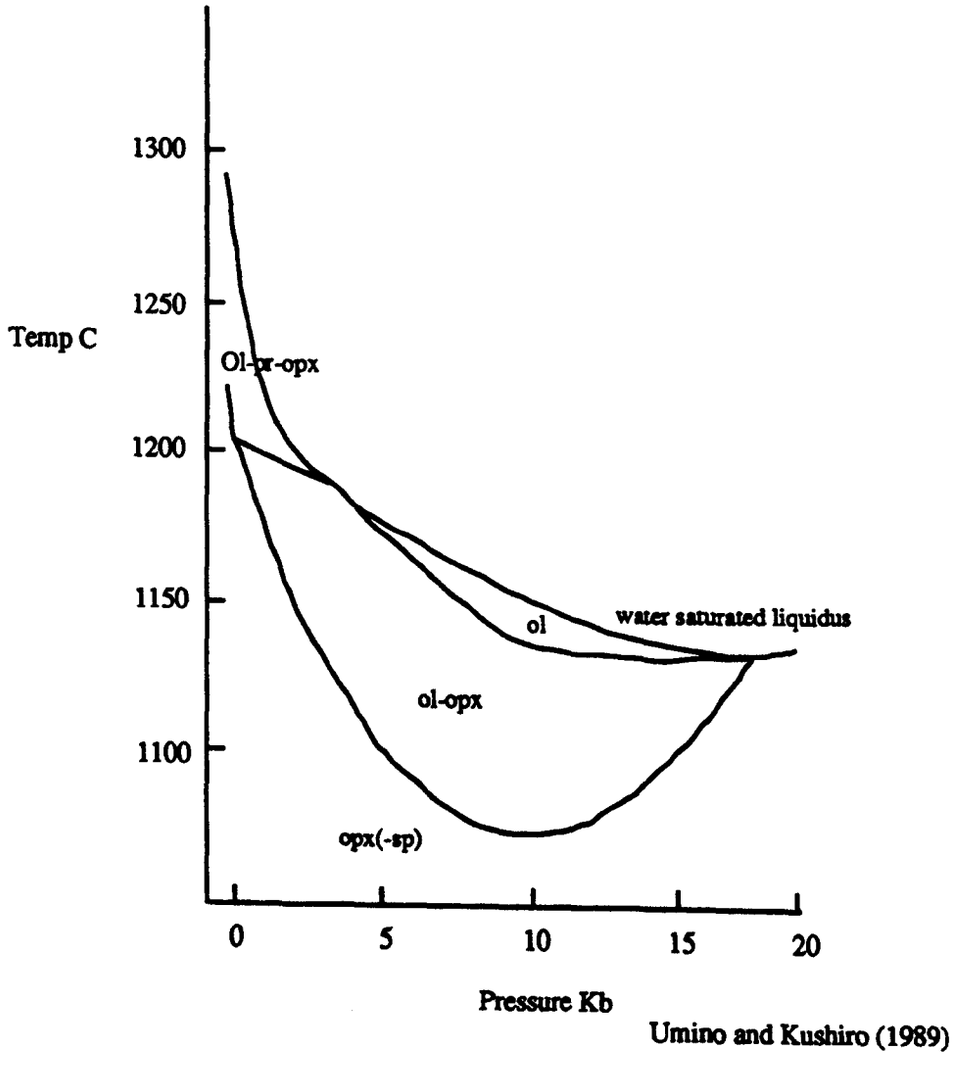

Figure 6.2.6a shows the liquidus relations of sample CH414 boninite (Bonin islands) from Umino and Kushiro (1989). The conditions are water-saturated (about 5wt% water). Centring around 8-10kb and 1160-1150 C, olivine is the only crystallising phase. Thus it is possible that dunitic bodies could crystallise from such a melt, which is of the low-Ca boninite type, early in the magmas evolution, at depths of 25-30km.

Figure 6.2.6b Normative mineral compositions for boninite melts

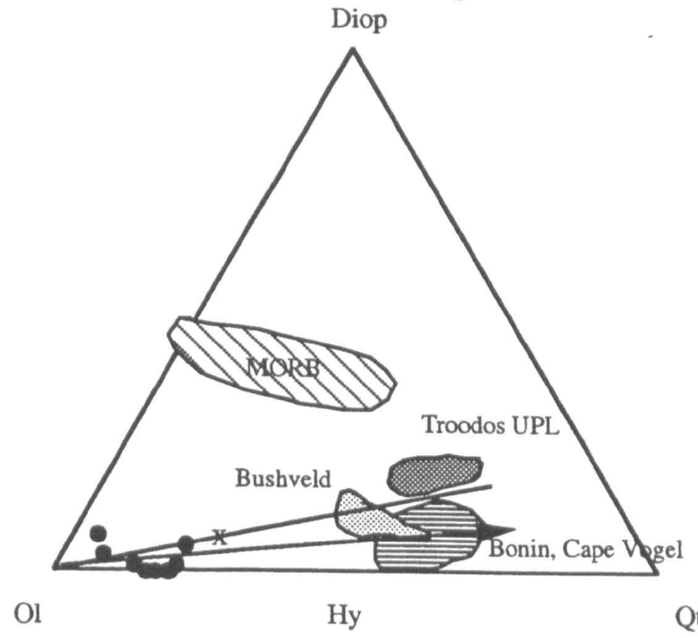

This section through a simplified basalt tetrahedron shows an olivine control line drawn through the Bragança sample compositions (source) into the field for boninitic melts. No partial melt composition can lie to the right of an olivine control line extrapolated through the source composition to the olivine apex (Green *et al.*1987). This means that a partial melt composition associated with the Tinaquillo lherzolite (likely MORB -type source) cannot be a source for most low-Ca boninites. In contrast most of the Bragança samples are likely sources for low-Ca boninites. From Crawford *et al.* (1989).
Nine Bragança hazburgite formation samples are plotted on the above diagram. The compositions were obtained by recalculation of olivine, diopside and quartz (after Walker *et al.* 1979) from whole rock analyses in appendix 7. All dunite/harzburgite samples with available analyses were plotted apart from those with high totals (>103wt%).

● Bragança sample

x Tinaquillo lherzolite, fields for MORB, Bushveld sills (low Ca boninites), Troodos Upper Pillow Lavas (high Ca boninites), Bonin islands and Cape Vogel (low Ca boninites) as indicated on diagram.

——► Olivine control line for Bragança samples

——— Olivine control line for Tinaquillo lherzolite

Crawford *et al.* (1989)

As low-Ca boninites are produced within mantle source regions which have undergone a high degree of melt extraction, by the model of Crawford *et al.* (*op. cit.*), the composition of the source can give information about the types of melts which may be derived from it. Fig. 6.2.6b shows the regions for MORB and boninite magmas drawn on an olivine-quartz-diopside projection of the basalt tetrahedron. The boninite magmas are of high-Ca type: the Troodos Upper Pillow Lavas and low-Ca type: the Bushveld samples, Bonin islands and Cape Vogel. Also plotted are four samples of the Bragança harzburgite formation, a likely MORB source lherzolite (Tinaquillo peridotite) and olivine control lines through these samples and the olivine apex (from Crawford *et al.* 1989). No partial melts may lie to the left of an olivine control line through a source composition and the olivine apex (Green *et al.*1987). This means that the Tinaquillo peridotite cannot be the source for most low-Ca boninites as it does not have a refractory enough composition. In contrast, the Bragança samples are a potential source composition for low-Ca boninites.

An example of the production of melts with boninitic affinity at a continental margin of the present day is present in the Baja peninsular of California (fig. 6.2.6c). From 29Ma, the predominant magmatic activity in this province had a calc-alkaline signature. Since 12Ma, coinciding with the cessation of subduction beneath Baja by the Pacific plate, the magmatism has had boninitic ("Bajaite") affinities (Saunders *et al.* 1987). The lavas produced have a maximum SiO_2 of 59%, a CaO/Al_2O_3 ratio maximum of 0.8 and $Mg/(Mg+Fe^{2+})$ ratios of up to 0.78.

Figure 6.2.6c Plate tectonic development of the Eastern Pacific during 29Ma-0Ma and location of boninitic affinity lava eruptions

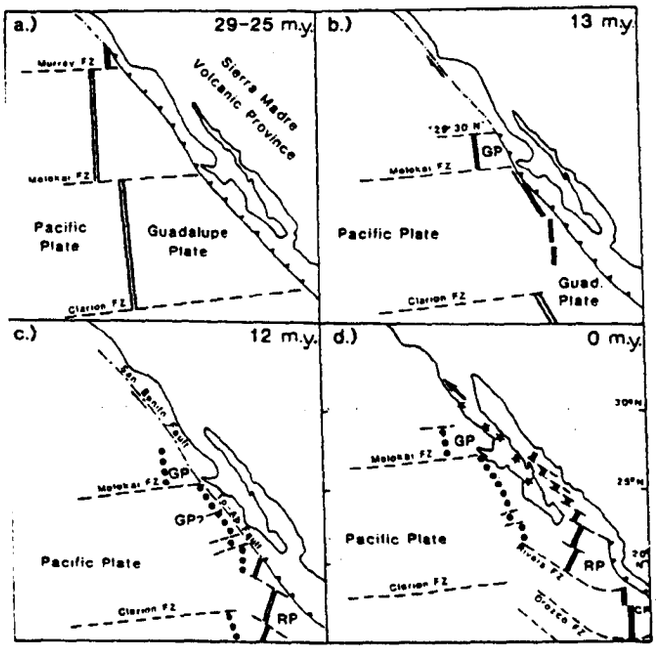

Saunders *et al.* 1987

The Baja peninsular of Mexico shows the development of a destructive continental margin from 29Ma to recent, when subduction ceased. Recent magmatic activity in Baja has boninitic affinities. (a) 29Ma the Guadelupe Plate was being subducted beneath the Baja Peninsular. The volcanism at this time was calc-alkaline. (b), (c) 13-12Ma The Pacific/Guadelupe spreading ridge meets the subduction trench; the spreading ridge is abandoned or subducted and the Tosco-Abreojos transform fault is created at the site of the former subduction zone. (d) 12-0Ma Boninite affinity lavas ("Bajaites") erupted in Baja. This boninite magmatism is developed during a relatively early phase of a destructive plate margin's development.
Gp Guadelupe plate, Rp Rivera Plate, To-Ab fault=Tosco-Abreojos fault, filled circles=abandoned spreading centre, stars="bajaite" lava fields.

6.3 A model for the geological setting of the Bragança and Morais UATC ultrabasic assemblage

The residual mantle and peridotite cumulates identified in the Bragança and Morais UATC (Upper Allochthonous Thrust Complex) are linked to the development of a destructive continental plate margin prior to 480-490ma. The subduction zone was situated close to the Gondwanaland/Moroccan land mass, possibly between the South Portuguese and Central Iberian zones or along the then eastern margin of the Ossa-Morena zone. Figures 6.3a-d are schematic cartoons of the development of the ultrabasic assemblage at a destructive plate margin and emplacement of the allochthonous thrust complexes. Figs. 6.3c,d are simplified after Ribeiro *et al.*1990b.

Within the upper 30km of the mantle wedge, an influx of fluid from the subducted oceanic crust and a high heat flow inititiated partial melting of an already depleted peridotite. This picritic melt was drained through conduits within which olivine and chromite crystallised. The chromite grains in the dunite/chromitite bodies have high 100Cr/Cr+Al ratios, clustering around 75. This suggests boninitic affinities to the melts from which the chromite bodies were derived. The highly refractory composition of the resulting residual mantle (harzburgite) is also consistent with the extraction of low-Ca type boninitic melts. In chapter 5 it was shown that the harzburgite formation contained a sulphide phase with a relatively high Pd tenor. The picritic melts derived from the residual mantle similarly have a high content of Pd relative to sulphide, as shown by their Pd/Cu ratio. This is consistent with the model of Hamlyn *et al.* (1985) and Hamlyn and Keays (1986) who proposed that boninitic melts characterised by high Pd and low Cu contents were obtained from a high degree of melting of a mantle source region which contains a residual Pd-enriched sulphide phase. The chromitite bodies acted to concentrate and fractionate the PGE within the ascending melts. This was achieved by a drop in solubility of the PGE associated with the localised high oxygen fugacities present during chromitite formation. As Pt remains more soluble under these conditions, it was incorporated into mineral phases at a later point during chromite grain crystallisation, with the Pt-bearing PGM now being found at the margins of or in between chromite grains.

The dunite and chromitite bodies of ophiolites are thought to be created in the top 30km of mantle (Gass 1990). This is consistent with the presence of an olivine-only stability field for low-Ca type, water saturated boninitic melts between 8-10kb (Umino and Kushiro 1989). Many of the processes that have operated in Bragança may be analagous to those of supra-subduction zone ophiolites so the chromite bodies described in this thesis may have originated at such depths as well. The peridotitic and gabbroic/troctolitic cumulate formations of the Morais UATC were probably created above this section of mantle. There is no definitive evidence for a genetic link between these cumulates and the harzburgite

formations but their similar structural position with regard to the other lithological units in Bragança and Morais (as deduced by Anthonioz 1972 and Ribeiro 1974) makes this very likely.

The granulite assemblage has been shown by Peucat *et al.* (1990) and others to have originated during a high pressure collisional event in a continental setting. This relatively late stage during the destructive plate margin's development at 480-490ma postdates the early dunite/chromitite formation related genesis of the ultrabasic asemblage previously described. This phase of high pressure crustal magmatism is distinct from the boninite melt generation with which the main ultrabasic rocks were associated.

Figure 6.3a Cartoon of subduction at Gondwanaland continental margin, Pre 480-490ma

Gondwanaland/Morocco (Ossa Morena and South Portuguese terranes?) – South Europe ?

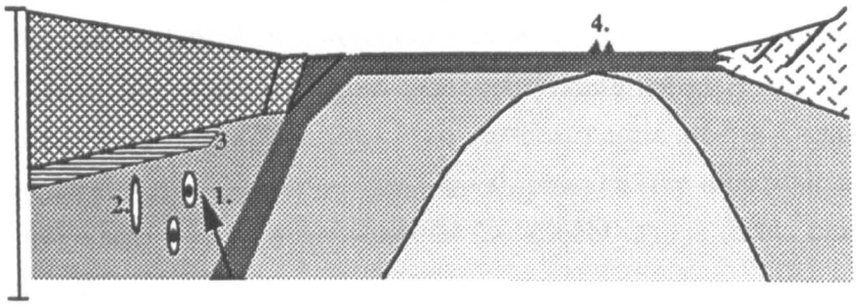

30km

1. Water and volatiles released from subducted oceanic crust into the mantle wedge of continental margin. **2.** Partial melting of already depleted mantle (with high Cr/Al ratio and Pd sulphide tenors) leads to the extraction of an olivine-rich melt with boninitic affinities. The dunite with chromitite bodies are the first crystallisation products of this melt; chromite has high Cr/(Cr+Al) ratios, and Pd is enriched relative to the sulphide content. The depleted mantle has a low opx harzburgite modal composition. **3.** Peridotitic and occasional gabbroic/troctolite cumulates formed in lower continental crust. **4.** The suture between the Central Iberian and Ossa Morena zones was reactivated at different times during the Palaeozoic. An ophiolite associated with the phase of subduction shown in the diagram is not preserved, though eclogite in the UATC is likely to have been derived from this subducted oceanic crust.

Figure 6.3b 480-490Ma Continent collision between west or south-westerly and east or north-eastern continental domain

W/SW E/NE

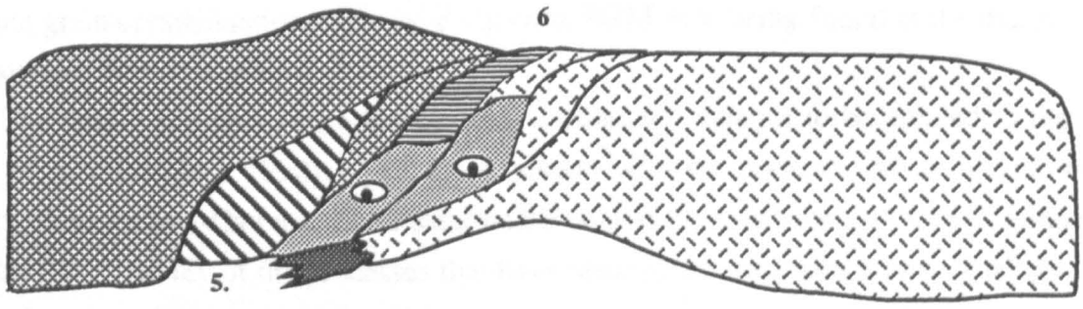

5. Granulite magmatism within the lower crust. **6.** Suture

Figure 6.3c Silurian re-activation and rifting along suture zone.

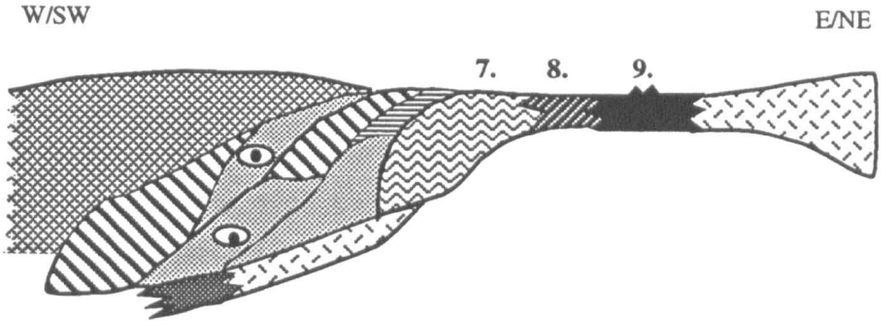

7. Continental margin **8.** Rifting-alkaline magmatism **9.** Ocean basin

Figure 6.3d Schematic rock relation diagram of thrust pile of NW Iberian massifs within Central Iberian Zone after late Devonian-Carboniferous collision

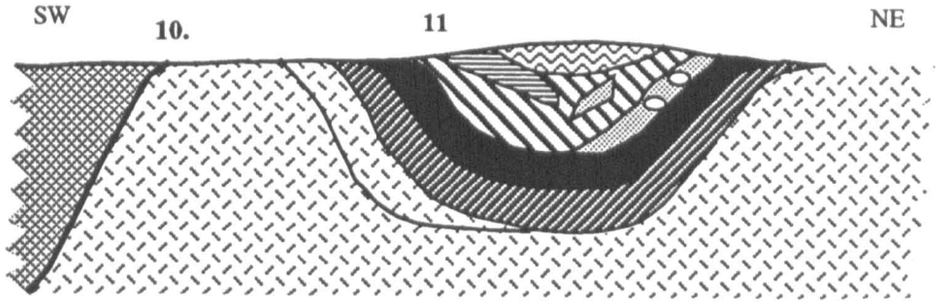

After Ribeiro *et al.* 1990a

10. Badajoz-Cordoba Shear Zone **11.** Thrust pile of the five N.W. Iberian massifs from Parautochthonous Thrust Complex to Upper Allochthonous Thrust Complex.

Key to Figures 6.3a-d

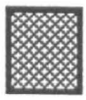
Gondwanaland zone/Ossa Morena terrane.


South European zone/Central Iberian terrane

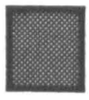
Ordovician ocean crust

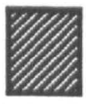
Silurian rift-related assemblage/Lower Allochthonous Thrust Complex.


Silurian/Devonian oceanic crust/ Ophiolitic Thrust Complex


Granitic gneiss and schist (Lagoa formations of Upper Allochthonous Thrust Complex)


Peridotite cumulates with minor troctolite/gabbro in Morais Upper Allochthonous Thrust Complex


Granulites/ Upper Allochthonous Thrust Complex assemblage


Harzburgite with dunite/chromitite mineralisation of Bragança Upper Allochthonous Thrust Complex

Chapter 7 Conclusions

The ultrabasic assemblage of the Upper Allochthonous Thrust Complex (UATC) in Bragança and Morais is the highly tectonised fragment of an upper mantle and lower crustal section of lithosphere formed at a destructive continental margin. Within the ultrabasic assemblage, the main rock type is a low-orthopyroxene harzburgite. This contains layers of websterite, clinopyroxenite, hornblendite and a separate chromitite-bearing dunite. All the olivine-bearing lithologies have undergone varying degrees of serpentinisation. The ultrabasic UATC samples from the Morais massif have a different mineralogy and composition from those of Bragança. At Vinhas the ultrabasic assemblage consists of serpentinised and mylonitised peridotite. At Caminho Velho small bodies of troctolite and metagabbro are present as well. The troctolite contains poikilitic textures typical of cumulates.

During the tectonic emplacement of the Bragança complex, the high strain imposed a porphyroclastic to mylonitic fabric upon the ultrabasic assemblage. Pyroxenite layers were boudinaged and thinned, creating a tectonic mixture of pyroxenite and harzburgite over much of the Bragança outcrop. The most massive chromitite was created from the boudinage of chromitite layers within dunite. The chromitites have taken on an annealed texture with polygonal grain boundaries as a result of this high strain deformation.

The pyroxenite layers (websterite and clinopyroxenite) within the harzburgite formation have been amphibolitised to varying degrees. An isochemical amphibolitisation within the websterites is shown by the alteration of diopside to tremolite or magnesium-hornblende in some samples. Amphibolitisation associated with metasomatism is present in the clinopyroxenite/hornblendite layers. These contain abundant apatite and sphene. Diopside grains are seen to alter in patches to ferroan-pargasitic hornblende. Where this alteration is complete, no diopside remains and the pegmatoidal hornblendite layers are created. Amphibolitisation occurred during the strain-induced recrystallisation of the UATC assemblages; diopside and enstatite within the pyroxenites and harzburgite contain deformation lamellae and kink bands, whereas the amphiboles occur as largely strain free neoblasts.

There is a transition from discrete amphibolitised pyroxenite layers to small clusters or disseminations of amphiboles within the harzburgite formation. This and the similarity in composition (tremolite to magnesian-hornblende) of both amphibole sets, suggests that the occasional amphiboles (originally diopside) within the harzburgite samples and the pyroxenite layers have a common origin. The crystallisation of dispersed pyroxenes and pyroxenite layers would postdate the creation of the harzburgite and dunite/chromitite formations. This relationship is often concealed by the high strain fabric present across much of the ultrabasic outcrop which has caused the disaggregation of discrete pyroxenite layers or clusters.

characteristic of depleted mantle assemblages formed in supra-subduction zone settings. The Morais UATC ultrabasic sample whole rock compositions are less depleted in Ti and Al than the Bragança residual formation. Major element plots of these peridotite samples are consistent with derivation from a liquid that has crystallised olivine and pyroxene. Similar trends have been produced for wehrlites derived by accumulation of olivine and pyroxene grains from the Cyprus ophiolite (Murton 1988).

Accessory chromite grain compositions from the Morais UATC have greater Ti/Fe ratio variation compared to the accessory chromites of the Bragança harzburgite formation. Ti/Fe variability of chromite grains is characteristic of crustal derived ultrabasic rocks compared to the low Ti/Fe variability of mantle derived chromite (Neary 1974). The harzburgite formation contains olivine with highly refractory compositions (Fo_{92-94}), which are typical of residual mantle assemblages.

Chromite grain composition also gives information about primary crystallisation and later alteration histories of the Bragança dunite/chromitite formation. The Mg and Fe^{2+} contents of the chromite grains and co-existing olivines re-equilibriated at temperatures of between 500 and 630°C. This overlaps with the temperatures inferred for the amphibolitisation of the complex (Munhá and Ribeiro 1986). Lower temperature alteration associated with chloritisation and serpentinisation has led to a zonation of chromite grain composition. In some chromite grains there is a depletion in Al and Mg, and an enrichment of Cr, Fe, Ti and Mn towards the grain margins. This is a transition towards the creation of ferritchromit at grain rims and crack margins. These alteration patches are not regular in size or distribution. The core compositions of Cr and Al are not affected by this compositional zonation or re-equilibriation with the co-existing olivine. The 100Cr/(Cr+Al) ratios (clustering around 75) of the chromite grain cores suggest a boninitic affinity for the melts from which the dunite/chromitite formation was derived.

Although the silicate assemblage is depleted, samples contain a high tenor of Pd relative to the sulphide content. Pd has been retained to a large extent relative to S-which is very scarce in the harzburgite samples-during the extraction of partial melts. This has created relatively high Pd concentrations within the remaining base-metal sulphide and high Pd/Cu whole rock ratios. The chromite-rich samples, which are thought to be associated with melt derived from the main ultrabasic formation, also have high Pd/Cu ratios. This is a characteristic of melts with broadly boninitic affinities.

Low-Ca type boninites contain a field of olivine-only crystallisation between 8-10kb under water-saturated conditions (Umino and Kushiro 1989). Thus the formation of a picritic (*ie* olivine-rich) melt with boninitic affinities, is possible within 30km depth. This melt was derived from depleted mantle with a high Pd content relative to sulphide. The normative mineral composition of some of the harzburgite formation samples is consistent with their being the source for low-Ca type boninites.

The crystallisation of chromitite has acted to fractionate the PGE within the picritic melts. Ru, Os and Ir start to be incorporated as laurite and irarsite platinum-group minerals

melts. Ru, Os and Ir start to be incorporated as laurite and irarsite platinum-group minerals (PGM) during the early part of the chromite grain's crystallisation. This is shown by their textural location throughout the chromite grains. Pt is clearly fractionated from Ru, Os and Ir as demonstrated by the location of Pt-bearing arsenides and sulpharsenides only at the margin of chromite grains or within the silicate matrix. Positive chondrite normalised PGE plots for some samples also demonstrate this fractionation. This mineralogical zonation, also noted in other chromitite-bearing complexes, is regarded as primary in agreement with Prichard and Tarkian (1988), Prichard and Neary (1991) and in contrast to Thalhammer *et al.* (1990). A secondary PGE mineralogical assemblage was created under conditions of low S fugacity during serpentinisation. Heazlewoodite and magnetite is the stable base-metal sulphide assemblage, replacing pentlandite. The Pd and some Pt was released during breakdown of the pentlandite. This led to the creation of Pt- and Pd-bearing alloys. The PGE are essentially immobile during serpentinisation, with only limited remobilisation occurring within samples.

The control on mineralisation of the five PGE Os, Ir, Ru, Rh and Pt is chromite crystallisation. Under the conditions of fO_2 likely during crystallisation of the chromitite bodies Pt is considerably more soluble within silicate melts than Ir (Amossé *et al.* 1989). This is considered to be the explanation for the fractionation of the PGE, with Pt starting to be incorporated into minerals after Ru, Os and Ir. Pd has separate controls on its mineralisation linked to the base-metal sulphide assemblage. This is illustrated by the change in slope at the Pd end of chondrite normalised graphs and by the association of some of the Pd-bearing minerals (Pd-S, Pd-Hg, Pt-Pd-Cu)with the base-metal sulphide.

The combined petrographic and geochemical characteristics of the Bragança and Morais UATC ultrabasic assemblage summarised here are consistent with formation as residual mantle and cumulate sections within the upper 30km of the lithosphere in a supra-subduction zone setting. The regional studies described in chapter 6 suggest that the probable source region for the UATC assemblage is at a destructive continental plate margin located between Gondwanaland or Moroccan related terranes (represented now by the South Portuguese and Ossa-Morena zones) and Armorican, southern European terranes (the Central Iberian zone). A collision associated with the creation of the high pressure granulite assemblage in the lower crust occurred at 480-490ma. This postdates the creation of the chromitite mineralisation and the Morais UATC cumulates. Subsequently the ultrabasic assemblage has a metamorphic history in common with the relict granulite assemblage, both are amphibolitised at 390ma. Final thrust emplacement from the west, over the Central-Iberian zone and a Silurian to Devonian ophiolite assemblage, at 350ma is part of the Hercynian orogenic cycle.

The flow diagram (fig. 7.1) summarises the sequence of events in the evolution of the Bragança and Morais UATC ultrabasic assemblages.

Figure 7.1 Summary of UATC ultrabasic rocks evolution

	Chromitite/Dunite Mineralisation	Platinum-Group Elements in chromitite	Harzburgite formation
Early Stage in destructive plate margin, pre480-490 Ma	Dunite and chromitite crystallised from olivine-rich melts with boninitic affinities within melt conduits in upper 30km of lithosphere. Derived from depleted source with high Cr/Al ratio.	PGE concentrated from melt with chromite. The $fO2$ conditions within chromite lead to a fractionation of the PGE. Pt is incorporated into sulphides and sulpharsenides (platarsite-sperrylite) after Ru, Os, Ir (laurite-irarsite). Pd mineralisation in solid solution within pentlandite and not controlled by the fractionation trend. Relatively high Pd/Cu ratio maximum due to boninitic affinity of the melt.	Melt removal within conduits leaves highly depleted silicate formation of harzburgite. Scarce sulphide phase remains into which much of Pd partitioned leaving progressively higher tenor of this element as formation undergoes melt extraction.
High pressure collisional stage 480-490Ma	Any effects of high pressure metamorphism (as shown by granulites) not preserved due to intense retrogradation in later phases.		
Amphibolitisation and thrusting 420-390 Ma	High strain leads to annealed, polygonal fabric. Mg and Fe2+ re-equilibration down to 500-630C.	Minerals included within chromite grains take polygonal outlines in response to the high strain imposed	Diopside amphibolitised to tremolite/Mg-horn blende.
Greenschist metamorphism and serpent. 350ma associated with continuing thrusting.	Irregular remobilisation of chromite towards grain margins, Al, Mg loss. Creation of pull apart cracks.	Breakdown of pentlandite to heazlewoodite and magnetite. Creation of PGE alloys and Pd-S grains. Limited remobilisation of S.	High degree of serpentinisation and mylonitisation. Formation of tectonic mix and axial planar fabric of the different formations in the ultrabasic assemblage.

Figure 7.1(cont.) Summary of UATC ultrabasic rocks evolution

	Morais UATC	Pyroxenite Layers
Early Stage in destructive plate margin, pre-480-490 Ma	Formation of peridotitic cumulates with occasional bodies of troctolite and gabbro overlying mantle sequence. Relationship to dunite/chromitite mineralisation not clear.	Websterite and clinopyroxenite layers and more diffuse aggregates created within mantle assemblage. Postdates chromite mineralisation and harzburgite creation but age relationship to other formations not clear.
High pressure collisional stage 480-490Ma		
Amphibolitisation and thrusting 420-390Ma	Amphibolitisation	Two styles of amphibolitisation: isochemical with alteration of diopside to tremolite/magnesium hornblende and metasomatic in clinopyroxenite with alteration to ferroan-pargasitic hornblende. Hornblendite layers created by complete metasomatic amphibolitisation.
Greenschist facies 350ma associated with continuing thrusting.	High degree of serpentinisation and mylonitisation	Chloritisation

Appendix 2. Scanning Electron Microscope

Scanning electron microscopes (SEM) allow mineralogical detail at the micron scale to be examined in polished rock sections. This is important for platinum-group minerals which are mostly smaller than 30μm. Photographs of mineral grains and textures may readily be obtained. In addition to this, when fitted, X-ray detectors linked to multichannel analysers allow X-ray spectra to be obtained on a video screen from SEM. Thus as well as visual examination of rock samples at very high magnification, qualitative identification of mineral grains down to the micron scale may be made. These are the main facilities which make SEM essential tools for PGM mineralogy. By using stored spectra on a computer system as standards, quantitative analysis of minerals using X-ray spectra is also possible.

Scanning electron microscope and associated computer system

At the start of the work in this thesis a Philips 501 SEM was used to obtain X-ray spectra of minerals within polished sections. This was fitted with a 'Link' detector series 2. The main part of the PGM mineralogy in this thesis, including the X-ray mapping and quantitative analyses, was carried out on a replacement system: the JEOL JSM-820 SEM. The JEOL microscope has facilities for observation of both backscattered and secondary electron emissions. An air lock is fitted, allowing rapid changeover between samples. This microscope is fitted with a 'Kevex' Si(Li) detector. The 'Kevex' detector is linked to a 'Kevex' computer system with twin disc drives, for ten megabyte 8 inch discs, and a terminal. This enables spectra and x-ray maps to be stored and processed using the 'Quantex' and 'Automated Imaging' software applications.

Operating procedure

The accelerating voltage most suitable for optimising the excitation and resolution of an X-ray peak occurs at an overvoltage of 2.5 to 3 fold (Vaughan 1983). Thus for exciting Os,Ir and Pt L peaks of 9 to 13keV an accelerating voltage of 25keV is suitable. Using these high energy peaks is necessary in order to be able to distinguish between the PGE present. The distinction between Os and Ir in particular requires the use of the more spaced out high energy L lines. The peaks used in this study are: As-K, Fe-K, S-K, Sb-L, Pd-L, Rh-L, Pt-L, Ir-L, Os-L, Ru-L and Ru-K. The energy ranges are shown in fig. A2.1. A possible disadvantage of using this relatively high voltage is that the problem of exciting material outside the mineral phase upon which the 'spot' is placed is increased. This means that for analysing mineral inclusions of less than about ten microns diameter within silicate or

chromite, Si or Cr peaks frequently appear on the spectra which would not be expected as part of the mineral formulae. The problem of sample inhomogeneity also becomes acute.

The filament current is saturated for a particular voltage using a line scan profile on the microscope screen. Electron gun alignment is checked at the same time. The filament needs to be checked after about half an hour. Back scattered images of the sample show up platinum-group minerals most clearly and brightly on the microscope screen due to their high atomic density relative to silicates and chromite. This type of electron emission is used to locate PGM rather than secondary electrons and is complimentary to reflected light microscopy with oil immersion lenses. All photographs were taken in back scattered electrons mode (BSE).

For obtaining spectra, quantitative analyses and X-ray dot mapping a working distance of exactly 39mm is required for the Kevex software. The working distance is the distance between the sample polished surface and the detector. A working distance of 15mm is used for taking photographs. The time constant is a parameter which controls the amount of high frequency noise within the analyser which is filtered out. Larger time constants increase the amount of filtering and thus improve the accuracy of analyses. All quantitative analyses were taken using a 12μs time constant, which is the largest available on the 'Kevex' system. Large time constants have the disadvantage that they decrease the rate at which counts can be processed. Dead time is the proportion of time within the analyser when X-ray peaks are not detected. It varies as a function of the probe current and time constant.

Once the operating conditions: working distance, focus and filament saturation have been set up on the microscope then the analysis spot is placed over the region of interest on the sample. A spectrum, with a keV energy range horizontal axis, may then be acquired. Two examples of spectra obtained are given in figures A2.2 (an Ir-As-S PGM), and A2.3 (the Pd-Hg grain described in chapter 4). K L M peak markers and a cursor can be put onto the screen in order to identify the peaks. Spectra can be either stored on a data disc or printed. If an offset between the spectra peaks and relevant K L M markers is suspected then the calibration is checked. This is done using a Cu grid attached to an Al stub. An autocalibration routine is executed from within the 'Quantex' program which matches the Al-K and Cu-K peaks obtained to expected values through up to twenty iterations.

In order to perform quantitative standard based analyses it was necessary to obtain spectra from standards for each of the elements in question. All primary standard spectra were obtained from pure samples of the elements apart from those for S and Fe which were obtained from a pyrite (FeS_2) grain. The standards used were ' Microanalysis Consultants ' block no. 262 for S, Fe, Ni, Cu and the Earth Sciences department standards block for the others.

Before obtaining a spectra to be used as a standard or for an analysis, the list of elements present, determined with a previous spectra, must be entered into the 'Kevex' software. A probe current reading is taken using the microscope probe current detector (PCD) and also entered. The count rate obtained will vary with differing probe currents and

the 'Kevex' software makes a linear correlation correction for this. The spectra is obtained for 200 seconds of livetime; that is the real time taken minus 'deadtime' within the analyser when no counts are taken. Deadtime is kept below 40% for quantitative analyses.

After the spectra has been obtained, the escape peaks are processed. Escape peaks are the result of X-ray emission from the Si-bearing detector and occur at 1.74keV below the main peaks. The counts from these escape peaks are added to the peaks of interest by this procedure. Following this, counts resulting from background emission are removed. The 'Kevex' software calculates a background boundary line based on accelerating voltage, the geometry of the SEM and an absorption factor which may be varied to to improve the boundarie's fit. Once the background counts have been removed the peaks must be deconvoluted. This is necessary to remove the effects of any overlapping peaks to determine the relative contributions of the peaks in question. The deconvolution procedure used assumes the peaks to be of gaussian distribution. A gaussian fit is synthesised for each peak and this is used as the region of interest. Once the spectra from the pure element or pyrite specimen has been deconvoluted it can be used as a standard.

For quantitative analysis of a sample the same sequence of commands is followed except at the deconvolution stage, when the names of the standards to be used are recalled. After this the analysis can be calculated using a ZAF procedure. Figure A2c.4 is a flow diagram summarising the sequence of commands performed to obtain a quantitative analysis.

Secondary standards

In order to demonstrate the accuracy and precision of the SEM quantitative analyses, secondary standards were used. Irarsite, sperrylite, hollingworthite and laurite grains from a Shetland ophiolite chromitite polished section sample, were used (section 1349D) and a pyrite (FeS_2) grain from the electron microscope suite standard block. Quantitative probe analyses obtained on a wavelength dispersive microprobe at an accelerating voltage of 20kv (Tarkian and Prichard 1987) are available for comparison with the SEM results on the same grains (table A2.1). The operating conditions used in the analysis of the secondary standard mineral grains were subsequently used for the Bragança samples.

The two sigma values of the weight% total ranges calculated for the secondary standards are fairly high (table A2.2). This suggests that the precision of the SEM probe technique is limited. Because of this, SEM analyses in the main part of this thesis are only quoted to one decimal place. The range of weight percent analyses do not all overlap the comparative analyses in table A2.1. For the laurite grain this may be explained by the relatively low total in the comparative analysis. The ranges of As in irarsite, S in hollingworthite and Sb in sperrylite also lie outside those shown in table A2.1. On the basis of these results only limited accuracy can be expected for mineral samples. The hollingworthite analysis shows the problem of excitation of material outside the mineral

grain of interest. Cr was included in the SEM analysis to show this, despite not being present in the mineral hollingworthite's structure.

In this study peaks were identified visually and this was used as a qualitative minimum detection limit (MDL). Values of the MDL in energy dispersive microprobe systems are often given as about 0.1wt%. Further study would be required to evaluate more precisely the value of MDL using the JEOL and 'Kevex' system for sulphides and PGM.

Sources of error for secondary standards and mineral samples

As with any microprobe technique, it is necessary to have a high degree of polish and an absence of charging on the sample that is being analysed. It is frequently necessary to probe a sample numerous times to obtain a reliable analysis. This degrades the minerals coated surface and thus cleaning, polishing on a 1μm lap and recoating need to be done frequently. This may however have the result of damaging the sulphides.

The ZAF correction procedure relies on the assumption that the X-rays that have been counted all come from one mineral source. In practice when one is dealing with submicroscopic sulphide grains fine intergrowths of different phases, such as magnetite, pentlandite and heazelwoodite are on a scale less than the area from which X-rays are received by the detector. Under such circumstances, although the weight % total may be reasonably close to 100% it is not a genuine mineral grain analysis. Rather it is a bulk composition of an aggregate of sub grains. This has meant that the great majority of the Fe-Ni-sulphide analyses taken from the chromite-rich samples with the SEM were not used, either having poor totals or implausible atomic ratios. Similarly the majority of platinum-group minerals could not be analysed successfully because they were too small. Prominent Cr peaks on the spectra obtained showed that the surrounding chromite was being excited. This results in low totals and unreliable atomic ratios. The minimum size for successful analysis by this technique is about 5μm diameter.

X-ray Mapping

The 'Kevex' system incorporates a fast X-ray mapping program. This allows dot maps to be produced on the video screen which show the distribution of elements in an area of interest. Up to 15 elements may be analysed at one time. A small time constant of 1.5μs is used which allows collection times for one scan of 0.5-2 minutes. The number of scans (frame averages) can be altered to vary the number of X-ray counts obtained. One frame scan was used in this study. A statistical noise filter allows the effects of random 'noise' to be reduced. The major limitation on the use of the X-ray mapping facility is that there is no way to deconvolute peaks. The 'Kevex' system analyses the entire energy range for the peak desired. This means for example that in analysing a grain that contains Ir, apparent Os

concentrations are also obtained on the dot map. The Os-L counts are a result of X-ray emission within the Ir-L energy range, which overlaps with that of Os-L. A solution is where possible to select non overlapping peaks.

Table A2.1 PGM standards

Wt%	Laurite	Irarsite	Holling-worthite	Sperrylite
Os				
Ir		61.22		
Ru	59.81			
Rh			47.62	
Pt		0.01		54.86
Pd				
Fe				
S	38.89	11.74	14.99	
As		26.05	37.02	42.59
Sb				3.66
Total	98.70	99.02	99.63	101.11
Atomic %				
Os				
Ir		30.81		
Ru	32.80			
Rh			32.49	
Pt		0.005		32.00
Pd				
Fe				
S	67.20	35.46	32.84	
As		33.72	34.647	64.60
Sb				3.40

These analyses were performed on chromitite section 1349D from the Shetland Ophiolite by Dr H.M Prichard. A wavelength dispersive microprobe (Camebax Microbeam CD) at a 20kV accelerating voltage was used (Tarkian and Prichard 1987).

Table A2.2 SEM analyses on PGM and pyrite standards

Laurite						
Wt%						
Ru	60.7	60.46	62.72	62.36	62.95	61.06
S	36.4	36.52	38.08	37.9	37.54	37.55
Total	97.1	96.98	100.8	100.26	100.49	98.61
At%						
S	65.4	65.56	65.68	65.7	65.28	65.97
Ru	34.6	34.44	34.32	34.3	34.72	34.03
Wt%						
Ru	61.17	60.75				
S	37.63	37.47				
Total	98.8	98.22				
At%						
S	65.98	66.03				
Ru	34.02	33.97				

	Range Wt%	Average	2sigma	Range At%		
S	60.46-62.95	61.52	1.87	65.28-66.03		
Ru	36.40-38.08	37.38	1.14	33.97-34.72		
Sperrylite Wt%						
Pt	53.64	55.07	53.83	53.48	55.39	54.2
As	43.61	43.71	42.87	42.2	43.87	43.05
Sb	2.3	2.3	2.08	2.17	2.08	2.16
Total	99.55	101.08	98.78	97.85	101.34	99.41
At%						
Pt	31.39	31.91	31.89	32.05	32.02	31.92
As	66.45	65.95	66.14	65.87	1.92	66.03
Sb	2.16	2.14	1.97	2.08	66.05	2.04
Wt%						
Pt	54.01	53.78	53.96	54.1		
As	42.2	43.59	42.44	41.6		
Sb	2.15	2.08	2.13	2.13		
Total	98.36	99.45	98.53	97.83		
At%						
Pt	32.28	31.52	32.14	32.62		
As	65.67	66.52	65.83	65.32		
Sb	2.06	1.96	2.03	2.06		
	Range Wt%	Average	2sigma	Range At%		
Pt	53.48-55.39	54.15	1.16	31.39-32.62		
As	41.60-43.87	42.91	1.48	65.32-66.52		
Sb	2.08-2.30	2.16	0.16	1.92-2.16		
Irarsite						
Wt%						
S	11.36	12.02	11.24	11.42	11.66	11.5
As	25.17	25.81	24.15	24.21	24.29	25.72
Ir	64.88	65.77	63.93	63.57	63.02	66.34
Total	101.41	103.6	99.32	99.2	98.97	103.56
At%						
S	34.48	11.24	34.87	35.25	35.8	34.25
As	32.68	24.15	32.06	32	31.92	32.78
Ir	32.84	63.93	33.08	32.75	32.28	32.96
Wt%						
S	11.72	12.37	12.55	12.14		
As	23.82	24.43	24.13	24.67		
Ir	62.41	62.6	61.19	64.67		
Total	97.95	99.4	97.87	101.48		

At%						
S	36.26	37.19	37.93	36.25		
As	31.54	31.42	31.22	31.53		
Ir	32.2	31.39	30.85	32.22		
	Range Wt%	Average	2sigma	Range At%		
S	11.24-12.55	11.8	0.85	34.25-37.93		
As	23.82-25.81	24.64	1.32	31.22-32.78		
Ir	61.19-66.34	63.84	3.04	30.85-33.08		
Holling-worthite						
Wt%						
S	13.47	13.52	13.83	14.61	14.74	13.04
Cr	1	0.96	0.96	1.12	1.06	1.13
As	37.56	34.22	34.22	34.19	33.01	34.48
Rh	47.45	49.31	49.31	51.66	51.94	47.86
Total	99.48	97.28	98.32	101.58	100.75	96.51
At%						
S	29.97	30.76	31.13	31.75	32.25	30.05
Cr	1.37	1.34	1.33	1.5	1.43	1.61
As	35.77	33.83	32.96	31.79	30.91	34
Rh	32.89	34.06	34.58	34.97	35.41	34.35
	Wt% Range	Average	2sigma	At% range		
S	13.04-14.74	13.89	1.23	29.97-32.25		
Cr	0.96-1.12	1.04	0.14	(1.33-1.61)		
As	33.01-37.56	34.7	2.78	30.91-35.77		
Rh	47.45-51.94	49.38	3.61	32.89-35.41		
Pyrite						
Wt%						
S	54.56	54.4	54.76	54.92	55.17	53.48
Fe	46.87	47.25	47.33	47.25	47.75	45.55
Total	101.43	101.65	102.09	102.17	102.92	99.03
At%						
S	66.97	66.72	66.83	66.94	66.8	67.16
Fe	33.03	33.28	33.17	33.06	33.2	32.84
Wt%						
S	53.28	53.59	53.31	53.39		
Fe	45.95	45.87	45.72	45.21		
Total	99.23	99.46	99.03	98.6		
At%						
S	66.88	67.05	67.01	67.29		
Fe	33.12	32.95	32.99	32.71		
	Range Wt%	Average	2sigma	Range At%		
S	53.28-55.17	54.09	1.41	66.72-67.29		
Fe	45.21-47.75	46.48	1.72	32.71-33.28		

Figure A2.1 X-ray Emission Energies

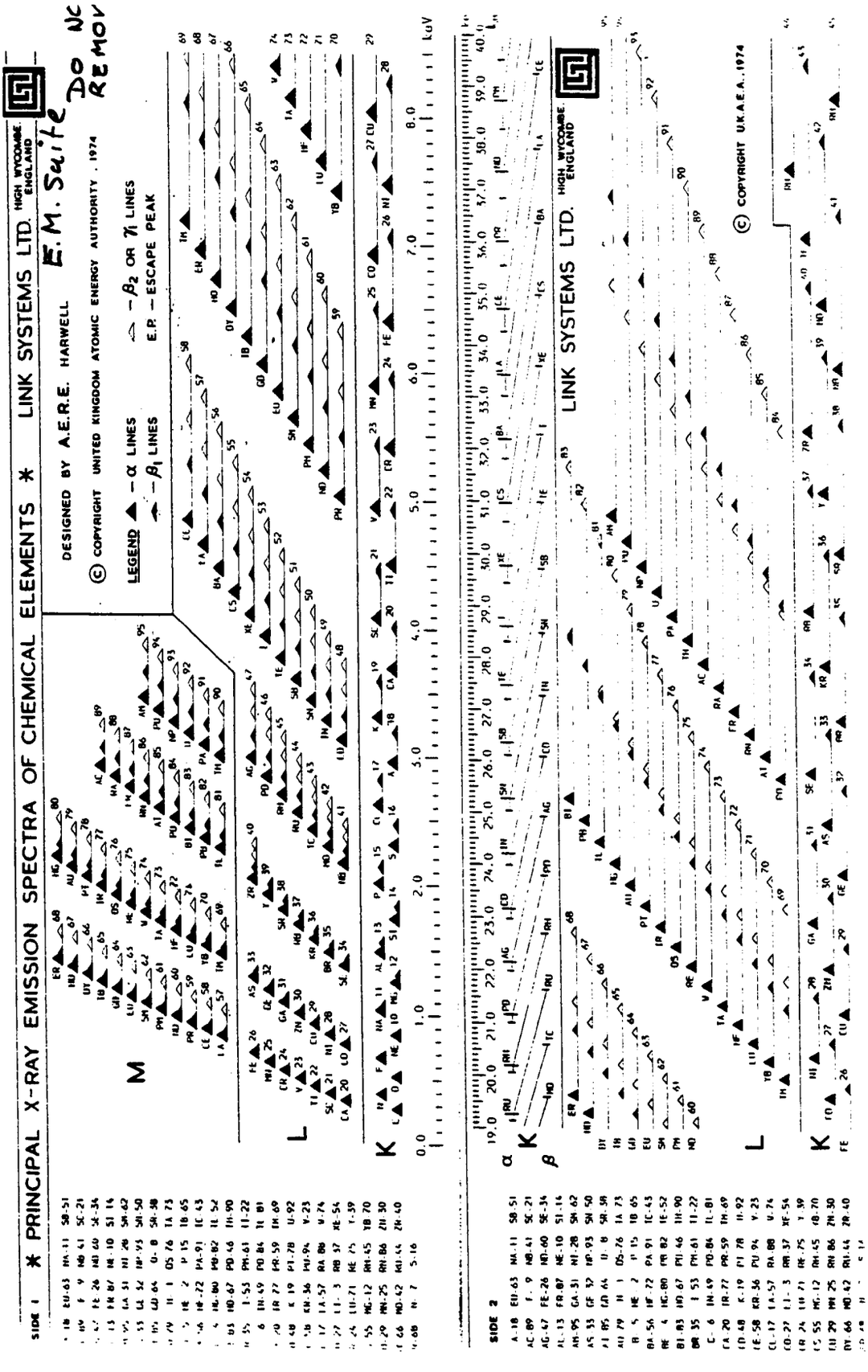

Figure A2.2 X-ray spectra of Ir-As-S grain and Figure A2.3 X-ray spectra of potarite (PdHg)

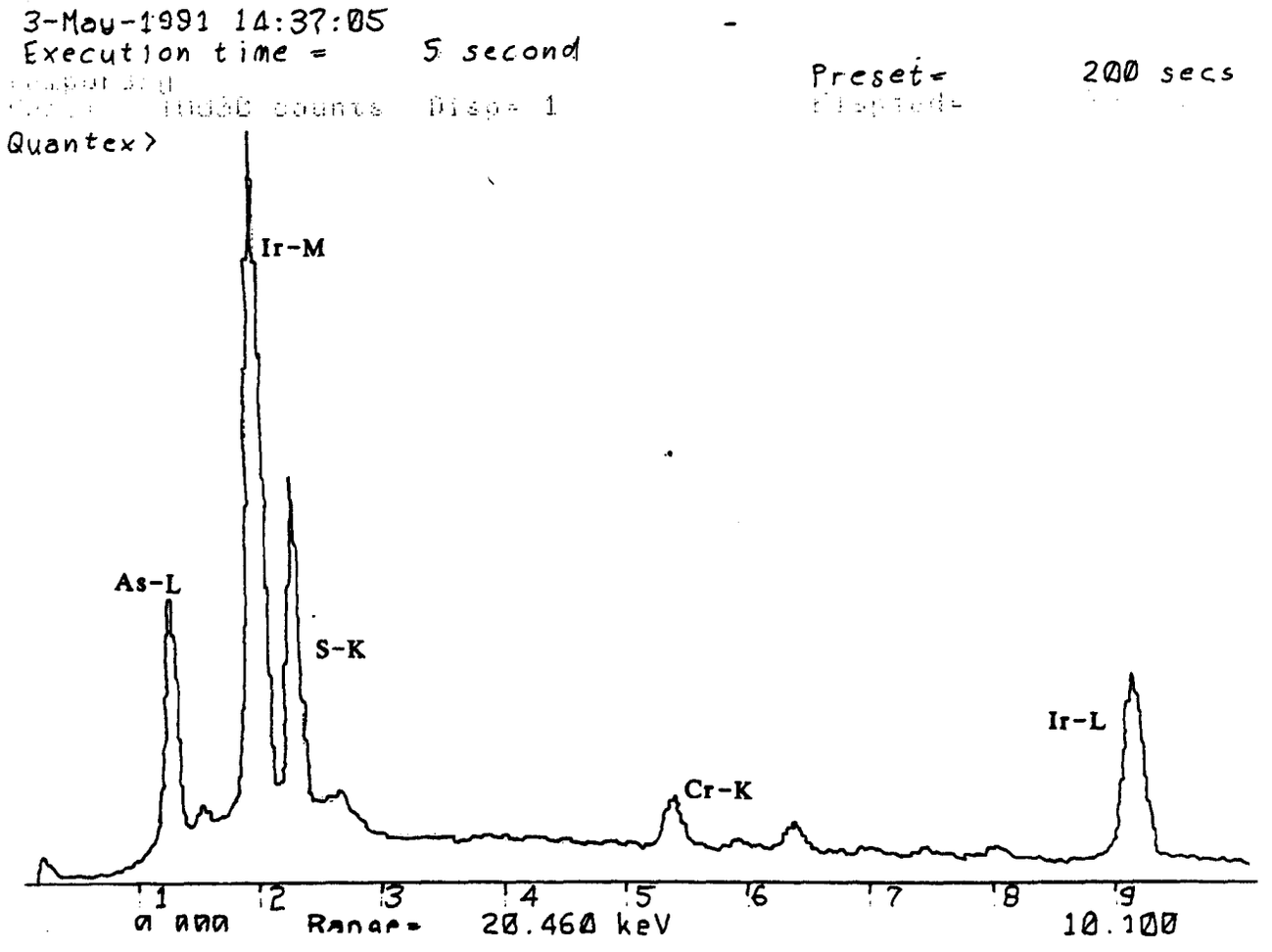

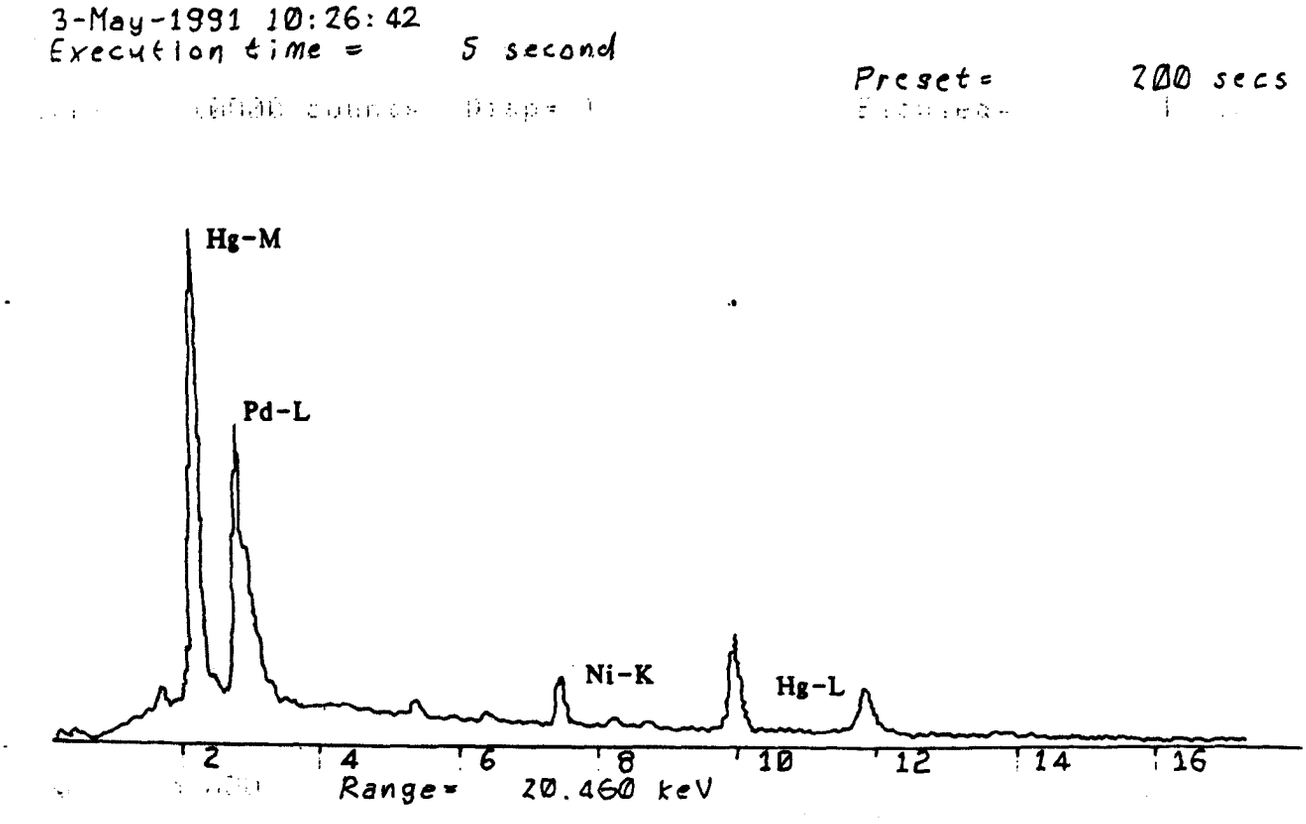

Figure A2.4 Flow Diagram showing the sequence of events followed to obtain a quantitative analysis

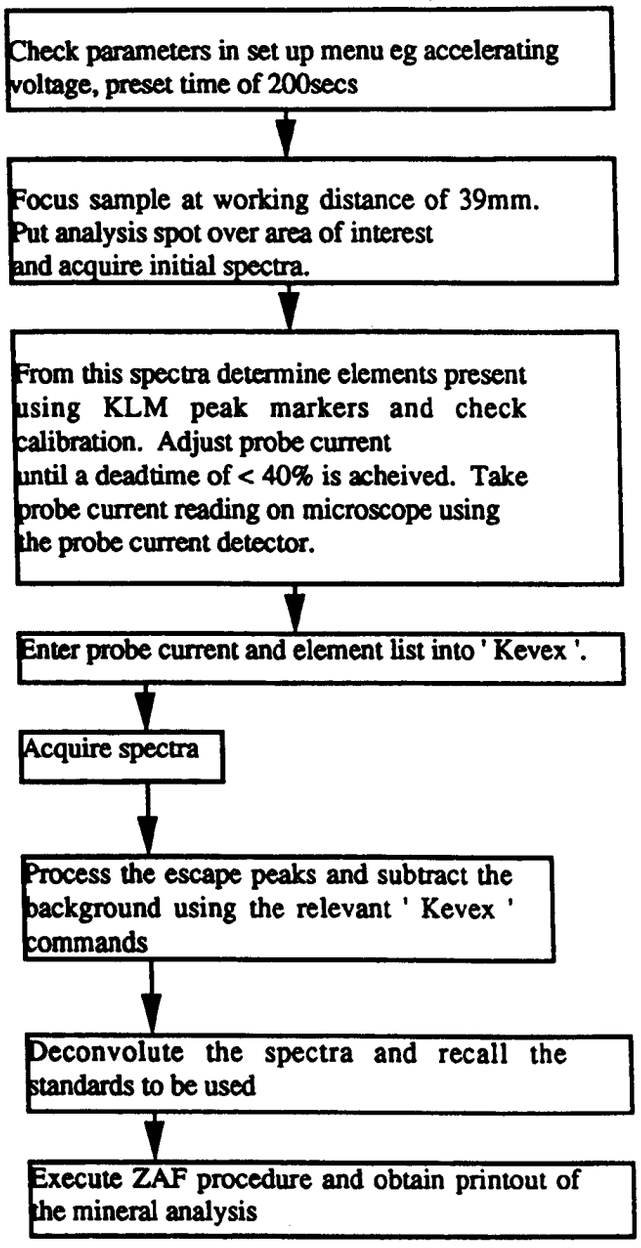

Appendix 3 Geochemical and microprobe data

3a Wavelength dispersive microprobe specifications

The wavelength dispersive microprobe used in this study was a Cambridge Instruments Microscan 9. This microprobe is fitted with twin crystal spectrometers allowing simultaneous element analyses. Crystal selection (LIF, TAP or PET), spectrometer drive, specimen stage drive, X-ray counting and a ZAF correction procedure are controlled by the user through a dedicated Apple Macintosh microcomputer.

Some specifications

1. Accelerating voltage 20kv
2. Specimen current 3.05×10^{-8}
3. Primary standards: Fe-olivine
   Ti-rutile
   K,Cl-KCl
   Si,Ca-wollastonite
   Na,Al-jadeite
   Mg-olivine
   Cr, Ni, Zn, Mn-metals
4. Secondary standards: basaltic glass ('ABX'), chromite ('ABY')

The secondary standards have previously been analysed and a mean and range of the compositions is available for comparison. ABY analyses are listed in appendix 4a alongside the sample analyses which they were used to check. Where the ABY analysis differed markedly from the mean of the ABY analyses recalibration took place on the primary standards. The average wt% of 24 ABY analyses is: SiO_2 0.09, TiO_2 0.22, Al_2O_3 10.33, FeO 15.41, MnO 0.34, MgO 13.31, CaO 0.03, Cr_2O_3 59.95, NiO 0.11.

Recalculation of mineral analyses

Recalculation of microprobe mineral analyses was performed on 'Excel' spreadsheets for chromite, pyroxene, amphibole and olivine or using 'Mintab' software (Rock and Carroll 1990) for garnet, sheet silicate and feldspar. The recalculation methods are based on an appropriate number of oxygens: chromite and spinel 32, pyroxene 6, olivine 4, sheet silicate 28, feldspar 8, garnet 12. The schemes for chromite and pyroxene incorporate Fe^{3+}/Fe^{2+} allocations based on apparent cation surplus as described in Browning (1982). This procedure requires normalising to 4 cations, though if the original number of cations is less than 4 then negative values for Fe^{3+} are calculated. Calculation of wollastonite, enstatite and ferrosilite end members was performed using the method of Cawthorn and Collerson

(1974). Amphiboles have been recalculated on the basis of 13 cations excluding Na and Ca (ΣFM). This gives the maximum possible Fe^{3+} content consistent with stoichiometry (Stout 1972). This method means that an apparent negative Fe^{2+} content is created in some analyses, which in turn creates apparent $Mg/(Mg+Fe^{2+})$ ratios of greater than 1. Recalculated mineral analyses used in this thesis are listed in appendix 4.

3b ICPMS analyses for PGE

Appendix 7 gives the complete set of Inductively Coupled Plasma Mass Spectrometry (ICPMS) analyses including standards. The first batch (28-2-90) was analysed by Sheen Analytical (Perth, Australia). The later (May 90 and March 91) batch of analyses was performed by Genalysis Laboratory Services Ltd. (Perth, Australia). This Genalysis laboratory technique involves precollection of the PGE by a Ni-sulphide fire assay technique. Following this the elements in solution are injected into an argon plasma at 7000°C and transfered as ions into a quadrupole mass spectrometer. The technique gives detection limits of 1ppb for Rh and 2ppb for the other PGE.

An international standard used for PGE analyses (SARM 7) is included within the analyses batches. The SARM 7 analyses for the May 90 and March 91 batches are much closer to the approved values than for the first batch. For instance the Pd values produced for the SARM7 standard are 2500ppb and 2400ppb in the first batch and 1500ppb,1475ppb for the second. This compares with an approved value of 1530ppm. The May 90 and March 91 batches also show better reproducibility in repeat analyses than the first batch. For these reasons it was considered that the batches from separate laboratories could not be considered together in chapter 4. Of the Sheen Analytical results only the analysis of sample Brag57 is used in chapter 4. It was possible to use this analysis because of the high degree of PGE enrichment which was clear despite the lower quality of the data set compared to the later batches. A blank (quartz) was analysed in the March 91 batch. This gave satisfactory results, with only Os giving a value of 2ppb, the other PGE being below detection limits as would be expected. A total of 65 samples were analysed for PGE in the three batches.

3c XRF analyses

Appendix 7 gives the complete set of X-ray fluorescence (XRF) trace element and major element analyses. Two systems were used to obtain these results. An energy dispersive Link Systems Mecca 20 was used for the trace element and major element batches prior to 1991. Trace elements were obtained from pressed powder pellets and major elements from glass discs. A full description of analytical procedure is given in Potts (1984). 1991 analyses utilised a different, wavelength dispersive system, the ARL 8420+.

The PCC1 standard result in the Link system major element data set is high (total 102.3% and 103.3%) compared to the approved total (100.4%). The S-2 and S-5 standard analyses are close to the approved values for all the oxides in the ARL 8420+ data set.

Comparison between glass disc analyses on sample 133BRG for both systems, shows that the ARL 8420+ result gives a total closer to 100% and lower Na_2O contents than the Mecca 20 result. Despite this, the two data sets give similar results and in this thesis they have been used interchangeably. The 1991 trace element data set was obtained specifically for sulphur. As noted beside the analyses, the S values are approximate, with errors quoted as 100% or 100ppm, whichever is greater.

Appendix 4 Microprobe data

The microprobe data obtained on minerals from the Bragança and Morais UATC rocks is tabulated in this appendix:

4a Chromite

4b Olivine

4c Pyroxene

4d Amphibole

4e Feldspar, apatite and garnet

4f Serpentine and chlorite

Identifier	Cr2O3	Al2O3	TiO2	Fe2O3	FeO	MgO	MnO	NiO	ZnO	Total	Cr	Al	Ti	Fe3+	Fe2+	Mg	Mn	Ni	Zn	Total	100Fe3*	100Mg*	100Cr*
Duplex/chromatite formation																							
Brug89 CHA	52.48	16.37	0.17	2.77	16.37	11.85	0.17	0.06	•	100.24	10.60	4.93	0.03	0.53	3.50	4.51	0.08	0.01	•	24.20	3.32	56.34	68.25
CHB	52.61	14.95	0.18	3.89	15.27	12.23	0.18	0.09	•	99.40	10.78	4.57	0.04	0.76	3.31	4.73	0.09	0.02	•	24.29	4.72	58.81	70.24
CHC	53.18	15.30	0.18	3.92	15.19	12.60	0.17	0.04	•	100.58	10.75	4.61	0.03	0.75	3.25	4.80	0.08	0.01	•	24.29	4.68	59.64	69.98
CHD	53.86	14.68	0.19	4.05	14.95	12.69	0.15	0.10	•	100.67	10.90	4.43	0.04	0.78	3.20	4.84	0.08	0.02	•	24.30	4.84	60.20	71.10
CHE	53.06	13.89	0.18	4.94	15.13	12.30	0.19	0.07	•	99.75	10.93	4.27	0.04	0.97	3.30	4.77	0.09	0.01	•	24.37	5.99	59.17	71.92
CHF	53.97	14.10	0.18	4.37	14.97	12.58	0.15	0.06	•	100.38	11.00	4.29	0.03	0.85	3.23	4.83	0.08	0.01	•	24.32	5.26	59.97	71.96
Brug99 CHG	53.35	11.09	0.18	6.24	19.45	9.18	0.28	0.03	•	99.79	11.42	3.54	0.04	1.27	4.40	3.70	0.11	0.01	•	24.49	7.83	45.69	76.34
CHH	50.68	11.37	0.16	8.23	17.85	10.05	0.26	0.04	•	98.63	10.96	3.67	0.03	1.69	4.08	4.10	0.11	0.01	•	24.65	10.38	50.09	74.93
CHI	52.12	10.59	0.16	6.28	19.54	8.59	0.29	0.04	•	97.61	11.46	3.47	0.03	1.31	4.54	3.56	0.12	0.01	•	24.50	8.09	43.93	76.75
CHJ	53.06	11.17	0.15	5.98	19.87	8.80	0.26	0.04	•	99.34	11.42	3.58	0.03	1.23	4.52	3.57	0.11	0.01	•	24.47	7.55	44.10	76.11
Standard ABY	59.86	10.28	•		15.38	12.92	0.33	0.10	•	98.87													
CHI	51.81	10.74	0.18	6.60	19.13	8.90	0.31	0.03	•	97.70	11.36	3.51	0.04	1.38	4.44	3.68	0.12	0.01	•	24.53	8.48	45.33	76.39
CHK	53.07	10.92	0.18	6.39	19.76	8.92	0.26	0.03	•	99.53	11.42	3.50	0.04	1.31	4.50	3.62	0.11	0.01	•	24.50	8.07	44.58	76.52
CHL	53.27	11.15	0.15	6.02	19.52	9.07	0.26	0.01	•	99.45	11.43	3.57	0.03	1.23	4.43	3.67	0.11	0.00	•	24.47	7.58	45.29	76.21
CHM	52.43	11.22	0.16	6.28	20.20	8.56	0.28	0.03	•	99.16	11.33	3.62	0.03	1.29	4.62	3.49	0.11	0.01	•	24.49	7.96	43.03	75.81
CHN	51.65	10.95	0.18	7.25	21.70	7.70	0.30	0.01	•	99.74	11.23	3.55	0.04	1.50	4.99	3.15	0.12	0.00	•	24.58	9.21	38.74	75.98
CHO	50.62	9.68	0.18	8.95	22.02	7.22	0.34	0.04	•	99.04	11.25	3.21	0.04	1.89	5.18	3.03	0.13	0.01	•	24.73	11.58	36.88	77.81
CHP	52.00	11.47	0.16	6.75	19.95	8.83	0.26	0.03	•	99.45	11.19	3.68	0.03	1.38	4.54	3.58	0.11	0.01	•	24.53	8.51	44.10	75.25
Standard ABY	59.37	10.36	0.21		15.55	13.22	0.30	0.10	•	99.11													
Brug22 CHQ	59.05	7.72	0.13	4.00	18.89	8.98	0.29	0.03	•	99.09	12.82	2.50	0.03	0.83	4.34	3.67	0.12	0.01	•	24.31	5.12	45.86	83.68
CHR	59.12	7.80	0.15	4.34	18.88	9.18	0.23	0.03	•	99.74	12.75	2.51	0.03	0.89	4.31	3.73	0.11	0.01	•	24.34	5.52	46.42	83.56
CHS	59.50	7.61	0.12	4.27	18.19	9.52	0.29	0.01	•	99.51	12.84	2.45	0.02	0.88	4.15	3.87	0.12	0.00	•	24.33	5.42	48.26	83.98
CHT	59.36	7.91	0.16	3.82	18.25	9.48	0.27	0.04	•	99.30	12.80	2.54	0.03	0.78	4.16	3.85	0.12	0.01	•	24.30	4.86	48.07	83.42
CHU	59.67	7.75	0.13	3.97	18.11	9.62	0.25	0.01	•	99.51	12.84	2.49	0.03	0.81	4.12	3.90	0.11	0.00	•	24.31	5.04	48.63	83.77
CHV	59.78	7.75	0.13	3.89	17.47	9.97	0.27	0.01	•	99.27	12.86	2.49	0.03	0.80	3.98	4.04	0.12	0.00	•	24.30	4.93	50.42	83.80
CHW	58.95	6.94	0.12	4.91	19.31	8.66	0.29	0.01	•	99.19	12.91	2.27	0.02	1.02	4.47	3.57	0.12	0.00	•	24.39	6.31	44.42	85.07
Brug31 CHX	53.81	11.53	0.18	3.57	17.26	10.53	0.22	0.06	•	99.16	11.42	3.65	0.04	1.13	3.87	4.21	0.10	0.01	•	24.43	6.95	52.09	75.78
CHY	54.79	10.70	0.16	5.19	17.79	10.03	0.25	0.04	•	98.95	11.72	3.41	0.03	1.06	4.02	4.04	0.11	0.01	•	24.40	6.53	50.12	77.45
CHZ	57.27	9.14	0.15	4.86	18.42	9.62	0.23	0.04	•	99.73	12.27	2.92	0.03	0.99	4.17	3.88	0.11	0.01	•	24.38	6.12	48.20	80.78
CRA	52.45	12.79	0.21	5.88	16.65	11.11	0.24	0.07	•	99.40	11.01	4.01	0.04	1.17	3.70	4.40	0.10	0.01	•	24.45	7.25	54.31	73.33
CRB	55.27	10.80	0.16	5.20	17.37	10.43	0.22	0.08	•	99.53	11.72	3.42	0.03	1.05	3.90	4.17	0.10	0.02	•	24.40	6.49	51.69	77.44
CRC	56.84	9.66	0.13	4.77	17.29	10.31	0.23	0.03	•	99.26	12.13	3.08	0.03	0.97	3.90	4.15	0.11	0.01	•	24.37	5.99	51.52	79.78
CRD	55.86	10.41	0.15	4.82	17.16	10.45	0.21	0.06	•	99.12	11.89	3.30	0.03	0.98	3.86	4.19	0.10	0.01	•	24.37	6.04	52.04	78.25
CRE	52.79	12.99	0.22	5.42	15.89	11.61	0.21	0.06	•	99.19	11.04	4.05	0.04	1.08	3.52	4.58	0.09	0.01	•	24.41	6.67	56.55	73.16
Standard ABY	59.93	10.19	0.22		15.30	13.42	0.32	0.14	0.06	99.59													
Brug11 CTA	54.86	12.65	0.16	4.39	17.32	10.86	0.20	0.10	•	100.54	11.37	3.91	0.03	0.87	3.80	4.24	0.09	0.02	0.00	24.33	5.37	52.78	74.41
CTB	55.01	12.47	0.18	4.22	17.04	10.91	0.23	0.06	0.10	100.22	11.43	3.86	0.04	0.83	3.75	4.27	0.10	0.01	0.02	24.32	5.17	53.29	74.74
CTC	55.49	12.84	0.16	3.83	16.23	11.56	0.20	0.07	0.03	100.40	11.43	3.94	0.03	0.75	3.53	4.49	0.09	0.01	0.01	24.28	4.65	55.94	74.35
CTD	55.28	12.92	0.16	3.92	16.08	11.67	0.17	0.04	0.04	100.28	11.39	3.97	0.03	0.77	3.50	4.53	0.09	0.01	0.01	24.29	4.77	56.39	74.15
CTE	54.44	13.29	0.18	4.09	16.58	11.35	0.18	0.04	0.09	100.24	11.23	4.09	0.04	0.80	3.62	4.41	0.09	0.01	0.02	24.30	4.98	54.95	73.31
CTF	54.44	13.91	0.19	4.07	15.82	12.02	0.17	0.07	0.09	100.78	11.10	4.23	0.04	0.79	3.41	4.62	0.09	0.01	0.02	24.30	4.90	57.53	72.41
Brug51 CTG	51.08	17.70	0.17	4.13	12.37	14.59	0.15	0.07	0.07	100.33	10.12	5.23	0.03	0.78	2.59	5.45	0.07	0.01	0.01	24.30	4.83	67.76	65.93
CTH	51.05	18.12	0.17	4.04	12.38	14.73	0.13	0.07	0.07	100.75	10.05	5.32	0.03	0.76	2.58	5.46	0.07	0.01	0.01	24.29	4.69	67.96	65.39
CTI	50.88	18.35	0.18	4.00	12.26	14.86	0.11	0.06	0.06	100.76	9.99	5.37	0.03	0.75	2.55	5.50	0.07	0.01	0.01	24.28	4.64	68.35	65.03

CTJ	51.41	17.71	0.17	4.13	12.69	14.64	0.12	0.07	0.04	100.79	10.14	5.21	0.03	0.78	2.61	5.44	0.07	0.01	0.01	24.29	4.81	67.62	66.06							
CTK	51.51	17.51	0.17	4.27	12.33	14.70	0.14	0.06	0.06	100.75	10.17	5.16	0.03	0.80	2.57	5.47	0.07	0.01	0.01	24.30	4.98	68.00	66.36							
CTL	51.96	17.31	0.17	3.80	12.64	14.44	0.12	0.10	0.03	100.57	10.28	5.11	0.03	0.72	2.65	5.39	0.07	0.02	0.01	24.27	4.44	67.06	66.81							
Mean(Bar)	Cr2O3	Al2O3	TiO2	Fe2O3	FeO	MgO	MnO	NiO	ZnO	Total	Cr	Al	Ti	Fe3+	Fe2+	Mg	Mn	Ni	Zn	Total	100*Fe3*	100Mg*	100Cr*							
Brag54 CTM	46.82	15.16	0.20	7.63	21.57	8.29	0.25	0.01	0.07	100.00	9.94	4.80	0.04	1.54	4.84	3.32	0.10	0.00	0.01	24.59	9.47	40.65	67.44							
CTN	46.98	15.29	0.24	7.59	21.59	8.34	0.25	0.04	0.16	100.48	9.92	4.81	0.05	1.53	4.82	3.32	0.10	0.01	0.03	24.59	9.38	40.77	67.32							
CTO	46.41	15.85	0.21	7.36	21.44	8.41	0.27	0.06	0.09	100.10	9.79	4.99	0.04	1.48	4.79	3.35	0.10	0.01	0.02	24.57	9.09	41.14	66.26							
CTP	47.28	15.26	0.23	7.39	21.89	8.17	0.28	0.06	0.10	100.66	9.97	4.80	0.05	1.48	4.88	3.25	0.11	0.01	0.02	24.57	9.12	39.94	67.51							
CTQ	46.38	15.26	0.24	7.44	21.98	7.97	0.24	0.03	0.06	99.60	9.89	4.85	0.05	1.51	4.96	3.20	0.10	0.01	0.01	24.58	9.29	39.26	67.08							
CTR	47.13	14.97	0.23	7.66	21.77	8.22	0.27	0.03	0.04	100.32	9.99	4.73	0.05	1.55	4.88	3.28	0.10	0.01	0.01	24.59	9.50	40.23	67.86							
Brag26 CTS	54.23	13.51	0.00	3.97	12.41	14.33	0.13	0.11	0.01	100.70	10.82	4.61	0.00	0.75	2.62	5.39	0.07	0.02	0.00	24.29	4.66	67.37	70.10							
CTT	54.80	15.21	0.17	3.66	12.44	14.41	0.18	0.10	0.01	100.98	10.90	4.51	0.03	0.69	2.62	5.40	0.09	0.02	0.00	24.26	4.30	67.37	70.73							
CTU	54.28	15.09	0.17	3.98	12.48	14.31	0.13	0.11	0.01	100.56	10.86	4.50	0.03	0.76	2.64	5.40	0.08	0.02	0.00	24.29	4.70	67.14	70.69							
CTV	54.93	14.95	0.18	3.63	12.62	14.27	0.13	0.10	0.01	100.82	10.96	4.45	0.03	0.69	2.66	5.37	0.07	0.02	0.00	24.26	4.29	66.83	71.13							
CTW	54.85	14.89	0.18	3.90	12.51	14.33	0.14	0.10	0.06	100.96	10.94	4.43	0.03	0.74	2.64	5.39	0.08	0.02	0.01	24.28	4.60	67.12	71.18							
CTX	54.49	15.06	0.17	3.63	12.47	14.24	0.16	0.10	0.04	100.36	10.91	4.50	0.03	0.69	2.64	5.38	0.08	0.02	0.01	24.26	4.29	67.06	70.81							
Brag70 COA	49.65	15.53	0.20	5.98	17.43	10.98	0.28	0.06	0.09	100.20	10.24	4.78	0.04	1.18	3.80	4.27	0.11	0.01	0.02	24.45	7.26	52.89	68.19							
COB	52.34	12.60	0.13	6.10	18.28	10.02	0.29	0.03	0.10	99.89	11.05	3.97	0.03	1.23	4.08	3.99	0.11	0.01	0.02	24.47	7.55	49.41	73.58							
COC	47.86	14.57	0.20	8.45	18.12	10.41	0.31	0.08	0.12	100.13	10.05	4.56	0.04	1.69	4.03	4.12	0.11	0.02	0.02	24.65	10.37	50.58	68.78							
COD	51.56	13.47	0.13	5.97	18.23	10.10	0.31	0.07	0.13	99.97	10.82	4.22	0.03	1.19	4.05	4.00	0.12	0.01	0.03	24.46	7.35	49.68	71.96							
COE	49.68	14.69	0.17	6.38	17.81	10.52	0.26	0.09	0.09	99.69	10.38	4.58	0.03	1.27	3.94	4.14	0.10	0.02	0.02	24.49	7.82	51.28	69.40							
COF	50.36	15.87	0.18	5.24	17.05	11.29	0.25	0.07	0.10	100.41	10.31	4.84	0.04	1.02	3.69	4.36	0.10	0.01	0.02	24.39	6.31	54.12	68.03							
Brag57 COG	48.06	18.02	0.17	5.29	17.77	11.09	0.33	0.07	0.12	100.94	9.72	5.43	0.03	1.02	3.80	4.23	0.11	0.01	0.02	24.39	6.30	52.66	64.15							
COH	48.92	16.68	0.14	5.93	18.03	10.77	0.32	0.06	0.06	101.01	9.99	5.08	0.03	1.15	3.89	4.15	0.11	0.01	0.03	24.44	7.10	51.57	66.29							
COI	48.22	17.88	0.17	5.30	18.05	10.93	0.29	0.04	0.13	101.03	9.76	5.40	0.03	1.02	3.86	4.18	0.10	0.01	0.02	24.39	6.32	51.95	64.39							
COJ	48.09	18.04	0.18	5.39	17.75	11.09	0.29	0.10	0.25	101.18	9.71	5.43	0.03	1.04	3.79	4.22	0.10	0.02	0.05	24.40	6.41	52.68	64.13							
COK	48.40	17.52	0.17	5.46	18.07	10.83	0.31	0.03	0.23	101.01	9.83	5.30	0.03	1.05	3.88	4.14	0.11	0.01	0.04	24.40	6.51	51.64	64.94							
COL	48.21	17.71	0.17	5.53	17.90	10.98	0.30	0.04	0.21	101.05	9.77	5.35	0.03	1.07	3.84	4.19	0.11	0.01	0.04	24.41	6.59	52.22	64.61							
Standard ABT	60.77	10.27	0.21		15.29	13.12	0.32	0.10	0.07	100.15																				
Brag79 COM	56.19	12.50	0.16	3.69	16.86	11.19	0.24	0.08	0.03	100.93	11.56	3.83	0.03	0.72	3.67	4.34	0.10	0.02	0.01	24.27	4.48	54.18	75.09							
CON	55.12	13.12	0.15	3.78	16.86	11.20	0.21	0.08	0.00	100.52	11.35	4.03	0.03	0.74	3.67	4.35	0.09	0.02	0.00	24.28	4.60	54.21	73.80							
COO	55.29	11.96	0.16	4.65	17.72	10.53	0.22	0.08	0.03	100.65	11.52	3.72	0.03	0.92	3.91	4.14	0.10	0.02	0.01	24.35	5.71	51.43	75.61							
COP	54.62	13.52	0.16	3.81	17.47	10.84	0.25	0.08	0.07	100.82	11.23	4.14	0.03	0.74	3.80	4.20	0.10	0.02	0.01	24.28	4.62	52.50	73.04							
COQ	55.79	12.19	0.13	3.95	17.59	10.57	0.24	0.11	0.04	100.61	11.58	3.77	0.03	0.78	3.86	4.14	0.10	0.02	0.01	24.30	4.84	51.70	75.42							
COR	55.05	14.00	0.16	3.10	16.11	11.74	0.23	0.09	0.04	100.52	11.23	4.26	0.03	0.60	3.48	4.51	0.10	0.02	0.01	24.23	3.74	56.50	72.50							
Brag16 COS	54.32	13.50	0.15	3.35	17.86	10.43	0.21	0.08	0.06	99.97	11.26	4.17	0.03	0.66	3.92	4.08	0.10	0.02	0.01	24.25	4.11	50.99	72.96							
COT	55.09	12.10	0.13	4.46	17.90	10.32	0.22	0.07	0.10	100.39	11.51	3.77	0.03	0.89	3.95	4.06	0.10	0.01	0.02	24.34	5.48	50.68	75.33							
COU	55.03	13.98	0.15	3.10	16.91	11.30	0.20	0.10	0.00	100.77	11.23	4.25	0.03	0.60	3.65	4.35	0.09	0.02	0.00	24.23	3.75	54.36	72.52							
COV	55.17	13.09	0.16	4.14	16.88	11.26	0.25	0.08	0.03	101.05	11.32	4.00	0.03	0.81	3.66	4.36	0.10	0.02	0.01	24.31	5.01	54.31	73.86							
COW	55.43	13.08	0.16	3.60	16.98	11.14	0.24	0.08	0.01	100.72	11.39	4.01	0.03	0.71	3.69	4.32	0.10	0.02	0.00	24.27	4.38	53.90	73.97							
COX	55.44	12.81	0.15	4.07	16.70	11.28	0.25	0.07	0.06	100.83	11.41	3.93	0.03	0.80	3.64	4.38	0.10	0.01	0.01	24.30	4.93	54.62	74.37							
Brag23 CBA	50.72	14.63	0.19	4.76	23.28	7.24	0.31	0.03	0.16	101.31	10.63	4.57	0.04	0.95	5.16	2.86	0.11	0.01	0.03	24.36	5.88	35.66	69.92							
CBB	49.45	15.57	0.21	4.71	23.17	7.32	0.33	0.06	0.15	100.97	10.34	4.86	0.04	0.94	5.13	2.89	0.12	0.01	0.03	24.36	5.82	36.02	68.05							
CBC	49.83	15.23	0.21	4.81	23.43	7.21	0.30	0.01	0.15	101.18	10.43	4.75	0.04	0.96	5.19	2.85	0.11	0.00	0.03	24.37	5.94	35.42	68.69							
CBD	49.99	15.71	0.21	4.39	23.10	7.50	0.32	0.04	0.12	101.38	10.39	4.87	0.04	0.87	5.08	2.94	0.12	0.01	0.02	24.33	5.39	36.65	68.09							
CBE	49.34	14.70	0.00	5.74	22.96	7.12	0.34	0.01	0.23	100.44	10.47	4.65	0.00	1.16	5.15	2.85	0.12	0.00	0.05	24.44	7.12	35.59	69.24							

4a Chromite

CEF	49.90	15.80	0.22	4.21	22.84	7.62	0.32	0.01	0.15	101.06	10.38	4.90	0.04	0.83	5.02	2.99	0.12	0.00	0.03	24.32	5.17	37.29	67.93
Identifier	Cr2O3	Al2O3	TiO2	Fe2O3	FeO	MgO	MnO	NiO	ZnO	Total	Cr	Al	Ti	Fe3+	Fe2+	Mg	Mn	Ni	Zn	Total	100Fe3*	100Mg*	100Cr*
180BRG PAA	61.45	8.60	0.09	3.43	16.39	11.22	0.22	0.00	•	101.41	12.78	2.67	0.02	0.68	3.61	4.40	0.10	0.00	•	24.26	4.21	56.34	82.73
PAB	62.12	8.15	0.07	3.37	16.28	11.25	0.21	0.00	•	101.46	12.93	2.53	0.01	0.67	3.59	4.42	0.10	0.00	•	24.25	4.15	58.81	83.64
PAC	60.85	8.57	0.15	3.59	15.95	11.39	0.25	0.00	•	100.75	12.73	2.67	0.03	0.72	3.53	4.49	0.11	0.00	•	24.27	4.44	56.34	82.64
PAD	61.60	8.36	0.09	3.35	16.51	11.06	0.25	0.00	•	101.22	12.86	2.60	0.02	0.67	3.65	4.35	0.11	0.00	•	24.25	4.13	58.81	83.17
PAE	61.40	8.14	0.07	3.33	16.28	11.03	0.24	0.00	•	100.49	12.91	2.55	0.01	0.67	3.62	4.37	0.11	0.00	•	24.25	4.13	56.34	83.49
PAF	55.23	13.69	0.09	4.44	15.17	12.58	0.18	0.00	•	101.38	11.18	4.13	0.02	0.86	3.25	4.80	0.09	0.00	•	24.33	5.29	58.81	73.01
PAG	61.67	7.71	0.06	3.52	16.19	11.03	0.22	0.00	•	100.41	13.01	2.43	0.01	0.71	3.62	4.39	0.11	0.00	•	24.27	4.38	56.34	84.29
145BRG PAH	57.82	9.81	0.13	4.61	17.83	10.29	0.24	0.00	•	100.73	12.17	3.08	0.03	0.92	3.97	4.08	0.11	0.00	•	24.35	5.71	58.81	79.81
PAI	58.10	10.09	0.15	4.06	17.65	10.45	0.23	0.00	•	100.73	12.17	3.15	0.03	0.81	3.91	4.13	0.10	0.00	•	24.31	5.02	56.34	79.43
PAJ	58.03	9.76	0.15	4.41	17.45	10.51	0.23	0.00	•	100.53	12.21	3.06	0.03	0.88	3.88	4.17	0.10	0.00	•	24.34	5.46	58.81	79.95
PAK	57.46	10.31	0.15	4.69	17.48	10.62	0.26	0.00	•	100.97	12.01	3.21	0.03	0.93	3.87	4.19	0.11	0.00	•	24.36	5.78	56.34	78.89
PAL	57.63	10.32	0.15	4.12	17.61	10.44	0.26	0.00	•	100.53	12.09	3.23	0.03	0.82	3.91	4.13	0.11	0.00	•	24.31	5.10	58.81	78.92
PAM	57.95	10.14	0.15	4.33	17.75	10.44	0.24	0.00	•	101.00	12.12	3.16	0.03	0.86	3.93	4.12	0.11	0.00	•	24.33	5.34	56.34	79.31
PAN	59.36	9.46	0.13	4.25	17.99	10.39	0.20	0.00	•	101.78	12.37	2.94	0.03	0.84	3.96	4.08	0.10	0.00	•	24.32	5.22	58.81	80.80
152BRG CEA	59.92	8.01	0.13	3.52	15.61	11.07	0.22	0.04	•	98.51	12.84	2.56	0.03	0.72	3.54	4.47	0.11	0.01	•	24.27	4.45	56.34	83.38
CEB	60.37	7.80	0.12	3.88	15.81	11.07	0.26	0.01	•	99.32	12.87	2.48	0.02	0.79	3.57	4.45	0.11	0.00	•	24.30	4.87	58.81	83.85
CEC	60.10	7.70	0.10	3.94	15.86	10.95	0.23	0.00	•	98.88	12.89	2.46	0.02	0.80	3.60	4.43	0.11	0.00	•	24.31	4.98	56.34	83.96
CED	60.06	8.08	0.13	3.40	15.70	11.06	0.23	0.01	•	98.67	12.85	2.58	0.03	0.69	3.55	4.46	0.11	0.00	•	24.26	4.30	58.81	83.29
CEE	59.76	8.10	0.12	3.45	15.56	11.06	0.23	0.03	•	98.32	12.82	2.59	0.02	0.71	3.53	4.47	0.11	0.01	•	24.27	4.38	56.34	83.19
CEF	60.08	7.91	0.12	3.39	15.84	10.91	0.20	0.03	•	98.48	12.89	2.53	0.02	0.69	3.60	4.41	0.10	0.01	•	24.26	4.29	58.81	83.59
CEG	60.16	7.49	0.10	4.07	16.10	10.74	0.25	0.06	•	98.97	12.93	2.40	0.02	0.83	3.66	4.35	0.11	0.01	•	24.32	5.15	56.34	84.34
CEH	59.85	8.06	0.12	3.70	15.64	11.09	0.23	0.03	•	98.72	12.81	2.57	0.02	0.75	3.54	4.47	0.11	0.01	•	24.29	4.67	58.81	83.28
8BRG CEI	49.05	15.89	0.09	5.55	17.46	10.78	0.23	0.07	•	99.13	10.20	4.93	0.02	1.10	3.84	4.23	0.10	0.01	•	24.42	6.78	56.34	67.43
CEJ	49.29	15.45	0.11	5.69	17.43	10.75	0.23	0.06	•	99.01	10.29	4.81	0.02	1.13	3.85	4.23	0.10	0.01	•	24.43	6.97	58.81	68.15
CEK	49.37	15.82	0.11	5.38	17.80	10.63	0.22	0.06	•	99.39	10.25	4.90	0.02	1.06	3.91	4.16	0.09	0.01	•	24.41	6.56	56.34	67.67
CEL	49.19	15.63	0.12	5.50	17.59	10.68	0.23	0.03	•	98.97	10.26	4.86	0.02	1.09	3.88	4.20	0.10	0.01	•	24.42	6.74	58.81	67.85
CEM	49.52	16.01	0.12	4.96	17.16	10.99	0.26	0.03	•	99.06	10.26	4.95	0.02	0.98	3.76	4.29	0.10	0.01	•	24.37	6.05	56.34	67.47
CEN	49.94	15.05	0.11	5.43	17.69	10.55	0.25	0.03	•	99.05	10.44	4.69	0.02	1.08	3.91	4.16	0.10	0.01	•	24.41	6.67	58.81	68.99
CEO	49.53	15.79	0.12	5.71	17.89	10.71	0.22	0.06	•	100.03	10.23	4.86	0.02	1.12	3.91	4.17	0.09	0.01	•	24.43	6.92	56.34	67.78
CEP	49.36	15.91	0.14	5.30	17.58	10.78	0.23	0.07	•	99.37	10.23	4.92	0.03	1.05	3.86	4.21	0.10	0.01	•	24.40	6.45	58.81	67.54
44BRG CEQ	51.59	15.69	0.23	4.24	15.98	11.94	0.19	0.06	0.13	100.06	10.52	4.77	0.04	0.82	3.45	4.59	0.09	0.01	0.02	24.31	5.11	56.34	68.80
CER	50.55	16.21	0.21	4.82	15.95	12.05	0.19	0.04	0.12	100.13	10.29	4.92	0.04	0.93	3.43	4.62	0.09	0.01	0.02	24.36	5.78	58.81	67.65
CES	50.68	15.49	0.24	5.54	16.25	11.83	0.26	0.04	0.10	100.43	10.36	4.72	0.05	1.08	3.51	4.56	0.10	0.01	0.02	24.41	6.68	56.34	68.69
CET	53.19	13.38	0.21	5.11	16.77	11.21	0.26	0.06	0.09	100.27	11.02	4.13	0.04	1.01	3.67	4.38	0.10	0.01	0.02	24.38	6.23	58.81	72.72
CEU	51.02	14.65	0.24	5.84	16.41	11.59	0.20	0.04	0.15	100.14	10.52	4.51	0.05	1.15	3.58	4.51	0.09	0.01	0.03	24.44	7.09	56.34	70.02
CEV	52.86	14.47	0.25	4.02	16.37	11.57	0.18	0.09	0.04	99.85	10.87	4.44	0.05	0.79	3.56	4.48	0.09	0.02	0.01	24.30	4.89	58.81	71.01
66BRG CEW	49.77	15.46	0.12	5.37	17.65	10.61	0.22	0.06	0.15	99.41	10.35	4.79	0.02	1.06	3.88	4.16	0.09	0.01	0.03	24.41	6.56	56.34	68.34
CEX	50.66	15.72	0.15	4.79	17.30	11.03	0.20	0.06	0.15	100.06	10.41	4.82	0.03	0.94	3.76	4.27	0.09	0.01	0.03	24.36	5.80	58.81	68.36
CEY	50.13	15.63	0.09	5.32	17.42	10.88	0.20	0.04	0.15	99.86	10.35	4.81	0.02	1.05	3.81	4.24	0.09	0.01	0.03	24.40	6.45	56.34	68.26
CEZ	51.76	13.80	0.15	5.62	17.94	10.42	0.25	0.03	0.13	100.11	10.80	4.29	0.03	1.12	3.96	4.10	0.10	0.01	0.03	24.43	6.88	58.81	71.55
CFA	51.29	13.69	0.12	6.17	17.77	10.49	0.21	0.04	0.13	99.91	10.74	4.27	0.02	1.23	3.94	4.14	0.09	0.01	0.03	24.47	7.57	56.34	71.53
CFB	54.40	12.53	0.21	4.27	17.81	10.38	0.24	0.03	0.13	100.00	11.37	3.90	0.04	0.85	3.94	4.09	0.10	0.01	0.03	24.32	5.26	58.81	74.43
Brag96 CFC	55.09	11.38	0.10	5.41	16.37	11.14	0.21	0.06	0.09	99.85	11.57	3.56	0.02	1.08	3.64	4.41	0.10	0.01	0.02	24.41	6.67	56.34	76.45
CFD	54.78	12.43	0.12	4.60	16.17	11.38	0.23	0.06	0.07	99.84	11.40	3.86	0.02	0.91	3.56	4.47	0.10	0.01	0.01	24.35	5.63	58.81	74.72

CFB	55.46	13.25	0.16	3.27	15.62	11.93	0.18	0.04	0.04	99.95	11.39	4.06	0.03	0.64	3.39	4.62	0.09	0.01	0.01	24.24	3.97	56.34	73.73
CFF	55.16	12.56	0.15	4.16	15.88	11.64	0.18	0.06	0.06	99.85	11.43	3.88	0.03	0.82	3.48	4.55	0.09	0.01	0.01	24.31	5.08	58.81	74.65
CFC	54.35	11.97	0.13	4.79	15.86	11.36	0.20	0.06	0.03	98.75	11.45	3.76	0.03	0.96	3.54	4.51	0.09	0.01	0.01	24.37	5.94	56.34	75.28
Monitor Cr2O3		Al2O3	TiO2	Fe2O3	FeO	MgO	MnO	NiO	ZnO	Total	Cr	Al	Ti	Fe3+	Fe2+	Mg	Mn	Ni	Zn	Total	100Fe3+	100Mg*	100Cr*			
CFH	55.26	12.33	0.13	4.25	15.78	11.63	0.17	0.07	0.07	99.68	11.49	3.82	0.03	0.84	3.47	4.56	0.09	0.01	0.01	24.32	5.20	58.81	75.03
123BG CFI	49.56	14.98	0.15	6.48	17.84	10.58	0.25	0.06	0.16	100.06	10.31	4.65	0.03	1.28	3.93	4.15	0.10	0.01	0.03	24.49	7.90	56.34	68.93
CFJ	49.68	15.07	0.17	6.40	17.86	10.65	0.30	0.06	0.07	100.25	10.31	4.66	0.03	1.26	3.92	4.16	0.11	0.01	0.01	24.48	7.78	58.81	68.85
CFK	49.95	14.66	0.15	6.49	17.71	10.64	0.25	0.06	0.09	99.94	10.42	4.54	0.03	1.29	3.91	4.18	0.10	0.01	0.02	24.49	7.93	56.34	69.64
CFL	49.72	15.37	0.17	5.68	17.13	11.00	0.25	0.09	0.06	99.47	10.32	4.76	0.03	1.12	3.76	4.30	0.10	0.02	0.01	24.43	6.92	58.81	68.45
CFM	49.62	15.10	0.18	6.04	17.50	10.77	0.23	0.09	0.09	99.62	10.33	4.69	0.04	1.20	3.85	4.23	0.10	0.02	0.02	24.46	7.38	56.34	68.78
CFN	49.33	15.64	0.18	5.95	16.80	11.29	0.22	0.07	0.09	99.57	10.21	4.83	0.04	1.17	3.68	4.40	0.09	0.01	0.02	24.45	7.23	58.81	67.90
134BRG CFT	46.65	13.26	0.03	8.31	21.73	7.24	0.30	0.06	0.36	97.94	10.28	4.36	0.01	1.74	5.07	3.01	0.12	0.01	0.07	24.67	10.64	58.81	70.23
CFU	53.57	9.12	0.04	5.88	22.54	6.33	0.30	0.03	0.29	98.09	11.98	3.04	0.01	1.25	5.33	2.67	0.12	0.01	0.06	24.48	7.69	56.34	79.75
CFT	48.38	11.02	0.04	8.53	22.16	6.64	0.32	0.03	0.39	97.51	10.88	3.69	0.01	1.83	5.27	2.81	0.12	0.01	0.08	24.71	11.14	58.81	74.64
CFO	53.99	8.13	0.04	6.27	21.69	6.62	0.31	0.03	0.31	97.39	12.21	2.74	0.01	1.35	5.19	2.82	0.13	0.01	0.07	24.52	8.28	58.81	81.66
H2B QWE	55.80	12.27	0.15	4.35	14.82	12.51	0.18	0.04	0	100.11	11.52	3.78	0.03	0.85	3.23	4.87	0.04	0.01	0	24.32	5.29	60.07	75.31
WER	55.82	12.20	0.16	4.32	14.75	12.53	0.17	0.04	0	99.99	11.53	3.76	0.03	0.85	3.22	4.88	0.04	0.01	0	24.32	5.26	60.21	75.42
ERT	55.50	12.26	0.18	4.26	14.74	12.46	0.21	0.04	0	99.64	11.50	3.79	0.04	0.84	3.23	4.87	0.05	0.01	0	24.32	5.21	60.11	75.22
RTY	56.07	12.23	0.16	4.30	14.66	12.65	0.18	0.04	0	100.29	11.54	3.75	0.03	0.84	3.19	4.91	0.04	0.01	0	24.32	5.22	60.59	75.46
TYU	55.95	11.96	0.13	4.29	14.74	12.42	0.18	0.06	0	99.73	11.61	3.70	0.03	0.85	3.24	4.86	0.04	0.01	0	24.32	5.24	60.02	75.83
YUI	55.51	12.08	0.15	4.45	14.58	12.50	0.21	0.04	0	99.52	11.53	3.74	0.03	0.88	3.20	4.89	0.05	0.01	0	24.33	5.45	60.43	75.50
UIO	55.88	12.08	0.16	4.20	15.09	12.26	0.20	0.04	0	99.91	11.58	3.73	0.03	0.83	3.31	4.79	0.04	0.01	0	24.31	5.13	59.14	75.62
H4 LZX	56.00	12.23	0.16	4.32	14.89	12.48	0.21	0.06	0	100.35	11.54	3.76	0.03	0.85	3.25	4.85	0.05	0.01	0	24.32	5.25	59.89	75.43
ZXC	56.31	12.13	0.16	4.07	14.92	12.44	0.20	0.06	0	100.29	11.60	3.73	0.03	0.80	3.25	4.83	0.05	0.01	0	24.30	4.95	59.77	75.69
IOA	50.63	17.39	0.18	3.40	14.96	12.86	0.15	0.07	0	99.64	10.21	5.23	0.03	0.65	3.19	4.89	0.03	0.01	0	24.25	4.06	60.51	66.13
OAS	44.81	16.02	0.22	7.23	11.84	13.53	0.20	0.20	0	94.06	9.64	5.14	0.05	1.48	2.69	5.49	0.05	0.04	0	24.57	9.11	67.06	65.23
ASD	51.93	15.87	0.17	3.92	15.25	12.55	0.18	0.06	0	99.93	10.55	4.81	0.03	0.76	3.28	4.81	0.04	0.01	0	24.29	4.70	59.45	68.69
HP1 SDF	53.33	14.71	0.13	3.85	15.53	12.27	0.17	0.04	0	100.02	10.90	4.48	0.03	0.75	3.36	4.73	0.04	0.01	0	24.28	4.64	58.47	70.85
DFG	51.77	15.93	0.17	3.92	15.35	12.49	0.19	0.03	0	99.85	10.53	4.83	0.03	0.76	3.30	4.79	0.04	0.01	0	24.29	4.70	59.19	68.55
FGH	51.31	16.34	0.17	3.78	15.09	12.60	0.20	0.09	0	99.58	10.43	4.95	0.03	0.73	3.24	4.83	0.04	0.02	0	24.28	4.54	59.81	67.80
HP4 GHJ	52.84	14.69	0.15	4.05	15.38	12.18	0.18	0.23	0	99.70	10.84	4.50	0.03	0.79	3.34	4.71	0.04	0.05	0	24.30	4.91	58.52	70.69
HJK	52.39	15.58	0.17	4.02	15.51	12.44	0.17	0.07	0	100.35	10.63	4.71	0.03	0.78	3.33	4.76	0.04	0.01	0	24.29	4.81	58.83	69.28
JKL	51.00	16.93	0.15	3.91	15.22	12.76	0.13	0.04	0	100.14	10.28	5.09	0.03	0.75	3.25	4.85	0.03	0.01	0	24.28	4.65	59.90	66.89
KLZ	51.96	14.03	0.20	4.18	15.76	11.63	0.19	0.09	0	98.04	10.90	4.39	0.04	0.83	3.50	4.60	0.04	0.02	0	24.32	5.18	56.81	71.29
Standard ABY	59.94	10.47	0.22		15.56	13.37	0.35	0.10	0	100.01													
QWE1	48.55	19.10	0.12	3.67	18.06	11.23	0.20	0.06	0	100.98	9.72	5.70	0.02	0.70	3.83	4.24	0.04	0.01	0	24.26	4.33	52.56	63.02
WER1	47.77	18.72	0.09	3.09	19.60	9.80	0.23	0.07	0	99.37	9.79	5.72	0.02	0.60	4.25	3.79	0.05	0.01	0	24.23	3.74	47.12	63.12
ERT1	46.39	18.71	0.09	3.03	18.38	10.12	0.20	0.06	0	96.99	9.68	5.82	0.02	0.60	4.06	3.98	0.05	0.01	0	24.23	3.74	49.52	62.44
RTY1	47.58	19.09	0.09	3.62	17.81	11.05	0.20	0.09	0	99.53	9.66	5.78	0.02	0.70	3.82	4.23	0.04	0.02	0	24.27	4.34	52.51	62.57
YUI1	48.08	18.94	0.11	3.55	18.21	10.91	0.20	0.07	0	100.06	9.73	5.71	0.02	0.68	3.90	4.16	0.04	0.01	0	24.26	4.24	51.64	62.99
UIO1	49.27	19.81	0.12	3.04	13.78	13.95	0.13	0.10	0	100.20	9.71	5.82	0.02	0.57	2.87	5.18	0.03	0.02	0	24.22	3.54	64.34	62.52
IOP1	53.81	11.85	0.09	4.98	22.66	7.42	0.36	0.04	0	101.21	11.44	3.76	0.02	1.01	5.10	2.97	0.08	0.01	0	24.38	6.21	36.85	75.28
OPA1	52.73	11.66	0.16	5.56	22.09	7.65	0.26	0.08	0	100.20	11.33	3.74	0.03	1.14	5.02	3.10	0.06	0.02	0	24.43	7.02	38.16	75.20
PAS1	51.24	13.11	0.13	5.90	21.84	7.98	0.33	0.11	0	100.64	10.88	4.15	0.03	1.19	4.91	3.20	0.07	0.02	0	24.46	7.35	39.43	72.38
SDF1	50.67	13.44	0.12	6.23	21.78	8.10	0.33	0.06	0	100.73	10.74	4.25	0.02	1.26	4.89	3.24	0.07	0.01	0	24.48	7.74	39.85	71.66
DFG1	51.49	13.35	0.18	5.87	22.11	8.05	0.30	0.10	0	101.45	10.84	4.19	0.04	1.18	4.92	3.19	0.07	0.02	0	24.45	7.26	39.35	72.12

Mnemonic	Cr2O3	Al2O3	TiO2	Fe2O3	FeO	MgO	MnO	NiO	ZnO	Total	Cr	Al	Ti	Fe3+	Fe2+	Mg	Mn	Ni	Zn	Total	100*Fe3+	100*Mg*	100*Cr*
PGRE	39.48	12.77	0.12	5.01	22.48	7.98	0.36	0.07	•	101.60	11.06	3.99	0.02	1.18	5.06	3.04	0.08	0.02	•	24.45	7.25	57.54	73.51
GRUE	32.23	13.60	0.15	5.10	18.74	10.02	0.29	0.06	•	100.19	10.92	4.34	0.03	1.02	4.15	3.95	0.07	0.01	•	24.39	6.28	48.79	72.03
KLAS	31.90	13.86	0.15	5.36	18.67	10.14	0.28	0.05	•	100.26	10.83	4.31	0.03	1.04	4.12	3.99	0.06	0.01	•	24.40	6.43	49.19	71.52
MPRA	34.48	13.88	0.16	3.29	17.19	11.13	0.24	0.05	•	100.45	11.20	4.25	0.03	0.64	3.74	4.31	0.05	0.02	•	24.24	4.00	53.57	72.47
NBVI	34.02	13.27	0.13	4.40	17.61	10.78	0.26	0.07	•	100.56	11.19	4.10	0.03	0.87	3.86	4.21	0.06	0.01	•	24.33	5.37	52.17	73.19
BVCS	34.23	13.52	0.16	3.77	17.66	10.78	0.25	0.06	•	100.45	11.21	4.17	0.03	0.74	3.86	4.20	0.06	0.02	•	24.28	4.60	52.10	72.90
VCRS	34.65	13.15	0.10	4.05	17.47	10.88	0.24	0.07	•	100.63	11.30	4.05	0.02	0.90	3.82	4.24	0.05	0.01	•	24.30	4.93	52.60	73.59
VCR4	32.91	14.36	0.16	3.65	18.27	10.42	0.25	0.03	•	100.04	10.96	4.43	0.03	0.72	4.00	4.07	0.06	0.01	•	24.27	4.47	50.41	71.19
Standard ABT	60.21	10.28	0.21		15.44	13.36	0.33	0.13	•	99.96									•				
Rep#2 MRB	31.66	13.91	0.18	4.97	16.31	11.57	0.22	0.09	•	98.72	10.83	4.35	0.04	0.99	3.62	4.49	0.05	0.02	•	24.38	6.14	55.40	71.35
NBV	30.32	14.98	0.18	5.76	15.41	12.15	0.19	0.10	•	99.00	10.42	4.64	0.04	1.14	3.38	4.75	0.04	0.02	•	24.43	7.03	58.42	69.21
VCR	30.79	14.15	0.18	6.04	15.80	11.82	0.23	0.09	•	99.09	10.60	4.41	0.04	1.20	3.49	4.65	0.05	0.02	•	24.46	7.40	57.15	70.65
BTTMB CRB	47.53	16.87	0.26	6.34	14.96	12.61	0.20	0.10	•	98.79	9.79	5.18	0.04	1.24	3.26	4.90	0.04	0.02	•	24.48	7.66	60.03	65.38
XDL	38.42	12.60	0.18	5.47	16.46	11.16	0.26	0.04	•	99.01	11.29	3.79	0.04	1.10	3.68	4.45	0.06	0.01	•	24.42	6.80	54.72	74.86
ZLK	40.57	17.12	0.14	3.59	15.90	11.93	0.16	0.09	•	98.50	10.17	5.24	0.03	0.70	3.45	4.63	0.04	0.02	•	24.27	4.33	57.21	66.00
LKJ	35.12	16.78	0.16	5.33	16.78	10.87	0.24	0.07	•	99.35	11.70	3.41	0.03	1.08	3.77	4.33	0.05	0.02	•	24.41	6.66	53.58	77.42
KJH	40.14	16.55	0.14	5.35	15.09	12.42	0.24	0.10	•	99.14	10.08	5.06	0.03	1.05	3.28	4.80	0.08	0.02	•	24.40	6.46	59.45	66.57
JHG	40.50	16.46	0.24	5.00	15.39	12.44	0.15	0.07	•	99.25	10.14	5.03	0.05	0.97	3.33	4.80	0.03	0.01	•	24.37	6.04	59.02	66.85
HGF	40.66	15.75	0.24	5.09	15.41	12.31	0.16	0.09	•	99.11	10.24	4.84	0.05	1.08	3.36	4.79	0.04	0.02	•	24.41	6.66	58.73	67.89
GPD	41.81	15.85	0.20	5.08	15.31	12.28	0.21	0.07	•	98.81	10.28	4.88	0.04	1.00	3.34	4.78	0.05	0.01	•	24.38	6.18	58.84	67.82
FDB	40.36	15.93	0.23	4.98	15.45	12.37	0.19	0.06	•	99.47	10.30	4.87	0.04	0.97	3.35	4.78	0.04	0.01	•	24.37	6.02	58.80	67.90
DBA	39.45	15.80	0.21	4.83	15.34	12.42	0.20	0.05	•	99.31	10.36	4.84	0.04	0.94	3.31	4.81	0.04	0.01	•	24.36	5.85	59.22	68.16
BAP	40.47	16.25	0.23	5.36	14.98	12.57	0.20	0.09	•	97.95	10.07	5.03	0.05	1.06	3.29	4.84	0.04	0.02	•	24.40	6.56	59.53	66.67
Standard ABT	60.53	10.23	0.19		15.38	13.28	0.33	0.10	•	100.04									•				
APO	49.53	17.13	0.17	4.26	14.44	12.95	0.18	0.14	•	98.77	10.10	5.21	0.03	0.83	3.11	4.97	0.04	0.03	•	24.31	5.12	61.46	65.97
FOS	49.39	17.91	0.14	3.96	14.43	13.14	0.16	0.06	•	99.19	9.97	5.39	0.03	0.76	3.08	5.00	0.04	0.01	•	24.29	4.72	61.88	64.90
ORU	49.39	17.91	0.15	4.13	14.93	12.78	0.16	0.04	•	99.57	10.19	5.14	0.03	0.80	3.21	4.99	0.03	0.01	•	24.30	4.93	60.41	66.46
YTR	50.20	16.99	0.18	4.84	20.34	9.88	0.26	0.03	•	99.83	10.57	4.62	0.04	0.97	4.51	3.59	0.06	0.01	•	24.37	5.98	44.31	69.57
TRE	51.18	13.59	0.13	5.03	20.57	8.67	0.33	0.03	•	99.53	10.67	4.30	0.03	1.03	4.68	3.47	0.07	0.01	•	24.39	6.28	42.90	71.63
BEW	47.11	14.34	0.14	6.44	19.56	8.85	0.34	0.05	•	96.82	10.26	4.66	0.03	1.34	4.51	3.63	0.08	0.01	•	24.51	8.22	44.63	68.78
EWQ	48.59	17.07	0.14	4.68	19.65	9.71	0.30	0.06	•	99.92	10.00	5.26	0.03	0.90	4.30	3.78	0.07	0.01	•	24.34	5.60	46.82	65.53
EKA	48.35	16.96	0.12	4.84	19.74	9.46	0.30	0.06	•	100.04	9.99	5.23	0.02	0.93	4.32	3.76	0.07	0.01	•	24.36	5.88	46.58	65.63
EKB	48.30	17.50	0.14	4.27	19.68	9.81	0.30	0.03	•	99.96	9.94	5.37	0.03	0.84	4.27	3.81	0.07	0.01	•	24.32	5.19	47.14	64.92
EKC	48.45	16.24	0.11	5.58	20.19	9.36	0.28	0.04	•	100.26	10.08	5.04	0.02	1.11	4.44	3.67	0.06	0.01	•	24.42	6.82	45.24	66.67
ZBRG MCA	51.21	16.01	0.15	3.46	14.41	12.67	0.16	0.08	0.01	98.08	10.52	4.91	0.03	0.68	3.13	4.91	0.08	0.00	0.00	24.26	4.21	58.81	68.20
MCB	50.47	16.52	0.15	3.76	14.46	12.74	0.13	0.08	0.03	98.25	10.34	5.06	0.03	0.73	3.13	4.92	0.07	0.00	0.01	24.28	4.55	56.34	67.20
MCC	51.29	16.10	0.15	3.31	14.72	12.52	0.11	0.07	0.03	98.25	10.52	4.93	0.03	0.65	3.20	4.84	0.07	0.00	0.01	24.24	4.02	58.81	68.11
MCD	51.78	14.52	0.17	4.36	15.18	12.07	0.12	0.05	0.00	98.23	10.77	4.50	0.03	0.86	3.34	4.73	0.07	0.01	0.00	24.33	5.34	56.34	70.51
MCE	51.87	12.19	0.17	6.25	13.34	12.72	0.12	0.06	0.03	96.73	11.08	3.88	0.03	1.27	3.01	5.12	0.08	0.00	0.01	24.49	7.83	58.81	74.05
MCF	51.38	15.51	0.15	3.87	14.55	12.52	0.12	0.04	0.07	98.21	10.59	4.77	0.03	0.76	3.17	4.87	0.07	0.01	0.02	24.34	4.71	56.34	68.96
MCG	52.99	13.90	0.16	4.46	17.94	10.19	0.22	0.00	0.09	98.85	11.01	4.34	0.03	0.89	4.00	4.05	0.10	0.00	0.02	24.34	5.54	58.81	72.20
MCH	49.69	15.77	0.15	3.43	17.30	10.80	0.26	0.03	0.13	98.57	10.22	4.90	0.03	1.08	3.81	4.34	0.10	0.01	0.03	24.41	6.65	56.34	67.61
MCI	49.52	15.08	0.17	5.61	17.38	10.64	0.22	0.09	0.16	98.87	10.37	4.71	0.03	1.12	3.85	4.20	0.09	0.02	0.03	24.43	6.90	58.81	68.77
MCJ	49.36	17.58	0.20	3.58	16.91	11.36	0.22	0.04	0.10	99.27	10.06	5.34	0.04	0.68	3.65	4.57	0.09	0.01	0.02	24.26	4.22	56.34	65.31
MCK	49.16	17.23	0.17	4.05	16.83	11.29	0.22	0.07	0.15	99.18	10.07	5.26	0.03	0.79	3.65	4.36	0.09	0.01	0.03	24.30	4.90	58.81	65.67

MCL	49.89	15.85	0.17	4.64	17.26	10.92	0.19	0.01	0.13	99.06	10.34	4.90	0.03	0.92	3.78	4.27	0.09	0.00	0.03	24.35	5.67	56.34	67.85
Mean88er	Cr2O3	Al2O3	TiO2	Fe2O3	FeO	MgO	MnO	NiO	ZnO	Total	Cr	Al	Ti	Fe3+	Fe2+	Mg	Mn	Ni	Zn	Total	100Fe3*	100Mg*	100Cr*
Standard ABT	60.08	10.42	0.21		15.32	13.42	0.30	0.12		99.87													
171BRG MAC	48.08	18.24	0.23	5.46	15.15	12.81	0.20	0.06	0.16	100.38	9.65	5.46	0.04	1.04	3.22	4.85	0.08	0.01	0.03	24.40	6.45	56.34	63.87
MBC	47.08	18.24	0.23	5.46	15.15	12.81	0.20	0.06	0.12	99.79	9.60	5.52	0.04	1.05	3.20	4.87	0.08	0.01	0.02	24.40	6.50	56.34	63.47
MBC	47.57	18.36	0.20	5.48	15.00	12.80	0.20	0.06	0.15	100.00	9.77	5.33	0.03	1.09	3.24	4.83	0.08	0.01	0.03	24.42	6.76	56.34	64.70
MCC	48.28	17.66	0.18	5.68	15.12	12.67	0.20	0.06	0.15	100.00	9.66	5.45	0.03	1.08	3.16	4.91	0.08	0.02	0.02	24.41	6.66	56.34	63.94
MDC	47.63	18.01	0.18	5.58	14.75	12.83	0.19	0.09	0.10	99.36	9.66	5.45	0.03	1.08	3.16	4.91	0.08	0.02	0.02	24.41	6.66	56.34	63.94
MEC	48.41	18.43	0.21	4.89	14.73	13.06	0.19	0.07	0.10	100.09	9.70	5.51	0.04	0.93	3.12	4.93	0.08	0.01	0.02	24.35	5.78	56.34	63.79
MFC	47.72	18.13	0.24	5.83	14.95	12.90	0.22	0.12	0.07	100.17	9.61	5.44	0.05	1.12	3.18	4.90	0.09	0.02	0.01	24.43	6.91	56.34	63.83
Harzburgite																							
133BRG CFT	46.65	13.26	0.03	8.31	21.73	7.24	0.30	0.06	0.36	97.94	10.28	4.36	0.01	1.74	5.07	3.01	0.12	0.01	0.07	24.67	10.64	37.26	70.23
CFU	53.57	9.12	0.04	5.88	22.54	6.33	0.30	0.03	0.29	98.09	11.98	3.04	0.01	1.25	5.33	2.67	0.12	0.01	0.06	24.48	7.69	33.35	79.75
Standard ABT	59.13	10.12	0.19		15.17	13.37	0.33	0.10		98.41													
CFT	48.38	11.02	0.04	8.53	22.16	6.64	0.32	0.03	0.39	97.51	10.88	3.69	0.01	1.83	5.27	2.81	0.12	0.01	0.08	24.71	11.14	34.81	74.64
CFU	53.99	8.13	0.04	6.27	21.69	6.62	0.31	0.03	0.31	97.39	12.21	2.74	0.01	1.35	5.19	2.82	0.13	0.01	0.07	24.52	8.28	35.23	81.66
Standard ABT	59.80	10.14	0.21		15.59	13.32	0.32	0.14		99.52													
146BRG SIA	39.97	22.91	0.05	6.86	20.01	9.85	0.26	0.07	0.40	100.39	8.07	6.90	0.01	1.32	4.28	3.75	0.09	0.01	0.08	24.51	8.10	46.72	53.92
SIC	47.84	16.42	0.06	5.98	21.42	8.36	0.27	0.06	0.34	100.75	9.97	5.10	0.01	1.19	4.72	3.28	0.10	0.01	0.07	24.45	7.30	41.03	66.14
SID	35.36	17.83	0.05	16.28	16.13	11.80	0.24	0.11	0.29	98.09	7.61	5.73	0.01	3.34	3.67	4.79	0.09	0.02	0.06	25.32	20.01	56.59	57.08
Standard ABT	59.58	10.37	0.24		15.56	13.37	0.35	0.09	0.04	99.60													
Brag24 CUG	35.71	23.74	0.05	9.07	20.45	9.46	0.28	0.10	0.34	99.20	7.34	7.27	0.01	1.77	4.45	3.66	0.09	0.02	0.07	24.68	10.83	45.19	50.22
CUH	37.22	22.25	0.05	9.13	20.41	9.33	0.27	0.12	0.28	99.07	7.71	6.88	0.01	1.80	4.48	3.65	0.09	0.03	0.05	24.70	10.99	44.89	52.87
CUI	33.44	26.83	0.03	8.41	19.86	10.22	0.29	0.13	0.25	99.46	6.72	8.04	0.01	1.61	4.22	3.87	0.09	0.03	0.05	24.62	9.83	47.83	45.53
CUJ	33.14	26.62	0.03	8.18	20.13	9.79	0.26	0.16	0.35	98.66	6.72	8.05	0.01	1.58	4.32	3.74	0.08	0.03	0.07	24.61	9.65	46.42	45.50
Standard ABT	59.65	10.45	0.22		15.49	13.49	0.36	0.14	0.04	99.84													
Standard ABT	59.92	10.33	0.21		14.89	13.18	0.35	0.12	0.01	99.01													
Brag34 MHC	43.23	12.44	0.20	12.82	23.24	6.86	0.33	0.13	0.00	99.24	9.64	4.14	0.04	2.72	5.48	2.89	0.12	0.03	0.00	25.07	16.49	34.47	69.97
MIC	42.41	14.17	0.14	12.00	22.09	7.68	0.27	0.13	0.00	98.88	9.33	4.65	0.03	2.51	5.14	3.19	0.10	0.03	0.00	24.98	15.23	38.26	66.74
MJC	41.72	14.70	0.15	11.88	22.35	7.52	0.30	0.12	0.00	98.74	9.18	4.82	0.03	2.49	5.20	3.12	0.11	0.03	0.00	24.97	15.09	37.48	65.55
166BRG CMA	42.77	14.16	0.05	11.78	22.95	6.89	0.32	0.09	0.47	99.48	9.41	4.65	0.01	2.47	5.34	2.86	0.12	0.02	0.10	24.96	14.93	34.85	66.95
CMB	41.39	16.04	0.06	11.53	21.42	7.99	0.30	0.13	0.57	99.44	8.95	5.17	0.01	2.37	4.90	3.26	0.11	0.03	0.12	24.92	14.39	39.93	63.37
CMC	41.27	13.62	0.05	13.33	22.30	7.10	0.32	0.13	0.51	98.63	9.22	4.54	0.01	2.83	5.27	2.99	0.12	0.03	0.11	25.11	17.08	36.20	67.02
CMD	41.42	14.17	0.05	12.66	21.27	7.78	0.29	0.10	0.45	98.20	9.19	4.69	0.01	2.68	5.00	3.26	0.11	0.02	0.09	25.05	16.16	39.46	66.22
CME	40.30	14.46	0.06	13.67	23.34	6.68	0.27	0.16	0.61	99.55	8.93	4.78	0.01	2.88	5.47	2.79	0.10	0.04	0.13	25.13	17.38	33.78	65.14
Standard ABT	60.25	10.38	0.21		15.39	13.48	0.36	0.10	0.07	100.24													
191BRG MSA	50.56	14.13	0.06	4.92	21.76	7.71	0.32	0.04	0.25	99.75	10.74	4.48	0.01	1.00	4.89	3.09	0.12	0.01	0.05	24.38	6.14	38.70	70.58
MSB	46.22	13.85	0.06	7.64	19.67	8.42	0.32	0.04	0.22	96.44	10.19	4.55	0.01	1.60	4.59	3.50	0.12	0.01	0.05	24.62	9.81	43.27	69.11
MSC	49.94	15.20	0.06	4.84	21.58	8.08	0.27	0.03	0.25	100.24	10.48	4.76	0.01	0.97	4.79	3.20	0.11	0.01	0.05	24.37	5.96	40.02	68.78
MSD	50.06	14.81	0.07	4.90	21.90	7.78	0.27	0.04	0.29	100.12	10.56	4.66	0.01	0.98	4.89	3.09	0.11	0.01	0.06	24.37	6.08	38.77	69.39
MSE	50.47	14.17	0.04	4.84	21.51	7.81	0.30	0.01	0.28	99.43	10.74	4.50	0.01	0.98	4.84	3.13	0.11	0.00	0.06	24.37	6.05	39.28	70.49
Pyroxenites																							
43BRG SLA	44.59	14.39	0.21	9.15	17.88	9.85	0.27	0.00	0.23	96.57	9.75	4.69	0.04	1.90	4.14	4.06	0.11	0.00	0.05	24.74	11.65	49.54	67.51
SLB	47.75	16.24	0.20	5.01	22.57	7.56	0.25	0.00	0.28	99.86	10.05	5.10	0.04	1.00	5.03	3.00	0.10	0.00	0.06	24.38	6.22	37.38	66.35
Brag83 SBG	42.44	13.54	0.29	12.50	22.15	7.60	0.23	0.18	0.22	99.15	9.37	4.46	0.06	2.63	5.17	3.16	0.09	0.04	0.05	25.03	15.96	37.94	67.76
Standard ABT	59.62	10.23	0.21		15.54	13.35	0.32	0.10	0.09	99.46													

Mineralogy	Cr2O3	Al2O3	TiO2	Fe2O3	FeO	MgO	MnO	NiO	ZnO	Total	Cr	Al	Ti	Fe3+	Fe2+	Mg	Mn	Ni	Zn	Total	100Fe3*	100Mg*	100Cr*
141 BRG CEA	40.70	19.81	0.37	6.55	24.44	6.64	0.34	0.09	0.22	99.09	8.60	6.24	0.07	1.32	5.46	2.64	0.11	0.01	0.04	24.50	8.15	32.63	57.94
CEO	41.08	17.95	0.41	7.74	24.96	6.09	0.33	0.01	0.22	98.71	8.84	5.77	0.08	1.59	5.69	2.48	0.11	0.00	0.04	24.61	9.81	30.30	60.50
CEH	41.05	17.88	0.50	7.61	25.08	6.07	0.31	0.01	0.23	98.74	8.85	5.75	0.10	1.56	5.72	2.47	0.11	0.00	0.05	24.60	9.67	30.13	60.62
CEI	42.26	16.58	0.53	7.90	25.63	5.64	0.36	0.04	0.22	99.16	9.16	5.36	0.11	1.63	5.88	2.31	0.12	0.01	0.04	24.63	10.10	28.17	63.09
CEK	41.18	19.88	0.37	5.88	24.64	6.51	0.33	0.01	0.22	99.01	8.69	6.26	0.07	1.18	5.50	2.39	0.11	0.00	0.04	24.45	7.33	32.01	58.14
Brag93 CEQ	46.32	11.98	0.28	10.28	23.50	6.57	0.25	0.13	0.19	99.50	10.25	3.95	0.06	2.16	5.50	2.74	0.10	0.03	0.04	24.84	13.23	33.25	72.17
CER	44.46	13.45	0.18	10.86	21.57	7.87	0.24	0.10	0.15	98.88	9.76	4.40	0.04	2.27	5.01	3.26	0.10	0.02	0.03	24.88	13.81	39.41	68.91
CES	40.43	18.25	0.15	10.58	18.21	10.48	0.17	0.13	0.16	98.56	8.54	5.75	0.03	2.13	4.07	4.17	0.07	0.03	0.03	24.82	12.95	50.63	59.77
Standard ABT	39.63	10.60	0.22		15.41	13.29	0.32	0.10	0.04	99.61													
CET	45.77	13.39	0.24	9.77	23.47	6.80	0.25	0.11	0.22	100.02	9.98	4.35	0.05	2.03	5.41	2.79	0.10	0.02	0.04	24.78	12.39	34.05	69.62
CEV	42.88	14.37	0.15	11.81	17.58	10.29	0.25	0.09	0.21	97.63	9.35	4.67	0.03	2.45	4.06	4.23	0.10	0.02	0.04	24.96	14.88	51.05	66.68
CEV	44.06	14.91	0.17	9.89	19.96	8.92	0.21	0.08	0.22	98.42	9.54	4.81	0.04	2.04	4.57	3.64	0.09	0.02	0.04	24.79	12.43	44.33	66.46
CEZ	43.52	13.99	0.20	11.00	21.05	8.19	0.23	0.08	0.19	98.45	9.55	4.58	0.04	2.30	4.89	3.39	0.09	0.02	0.04	24.89	13.99	40.95	67.60
43BRG CFE	30.07	14.13	0.18	4.48	23.22	6.84	0.24	0.00	0.22	99.39	10.72	4.51	0.04	0.91	5.26	2.76	0.10	0.00	0.04	24.35	5.66	34.42	70.38
Cassinho Valley/Vinhas																							
76BRG THG	16.41	46.04	0.07	6.08	16.32	14.95	0.17	•		0.00	100.04	2.93	12.26	0.01	1.03	3.08	5.03	0.05	0.00	•		24.39	6.37	62.01	19.29
THH	15.50	44.22	0.07	7.81	14.12	15.73	0.15	•		0.00	97.60	2.84	12.09	0.01	1.36	2.74	5.44	0.04	0.00	•		24.52	8.37	66.50	19.03
THF	18.28	43.34	0.05	6.19	17.98	13.47	0.15	•		0.00	99.46	3.34	11.82	0.01	1.08	3.48	4.64	0.04	0.00	•		24.41	6.64	57.17	22.05
THE	16.13	46.47	0.03	5.27	16.70	14.57	0.18	•		0.00	99.34	2.89	12.42	0.01	0.90	3.16	4.92	0.05	0.00	•		24.34	5.55	60.86	18.88
73BRG THO	10.67	56.04	0.03	1.95	13.27	18.01	0.08	•		0.00	100.05	1.78	13.97	0.00	0.31	2.35	5.68	0.02	0.00	•		24.12	1.94	70.74	11.32
THQ	9.74	57.00	0.03	2.00	12.62	18.51	0.10	•		0.00	100.00	1.62	14.13	0.00	0.32	2.22	5.80	0.02	0.00	•		24.12	1.97	72.33	10.28
96BRG THU	35.29	14.60	2.41	13.28	28.12	5.24	0.40	0.10	0.00	99.44	7.89	4.87	0.51	2.83	6.65	2.21	0.13	0.02	•			25.11	18.13	34.93	61.84
THV	33.40	13.60	2.46	15.41	28.69	4.75	0.43	0.16	0.00	98.90	7.64	4.64	0.54	3.35	6.94	2.05	0.14	0.04	•			25.33	21.46	22.78	62.22
THW	34.47	14.47	2.26	13.64	28.10	4.96	0.38	0.12	0.00	98.40	7.82	4.89	0.49	2.94	6.74	2.12	0.13	0.03	•			25.16	18.81	23.93	61.50
THX	37.24	16.98	1.62	10.47	26.15	6.16	0.31	0.10	0.00	99.03	8.12	5.52	0.34	2.17	6.03	2.53	0.11	0.02	•			24.84	13.74	29.57	59.53
Standard ABT	39.29	10.14	0.21		15.55	13.37	0.32	0.13		99.01													
100BRG SEJ	33.84	23.54	0.47	9.27	25.58	6.39	0.34	0.13	0.44	100.00	7.06	7.33	0.09	1.84	5.65	2.51	0.11	0.03	0.09	24.71	11.34	30.80	49.08
SEL	33.71	13.16	1.25	17.99	29.07	4.03	0.42	0.15	0.22	100.00	7.77	4.52	0.27	3.95	7.09	1.75	0.14	0.04	0.05	25.58	24.31	19.81	63.20
76BRG GGD	14.16	49.35	0.07	4.86	14.19	16.56	0.12	•		0.00	99.33	2.48	12.88	0.01	0.81	2.63	5.46	0.03	0.00	0.00		24.31	5.03	67.53	16.14
GGE	13.92	49.62	0.07	5.12	14.06	16.73	0.14	•		0.00	99.66	2.43	12.90	0.01	0.85	2.59	5.50	0.04	0.00	0.00		24.32	5.25	67.96	15.83
GGF	14.13	50.40	0.05	3.99	14.84	16.34	0.12	•		0.00	99.87	2.45	13.03	0.01	0.66	2.72	5.34	0.03	0.00	0.00		24.25	4.08	66.24	15.82
96BRG CUA	36.80	18.49	1.75	9.33	25.80	6.52	0.38	0.10	0.12	99.30	7.90	5.92	0.36	1.91	5.86	2.64	0.12	0.02	0.02	24.74	12.13	31.05	57.17
CUC	37.61	17.74	5.03	2.91	28.69	6.38	0.31	0.09	0.07	98.83	7.95	5.59	1.01	0.59	6.41	2.54	0.10	0.02	0.01	24.22	4.15	28.38	58.71
CUD	37.83	25.36	0.84	3.26	23.13	8.45	0.30	0.04	0.12	99.34	7.60	7.61	0.16	0.62	4.92	3.20	0.10	0.01	0.02	24.24	3.94	39.43	49.99
CUE	35.20	19.10	2.31	9.31	26.81	6.29	0.38	0.09	0.22	99.71	7.52	6.08	0.47	1.89	6.06	2.53	0.12	0.02	0.04	24.73	12.22	29.48	55.27
CUF	36.65	15.16	2.11	12.00	27.23	5.44	0.41	0.11	0.31	99.43	8.12	5.01	0.44	2.53	6.38	2.27	0.13	0.02	0.06	24.99	16.17	26.25	61.85
Other																							
32BRG SEO	40.59	20.85	0.18	6.32	23.76	7.00	0.30	0.00	0.59	99.58	8.48	6.49	0.04	1.26	5.25	2.76	0.10	0.00	0.12	24.48	7.74	34.43	56.62
SEP	52.21	11.65	0.18	4.95	24.69	5.56	0.33	0.01	0.45	100.03	11.36	3.78	0.04	1.03	5.68	2.28	0.13	0.00	0.09	24.39	6.34	28.64	75.03
SEQ	46.54	15.32	0.24	6.09	23.51	6.55	0.31	0.04	0.45	99.05	10.03	4.92	0.05	1.25	5.36	2.66	0.12	0.01	0.09	24.48	7.71	33.17	67.07
SER	42.92	19.58	0.21	5.65	23.17	7.28	0.29	0.07	0.53	99.69	8.96	6.10	0.04	1.12	5.12	2.87	0.10	0.01	0.10	24.43	6.94	35.90	59.51
SES	42.26	20.00	0.17	5.47	23.31	7.08	0.31	0.03	0.60	99.26	8.85	6.25	0.03	1.09	5.17	2.80	0.11	0.01	0.12	24.42	6.74	35.11	58.64
Standard ABT	40.21	10.21	0.19		15.47	13.31	0.35	0.08	•	99.82													
80BRG SEN	46.53	10.35	0.24	11.62	24.30	5.93	0.48	0.04	•	99.50	10.48	3.48	0.05	2.49	5.79	2.52	0.16	0.01	•		24.97	15.15	30.31	75.09
SLO	45.85	7.58	0.30	14.14	25.27	4.97	0.51	0.08	•	98.70	10.73	2.65	0.07	3.15	6.26	2.19	0.17	0.02	•		25.24	19.07	25.95	80.22

SLP	47.07	9.09	0.30	12.93	24.74	5.76	0.49	0.11	•	100.50	10.63	3.06	0.06	2.78	5.91	2.45	0.16	0.03	•	25.09	16.88	29.32	77.64
SLQ	46.43	8.97	0.31	13.23	25.00	5.52	0.48	0.10	•	100.05	10.57	3.05	0.07	2.87	6.02	2.37	0.16	0.02	•	25.13	17.40	28.23	77.63
SLS	45.81	7.60	0.33	15.26	25.79	5.08	0.48	0.10	•	100.45	10.58	2.62	0.07	3.36	6.30	2.21	0.16	0.02	•	25.33	20.27	25.98	80.17
Mnemonic	Cr2O3	Al2O3	TiO2	Fe2O3	FeO	MgO	MnO	NiO	ZnO	Total	Cr	Al	Ti	Fe3+	Fe2+	Mg	Mn	Ni	Zn	Total	100Fe3+/	100Mg/	100Cr/
Grain Scan																							
Standard ABY	60.06	10.32	0.22		15.40	13.25	0.35	0.08	0.04	99.72	10.77	3.27	0.05	2.39	5.39	2.88	0.14	0.00	0.03	24.93	14.54	34.83	76.71
Brag9 C8A	47.83	9.74	0.22	11.14	22.64	6.79	0.41	0.00	0.13	98.91	10.77	3.27	0.05	2.39	5.39	2.88	0.14	0.00	0.03	24.93	14.54	34.83	76.71
C8B	46.77	18.84	0.09	4.87	19.04	10.16	0.27	0.00	0.25	100.29	9.53	5.72	0.02	0.94	4.10	3.90	0.10	0.00	0.05	24.36	5.83	48.74	62.47
C8D	47.09	19.15	0.17	4.22	19.04	10.30	0.24	0.00	0.23	100.44	9.53	5.78	0.03	0.81	4.08	3.93	0.09	0.00	0.04	24.31	5.05	49.08	62.25
C8E	46.98	19.16	0.17	4.28	19.05	10.23	0.29	0.00	0.29	100.45	9.52	5.79	0.03	0.83	4.08	3.91	0.10	0.00	0.05	24.31	5.12	48.91	62.18
C8F	46.15	19.21	0.15	4.53	19.09	10.10	0.28	0.00	0.22	99.72	9.42	5.85	0.03	0.88	4.12	3.89	0.10	0.00	0.04	24.33	5.45	48.53	61.70
C8G	46.24	18.81	0.11	4.90	19.14	10.00	0.25	0.00	0.25	99.70	9.48	5.75	0.02	0.96	4.15	3.86	0.09	0.00	0.05	24.36	5.91	48.21	62.24
C8H	46.98	10.47	0.21	11.79	22.51	7.11	0.39	0.00	0.17	99.63	10.48	3.48	0.04	2.50	5.31	2.99	0.14	0.00	0.04	24.98	15.21	36.02	75.06
Standard ABY	59.12	10.26	0.22		15.26	13.15	0.33	0.09	0.03	98.46													
Brag9 C8I	46.44	11.87	0.18	10.50	21.80	7.49	0.35	0.00	0.20	98.84	10.28	3.92	0.04	2.21	5.11	3.13	0.13	0.00	0.04	24.86	13.48	37.97	72.40
C8J	48.02	16.30	0.11	5.25	19.32	9.40	0.30	0.00	0.25	98.85	10.08	5.07	0.02	1.05	4.29	3.72	0.11	0.00	0.04	24.40	6.48	46.43	66.53
C8K	48.83	17.13	0.14	4.84	19.68	9.72	0.27	0.00	0.23	100.85	10.00	5.23	0.03	0.94	4.26	3.75	0.10	0.00	0.04	24.36	5.84	46.81	65.65
C8L	47.76	16.94	0.12	4.99	19.39	9.54	0.27	0.00	0.26	99.27	9.94	5.26	0.02	0.99	4.27	3.74	0.10	0.00	0.05	24.38	6.11	46.72	65.40
C8M	49.35	9.41	0.16	10.01	22.33	6.82	0.41	0.00	0.13	98.63	11.11	3.16	0.03	2.15	5.32	2.89	0.15	0.00	0.03	24.83	13.07	35.24	77.86
Standard ABY	59.97	10.34	0.22		15.25	13.20	0.33	0.14	•	99.45													
Brag57 N5W	49.95	14.72	0.15	6.13	18.09	10.43	0.45	0.04	•	99.96	10.43	4.58	0.03	1.22	4.00	4.10	0.10	0.01	•	24.47	7.51	50.67	69.47
N5X	49.57	15.75	0.17	5.90	17.71	10.89	0.45	0.07	•	100.51	10.21	4.84	0.03	1.16	3.86	4.23	0.10	0.01	•	24.44	7.14	52.29	67.85
N5Y	49.74	16.97	0.21	4.01	16.80	11.47	0.40	0.07	•	99.67	10.16	5.17	0.04	0.78	3.63	4.42	0.09	0.01	•	24.30	4.84	54.88	66.28
N5Z	48.97	15.97	0.15	5.28	16.98	11.07	0.42	0.04	•	98.88	10.19	4.95	0.03	1.05	3.74	4.34	0.09	0.01	•	24.40	6.46	53.75	67.28
SA0	50.45	13.32	0.16	6.62	18.31	10.03	0.43	0.07	•	99.39	10.70	4.21	0.03	1.34	4.11	4.01	0.10	0.02	•	24.51	8.23	49.39	71.75
SA1	53.77	14.83	0.15	3.82	12.83	13.85	0.30	0.10	•	99.65	10.90	4.48	0.03	0.74	2.75	5.29	0.07	0.02	•	24.28	4.57	65.79	70.86
Brag26 N5O	53.36	15.12	0.14	3.75	13.02	13.70	0.35	0.09	•	99.53	10.82	4.57	0.03	0.72	2.79	5.24	0.08	0.02	•	24.27	4.49	65.22	70.30
N5P	53.19	15.37	0.15	3.59	12.91	13.78	0.35	0.09	•	99.43	10.77	4.64	0.03	0.69	2.77	5.26	0.08	0.02	•	24.26	4.29	65.54	69.88
N5Q	54.05	15.54	0.15	3.57	13.03	14.03	0.33	0.07	•	100.77	10.80	4.63	0.03	0.68	2.75	5.28	0.07	0.01	•	24.26	4.22	65.75	69.99
N5R	53.32	15.53	0.17	3.89	12.99	13.93	0.35	0.10	•	100.28	10.72	4.65	0.03	0.74	2.76	5.28	0.08	0.02	•	24.28	4.62	65.65	69.72
N5S	53.34	15.11	0.17	4.08	12.94	13.83	0.36	0.09	•	99.96	10.78	4.56	0.03	0.79	2.77	5.27	0.08	0.02	•	24.30	4.87	65.51	70.30
N5T	52.91	15.49	0.15	3.66	12.80	13.86	0.33	0.07	•	99.27	10.72	4.68	0.03	0.71	2.74	5.30	0.07	0.01	•	24.27	4.38	65.87	69.61
N5U	54.78	14.94	0.16	3.56	13.30	13.80	0.36	0.11	•	101.02	10.96	4.46	0.03	0.68	2.82	5.21	0.08	0.02	•	24.26	4.22	64.90	71.09
N5V																							
Standard ABY mean of 24 analyses for comparison with results obtained																							
	59.95	10.33	0.22		15.41	13.31	0.34	0.11		99.79													

4b Olivine

Dunite/chromitite	SiO2	TiO2	Al2O3	FeO	MnO	MgO	CaO	NiO	Total	Si	Fe	Mn	Mg	Ni	Mg#
Drag39 OL3	41.50	0.02	0.00	6.39	0.11	51.09	0.01	0.26	99.38	1.01	0.13	0.00	1.85	0.01	0.93
OL2	41.54	0.02	0.00	6.61	0.11	51.01	0.00	0.27	99.56	1.00	0.13	0.00	1.85	0.01	0.93
OL1	41.50	0.02	0.00	6.42	0.11	51.22	0.01	0.26	99.55	1.00	0.13	0.00	1.86	0.01	0.93
OL1	41.05	0.00	0.02	6.24	0.11	49.84	0.04	0.29	96.82	1.02	0.13	0.00	1.85	0.01	0.93
OL5	41.28	0.02	0.00	6.68	0.11	50.93	0.01	0.26	99.30	1.00	0.14	0.00	1.85	0.01	0.93
OL1	41.36	0.02	0.00	6.75	0.11	51.07	0.01	0.26	99.54	1.00	0.14	0.00	1.86	0.01	0.93
OL1	40.84	0.02	0.10	7.00	0.11	48.80	0.03	0.27	97.17	1.01	0.14	0.00	1.82	0.01	0.93
Drag84 POC	41.23	0.02	0.00	5.98	0.09	51.49	0.01	0.44	99.26	1.00	0.12	0.00	1.87	0.01	0.94
POD	41.90	0.02	0.00	5.89	0.09	52.12	0.01	0.42	100.46	1.00	0.12	0.00	1.87	0.01	0.94
POF	41.45	0.02	0.00	5.98	0.09	51.43	0.03	0.47	99.47	1.00	0.12	0.00	1.86	0.01	0.94
POG	41.36	0.02	0.00	6.02	0.09	51.53	0.01	0.42	99.47	1.00	0.12	0.00	1.87	0.01	0.94
Drag31 IDE	41.43	0.02	0.00	5.98	0.09	51.40	0.01	0.48	99.43	1.00	0.12	0.00	1.86	0.01	0.94
IDF	41.40	0.02	0.00	4.82	0.09	52.29	0.01	0.51	99.15	1.00	0.10	0.00	1.89	0.01	0.95
IDH	40.96	0.02	0.00	4.81	0.06	51.52	0.01	0.53	97.94	1.00	0.10	0.00	1.89	0.01	0.95
Drag7 LOA	41.11	0.02	0.00	5.44	0.06	51.73	0.01	0.44	98.81	1.00	0.11	0.00	1.88	0.01	0.94
LOB	41.73	0.02	0.00	5.09	0.08	50.95	0.03	0.48	98.38	1.01	0.10	0.00	1.86	0.01	0.95
LOC	41.48	0.02	0.00	5.45	0.08	52.29	0.01	0.42	99.75	1.00	0.11	0.00	1.89	0.01	0.95
Harzburgite															
Drag24 PBB	41.80	0.02	0.00	8.86	0.16	49.69	0.01	0.00	100.54	1.01	0.18	0.00	1.80	0.00	0.91
PBF	41.50	0.02	0.00	8.72	0.13	49.76	0.01	0.00	100.14	1.01	0.18	0.00	1.81	0.00	0.91
PBG	42.16	0.02	0.02	8.43	0.14	49.41	0.01	0.00	100.39	1.02	0.17	0.00	1.79	0.00	0.91
123BRG BAE	40.03	0.02	0.00	8.02		48.92	0.01		97.00	1.00	0.17	0.00	1.83	0.00	0.92
191BRG MOA	41.50	0.02		8.00	0.14	49.06		0.41	99.93	1.01	0.18	0.00	1.79	0.01	0.91
MOB	41.52	0.00		8.06	0.16	48.92		0.42	99.08	1.01	0.18	0.00	1.79	0.01	0.91
MOC	41.24	0.00	0.00	8.09	0.12	48.87		0.42	99.04	1.01	0.18	0.00	1.79	0.01	0.91
MOD	41.76	0.02		8.04	0.14	49.16		0.41	100.37	1.01	0.18	0.00	1.79	0.01	0.91
MOE	41.65	0.02		9.20	0.12	48.75		0.44	100.18	1.01	0.19	0.00	1.78	0.01	0.91
123BRG BBN	40.64	0.02		8.06	0.12	49.71		0.42	98.98	1.00	0.16	0.00	1.83	0.01	0.92
BBO	40.60	0.02		8.14	0.12	49.86		0.36	99.11	1.00	0.17	0.00	1.83	0.01	0.92
BBP	40.78	0.02		7.91	0.11	49.57		0.36	98.78	1.00	0.16	0.00	1.83	0.01	0.92
123BRG YON	39.92			8.32	0.12	49.59		0.42	98.37	0.99	0.17	0.00	1.84	0.01	0.91
YOO	39.59			8.05	0.12	49.39		0.42	97.57	0.99	0.17	0.00	1.85	0.01	0.92
146BRG OEA	41.45	0.02	0.00	8.52	0.14	49.60	0.01	0.44	100.18	1.01	0.17	0.00	1.81	0.01	0.91
OEB	41.53	0.02	0.00	8.57	0.12	49.64	0.01	0.45	100.34	1.01	0.17	0.00	1.80	0.01	0.91
146BRG OEC	41.16	0.02	0.02	7.76	0.14	49.09	0.01	0.36	98.49	1.01	0.16	0.00	1.81	0.01	0.92
Drag24 OED	41.40	0.02	0.00	9.11	0.14	49.36	0.00	0.41	100.38	1.00	0.18	0.00	1.80	0.01	0.91
OEE	41.52	0.00	0.00	9.05	0.14	49.25	0.00	0.39	100.35	1.01	0.18	0.00	1.79	0.01	0.91
OEF	41.44	0.00	0.00	9.14	0.16	49.38	0.00	0.39	100.51	1.00	0.18	0.00	1.80	0.01	0.91
OEG	41.40	0.02	0.00	9.06	0.14	49.58	0.00	0.36	100.54	1.00	0.18	0.00	1.80	0.01	0.91
Drag7 MOW	41.25	0.02	0.00	8.88	0.11	49.45	0.01	0.39	100.11	1.00	0.18	0.00	1.80	0.01	0.91
MOX	40.99	0.02	0.00	8.73	0.12	49.35	0.01	0.38	99.60	1.00	0.18	0.00	1.81	0.01	0.91
MOY	41.49	0.00	0.00	8.95	0.12	49.69	0.01	0.36	100.64	1.01	0.18	0.00	1.80	0.01	0.91
MOZ	41.52	0.02	0.00	8.85	0.12	49.64	0.01	0.38	100.54	1.00	0.18	0.00	1.81	0.01	0.91
MOA	41.54	0.02	0.00	8.80	0.12	49.50	0.01	0.35	100.34	1.00	0.18	0.00	1.80	0.01	0.91
MOB	41.43	0.02	0.00	8.94	0.12	49.65	0.01	0.41	100.58	1.00	0.18	0.00	1.80	0.01	0.91
MOD	41.39	0.00	0.00	8.88	0.16	49.74	0.01	0.41	100.58	1.00	0.18	0.00	1.81	0.01	0.91
Mamba UATC															
168BRG EXG	40.84	0.02	0.00	14.35	0.22	45.14	0.01		100.58	1.01	0.30	0.00	1.68	0.00	0.85
EXI	40.99	0.02	0.00	14.56	0.25	45.12	0.00		100.91	1.01	0.30	0.01	1.67	0.00	0.85
EXK	41.01	0.02	0.00	14.22	0.23	45.16	0.00		100.48	1.01	0.29	0.00	1.67	0.00	0.85
168BRG EXB	39.50	0.04		13.87	0.23	45.30		0.21	99.24	0.99	0.29	0.00	1.71	0.00	0.85
EXA	40.00	0.02		13.94	0.22	45.40		0.25	99.84	1.00	0.29	0.00	1.70	0.01	0.85
Drag73 YOA	41.12			7.71	0.16	49.42		0.41	100.97	1.01	0.16	0.00	1.81	0.01	0.92
YOB	41.34			8.88	0.12	49.34		0.29	101.67	1.00	0.20	0.00	1.79	0.01	0.90
YOC	41.21			10.08	0.16	49.40		0.42	101.27	1.00	0.20	0.00	1.79	0.01	0.90
YOD	41.17			9.92	0.16	49.37		0.38	101.09	1.00	0.20	0.00	1.79	0.01	0.90
YOE	41.26			10.18	0.16	49.35		0.38	101.33	1.00	0.21	0.00	1.79	0.01	0.90
YOF	41.31			9.77	0.16	49.12		0.42	100.79	1.00	0.20	0.00	1.79	0.01	0.90
YOG	41.11			9.78	0.14	49.46		0.36	100.85	1.00	0.20	0.00	1.80	0.01	0.90
OBH	41.50	0.02	0.00	9.07	0.16	49.69	0.00	0.41	100.85	1.00	0.18	0.00	1.80	0.01	0.91
19-BRG MBE	40.78	0.00	0.00	10.46	0.17	48.16	0.01	0.36	99.80	1.00	0.21	0.00	1.77	0.01	0.89
MBJ	41.48	0.00	0.05	10.05	0.17	47.55	0.45	0.36	100.11	1.02	0.21	0.00	1.75	0.01	0.89
MBK	41.05	0.00	0.00	10.56	0.17	48.27	0.01	0.36	100.42	1.00	0.21	0.00	1.77	0.01	0.89
MBL	41.01	0.00	0.00	10.48	0.16	48.41	0.01	0.36	100.45	1.00	0.21	0.00	1.77	0.01	0.89
9-BRG THY	40.86	0.02		13.77	0.25	45.83	0.04	0.29	100.89	1.01	0.28	0.01	1.69	0.00	0.86
THZ	40.82	0.02		13.69	0.23	45.83	0.05	0.29	100.78	1.01	0.28	0.00	1.70	0.00	0.86
OEA	40.58	0.02		13.77	0.20	46.09	0.04	0.18	100.88	1.00	0.28	0.00	1.71	0.00	0.86
OEB	40.69	0.02		13.63	0.23	45.71	0.07	0.21	100.76	1.01	0.28	0.00	1.69	0.00	0.86
OEC	40.73	0.20		13.55	0.19	45.66	0.01	0.17	100.75	1.00	0.28	0.00	1.70	0.00	0.86
OED	40.85	0.02	0.02	13.43	0.22	45.58	0.03	0.20	100.65	1.01	0.28	0.00	1.69	0.00	0.86
7-BRG THH	41.12			10.04	0.17	48.56	0.02	0.33	100.27	1.00	0.20	0.00	1.78	0.01	0.90
THJ	40.79			9.92	0.17	48.66	0.07	0.23	99.85	1.00	0.20	0.00	1.78	0.01	0.90
THK	41.19			9.77	0.14	48.51	0.02	0.32	99.96	1.01	0.20	0.00	1.78	0.01	0.90
Other															
38BRG POC	41.46	0.02	0.00	10.43	0.16	47.91	0.01		100.19	1.02	0.21	0.00	1.75	0.00	0.89
POF	41.33	0.02	0.00	10.47	0.14	47.91	0.01		99.89	1.01	0.21	0.00	1.76	0.00	0.89
POG	41.37	0.01	0.00	10.14	0.16	48.23	0.01		99.88	1.01	0.21	0.00	1.77	0.00	0.90
POH	40.93	0.02	0.00	10.29	0.17	47.82	0.01		99.26	1.01	0.21	0.00	1.77	0.00	0.89
POK	41.27	0.02	0.00	10.39	0.17	47.69	0.01		99.46	1.01	0.21	0.00	1.75	0.00	0.89
POL	41.36	0.01	0.00	10.44	0.17	47.97	0.01		99.87	1.01	0.21	0.00	1.76	0.00	0.89
38BRG YOH	40.97			10.40	0.16	48.78		0.33	100.64	1.00	0.21	0.00	1.78	0.01	0.89
YOI	41.34			10.60	0.17	48.61		0.32	100.84	1.00	0.21	0.00	1.77	0.01	0.89
YOL	41.41			10.39	0.19	48.67		0.32	100.99	1.00	0.21	0.00	1.78	0.01	0.89
YOM	40.86			10.46	0.17	48.42		0.32	100.33	1.00	0.21	0.00	1.78	0.01	0.89
38BRG BBH	40.62	0.02		10.04	0.17	48.01		0.36	99.39	1.01	0.21	0.00	1.77	0.01	0.90
BBI	40.75	0.02		9.98	0.16	48.60		0.36	99.78	1.01	0.20	0.00	1.78	0.01	0.90
6-BRG MBE	41.09	0.00	0.00	10.07	0.14	48.64	0.00	0.29	99.68	1.00	0.20	0.00	1.79	0.01	0.90
MBF	41.30	0.00	0.00	10.71	0.14	48.66	0.00	0.21	101.11	1.00	0.22	0.00	1.77	0.00	0.89
MBG	41.23	0.00	0.00	10.80	0.16	48.41	0.00	0.22	100.87	1.00	0.22	0.00	1.77	0.00	0.89
6BRG MBH	41.49	0.00	0.00	8.46	0.14	49.56	0.00	0.26	99.88	1.01	0.17	0.00	1.81	0.01	0.91
MBK	41.39	0.00	0.00	8.57	0.11	49.79	0.00	0.27	100.04	1.00	0.17	0.00	1.81	0.01	0.91
MBM	41.34	0.00	0.00	8.36	0.14	49.84	0.00	0.27	99.95	1.00	0.17	0.00	1.82	0.01	0.91
MBO	41.44	0.00	0.00	8.42	0.11	50.28	0.00	0.24	100.29	1.01	0.16	0.00	1.83	0.00	0.92
MBV	41.46	0.00	0.00	8.06	0.12	50.38	0.00	0.27	100.29	1.00	0.16	0.00	1.83	0.01	0.92

Opx	Sample No.	Mount No.	SiO2	TiO2	FeO	MnO	MgO	Na2O	CaO	NiO	Cr2O3	Al2O3	Total wt%	Si	Ti	Al	Fe	Mn	Mg	Ca	Na	Ni	Cr	Total	100Mg/	100Fe/	100Ca/	Wo%	En%	Fs%
Harzburgite	166BRG	OXA	58.08	0.02	5.85	0.10	34.87	0.01	0.14	0.00	0.53	0.81	100.43	1.99	0.00	0.03	0.17	0.00	1.77	0.01	0.00	0.00	0.01	3.99	99.28	10.46	0.26	*	*	*
		OXB	57.40	0.02	6.07	0.10	34.86	0.00	0.14	0.05	0.58	0.85	99.89	1.98	0.00	0.03	0.17	0.00	1.78	0.01	0.00	0.00	0.02	4.00	99.24	9.49	0.26	*	*	*
		OXC	58.04	0.02	5.92	0.10	34.74	0.00	0.16	0.00	0.36	0.72	100.22	1.99	0.00	0.03	0.17	0.00	1.78	0.01	0.00	0.00	0.01	3.99	99.40	10.21	0.30	*	*	*
		OXD	57.90	0.02	6.06	0.14	34.39	0.00	0.19	0.00	*	1.01	99.44	1.99	0.00	0.04	0.18	0.00	1.77	0.00	0.00	*	*	3.99	99.25	10.51	0.24	*	*	*
	Brag24	MHE	58.56	0.02	6.39	0.17	33.55	0.00	0.59	0.11	*	1.86	99.25	1.97	0.00	0.08	0.19	0.01	1.74	0.02	0.00	0.00	*	3.99	99.06	10.53	0.51	*	*	*
		MHF	58.90	0.02	6.44	0.17	33.86	0.00	0.27	0.00	*	1.86	99.36	1.97	0.00	0.07	0.19	0.00	1.77	0.01	0.00	0.00	*	3.99	99.00	10.78	0.35	*	*	*
		MHG	58.06	0.02	6.34	0.17	34.54	0.00	0.19	0.00	*	0.70	100.10	2.00	0.00	0.03	0.18	0.00	1.77	0.01	0.00	0.00	*	4.02	99.77	7.01	0.22	*	*	*
	Brag24	P8D	58.19	0.02	6.50	0.19	36.13	0.00	0.12	0.00	*	0.27	101.42	1.98	0.00	0.01	0.18	0.01	1.83	0.00	0.00	0.00	*	4.00	99.81	9.82	0.37	*	*	*
		P8H	58.19	0.02	6.55	0.20	34.96	0.01	0.20	0.00	*	1.15	101.27	1.99	0.00	0.05	0.19	0.01	1.77	0.01	0.00	0.00	*	4.00	99.51	11.17	0.32	*	*	*
		P8I	57.04	0.04	6.17	0.17	33.81	0.00	0.17	0.00	*	0.94	98.34	1.99	0.00	0.04	0.18	0.01	1.76	0.01	0.00	*	*	3.94	99.28	10.44	0.28	*	*	*
	133BRG	HAA	61.47	0.02	5.49	0.14	34.20	0.00	0.16	*	*	0.44	102.01	2.05	0.00	0.02	0.15	0.00	1.71	0.01	0.00	*	*	3.96	99.06	14.03	0.31	*	*	*
		HAB	58.86	0.02	5.59	0.00	33.84	0.00	0.17	*	*	0.78	99.28	2.02	0.00	0.03	0.16	0.00	1.73	0.01	0.00	*	*	3.96	98.38	11.31	0.31	*	*	*
		HAC	58.13	0.02	5.59	0.00	34.46	0.00	0.17	*	*	0.87	99.28	2.00	0.00	0.04	0.16	0.00	1.77	0.01	0.00	*	*	3.99	98.36	11.49	0.13	*	*	*
		HAD	58.38	0.02	5.61	0.00	34.69	0.00	0.07	*	*	0.87	99.58	2.01	0.00	0.03	0.17	0.00	1.77	0.00	0.00	*	*	3.99	99.55	10.13	0.32	*	*	*
		HAF	57.90	0.02	5.44	0.00	34.62	0.00	0.17	*	*	0.63	98.48	2.00	0.00	0.03	0.16	0.00	1.84	0.01	0.00	0.00	*	4.00	99.75	6.89	0.36	*	*	*
	146BRG	LBK	59.08	0.02	5.37	0.16	36.64	0.00	0.20	0.05	*	0.32	101.85	1.98	0.00	0.01	0.15	0.00	1.84	0.01	0.00	0.00	*	4.00	99.72	9.46	0.31	*	*	*
		LBN	59.02	0.00	5.62	0.16	35.77	0.00	0.17	0.05	*	0.74	101.14	1.99	0.00	0.03	0.16	0.00	1.81	0.01	0.00	0.00	*	4.00	99.23	8.46	0.31	*	*	*
		LBO	59.36	0.00	5.63	0.16	35.84	0.00	0.19	0.05	*	0.80	101.44	1.99	0.00	0.04	0.17	0.00	1.81	0.01	0.00	0.00	*	4.01	99.07	7.58	0.35	*	*	*
Pyroxenite	161BRG	PXB	58.88	0.04	6.66	0.30	31.99	0.02	0.22	*	*	0.99	99.92	1.98	0.00	0.04	0.20	0.01	1.67	0.01	0.00	*	*	4.00	84.56	15.02	0.42	*	*	*
		PXC	58.64	0.04	6.97	0.20	32.01	0.02	0.17	*	*	0.74	99.87	1.99	0.00	0.03	0.20	0.01	1.67	0.01	0.00	*	*	4.00	84.65	15.03	0.32	*	*	*
		PXD	57.23	0.04	6.10	0.25	32.20	0.00	0.23	*	*	0.79	98.84	2.00	0.00	0.03	0.27	0.01	1.67	0.01	0.00	*	*	3.99	84.12	15.45	0.43	*	*	*
		PXE	58.22	0.05	6.10	0.25	32.00	0.00	0.20	*	*	1.37	98.33	1.99	0.00	0.06	0.27	0.01	1.70	0.01	0.00	*	*	4.01	86.85	12.84	0.51	*	*	*
		PXF	58.42	0.04	6.11	0.27	32.03	0.00	0.23	*	*	0.86	98.36	1.99	0.00	0.03	0.27	0.01	1.71	0.01	0.00	*	*	4.00	86.50	13.07	0.44	*	*	*
		PXG	58.94	0.04	6.27	0.27	32.19	0.00	0.20	*	*	0.67	98.57	1.99	0.00	0.03	0.27	0.01	1.70	0.01	0.00	*	*	4.00	86.04	13.58	0.38	*	*	*
		PXM	57.83	0.04	6.43	0.28	31.98	0.00	0.25	*	*	0.90	100.01	2.00	0.00	0.04	0.27	0.01	1.65	0.01	0.00	*	*	3.98	82.57	16.97	0.46	*	*	*
	43BRG	LBB	57.90	0.04	7.69	0.20	33.72	0.01	0.14	0.00	*	0.97	100.61	1.99	0.00	0.04	0.22	0.01	1.73	0.01	0.00	0.00	*	3.99	87.06	12.66	0.28	*	*	*
		LBC	57.81	0.02	7.77	0.23	33.65	0.00	0.16	0.02	*	1.03	100.68	1.99	0.00	0.04	0.22	0.01	1.72	0.01	0.00	0.00	*	3.99	87.04	12.66	0.30	*	*	*
		LBD	58.01	0.04	7.44	0.20	33.93	0.00	0.22	0.00	*	0.86	101.83	2.00	0.00	0.04	0.21	0.01	1.71	0.01	0.00	0.00	*	3.98	85.89	13.70	0.40	*	*	*
		LBE	58.84	0.02	7.74	0.19	33.70	0.01	0.20	0.02	*	1.19	101.61	1.99	0.00	0.05	0.22	0.01	1.71	0.01	0.00	0.00	*	3.98	86.09	13.54	0.37	*	*	*
		LBF	58.33	0.04	7.13	0.19	32.98	0.00	1.19	0.00	*	0.91	101.77	2.01	0.00	0.04	0.20	0.01	1.67	0.04	0.00	0.00	*	3.97	83.03	14.82	2.15	*	*	*
		LBJ	58.01	0.04	7.32	0.19	34.78	0.00	0.14	0.00	*	0.64	101.02	1.99	0.00	0.02	0.21	0.01	1.77	0.01	0.00	0.00	*	4.00	89.55	10.19	0.26	*	*	*
	Brag23	JCA	57.12	0.04	6.44	0.16	35.54	0.00	0.19	*	*	0.88	100.37	1.98	0.00	0.04	0.19	0.00	1.82	0.01	0.00	*	*	4.02	92.90	6.74	0.36	*	*	*
		JCB	58.19	0.04	5.65	0.14	36.12	0.00	0.19	*	*	0.50	100.99	1.99	0.00	0.02	0.17	0.00	1.83	0.01	0.00	*	*	4.01	92.71	6.94	0.35	*	*	*
		JCC	58.39	0.04	5.74	0.14	34.18	0.00	1.04	*	*	1.41	99.01	1.99	0.00	0.06	0.17	0.00	1.77	0.04	0.00	*	*	4.01	90.89	7.12	1.99	*	*	*
		JCD	58.67	0.04	6.23	0.16	34.78	0.00	0.14	*	*	1.06	99.00	1.97	0.00	0.04	0.18	0.00	1.80	0.01	0.00	*	*	4.01	91.58	8.15	0.27	*	*	*
		JCF	58.73	0.04	6.10	0.16	35.36	0.00	0.16	*	*	0.78	99.34	1.97	0.00	0.03	0.18	0.00	1.83	0.01	0.00	*	*	4.02	93.07	6.63	0.30	*	*	*
		JCH	57.80	0.02	6.06	0.16	35.44	0.01	0.12	*	*	1.02	101.03	1.97	0.00	0.04	0.19	0.00	1.80	0.00	0.00	*	*	4.01	91.95	7.83	0.22	*	*	*
		JCI	58.45	0.04	5.97	0.16	35.60	0.00	0.14	*	*	0.25	100.91	1.99	0.00	0.01	0.17	0.00	1.82	0.01	0.00	*	*	4.00	91.70	8.04	0.26	*	*	*
		JCJ	58.77	0.04	6.13	0.16	35.79	0.00	0.17	*	*	0.50	101.50	1.99	0.00	0.02	0.17	0.00	1.80	0.01	0.00	*	*	4.00	90.77	8.02	0.31	*	*	*
		JCL	57.37	0.04	6.43	0.13	35.32	0.01	0.12	*	*	0.78	100.21	1.97	0.00	0.03	0.18	0.00	1.81	0.00	0.00	*	*	4.01	91.94	7.83	0.22	*	*	*
		JCM	58.71	0.04	6.22	0.16	35.46	0.00	0.17	*	*	0.61	101.37	1.99	0.00	0.02	0.18	0.00	1.79	0.01	0.00	*	*	4.00	90.19	9.51	0.31	*	*	*
		JCN	58.08	0.04	6.05	0.14	35.66	0.00	0.17	*	*	0.36	100.72	1.98	0.00	0.02	0.17	0.00	1.83	0.01	0.00	*	*	4.01	92.16	7.53	0.31	*	*	*
Mantle UATC	736RG	BLH	55.36	0.13	6.80	0.17	33.13	0.01	0.43	0.06	*	3.53	99.71	1.92	0.00	0.14	0.20	0.00	1.71	0.02	0.00	0.00	*	4.00	89.40	9.78	0.83	*	*	*
		BLJ	55.00	0.11	6.70	0.17	33.11	0.01	0.58	0.06	*	4.06	99.88	1.91	0.00	0.17	0.19	0.00	1.71	0.02	0.00	0.00	*	4.01	89.83	9.04	1.13	*	*	*
		BLK	55.91	0.08	6.62	0.16	33.22	0.01	0.39	0.06	*	3.44	99.83	1.93	0.00	0.14	0.20	0.01	1.71	0.01	0.00	0.00	*	4.00	89.32	9.93	0.75	*	*	*
		BLN	56.47	0.07	6.66	0.16	33.83	0.01	0.52	0.06	*	3.70	101.16	1.93	0.00	0.15	0.19	0.00	1.70	0.02	0.00	0.00	*	4.00	88.76	10.25	0.99	*	*	*
		BLP	55.55	0.11	6.67	0.17	33.43	0.01	0.43	0.06	*	4.44	101.19	1.91	0.00	0.18	0.19	0.00	1.70	0.02	0.00	0.00	*	4.00	89.47	9.70	0.83	*	*	*
		BLQ	54.47	0.08	6.70	0.17	33.42	0.01	0.48	0.11	*	4.38	99.83	1.89	0.00	0.18	0.19	0.00	1.73	0.02	0.00	0.00	*	4.02	91.78	7.27	0.95	*	*	*
		BLR	55.59	0.07	6.69	0.16	33.76	0.00	0.29	0.06	*	2.91	99.78	1.93	0.00	0.12	0.20	0.00	1.74	0.01	0.00	0.00	*	4.01	90.76	8.66	0.58	*	*	*
		BLS	55.22	0.08	6.73	0.14	33.37	0.01	0.38	0.06	*	3.81	99.93	1.91	0.00	0.16	0.19	0.00	1.72	0.01	0.00	0.00	*	4.01	90.31	8.95	0.74	*	*	*

4c Pyroxene

Sample No	Identification	TiO2	FeO	MnO	MgO	NiO	CaO	Cr2O3	Al2O3	Total wt%	Si	Ti	Al	Fe	Mn	Mg	Ca	Na	Ni	Cr	Total	100Mg#	100Fe	100Ca	Wo#%	En%	Fs%
Clinopyroxenite	PAA	0.10	3.28	0.14	10.41	0.00	24.23	*	0.67	99.10	2.00	0.00	0.03	0.10	0.00	0.00	0.96	0.00	*	*	3.00	45.17	6.07	47.66	47.07	44.97	7.06
	PAB	0.11	3.26	0.17	10.51	0.02	24.07	*	0.76	100.02	1.00	0.00	0.03	0.10	0.01	0.00	0.96	0.00	*	*	4.00	45.02	4.50	48.00	48.13	45.00	4.88
	PAC	0.11	3.26	0.14	10.47	0.02	24.06	*	0.66	99.04	1.07	0.00	0.04	0.10	0.00	0.00	0.96	0.00	*	*	4.00	45.79	4.34	48.87	48.09	46.04	4.62
	PAD	0.11	3.26	0.14	10.47	0.02	24.30	*	0.79	99.97	1.00	0.00	0.03	0.10	0.01	0.00	0.97	0.00	*	*	4.00	46.20	5.00	48.00	48.27	46.44	5.29
	PAE	0.10	3.26	0.14	10.53	0.02	24.40	*	1.00	99.02	1.07	0.00	0.06	0.11	0.00	0.00	0.97	0.00	*	*	4.00	45.64	5.18	48.21	48.46	46.11	5.43
	PAF	0.10	3.42	0.14	10.53	0.02	24.30	*	1.36	100.06	2.01	0.00	0.06	0.10	0.01	0.01	0.74	0.01	0.00	*	3.00	30.33	12.82	46.16	46.86	38.00	12.67
2B6B	PAP	0.00	0.24	0.22	13.05	0.07	23.28	*	2.03	100.04	1.00	0.00	0.11	0.21	0.01	0.01	0.71	0.00	0.00	*	4.00	30.02	11.01	45.28	43.70	39.10	11.33
	PAG	0.17	7.01	0.22	12.70	1.12	23.10	*	2.04	100.01	1.00	0.01	0.13	0.22	0.01	0.01	0.70	0.01	0.00	*	4.01	30.88	10.70	50.69	40.40	39.10	11.33
	PAR	0.11	7.01	0.22	12.70	1.12	23.57	*	2.04	99.96	1.00	0.00	0.09	0.20	0.00	0.03	0.96	0.03	0.02	*	4.00	47.50	4.74	47.07	47.41	47.03	4.97
	APC	0.04	2.83	0.14	10.02	0.25	23.57	0.18	0.66	99.06	1.00	0.00	0.03	0.09	0.01	0.03	0.96	0.02	0.02	*	4.01	47.07	2.77	49.26	48.66	48.36	3.07
2B6B8	APD	0.04	2.79	0.17	10.01	0.30	24.15	0.16	0.61	99.05	1.00	0.00	0.03	0.09	0.00	0.03	0.96	0.03	0.02	*	4.01	47.78	3.23	49.06	48.53	48.04	3.43
	APG	0.02	2.79	0.11	17.00	0.30	24.30	0.00	0.67	99.00	1.00	0.00	0.02	0.06	0.00	0.02	0.96	0.03	0.02	*	4.01	47.44	3.28	49.31	48.66	47.66	3.49
	APE	0.07	2.79	0.14	10.00	0.29	24.04	0.47	0.66	97.52	1.07	0.00	0.03	0.10	0.00	0.02	0.96	0.03	0.02	*	4.02	47.00	3.01	49.30	48.16	48.74	3.10
	APF	0.04	3.34	0.14	10.01	0.28	23.64	0.11	0.50	99.41	1.00	0.00	0.03	0.09	0.00	0.03	0.96	0.03	0.01	*	4.01	47.00	1.84	50.37	48.40	48.61	2.06
	APG	0.04	2.87	0.14	10.00	0.29	24.00	*	0.72	99.79	1.07	0.00	0.03	0.09	0.00	0.02	0.96	0.03	0.02	*	4.01	47.81	1.25	50.04	48.79	48.79	1.51
	APH	0.04	2.86	0.14	10.06	0.27	24.00	0.36	0.72	99.70	1.07	0.00	0.04	0.10	0.00	0.04	0.96	0.03	0.02	*	4.02	48.66	2.70	49.40	47.30	49.00	2.06
	API	0.02	3.10	0.13	10.04	0.33	23.97	0.46	0.66	99.33	1.00	0.00	0.04	0.08	0.00	0.02	0.96	0.03	0.02	*	4.01	47.06	2.89	50.05	48.85	47.33	3.12
	APA11	0.04	2.86	0.13	10.79	0.23	24.04	*	0.65	99.80	1.00	0.00	0.03	0.09	0.00	0.03	0.96	0.03	0.02	*	4.00	47.44	3.00	49.68	48.30	47.80	4.11
	APB1	0.04	2.86	0.13	10.06	0.26	24.11	*	0.66	99.34	2.00	0.00	0.03	0.09	0.00	0.03	0.96	0.03	0.02	*	4.00	47.22	3.20	47.68	47.51	47.10	5.39
	APC1	0.04	2.86	0.13	10.76	0.29	23.52	*	0.70	99.80	2.00	0.00	0.03	0.09	0.00	0.02	0.97	0.03	0.02	*	4.00	48.91	5.02	46.27	48.44	45.61	5.95
	MAA	0.05	2.40	0.11	10.02	0.00	24.74	0.11	0.41	99.80	2.00	0.00	0.03	0.08	0.00	0.03	0.96	0.03	0.02	*	3.00	48.91	5.02	46.27	48.44	45.61	5.95
1416MA	MAB	0.05	2.40	0.08	17.26	0.03	24.65	0.12	0.61	100.20	1.00	0.00	0.03	0.07	0.00	0.03	0.96	0.03	0.02	*	3.00	48.93	4.65	46.53	48.38	46.04	4.97
	MAC	0.05	2.40	0.08	17.26	0.03	24.69	0.14	0.48	99.07	2.00	0.00	0.03	0.08	0.00	0.03	0.96	0.03	0.02	*	3.00	48.93	4.01	47.06	48.26	46.60	4.84
	MAD	0.04	2.29	0.08	17.29	0.03	24.65	0.14	0.47	100.20	1.00	0.00	0.03	0.07	0.00	0.03	0.97	0.03	0.02	*	3.00	48.91	4.54	46.55	48.42	46.00	4.06
	MAE	0.04	2.30	0.08	17.27	0.02	24.64	0.14	0.47	100.20	1.00	0.00	0.03	0.07	0.00	0.03	0.96	0.03	0.02	*	3.00	48.91	4.54	46.55	48.42	46.00	4.06
	MAF	0.04	2.30	0.08	17.27	0.02	24.64	0.14	0.47	100.20	1.00	0.00	0.03	0.07	0.00	0.03	0.96	0.03	0.02	*	3.00	48.91	4.54	46.55	48.42	46.00	4.06
	MAG	0.04	2.30	0.11	17.04	0.02	24.46	0.30	0.67	99.40	1.00	0.00	0.03	0.07	0.00	0.03	0.96	0.03	0.02	*	3.00	48.82	4.66	46.52	48.04	46.02	5.04
7B6B6	BLV	0.14	0.28	0.11	18.27	1.22	21.16	0.03	0.72	4.00	99.71	1.01	0.01	0.21	0.00	0.00	0.84	0.03	0.00	0.00	0.02	4.00	47.03	4.54	47.03	45.13	48.04	4.03

												T site		C site							B site				A site	
Identifier	SiO2	TiO2	Al2O3	FeO*	MnO	MgO	CaO	Na2O	K2O	Cr2O3	Total	Si	Al	Al	Cr3+	Ti	Fe3+	Mg	Fe2+	Mn	Fe2+	Ca	Na	Sum	Na	K
Pyroxenite																										
3BRG EXA	42.68	0.72	13.56	13.01	0.23	12.05	12.21	2.84	0.66	•	97.96	6.29	1.71	0.64	•	0.08	0.12	2.65	1.48	0.03	0.00	1.93	0.07	2.00	0.74	0.12
EXB	42.91	0.68	13.27	13.16	0.20	12.24	11.78	2.81	0.62	•	97.67	6.30	1.70	0.60	•	0.08	0.32	2.68	1.30	0.02	0.00	1.85	0.15	2.00	0.65	0.12
EXC	43.76	0.66	13.08	12.17	0.20	13.04	12.03	2.69	0.91	•	98.54	6.36	1.64	0.60	•	0.07	0.22	2.82	1.25	0.02	0.00	1.87	0.13	2.00	0.63	0.17
EXD	42.83	1.07	13.38	12.16	0.22	12.70	11.71	2.67	0.98	•	97.72	6.28	1.72	0.59	•	0.12	0.28	2.77	1.21	0.03	0.00	1.84	0.16	2.00	0.60	0.18
10BRG HOB	40.71	1.14	13.10	19.22	0.20	8.11	11.18	2.01	1.19	•	96.86	6.20	1.80	0.55	•	0.13	0.51	1.84	1.94	0.03	0.00	1.82	0.18	2.00	0.42	0.23
HOD	40.30	1.23	13.65	18.68	0.26	8.02	11.38	2.09	1.03	•	96.64	6.16	1.84	0.61	•	0.14	0.40	1.83	1.98	0.03	0.00	1.86	0.14	2.00	0.48	0.20
HOF	41.42	1.29	13.00	17.76	0.20	8.66	11.27	2.00	0.91	•	96.51	6.29	1.71	0.61	•	0.15	0.37	1.96	1.88	0.03	0.00	1.83	0.17	2.00	0.42	0.18
HOI	41.05	1.52	12.80	18.57	0.25	8.40	11.19	2.00	0.97	•	96.75	6.24	1.76	0.53	•	0.17	0.46	1.90	1.90	0.03	0.00	1.82	0.18	2.00	0.41	0.19
HOK	42.07	1.34	13.39	17.93	0.28	8.62	11.16	2.10	0.97	•	97.86	6.29	1.71	0.65	•	0.15	0.39	1.92	1.85	0.04	0.00	1.79	0.21	2.00	0.40	0.19
4BRG HOL	40.98	1.25	13.99	17.09	0.23	9.41	11.41	2.49	0.84	•	97.69	6.13	1.87	0.59	•	0.14	0.46	2.10	1.68	0.03	0.00	1.83	0.17	2.00	0.55	0.16
HOM	41.59	1.22	13.55	17.11	0.20	9.33	11.41	2.61	0.83	•	97.85	6.22	1.78	0.61	•	0.14	0.31	2.08	1.83	0.03	0.00	1.83	0.17	2.00	0.59	0.16
HON	41.53	1.25	13.63	17.21	0.20	9.23	10.69	2.51	0.67	•	96.92	6.22	1.78	0.62	•	0.14	0.60	2.06	1.56	0.03	0.00	1.71	0.29	2.00	0.44	0.13
HOO	41.66	1.27	13.99	17.40	0.25	9.23	11.12	2.47	0.78	•	98.17	6.18	1.82	0.63	•	0.14	0.52	2.04	1.64	0.03	0.00	1.77	0.23	2.00	0.48	0.15
HOP	41.28	1.25	13.97	17.16	0.23	9.05	11.15	2.51	0.80	•	97.40	6.19	1.81	0.66	•	0.14	0.41	2.02	1.74	0.03	0.00	1.79	0.21	2.00	0.52	0.15
BRAG60 PAY	43.19	0.68	13.47	12.75	0.22	12.23	12.03	2.83	0.77	•	98.17	6.33	1.67	0.66	•	0.07	0.13	2.67	1.44	0.03	0.00	1.89	0.11	2.00	0.69	0.14
141BRG PXK	55.60	0.09	3.49	3.04	0.09	21.07	13.02	0.41	0.03	•	96.84	7.71	0.29	0.28	•	0.01	0.02	4.35	0.33	0.01	0.00	1.93	0.07	2.00	0.04	0.01
PXL	55.77	0.09	2.98	3.07	0.09	21.50	12.55	0.35	0.03	•	96.43	7.71	0.29	0.19	•	0.01	0.26	4.43	0.09	0.01	0.00	1.86	0.09	1.95	0.00	0.01
6 BRG PAF	53.46	0.22	4.63	4.71	0.13	19.90	12.61	0.49	0.00	•	96.15	7.49	0.51	0.25	•	0.02	0.29	4.16	0.26	0.02	0.00	1.89	0.11	2.00	0.03	0.00
PAG	53.71	0.24	5.15	4.80	0.09	19.85	12.55	0.55	0.00	•	96.94	7.46	0.54	0.30	•	0.03	0.31	4.11	0.24	0.01	0.00	1.87	0.13	2.00	0.01	0.00
32BRG POB	55.20	0.13	4.35	2.58	0.08	21.59	13.39	0.85	0.01	•	98.18	7.57	0.43	0.27	•	0.01	-0.02	4.41	0.32	0.01	0.00	1.97	0.03	2.00	0.19	0.00
POD	52.74	0.13	4.68	2.94	0.09	22.01	12.20	0.84	0.02	•	95.65	7.32	0.68	0.08	•	0.01	0.72	4.55	-0.38	0.01	0.00	1.81	0.19	2.00	0.04	0.00
POE	53.48	0.15	4.68	2.77	0.08	21.33	12.52	0.93	0.02	•	95.96	7.45	0.55	0.22	•	0.02	0.30	4.43	0.02	0.01	0.00	1.87	0.13	2.00	0.12	0.00
POH	53.77	0.13	4.39	2.61	0.08	21.65	13.08	0.82	0.02	•	96.55	7.47	0.53	0.19	•	0.01	0.19	4.48	0.11	0.01	0.00	1.95	0.05	2.00	0.17	0.00
POJ	53.14	0.19	5.41	2.65	0.08	20.89	13.23	1.12	0.03	•	96.74	7.42	0.58	0.31	•	0.02	-0.04	4.35	0.35	0.01	0.00	1.98	0.02	2.00	0.28	0.01
Brag83 JCE	52.57	0.08	4.44	2.48	0.06	21.77	12.72	0.88	0.12	•	95.12	7.39	0.61	0.13	•	0.01	0.37	4.56	-0.07	0.01	0.00	1.92	0.08	2.00	0.16	0.02
JCG	53.91	0.09	5.08	2.51	0.06	21.97	12.93	0.94	0.14	•	97.63	7.39	0.61	0.21	•	0.01	0.31	4.49	-0.03	0.01	0.00	1.90	0.10	2.00	0.15	0.02
JCK	53.01	0.09	5.08	2.68	0.05	21.70	12.61	0.97	0.20	•	96.39	7.35	0.65	0.19	•	0.01	0.40	4.49	-0.08	0.01	0.00	1.87	0.13	2.00	0.14	0.04
43BRG LBG	55.41	0.11	3.22	2.63	0.08	22.22	12.64	0.45	0.01	•	96.77	7.61	0.39	0.13	•	0.01	0.40	4.55	-0.10	0.01	0.00	1.86	0.12	1.98	0.00	0.00
LBH	55.75	0.08	3.12	2.54	0.08	22.56	12.64	0.46	0.04	•	97.27	7.60	0.40	0.11	•	0.01	0.45	4.59	-0.16	0.01	0.00	1.85	0.12	1.97	0.00	0.01
Harzburgite																										
191BRG MPB	55.64	0.04	3.08	2.30	0.06	21.65	13.26	0.36	0.00	0.28	96.67	7.70	0.30	0.25	0.04	0.00	-0.03	4.44	0.29	0.01	0.00	1.97	0.03	2.00	0.07	0.00
MPC	55.70	0.04	3.37	2.27	0.06	21.55	13.30	0.36	0.00	0.38	97.03	7.65	0.35	0.23	0.06	0.00	-0.03	4.44	0.29	0.01	0.00	1.99	0.01	2.00	0.09	0.00
MPD	54.85	0.04	3.52	2.28	0.05	21.33	13.28	0.39	0.01	0.51	96.26	7.75	0.25	0.23	0.03	0.00	-0.13	4.46	0.39	0.01	0.00	2.01	0.00	2.01	0.09	0.00
Brag34 MHA	54.14	0.06	3.60	2.14	0.06	22.02	12.62	0.88	0.09	0.58	96.19	7.52	0.48	0.11	0.06	0.01	0.28	4.56	-0.03	0.01	0.00	1.88	0.12	2.00	0.12	0.02
Brag24 PBA	48.96	0.06	9.55	3.28	0.06	19.39	12.80	1.66	0.23	•	95.99	6.92	1.08	0.51	•	0.01	0.18	4.09	0.21	0.01	0.00	1.94	0.06	2.00	0.39	0.04
PBC	49.86	0.06	8.66	3.28	0.05	19.72	12.67	1.52	0.20	•	96.02	7.02	0.98	0.46	•	0.01	0.23	4.14	0.16	0.01	0.00	1.91	0.09	2.00	0.33	0.04
MorraisUATC																										
184BRG MHM	54.81	0.11	3.20	2.51	0.00	21.84	12.60	0.69	0.02	0.98	96.76	7.57	0.43	0.09	0.11	0.01	0.29	4.50	0.00	0.00	0.00	1.87	0.13	2.00	0.05	0.00
MHO	56.74	0.08	1.82	2.13	0.00	22.55	12.83	0.46	0.01	0.16	96.78	7.81	0.19	0.10	0.02	0.01	0.15	4.63	0.10	0.00	0.00	1.89	0.11	2.00	0.01	0.00
76BRG OPA	43.00	0.76	14.30	4.57	0.06	17.40	11.87	2.70	0.65	•	95.31	6.19	1.81	0.62	•	0.08	0.48	3.74	0.07	0.01	0.00	1.83	0.17	2.00	0.59	0.12
OPB	43.00	0.75	13.97	4.55	0.08	17.33	12.28	2.68	0.62	•	95.26	6.23	1.77	0.61	•	0.08	0.31	3.74	0.24	0.01	0.00	1.91	0.09	2.00	0.66	0.11
OPC	42.87	0.76	14.81	4.78	0.05	17.24	11.47	2.78	0.58	•	95.34	6.15	1.85	0.65	•	0.08	0.63	3.69	-0.06	0.01	0.00	1.76	0.24	2.00	0.54	0.11
OPD	42.91	0.78	14.61	4.57	0.09	17.24	12.01	2.73	0.51	•	95.45	6.18	1.82	0.66	•	0.08	0.44	3.70	0.11	0.01	0.00	1.85	0.15	2.00	0.61	0.09

4d Amphibole

Identifier	SiO2	TiO2	Al2O3	FeO*	MnO	MgO	CaO	Na2O	K2O	Cr2O3	Total	Si	Al	Al	Cr3+	Ti	Fe3+	Mg	Fe2+	Mn	Fe2+	Ca	Na	Sum	Na	K
OPE	42.21	0.84	14.74	4.65	0.08	17.09	12.19	2.71	0.76	-	95.27	6.12	1.88	0.64	-	0.09	0.36	3.69	0.20	0.01	0.00	1.89	0.11	2.00	0.66	0.14
OPF	43.13	0.75	14.51	4.61	0.08	17.32	11.87	2.79	0.63	-	95.69	6.19	1.81	0.65	-	0.08	0.45	3.71	0.10	0.01	0.00	1.83	0.17	2.00	0.60	0.12
OPG	43.37	0.82	14.49	4.49	0.05	17.23	11.76	2.70	0.73	-	95.64	6.23	1.77	0.68	-	0.09	0.41	3.69	0.13	0.01	0.00	1.81	0.19	2.00	0.56	0.13
OPH	42.94	0.84	14.25	4.47	0.06	17.28	12.05	2.63	0.56	-	95.08	6.21	1.79	0.64	-	0.09	0.40	3.72	0.14	0.01	0.00	1.87	0.13	2.00	0.60	0.10
OPI	42.68	0.78	14.87	4.53	0.09	17.19	11.88	2.76	0.67	-	95.45	6.15	1.85	0.67	-	0.08	0.46	3.69	0.09	0.01	0.00	1.83	0.17	2.00	0.60	0.12
100BKG EXE	47.60	0.41	9.90	4.70	0.13	19.16	11.27	1.76	0.17	-	95.10	6.71	1.29	0.36	-	0.04	0.92	4.03	-0.37	0.02	0.00	1.70	0.30	2.00	0.18	0.03
EXF	47.37	0.47	9.69	5.12	0.20	19.17	11.60	1.68	0.16	-	95.46	6.68	1.32	0.29	-	0.05	0.93	4.03	-0.33	0.02	0.00	1.75	0.25	2.00	0.21	0.03
EXH	49.42	0.49	9.36	3.16	0.24	18.76	11.96	1.64	0.16	-	97.39	6.87	1.13	0.43	-	0.05	0.56	3.89	0.04	0.03	0.00	1.78	0.22	2.00	0.22	0.03
EXJ	49.99	0.45	9.57	4.94	0.11	18.70	12.16	1.88	0.20	-	98.00	6.93	1.07	0.50	-	0.05	0.32	3.87	0.26	0.01	0.00	1.81	0.19	2.00	0.31	0.04
Other																										
Brag3 JCU	45.09	0.37	13.98	5.84	0.22	17.33	11.93	2.68	0.08	-	97.52	6.32	1.68	0.63	-	0.04	0.65	3.62	0.04	0.03	0.00	1.79	0.21	2.00	0.52	0.01
JCV	47.64	0.28	10.19	5.03	0.14	20.38	11.41	1.92	0.05	-	97.04	6.55	1.45	0.20	-	0.03	1.31	4.18	-0.73	0.02	0.00	1.68	0.32	2.00	0.19	0.01
JCW	45.76	0.17	12.58	5.44	0.16	18.06	11.75	2.47	0.09	-	96.48	6.44	1.56	0.53	-	0.02	0.75	3.79	-0.11	0.02	0.00	1.77	0.23	2.00	0.45	0.02
JCY	44.80	0.28	13.61	5.73	0.17	17.71	11.82	2.63	0.12	-	96.87	6.30	1.70	0.56	-	0.03	0.77	3.71	-0.10	0.02	0.00	1.78	0.22	2.00	0.50	0.02
JBC	43.71	0.47	14.05	6.10	0.19	17.58	12.00	2.63	0.16	-	96.89	6.17	1.83	0.51	-	0.05	0.84	3.70	-0.12	0.02	0.00	1.82	0.18	2.00	0.53	0.03
JBD	44.51	0.47	13.92	5.68	0.14	17.44	12.69	2.59	0.17	-	97.61	6.28	1.72	0.60	-	0.05	0.45	3.67	0.22	0.02	0.00	1.92	0.08	2.00	0.63	0.03
JBE	45.24	0.11	13.43	5.46	0.16	18.16	12.68	2.66	0.03	-	97.93	6.33	1.67	0.54	-	0.01	0.58	3.79	0.06	0.02	0.00	1.90	0.10	2.00	0.62	0.01
JBG	43.75	0.47	13.85	5.77	0.16	17.29	11.81	2.74	0.16	-	96.00	6.24	1.76	0.57	-	0.05	0.70	3.68	-0.01	0.02	0.00	1.80	0.20	2.00	0.56	0.03
												Sites allocated to T, C, B, A on basis of amphibole formula A(0-1)B(2)C(5)T(8)O(22)OH(2)															

Identifier																									
Feldspar	SiO2	TiO2	Al2O3	FeO	MgO	CaO	Na2O	K2O	Total	Si	Al	Fe2	Mg	Ca	Na	K	Tl	Total	%Ab	%An	%Orth
100RG	FEB	64.01	0.02	25.01	0.07	0.00	5.06	8.46	0.08	102.71	2.75	1.27	0.00	0.00	0.23	0.71	0.00	0.00	4.97	74.81	24.73	0.47
	FED	62.60	0.02	24.65	0.08	0.00	5.28	8.52	0.07	101.22	2.74	1.27	0.00	0.00	0.25	0.72	0.00	0.00	4.99	74.19	25.41	0.40
	FEF	64.07	0.02	24.41	0.08	0.00	5.36	8.65	0.06	102.65	2.76	1.24	0.00	0.00	0.25	0.72	0.00	0.00	4.98	74.24	25.42	0.34
	FEG	62.52	0.02	23.80	0.10	0.00	4.95	8.45	0.10	99.94	2.77	1.24	0.00	0.00	0.24	0.73	0.01	0.00	4.98	75.10	24.31	0.59
	FEH	63.59	0.02	24.22	0.07	0.02	4.65	8.53	0.10	101.20	2.77	1.25	0.00	0.00	0.22	0.72	0.01	0.00	4.97	76.40	23.01	0.59
	FEI	62.57	0.02	23.81	0.07	0.00	4.69	8.59	0.06	99.81	2.77	1.24	0.00	0.00	0.22	0.74	0.00	0.00	4.98	76.55	23.10	0.35
	FEJ	63.10	0.02	24.04	0.06	0.00	4.63	8.64	0.08	100.57	2.77	1.24	0.00	0.00	0.22	0.74	0.00	0.00	4.98	76.79	22.74	0.47
	FEK	62.62	0.02	23.72	0.06	0.00	4.74	8.61	0.02	99.79	2.77	1.24	0.00	0.00	0.23	0.74	0.00	0.00	4.98	76.58	23.30	0.12
	FEL	62.42	0.02	23.75	0.10	0.00	4.92	8.51	0.32	100.04	2.76	1.24	0.00	0.00	0.23	0.73	0.02	0.00	4.99	74.39	23.77	1.84
	FEL	63.44	0.02	24.56	0.10	0.00	4.88	8.43	0.38	99.81	2.79	1.27	0.00	0.00	0.23	0.55	0.02	0.00	4.86	68.57	28.76	2.67
	FEM	63.11	0.02	24.50	0.10	0.00	5.09	8.47	0.06	101.35	2.75	1.26	0.00	0.00	0.24	0.72	0.00	0.00	4.98	74.81	24.84	0.35
	FEN	62.87	0.04	24.41	0.10	0.00	4.73	8.48	0.07	100.70	2.76	1.26	0.00	0.00	0.22	0.72	0.00	0.00	4.97	76.12	23.46	0.41
Brag96	JBR	48.39	0.00	33.05	0.11	0.00	17.24	2.26	0.01	101.06	2.20	1.77	0.00	0.00	0.84	0.20	0.00	0.00	5.02	19.16	80.78	0.06
	JBT	47.20	0.00	33.42	0.30	0.00	16.19	2.40	0.43	99.94	2.17	1.81	0.01	0.00	0.80	0.21	0.03	0.00	5.04	20.84	76.93	2.43
	JBX	49.47	0.00	33.77	0.10	0.00	15.68	2.49	0.15	101.66	2.22	1.79	0.00	0.00	0.76	0.22	0.01	0.00	5.00	22.13	77.00	0.88
	JBZ	47.94	0.06	34.89	0.11	0.02	16.69	1.96	0.01	101.68	2.16	1.85	0.00	0.00	0.81	0.17	0.00	0.00	5.00	17.52	82.43	0.06
	BLD	46.46	0.04	34.58	0.17	0.00	16.52	1.81	0.37	99.95	2.14	1.87	0.01	0.00	0.81	0.16	0.02	0.00	5.02	16.19	81.64	2.18
	BLE	47.09	0.04	34.62	0.35	0.05	16.81	1.84	0.03													

Apatite														
Brag4	K2O	P2O5	CaO	MnO	MgO	FeO	Cl	F	Total	O=F	Recalc. Total			
	APX	0.00	39.96	55.43	0.03	0.00	0.04	0.01	3.81	99.28	1.60	97.68		
	APD	0.00	40.65	52.94	0.08	0.02	1.64	0.11	1.63	97.07	0.69	96.38		
	APE	0.01	41.82	52.31	0.03	0.15	0.53	0.07	1.79	96.71	0.75	95.96		
	APR	0.00	39.88	55.94	•	•	0.53	0.08	1.82	98.25	0.77	97.48		
	APX	0.00	38.31	59.50	•	•	0.06	0.01	3.86	101.74	1.63	100.11		
	APU	0.00	38.71	58.21	•	•	0.17	0.09	2.07	99.25	0.87	98.38		
	APY	0.00	37.30	56.53	•	•	0.90	0.08	2.01	96.82	0.85	95.97		
	APZ	0.00	38.81	57.83	•	•	0.14	0.09	2.05	98.92	0.86	98.06		
	AEA	0.00	37.15	56.89	•	•	0.28	0.09	2.22	96.63	0.93	95.70		
	AEB	0.00	35.50	59.42	•	•	0.24	0.13	1.89	97.18	0.80	96.38		
	AEC	0.00	40.58	54.01	•	•	0.21	0.13	2.05	96.98	0.86	96.12		
	AED	0.00	44.48	54.84	•	•	0.52	0.11	1.92	101.87	0.81	101.06		

Garnet							
100RG	SiO2	TiO2	Al2O3	FeO	MnO	MgO	CaO	Total
	GTD	39.42	0.11	21.27	23.13	1.79	3.72	12.10	101.54
	GTE	39.28	0.09	21.07	22.52	2.00	3.23	13.71	101.90
	GTE	39.48	0.13	21.96	23.50	1.71	3.88	12.10	102.78
	GTF	39.05	0.16	21.09	22.80	1.97	3.97	12.04	101.12
	GTG	38.92	0.11	21.30	21.79	2.31	3.19	14.41	102.05
Brag4	GTJ	37.85	0.48	21.11	22.97	1.10	3.04	12.60	99.17
	GTK	38.24	0.38	20.82	23.87	0.92	3.28	12.75	100.08
	GTL	37.94	0.59	20.66	23.55	0.96	3.23	12.66	99.61
	GTM	37.93	0.50	20.60	23.71	0.95	3.32	12.30	99.31
	GTN	29.73	35.70	2.29	0.70	0.05	0.02	28.94	97.43
	GTO	38.01	0.11	21.45	23.24	1.07	2.95	13.23	100.06
	GTP	37.72	0.63	20.37	23.31	0.80	3.34	13.02	99.21

4f Serpentine and chlorite

Appendix 5 Rock sample catalogue

This appendix is the catalogue of all the samples collected during fieldwork in the Bragança and Morais massifs. It includes information on date and location of sampling, lithologies, analytical techniques and storage.

In addition to the samples listed, six polished thin sections collected by Dr H.M. Prichard were used. These sections were of chromitites from Minas de Abicedo (HPP3), Sardoal (H4, HPP4B, HP4), Carrazedo (HPP6A), Carrascale (HPP2B). Carrascale is located at GR303 538. Probe analyses were taken from some of these samples.

		Details of sample and origin:						Slicing/sectioning				Analytical			
													Sample prepared for:-		
Sample Identifier	Rock/Spec. Type	Description/Special Features of sample	Place of Origin (grid reference)	Description of Locality	Date Collected	Rock Storage (Box no.)	Thin Section	Polished Section	Polished Block	Crushate (box no.)	Powder (box no.)	XRF Major (date)	XRF Trace (date)	ICPMS with Ni-S preconcention (date)	Minerals analysed
Brag1	Dunite		3085 5364	Minas de Abicodo	7.10.88	1	1						15/5/90	28/2/89	Cr,Chl,Serp,Pn
Brag2	Chromitite>80%		3085 5364	Minas de Abicodo	7.10.88	1		1		21	25				
Brag3	Chromite-rich>80%		3085 5364	Minas de Abicodo	7.10.88	1				21				May-90	Am,Gt,Ap
Brag4	Hornblendite		3085 5364	Minas de Abicodo	7.10.88	1	1				25		15/5/90		
Brag5	Chromitite>80%	Weathered	3028 5347	Carrazedo cemetry	7.10.88	1								May-90	
Brag6	Dunite		3028 5347	Carrazedo cemetry	7.10.88	1					25	4/5/90	15/5/90		Ol
Brag7	Dunite		3028 5347	Carrazedo cemetry	7.10.88	1	1							May-90	
Brag8	Hornblendite		3028 5347	Carrazedo cemetry	7.10.88	1					25	4/5/90		May-90	
Brag9	Dunite/harzburgite		3028 5347	Carrazedo cemetry	7.10.88	1	1		1		25	4/5/90	15/5/90+25/	May-90	Pn,Ol
Brag10	Garnet-pyroxenite		3045 5375	Almendo road cutting	7.10.88	2				21	25	4/5/90			
Brag11	Chromite-bearing>80%		3040 5376	Almendo mine	7.10.88	2		1							Cr
Brag12	Dunite/harzburgite		3040 5376	Almendo mine	8.10.88	2				21	25		15/5/90		
Brag13	Dunite/harzburgite		3045 5349	Chã Toure	8.10.88	2									
Brag14	Dunite		3045 5349	Chã Toure	8.10.88	2									
Brag15	Dunite		3045 5349	Chã Toure	8.10.88	2			1		25		15/5/90	May-90	
Brag16	Dunite		3045 5349	Chã Toure	8.10.88	2									
Brag17	Dunite/harzburgite		3053 5337	Videodo	8.10.88	2	1								
Brag18	Dunite		3053 5337	Videodo	8.10.88	2			1		25			May-90	
Brag19	Dunite		3053 5337	Videodo	8.10.88	2				21	25		15/5/90		
Brag20	Dunite/harzburgite		3053 5337	Videodo	8.10.88	2					25		15/5/90	May-90	
Brag21	Pyroxenite		3053 5337	Videodo	8.10.88	2				21	25	13/6/91	15/5/90		
Brag22	Chromite-rich>80%		3010 5368	Ribeira de Regua	8.10.88	3		1							Cr,Serp
Brag23	Dunite		3010 5368	Ribeira de Regua	8.10.88	3			1		25			May-90	
Brag24	Dunite/harzburgite		3010 5368	Ribeira de Regua	8.10.88	3					25	4/5/90	15/5/90+25/	May-90	Am,Cr,Ol,Opx
Brag25	Dunite		3010 5368	Ribeira de Regua	8.10.88	3	1								
Brag26	Chromitite>80%		3015 5365	Campoo	8.10.88	3		2							Cr
Brag27	Dunite		3015 5365	Campoo	8.10.88	3								28/2/89	
Brag28	Chromitite>80%		3015 5365	Campoo	8.10.88	3		1		21	25				
Brag29	Dunite/harzburgite		3015 5365	Campoo	8.10.88	3									
Brag30	Dunite		2978 5406	Vila Verde mine	8.10.88	3									
Brag31	Chromite-bearing	Nodular texture	2978 5406	Vila Verde mine	8.10.88	3		1							Cr,Ol
Brag32	Pyroxenite		2978 5406	Vila Verde mine	9.10.88	3									
Brag33	Hornblendite		2978 5406	Vila Verde mine	9.10.88	3									
Brag34	Dunite/harzburgite		2978 5406	Vila Verde mine	9.10.88	3	1		1	21	25	4/5/90		Mar-91	Am,Cr,Ol,Opx,Pn
Brag35	Peridotite	Talc alteration	3042 5422	Sete Fontes talc quarry	9.10.88	4				21	25			28/2/89	
Brag36	Peridotite	Talc alteration	3106 5368	Cabos Penedos talc quarry	9.10.88	4									
Brag37	Peridotite	Carbonate alteration	3106 5368	Cabos Penedos talc quarry	9.10.88	4	1								
Brag38	Peridotite	Talc alteration	3106 5368	Cabos Penedos talc quarry	9.10.88	4		1							
Brag39	Chromite-rich50-80%		3055 5350	Pena de Velhos	9.10.88	4		1			25		15/5/90+25/	May-90	Cr,Ol
Brag40	Pyroxenite		3055 5350	Pena de Velhos	9.10.88	4				21	25		15/5/90		
Brag41	Chromite-bearing10-20%		3055 5350	Pena de Velhos	9.10.88	4					26				
Brag42	Pyroxenite		3055 5354	N. Pena de Velhos	10.10.88	4	1								
Brag43	Chromite-bearing10%		3055 5354	N. Pena de Velhos	10.10.88	4			1		26			May-90	Ol
Brag44	Hornblendite		3055 5354	N. Pena de Velhos	10.10.88	5									
Brag45	Dunite/harzburgite		3055 5354	N. Pena de Velhos	10.10.88	5					26	13/6/91	15/5/90	May-90	
Brag46	Chromite-bearing10%		3045 5366	Serralhos	10.10.88	5			1						
Brag47	Chromite-bearing30%		3045 5366	Serralhos	10.10.88	5									
Brag48	Dunite/harzburgite	Pyroxenite layers	3045 5366	Serralhos	10.10.88	5									
Brag49	Dunite		3045 5366	Serralhos	10.10.88	5									Cr,Chl
Brag50	Pyroxenite	Mylonite	3045 5366	Serralhos	10.10.88	5									
Brag51	Chromite-rich50-80%		3045 5366	Serralhos	10.10.88	5		1			26		15/5/90	May-90	
Brag52	Chromitite		3045 5366	Serralhos	10.10.88	5		1		21	26		15/5/90	28/2/89	Cr
Brag53	Chromite-rich50-80%		3045 5366	Serralhos	10.10.88	5		1		21	26		15/5/90	28/2/89	
Brag54	Chromite-bearing10%		3045 5366	Serralhos	10.10.88	5			1		26		15/5/90		
Brag55	Pyroxenite		3045 5366	Serralhos	10.10.88	5					26		15/5/90		
Brag56	Chromite-rich50%		3043 5368	Dernada mines	10.10.88	5		1	1		26		15/5/90	May-90	Cr
Brag57	Chromitite>80%		3043 5368	Dernada mines	10.10.88	5		1			26		15/5/90	28/2/89	Cr,La,Ir,Hz
Brag58	Dunite		3043 5368	Dernada mines	10.10.88	6	1			21	26		15/5/90	28/2/89	

Sample Identifier	Rock/Spec. Type	Description/Special Features of sample	Place of Origin (grid reference)	Description of Locality	Date Collected	Rock Storage (box no.)	Thin Section	Polished Section	Polished Block	Crushate (box no.)	Powder (box no.)	XRF Major (date)	XRF Trace (date)	ICPMS with Ni-S precollection (date)	Minerals analysed
Brag59	Chromite-rich50%		3043 5358	Derruida mines	10.10.88	6			1		28	4/5/90	15/5/90+25/	May-90	Am
Brag60	Pyroxenite		3040 5360	Lower Derruida track	10.10.88	6									
Brag61	Dunite/harzburgite		3040 5360	Lower Derruida track	10.10.88	6				21					
Brag62	Pyroxenite	Amphibolitised	3040 5360	Lower Derruida track	10.10.88	6	1	1			28	4/5/90			Am
Brag63	Pargasite-peridotite		3038 5358	Lower Derruida track	10.10.88	6		1	1		28		15/5/90+25/	May-90	Cr,Ol,Pn
Brag64	Chromite-bearing25-50%		3005 5305	Leutlecais	11.10.88	6									
Brag65	Chromite-rich50%		3005 5305	Leutlecais	11.10.88	6									
Brag66	Pyroxenite		3005 5305	Leutlecais	11.10.88	6									
Brag67	Chromite-bearing10-20%		3003 5308	W. Leutlecais	11.10.88	6									
Brag68	Chromite-bearing10-20%		3003 5308	W. Leutlecais	11.10.88	6									
Brag69	Hornblendite		3003 5308	W. Leutlecais	11.10.88	6	1								
Brag70	Chromite-rich50%		3002 5307	W. Leutlecais	11.10.88	6	1	1			28		15/5/90	May-90	Cr
Brag71	Chromite-bearing25-40%		3002 5307	W. Leutlecais	11.10.88	7				21	28		15/5/90	28/2/89	
Brag72	Garnet-pyroxenite		3002 5307	W. Leutlecais	11.10.88	7	1						15/5/90	May-90	Ol
Brag73	Dunite		3007 5308	N. Leutlecais	11.10.88	7		1	1						
Brag74	Dunite/harzburgite		3007 5308	N. Leutlecais	11.10.88	7									
Brag75	Dunite/harzburgite		3007 5308	N. Leutlecais	11.10.88	7	1							May-90	Cr,La
Brag76	Chromitite		3013 5401	Conleias	11.10.88	7		1			28				
Brag77	Chromite	Nodular	2978 5408	Vila Verde mine	13.10.88	7		1							
Brag78	Chromite-rich60%		3026 5375	Sardoal mines	13.10.88	7		1		21	28		15/5/90	28/2/89	
Brag79	Chromitite60%		3040 5378	Almonde mine	13.10.88	7		1							Cr
Brag80	Pyroxenite		3152 5353	Samil	17.10.88	7									
Brag81	Chromite-bearing20%		3151 5350	Samil	17.10.88	7		1							
Brag82	Dunite		3155 5350	Samil	17.10.88	7									Am,Cr,Opx
Brag83	Websterite		3155 5350	Samil	17.10.88	7	1		1						Ol
Brag84	Chromite-rich50%		3148 5355	Samil	17.10.88	8		1							
Brag85	Dunite		3143 5334	San Pedro de Serracenos	17.10.88	8									
Brag86	Amphibolite		3137 5334	San Pedro de Serracenos	17.10.88	8	1								
Brag87	Dunite		3136 5336	San Pedro de Serracenos	17.10.88	8	2								
Brag88	Dunite		3123 5368	Tojal de Pereiros	17.10.88	8				21	28		15/5/90		
Brag89	Dunite		3122 5367	Tojal de Pereiros	17.10.88	8				21	28			May-90	Cr
Brag90	Fault breccia		3118 5430	Pedrosa	18.10.88	8	1								
Brag91	Peridotite	Talc alteration	3147 5425	Oterinhos	19.10.88	8									
Brag92	Dunite		3150 5415	Cortinheros	19.10.88	8	1								
Brag93	Dunite		3045 5484	Cortinheros	19.10.88	8									
Brag94	Peridotite		3060 5410	Ladeiro hill	19.10.88	8									
Brag95	Amphibolite		3073 5316	Rebordaos	19.10.88	8	1			21					
						8									
1BRG	Dunite/harzburgite		3040 5360	Lower Derruida track	30.4.89	9					28	13/6/91	15/5/90	May-90	
2BRG	Dunite/harzburgite	Pyroxenite layers	3040 5360	Lower Derruida track	30.4.89	9				22	27				Am,Cpx
3BRG	Pyroxenite	Amphibole alteration	3040 5360	Lower Derruida track	30.4.89	9		1							
4BRG	Pyroxenite		3040 5360	Lower Derruida track	1.5.89	9		1							Am,Cpx,Chl
5BRG	Pyroxenite	Amphibolitised	3040 5360	Lower Derruida track	1.5.89	9									
6BRG	Pyroxenite		3040 5360	Lower Derruida track	1.5.89	9									
7BRG	Dunite/harzburgite		3043 5358	Derruida mines	1.5.89	9									Cr
8BRG	Chromite-rich50-60%		3043 5357	South Derruida mines	1.5.89	9		1							
9BRG	Pyroxenite	Amphibole alteration	3043 5358	Derruida mines	2.5.89	9									
10BRG	Gt-fsp-parg-gneiss		3042 5358	Derruida track	2.5.89	9		1			27	4/5/90		May-90	Am,Fel,Gt
11BRG	Pyroxenite		3042 5358	Derruida track	2.5.89	9									
12BRG	Chromite-rich50-60%		3043 5358	Derruida mines	2.5.89	9		1							Cr,La
13BRG	Pyroxenite		3041 5358	Derruida track	2.5.89	9									
14BRG	Pyroxenite		3039 5358	Derruida track	2.5.89	9	1				27		15/5/90	May-90	
15BRG	Pyroxenite	Mylonite	3039 5358	Derruida track	2.5.89	10									
16BRG	Dunite/harzburgite		3042 5358	S. E. Derruida	3.5.89	10									
17BRG	Gt-plag-mica-gneiss	Leucocratic gneiss	3042 5358	S. E. Derruida	3.5.89	10	1								
18BRG	Gt-fsp-parg-gneiss		3042 5358	S. E. Derruida	3.5.89	10									
19BRG	Gt-fsp-parg-gneiss		3042 5358	Lower Derruida track	4.5.89	10									
20BRG	Dunite/harzburgite	Pyroxenite layers	3045 5355	Serralhos	4.5.89	10			1		27		15/5/90	May-90	
21BRG	Websterite		3045 5355	Serralhos	5.5.89	10									
22BRG	Dunite/harzburgite	Pyroxenite layers	3045 5355	Serralhos	5.5.89	10									
23BRG	Dunite/harzburgite		3046 5366	E. Serralhos	5.5.89	10									

Sample Identifier	Rock type	Description/Special Features of sample	Place of Origin (grid reference)	Description of Locality	Date Collected	Rock Storage (box no.)	Thin Section	Polished Section	Polished Block	Crushate (box no.)	Powder (box no.)	XRF Major (date)	XRF Trace (date)	ICPMS with Ni-S preconcentration (date)	Minerals analysed
2SERG	Gt-fsp-pyrg-gneiss	Mylonite	3040 5366	E. Somalhos	5.5.90	10	1								
3SERG	Thrust mylonite		3040 5366	E. Somalhos	5.5.90	10									
4SERG	Thrust mylonite		3040 5366	E. Somalhos	5.5.90	10									
5SERG	Thrust mylonite		3040 5366	E. Somalhos	5.5.90	10									
6SERG	Thrust mylonite		3040 5366	E. Somalhos	5.5.90	11					27			May-90	
7SERG	Dunite		3040 5370	Allmende mine	6.5.90	11	1				27			May-90	
8SERG	Amphibolite	Layer in ultrabasics	3040 5370	Allmende mine	6.5.90	11									Am,Cr,Ol
9SERG	Chromitite 80%	Small sample	3040 5370	Allmende mine track	6.5.90	11		1							
10SERG	Dunite/herzburgite	Pyroxenite layers	3042 5370	N.W. of Allmende mine	6.5.90	11									
11SERG	Chromite-rich50-80%		3066 5364	Minas de Abicada	7.5.90	11									
12SERG	Chromitite80%		3066 5364	Minas de Abicada	7.5.90	11									
13SERG	Hornblendite		3066 5364	Minas de Abicada	7.5.90	11	1								
14SERG	Chromitite80%		3020 5377	Sardoal	7.5.90	11									
15SERG	Hornblendite		3066 5364	Minas de Abicada	8.5.90	11									
16SERG	Chromitite80%		3066 5364	Minas de Abicada	8.5.90	11									
17SERG	Chromitite80%		3066 5364	Minas de Abicada	8.5.90	11				22	27		15/5/90	May-90	
18SERG	Chromitite80%		3066 5364	Minas de Abicada	8.5.90	11									
19SERG	Chromitite80%		2978 5408	Vila Verde mine	8.5.90	11									
20SERG	Dunite/herzburgite	Pyroxenite layers	2978 5407	Vila Verde track	8.5.90	11	1								
21SERG	Pyroxenite		2978 5407	Vila Verde track	8.5.90	11	1								Am,Cr,Opx
22SERG	Websterite		2978 5407	Vila Verde track	8.5.90	11			1		27		15/5/90	Mar-91	Cr
23SERG	Pyroxenite	Vein	3015 5366	Campos	10.5.90	11									
24SERG	Chromitite80%		3015 5366	Campos	10.5.90	12			1		27		15/5/90	May-90	
25SERG	Pyroxenite		3015 5366	Campos	10.5.90	12									
26SERG	Chromite-bearing 25-50%		3015 5366	Campos	10.5.90	12					27		15/5/90	May-90	
27SERG	Pyroxenite	Mylonite	3006 5366	Loutiosais	11.5.90	12									
28SERG	Hornblendite		3003 5366	W. Loutiosais	11.5.90	12									
29SERG	Websterite		3003 5366	W. Loutiosais	11.5.90	12	1	1							Cpx
30SERG	Dunite	Pyroxenite vein	3003 5366	W. Loutiosais	11.5.90	12	1								
31SERG	Hornblendite		3023 5346	Carrazede	12.5.90	12									
32SERG	Hornblendite in Gt-fspr-pyrg-gneiss		3023 5346	Carrazede	12.5.90	12	1								
33SERG	Hornblendite in Gt-fspr-pyrg-gneiss		3023 5346	Carrazede	12.5.90	12				22	27		15/5/90		
34SERG	Chromite-bearing20%		3148 5366	Sandi	14.5.90	12	1				27		15/5/90	May-90	
35SERG	Pyroxenite	Mylonite	3148 5366	Sandi	14.5.90	12				22					
37SERG	Pyroxenite	Amphibolite alteration	3155 5369	Sandi	14.5.90	12									
38SERG	Kyanite-schist		3149 5364	San Pedro de Sarracenos	14.5.90	12									
39SERG	Hornblendite in Gt-fspr-pyrg-gneiss		3122 5369	Tojal de Pereiros	14.5.90	12								+	
40SERG	Dunite		3122 5369	Tojal de Pereiros	14.5.90	12									
41SERG	Pyroxenite	Amphibolite alteration	3026 5375	Sardoal	16.5.90	13									
42SERG	Dunite/herzburgite	Pyroxenite layers	3026 5375	Sardoal	16.5.90	13			1		27	4/5/90	15/5/90	May-90	
43SERG	Dunite		3026 5375	Sardoal	16.5.90	13									
44SERG	Chromitite80%		3026 5375	Sardoal	16.5.90	13			1						
45SERG	Dunite	Pyroxenite vein	3026 5375	Sardoal	16.5.90	13									
46SERG	Chromite-rich25-50%		3025 5376	N. Sardoal	16.5.90	13		1							Cr
47SERG	Pyroxenite		3025 5376	N. Sardoal	16.5.90	13									
48SERG	Chromite-rich50-80%		3029 5377	N.E. Sardoal	16.5.90	13									
49SERG	Peridotite		3144 4964	N. Vinhas	18.5.90	13									
70SERG	Peridotite		3144 4964	N. Vinhas	18.5.90	13									
71SERG	Amphibolite		3145 4949	Vinhas, N. bank Rio Sabor	19.5.90	13									
72SERG	Peridotite		3146 4963	N. Vinhas traverse S. to river	20.5.90	13			1		27		15/5/90	May-90	
73SERG	Peridotite		3145 4963	N. Vinhas	20.5.90	14		1		22	27	13/6/91			Cr,Opx,Opx
74SERG	Peridotite		3146 4963	N. Vinhas	20.5.90	14	1								
75SERG	Peridotite		3146 4963	N. Vinhas	20.5.90	14				22	27	13/6/91			Am,Cr,Ol
76SERG	Peridotite		3146 4963	N. Vinhas	20.5.90	14		1							
77SERG	Peridotite		3146 4963	N. Vinhas	20.5.90	14									
78SERG	Peridotite		3146 4963	N. Vinhas	20.5.90	14									
79SERG	Peridotite		3146 4963	N. Vinhas	20.5.90	14									
80SERG	Peridotite		3146 4963	N. Vinhas	20.5.90	14									
81SERG	Peridotite		3146 4963	N. Vinhas	20.5.90	14			1		27		15/5/90	May-90	
82SERG	Peridotite		3163 5056	Morais-Limaos road	21.5.90	14	1								
83SERG	Peridotite		3163 5056	Morais-Limaos road	21.5.90	14									
84SERG	Amphibolite	Layer in peridotite	3163 5056	Morais-Limaos road	21.5.90	14									

Sample Identifier	Rock/Spec. Type	Description/Special Features of sample	Place of Origin (grid reference)	Description of Locality	Date Collected	Rock Storage (Box no.)	Thin Section	Polished Section	Polished Block	Crushate (box no.)	Powder (box no.)	XRF Major (date)	XRF Trace (date)	ICPMS with NI-S preconcetion (date)	Minerals analysed
	Dunite		3103 5055	Morais-Limoes road	21.5.89	14			1	22	27		15/5/90	May-90	
85BRG	Amphibolite	Layer in peridotite	3103 5055	Morais-Limoes road	21.5.89	14				22	27		15/5/90		
87BRG	Dolerite		3104 5045	Sobreda road	21.5.89	14			1		27	4/5/90		May-90	Cr
88BRG	Peridotite		3104 5045	Sobreda road	21.5.89	14									
89BRG	Peridotite		3100 5045	Sobreda road	21.5.89	14									
90BRG	Amphibolite	Layer in peridotite	3090 5090	Lameira Redonda	21.5.89	14									
91BRG	Amphibolite Sacer gabbro		3144 5042	Road N.E. of Morais	22.5.89	14					27			May-90	
92BRG	Peridotite		3148 5055	Road N.E. of Morais	22.5.89	15									
93BRG	Peridotite		3153 5067	Castelei	22.5.89	15								May-90	
94BRG	Peridotite		3215 4957	1km E. of Sampaio	22.5.89	15					27		15/5/90		
95BRG	Peridotite		3118 5018	Caminho Velho	23.5.89	15		1		22	27		15/5/90		Cr,Ol,Fel
96BRG	Troctolite	Ophitic texture	3112 5013	Caminho Velho	23.5.89	15	1			22					
97BRG	Amphibolite		3112 5013	Caminho Velho	23.5.89	15					27	13/6/91		May-90	
98BRG	Peridotite		3112 5013	Caminho Velho	24.5.89	15	1								
99BRG	Peridotite		3112 5009	Caminho Velho	24.5.89	15		1		22					Am,Cr,Ol
100BRG	Peridotite		3112 5007	Caminho Velho	24.5.89	15									
101BRG	Gt-fspr-parg-gneiss	Mylonite	3112 5013	Caminho Velho	24.5.89	15									
102BRG	Peridotite		3153 4950	Vinhas, Picarrao summit	24.5.89	15	1				27	13/6/91			
103BRG	Gt-fspr-parg-gneiss		3153 4950	Vinhas, Picarrao summit	24.5.89	15									
104BRG	Peridotite		3228 4976	Prado, S. of Zamborinho Mt.	25.5.89	15	1								
105BRG	Peridotite		3228 4976	Prado, S. of Zamborinho Mt.	25.5.89	15					27	4/5/90		May-90	
106BRG	Peridotite		3228 4976	Prado, S. of Zamborinho Mt.	25.5.89	15									
107BRG	Peridotite		3229 4976	Prado summit	25.5.89	15									
108BRG	Dunite	Pyroxenite vein	3026 5379	N. Sardoal	27.5.89	15	1								
109BRG	Websterite		3018 5383	E. Sardoal	27.5.89	15									
110BRG	Chromitite80%		3029 5377	N.E. Sardoal	27.5.89	15		1							
111BRG	Gt-fspr-parg-gneiss		3025 5378	N. Sardoal	27.5.89	16									
112BRG	Gt-fspr-parg-gneiss		3030 5360	N. Sardoal to Almonde path	27.5.89	16									
113BRG	Dunite	Pyroxenite vein	3045 5464	Parameio, on hillock	29.5.89	16									
114BRG	Gt-fspr-parg-gneiss		3044 5464	Parameio, 200m to W. of hillock	29.5.89	16									
115BRG	Gt-plag-mica-gneiss	Leucocratic gneiss	3045 5470	Parameio, along path to main road	29.5.89	16									
116BRG	Gt-plag-mica-gneiss	Leucocratic gneiss	3113 5365	Donai/Vinhais road junction	29.5.89	16	1								
117BRG	Dunite	Pyroxenite layer	3093 5428	Donai village, Serro hill	30.5.89	16				22	27	13/6/91	15/5/90		
118BRG	Peridotite		3054 5416	Ladeiro hill	30.5.89	16	1			22					
119BRG	Peridotite	Visible sulphides	3056 5417	Ladeiro hill, E. of trig point	30.5.89	16									
120BRG	Peridotite	Talc alteration	3022 5450	Soeira Hill	31.5.89	16									
121BRG	Peridotite		3022 5450	Soeira Hill	31.5.89	16									
122BRG	Peridotite		3086 5404	Lagomar hill, near Grandais	31.5.89	16									
123BRG	Peridotite		3086 5404	Lagomar hill, near Grandais	31.5.89	16									
124BRG	Peridotite		3086 5404	Lagomar hill, near Grandais	31.5.89	16									
125BRG	Amphibolite		3063 5400	Lagomar hill, road cutting	31.5.89	16									
126BRG	Pyroxenite		305 530	Vidoedo	1.6.89	16									
127BRG	Amphibolite		3150 5115	Cortinheiros	1.6.89	16									
128BRG	Peridotite	Talc alteration	3150 5115	Cortinheiros	1.6.89	16									
129BRG	Dunite		3040 5376	Almonde mine	2.6.89	17				22	27		15/5/90+25/	May-90	
130BRG	Chromite-rich50-80%		3040 5376	Almonde mine	2.6.89	17					28	4/5/90		May-90	
131BRG	Hornblendite	Pegmatoidal	3026 5347	Carrazedo chapel	3.6.89	17				22	28		15/5/90		
132BRG	Hornblendite	Pegmatoidal	3040 5360	Lower Derruida Track	3.6.89	17	1		1	22	28	13/6/1991+4	15/5/90+25/	May-90	Cr,Ol,OPx
133BRG	Dunite/harzburgite		3042 5358	S.E. Derruida	3.6.89	17			1	23	28		15/5/90	May-90	Cr
134BRG	Chromite-rich50-80%		3045 5355	Serralhoe	3.6.89	17				23					
135BRG	Dunite/harzburgite		3045 5355	Serralhoe	3.6.89	17	1								
136BRG	Pyroxenite	Amphibolite alteration	3045 5355	Serralhoe	3.6.89	17	1			23	28		15/5/90		
137BRG	Amphibolite		3034 5363	Serralhoe/Ribeira Almonde	3.6.89	17									
138BRG	Amphibolite		3034 5363	Serralhoe/Ribeira Almonde	3.6.89	17	1								
139BRG	Websterite		5395 2983	Rio Tuela, east bank	4.6.89	17									
140BRG	Dunite		5395 2983	Rio Tuela, east bank	4.6.89	17		1			28	4/5/90	15/5/90+25/	May-90	Cr,Opx,Cpx
141BRG	Websterite		5395 2983	Rio Tuela, east bank	4.6.89	17			1		28		15/5/90+25/	May-90	
142BRG	Chromitite		2989 5401	Cabeço da Pedrosa mine trench	4.6.89	17									
143BRG	Chromite-rich80%		2989 5401	Cabeço da Pedrosa mine trench	4.6.89	18									
144BRG	Chromitite80%		2989 5401	Cabeço da Pedrosa mine trench	4.6.89	18									
145BRG	Chromitite70-80%		2989 5401	Cabeço da Pedrosa mine trench	4.6.89	18		1			28		15/5/90	May-90	Cr

Sample identifier	Rock/type. Type	Description/Special Features of sample	Place of Origin (grid reference)	Description of Locality	Date Collected	Rock Storage (box no.)	Thin Section	Polished Section	Polished Block	Crushate (box no.)	Powder (box no.)	XRF Major (date)	XRF Trace (date)	ICPMS with Ni-S preselection (date)	Minerals analysed
															Cr,Ol,Opx
1468RG	Dunite/harzburgite	Pyroxenite dissemination	3888 5401	Cabeço da Pedreca mine trench	4.6.90	18		1	1					May-90	
1470RG	Amphibolite	Magnetite-rich	3138 5864	Paiva hill	6.6.90	18					28				
1469RG	Amphibolite	Magnetite-rich	3138 5864	Paiva hill	6.6.90	18					28			May-90	
1467RG	Peridotite		388 468	Pass main road	6.6.90	18									
1466RG	Chlorite-amphibolite		388 468	Pass main road	6.6.90	18									
1465RG	Peridotite	Visible sulphides	388 468	Pass main road	6.6.90	18									
1464RG	Chromite-rich80%		3886 5363	Cabeço Corro Paiva	6.6.90	18		1			28		15/5/90	May-90	Cr
1463RG	Chromite-bearing60%		3886 2863	Rio Tuela, east bank	9.6.90	18									
1462RG	Chromite-rich70%		3886 2863	Rio Tuela, east bank	9.6.90	18					29		15/5/90+25/	May-90	
1461RG	Chromite-rich70%		3886 2863	Rio Tuela, east bank	9.6.90	19		1			29		15/5/90	May-90	Cr
1460RG	Chromite-rich60-70%		3886 2863	Rio Tuela, east bank	9.6.90	19	1				29		15/5/90		
1464RG	Websterite		3886 2863	Rio Tuela, east bank	9.6.90	19									
1479RG	Pyroxenite	Amphibole alteration	3886 2863	Rio Tuela, east bank	9.6.90	19									
1458RG	Pyroxenite		3886 2863	Rio Tuela, east bank	9.6.90	19									
1457RG	Dunite		3886 2863	Rio Tuela, east bank	9.6.90	19			1						
1456RG	Pyroxenite		3886 2863	Rio Tuela, east bank	9.6.90	19									
1455RG	Pyroxenite		3886 2863	Rio Tuela, east bank	9.6.90	19					29	4/5/90	15/5/90	May-90	
1454RG	Dunite		3142 5364	Bragança town car park	10.6.90	20	1								
1453RG	Gt-fspr-perg-gneiss		3887 5356	Pseudotorre quarry Porto road	10.6.90	20	1						15/5/90		
1452RG	Eclogite		3936 5375	Allmendo village road north	9.6.90	20	1			23	28				
1455RG	Peridotite	Talc alteration	3882 5410	Ladeira	4.6.90	20									
1456RG	Dunite/harzburgite		3940 5369	Serralhos	6.6.90	20	1		1	23	29	13/6/91	15/5/90	Mar-91	Cr,Ol,Opx,Pn
1457RG	Perg-peridotite	Mylonite	3931 5361	N. Dormida/Serralhos	6.6.90	20	1			23	29		15/5/90		
1458RG	Gt-plag-mica-gneiss	Leucocratic gneiss	3938 5356	S. Dormida	6.6.90	20				23	29		15/5/90		
1459RG	Garnet-pyroxenite		3900 5404	S. Vila Verde	10.6.90	20	1			23	29		15/5/90		
1460RG	Gt-fspr-perg-gneiss		3881 5409	R. Tuela west bank	10.6.90	20	1			23	29		15/5/90		
1470RG	Chromitite		3888 5368	Ouelhas mine	12.6.90	20			1						Cr
1471RG	Garnet-pyroxenite	Amphibolite alteration	3883 5366	W. Loudosais	12.6.90	20				23	29		15/5/90		
1472RG	Amphibolite		3146 4940	Vinhas N. bank R. Sabor	19.6.90	20				23	29		15/5/90		
1473RG	Gt-fspr-perg-gneiss		3147 4964	Vinhas N. bank R. Sabor, tributary	19.6.90	20				23	29		15/5/90		
1474RG	Mica-schist		3144 4962	Lagoa road	20.6.90	20				23	29				
1475RG	Mica-schist		3144 4962	Lagoa road	20.6.90	20	1								
1476RG	Augen gneiss	Granitic	3144 4962	Lagoa road	20.6.90	20				23	29		15/5/90		
1477RG	Pyroxenite in Gt-fspr-perg-gneiss		3887 5356	Pseudotorre quarry Porto road	21.6.90	20	1			24	29		15/5/90		
1478RG	Gt-fspr-perg-gneiss		3887 5356	Pseudotorre quarry Porto road	21.6.90	20				24	29		15/5/90		
1479RG	Gt-plag-mica-gneiss	Leucocratic gneiss	3936 5375	Allmendo village road north	21.6.90	20									
1480RG	Amphibolite	Layer in ultrabasics	3940 5370	Allmendo mine track	21.6.90	20				24	29		15/5/90		
1481RG	Marble		385 548	Near Paramelo village	23.6.90	20									
1482RG	Eclogite		918 536	Bragança to Gimonde road	23.6.90	20	1								
1483RG	Peridotite		3145 4962	Vinhas, E. side Rio Sabor	24.6.90	20	1		1	24	29	13/6/91	15/5/90		Am,Ol
1484RG	Gt-fspr-perg-gneiss		3161 4955	Vinhas hill	24.6.90	20				24	29		15/5/90		
1485RG	Peridotite		3215 4957	E. Sarzeda	25.6.90	20	1			24	29		15/5/90		
1486RG	Tremolite		3112 5013	Caminho velho	1.6.90	20				24	29	13/6/91	15/5/90		
1487RG	Amphibolite		3112 5013	Caminho velho	1.6.90	20				24	29	13/6/91	15/5/90		
1488RG	Augen gneiss	Granitic	3112 5013	Caminho velho	1.6.90	20	1			24	29	13/6/91	15/5/90		
1489RG	Amphibolite		3163 4934	Mogadouro road	1.6.90	20	1			24	29		15/5/90		
1490RG	Dunite/harzburgite		3888 5366	R. Tuela east side	2.6.90	20	1		1	24	29	13/6/91	15/5/90	Mar-91	Am,Cr,Ol,Pn

Grid reference refers to Carta Militar de Portugal
Serviços Cartográficos do exército. 1950 1:25 000 scale
Map numbers 23,24,25,36,37,38,49,50,51,78,79,80,92,93,94,106,107,108

Box no. refers to OU Earth sciences rock store

Dunite/harzburgite descriptions equivalent to harzburgite formation in main part of thesis
% given is amount chromite, remainder of sample dunite
Samples: 69-1675RG, 173-1775RG, 184-1905RG from Morais massif

Serp=serpentine	Ap=apatite
Fel=feldspar	Am=amphibole
Ol=olivine	Opx=orthopyroxene
Pn=pentlandite	Cpx=clinopyroxene
Hz=heazelwoodite	Gt=garnet
La=laurite	Cr=chrome spinel
Ir=irarsite	Chl=chlorite
Pn,Hz,La,Ir analysed on SEM	
Other minerals analysed on WD probe	

Appendix 6 Rock and mineral nomenclature

6a Dunite to chromitite distinction

Dunite <5% chromite

Chromite-bearing 5-50% chromite

Chromite-rich 50-75% chromite

Chromitite >75% chromite

6B Ultrabasic (ultramafic) rock classification

After Streckeisen (1976)

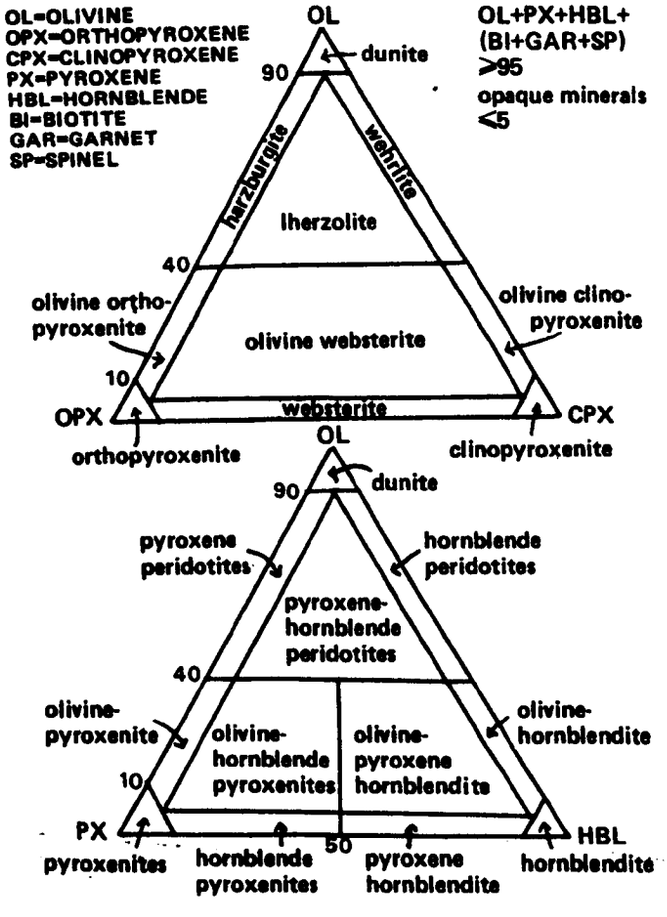

6C Calcic amphibole nomenclature

From Leake (1978)

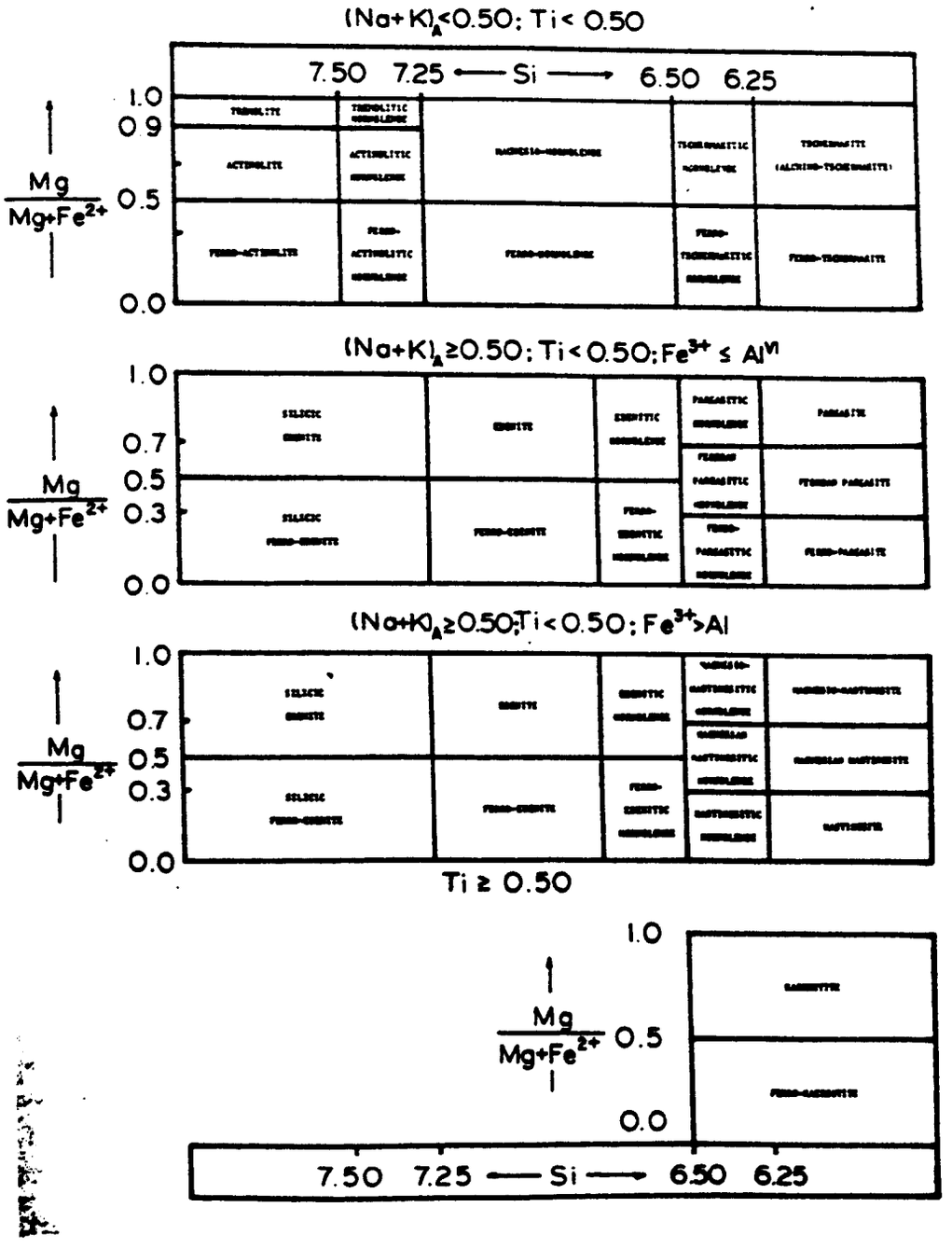

Appendix 7 Geochemical Data

7a XRF Major element analyses on glass discs

7b XRF Trace element analyses on powder pellets

7c ICPMS PGE analyses

ARL8420+ WD XRF 1991 analyses																	
	SiO2	TiO2	Al2O3	Fe2O3	MnO	MgO	CaO	Na2O	K2O	P2O3	S	LOI	tal wt %	Al ppm	Ba ppm	Cr ppm	Ni ppm
BRAG21	40.11	0.04	1.67	8.12	0.10	38.39	0.83	0.15	0.01	0.01	0.01	10.50	99.94	8851	1	2437	2092.00
BRAG45	39.23	0.05	1.60	9.83	0.14	37.47	2.72	0.27	0.01	0.01	0.01	8.03	99.37	8480	2	5901	2202.00
1BRG	42.19	0.02	0.82	9.00	0.13	38.72	0.65	0.17	0.01	0.01	0.00	7.83	99.55	4346	7	2888	2577.00
73BRG	41.93	0.12	2.75	8.49	0.12	35.38	2.48	0.32	0.03	0.01	0.00	8.46	100.09	14575	24	1929	1993.00
75BRG	44.34	0.37	7.18	7.95	0.13	29.11	6.00	1.20	0.28	0.03	0.00	2.54	99.13	38054	169	2798	1416.00
98BRG	36.13	0.20	4.62	13.61	0.19	31.10	2.15	0.36	0.04	0.03	0.01	8.42	96.86	24486	18	16027	1356.00
102BRG	39.89	0.03	1.66	8.60	0.12	36.75	0.79	0.10	0.01	0.00	0.00	12.31	100.27	8798	2	2205	2025.00
117BRG	42.13	0.03	1.39	8.18	0.12	33.22	2.19	0.25	0.02	0.01	0.00	10.07	99.80	8427	8	2432	2318.00
133BRG	39.78	0.02	0.69	7.72	0.11	38.51	0.07	0.08	0.00	0.01	0.00	12.66	99.64	3657	2	2754	2221.00
166BRG	39.99	0.02	0.65	7.62	0.09	37.86	0.05	0.22	0.01	0.01	0.01	12.95	99.47	3445	63	2393	2430.00
184BRG	41.11	0.04	2.06	8.18	0.12	36.65	2.05	0.14	0.01	0.01	0.00	9.66	100.03	10918	13	2496	1987.00
187BRG	39.01	0.09	10.91	9.13	0.14	25.40	5.91	0.77	0.27	0.02	0.03	7.56	99.23	57823	7	1379	978.00
188BRG	46.28	0.26	20.46	4.99	0.08	9.60	11.02	2.69	0.14	0.03	0.00	4.20	99.75	108438	29	644	251.00
189BRG	66.08	0.89	15.18	5.53	0.08	1.66	2.97	3.60	1.94	0.16	0.03	1.91	100.03	80454	1104	22	28.00
191BRG	41.47	0.01	0.58	8.57	0.13	41.64	0.67	0.16	0.01	0.01	0.00	6.71	99.96	3074	1	2468	2326.00
Standards																	
S-2 XRF	42.30	0.38	8.48	11.92	0.17	28.22	5.71	0.74	0.08	0.06	0.00	2.19	100.26		81	840	1185.00
S-2 Expected	42.27	0.37	8.42	11.99	0.18	28.37	5.63	0.84	0.08	0.06		2.19	100.40		70	898	1150.00
S-5 XRF	57.96	1.02	15.90	6.32	0.10	4.73	5.37	4.20	3.36	0.48	0.04	0.48	99.96		1371	194	95.00
S-5 Expected	58.10	1.00	15.89	6.31	0.11	4.77	5.38	3.97	3.36	0.47		0.48	99.84				
Link Systems Mecca 20															BaO	Cr2O3	NiO
10BRG	41.83	2.82	13.18	16.73	0.22	6.21	12.62	1.83	0.41	0.45	0.01	1.76	98.07		0.00	0.18	0.00
141BRG	53.24	0.05	2.05	6.26	0.14	22.67	14.37	0.78	0.04	0.00	0.03	1.56	101.17		0.00	0.71	0.08
162BRG	37.95	0.00	1.57	13.69	0.13	37.07	0.12	1.03	0.00	0.00	0.01	12.40	103.96		0.10	0.67	0.20
131BRG	38.82	1.23	11.92	11.12	0.12	13.63	14.84	1.87	0.94	3.44	0.00	2.13	100.06		0.00	0.04	0.00
133BRG	40.85	0.00	0.97	8.12	0.10	39.45	0.09	0.57	0.00	0.00	0.01	13.28	103.44		0.09	0.44	0.30
105BRG	42.87	0.04	2.28	8.64	0.13	36.83	2.69	0.87	0.02	0.00	0.01	8.92	103.27		0.00	0.48	0.26
BRAG24	42.86	0.00	1.10	8.99	0.12	42.52	0.93	1.50	0.03	0.00	0.01	6.96	105.02		0.00	0.39	0.31
62BRG	39.54	0.01	1.52	11.89	0.13	38.92	0.23	0.90	0.02	0.00	0.01	10.28	103.45		0.00	1.08	0.38
BRAG60	49.74	0.06	2.02	9.11	0.15	31.28	6.98	0.88	0.04	0.00	0.01	2.81	103.08		0.00	0.56	0.11
BRAG63	39.16	0.23	4.72	13.77	0.21	33.50	2.71	1.57	0.04	0.00	0.02	7.28	103.20		0.00	0.42	0.19
BRAG10	45.87	0.17	13.70	12.05	0.28	13.52	13.88	0.83	0.14	0.00	0.01	0.46	100.91		0.00	0.05	0.00
72BRG	39.47	0.02	1.71	9.78	0.14	35.67	0.31	0.59	0.00	0.00	0.00	13.17	100.86		0.08	2.32	0.29
BRAG9	40.79	0.00	0.50	8.61	0.12	40.61	0.39	0.00	0.00	0.00	0.01	9.18	100.21		0.00	0.46	0.29
BRAG8	34.24	1.85	12.85	20.56	0.25	6.84	12.34	1.85	1.31	3.52	0.01	1.50	97.13		0.00	0.02	0.00
BRAG6	40.27	0.00	0.40	9.72	0.14	40.83	0.11	0.00	0.02	0.00	0.01	10.29	101.78		0.10	0.63	0.32
88BRG	41.55	0.03	2.19	9.64	0.15	36.24	0.40	0.00	0.01	0.00	0.01	11.49	101.72		0.00	0.41	0.35
BRAG34	41.50	0.00	0.67	8.32	0.12	41.37	0.84	0.64	0.02	0.55	0.01	8.68	102.72		0.00	0.39	0.29
Standard																	
PCCI expected	42.10	0.01	0.73	8.28	0.12	43.50	0.55	?	?	?	?	4.30	100.40				
PCCI obtained	42.78	0.00	1.00	8.74	0.12	44.68	0.57	1.15	0.00	0.00	0.01	4.30	103.33				
PCCI obtained	42.52	0.00	0.81	8.58	0.12	44.42	0.58	0.94	0.00	0.00	0.01	4.30	102.27				

	Wt%									Wtppm																				
	Na2O	MgO	Al2O3	SiO2	P2O5	S	K2O	CaO	Ti	V	Cr	Mn	Fe	Co	Ni	Cu	Zn	Ga	As	Rb	Sr	Y	Zr	Nb	Mo	Ba	W	Pb	Th	U	Total
Dunite/chromitite formation																														
BRAG39	0.00	46.77	1.45	36.59	0.00	0.04	0.00	0.22	0.06	490	97809	0.27	10.07	68	1608	87	131	9	0	0	2	0	2	2	0	0	0	0	0	0	95.46
BRAG54	0.00	47.12	0.61	45.84	0.03	0.03	0.00	0.25	0.06	200	47247	0.16	7.92	50	3001	12	72	6	0	0	15	0	4	2	0	0	0	0	0	0	102.00
BRAG78	0.71	28.92	7.15	22.82	0.00	0.01	0.00	0.11	0.11	874	188119	0.43	15.77	114	1275	0	468	0	0	0	0	0	0	4	0	0	0	0	0	0	76.03
BRAG70	0.00	44.83	0.00	47.90	0.00	0.04	0.00	0.43	0.02	0	1997	0.18	10.03	122	2932	0	58	0	7	0	15	0	0	0	0	341	0	0	0	0	103.42
142BRG	0.00	15.02	5.82	11.29	0.00	0.01	0.00	0.28	0.11	528	242353	0.82	18.46	113	755	0	763	0	0	0	0	0	5	5	0	0	0	0	0	0	51.79
BRAG2	1.88	23.20	9.73	15.40	0.00	0.01	0.00	0.06	0.14	475	226957	0.35	14.54	91	1942	108	332	0	0	0	0	0	0	4	0	0	0	0	0	0	65.30
BRAG51	1.31	29.94	5.70	25.99	0.00	0.11	0.00	0.04	0.14	356	194319	0.30	11.78	74	3503	0	188	16	0	0	8	0	0	3	0	0	0	0	0	0	75.26
45BRG	0.00	39.14	3.96	33.97	0.00	0.02	0.00	0.42	0.13	471	144389	0.33	11.74	95	2057	26	326	18	0	0	0	0	0	0	0	0	0	0	0	0	89.70
BRAG28	1.46	25.01	7.49	18.07	0.00	0.00	0.00	0.07	0.15	607	213918	0.49	15.63	122	1903	0	537	30	0	0	0	0	0	0	0	0	0	0	0	0	68.36
BRAG52	1.25	38.90	7.00	31.80	0.00	0.02	0.00	0.05	0.14	380	143484	0.40	13.14	99	1685	17	272	15	0	0	0	0	3	3	0	0	0	0	0	0	92.69
145BRG	0.00	21.28	5.00	15.35	0.00	0.00	0.00	0.06	0.07	227	229633	0.55	15.70	132	915	0	461	0	0	0	0	0	0	0	0	0	0	0	0	0	58.00
BRAG56	0.00	44.40	1.20	44.54	0.00	0.03	0.00	0.06	0.04	77	45138	0.18	7.43	86	2646	16	94	5	6	0	2	0	3	3	0	0	0	0	0	0	97.88
BRAG64	0.76	36.33	5.71	34.07	0.00	0.07	0.00	0.07	0.14	577	117578	0.34	18.88	287	9778	1793	440	20	26	0	0	0	3	3	0	0	0	0	0	0	96.33
BRAG57	0.73	32.81	8.36	25.14	0.00	0.00	0.00	0.05	0.10	487	176682	0.44	15.09	90	1384	0	430	20	0	0	0	0	0	0	0	0	0	0	0	0	82.71
154BRG	0.00	16.47	4.28	12.40	0.00	0.01	0.00	0.10	0.10	495	244939	0.56	18.94	113	569	0	480	0	0	0	0	0	0	0	0	0	0	0	0	0	52.84
47BRG	0.00	44.59	1.73	42.85	0.00	0.04	0.00	0.09	0.05	188	75071	0.24	9.53	93	3147	13	136	9	6	0	0	0	0	0	0	0	0	0	0	0	99.11
130BRG	0.00	28.49	6.74	21.63	0.00	0.00	0.00	0.04	0.11	916	210170	1.19	14.85	0	1157	0	984	17	0	0	0	0	0	4	0	0	0	0	0	0	73.04
155BRG	1.39	28.67	3.24	22.03	0.00	0.01	0.00	0.18	0.12	673	219640	0.37	15.61	62	847	0	348	0	0	0	0	0	0	4	0	0	0	0	0	0	71.62
BRAG 53	0.82	43.09	4.72	37.84	0.04	0.31	0.00	0.39	0.11	606	110300	0.29	10.70	0	2266	34	184	12	0	0	2	0	2	0	0	0	0	0	0	0	98.14
39BRG	1.01	36.35	4.47	29.34	0.02	0.01	0.00	0.93	0.13	575	175530	0.32	11.05	0	1865	0	327	14	0	0	8	0	2	0	0	0	0	0	0	0	83.62
134BRG	0.77	33.89	8.18	25.63	0.00	0.03	0.00	0.05	0.13	628	186278	0.62	11.73	0	1815	107	325	15	0	0	0	0	0	3	0	0	0	0	0	0	81.01
BRAG71	0.00	41.79	5.85	35.13	0.03	0.02	0.00	0.16	0.12	328	108038	0.27	9.12	51	2177	14	149	10	0	0	11	0	6	3	0	0	0	0	0	0	92.48
55BRG	0.00	38.16	6.39	30.03	0.00	0.01	0.00	0.06	0.12	268	166839	0.45	11.11	59	1700	0	307	15	0	0	0	0	2	3	0	0	0	0	0	0	86.33
152BRG	1.25	34.68	4.24	28.57	0.00	0.01	0.00	0.46	0.09	136	186246	0.39	12.38	61	1159	45	312	0	0	0	0	0	0	3	0	0	0	0	0	0	82.07
Harzburgite																														
BRAG9	0.00	48.06	0.00	46.23	0.00	0.03	0.00	0.45	0.00	0	2206	0.13	8.69	85	2358	0	42	6	0	0	17	0	2	2	0	241	0	0	0	0	103.58
BRAG24	0.00	46.36	0.00	45.13	0.00	0.06	0.00	1.02	0.02	0	2181	0.13	8.68	105	2410	12	42	0	0	0	30	0	2	0	0	337	0	0	0	0	101.38
162BRG	0.00	46.18	0.94	43.66	0.00	0.03	0.00	0.11	0.03	67	4051	0.16	13.51	155	1737	317	50	6	11	3	0	0	2	0	0	195	0	0	0	0	104.60
191BRG	0.00	44.80	0.00	44.62	0.00	0.02	0.00	0.81	0.00	0	2149	0.13	8.76	89	2390	0	42	0	0	0	0	0	2	0	0	364	0	0	0	0	99.14
133BRG	0.00	48.43	0.00	46.91	0.00	0.03	0.00	0.09	0.02	42	2099	0.11	7.72	96	2588	16	38	0	0	0	0	0	2	2	0	266	0	0	0	0	103.30
166BRG	0.59	48.32	0.00	48.21	0.00	0.05	0.00	0.09	0.00	43	2561	0.09	8.24	95	2628	11	44	4	0	0	3	0	0	0	0	383	0	0	0	0	105.57
1BRG	0.00	44.74	0.00	47.13	0.00	0.04	0.00	0.69	0.02	57	2390	0.14	9.23	116	2857	0	46	0	0	0	24	0	2	2	0	219	0	0	0	0	101.98
20BRG	0.00	44.27	0.44	44.91	0.00	0.03	0.00	1.41	0.03	79	2435	0.13	8.74	101	2849	0	45	0	0	0	10	0	2	2	0	372	0	0	0	0	99.94
62BRG	0.00	41.67	0.00	44.79	0.00	0.03	0.00	0.22	0.03	59	4571	0.15	11.84	147	3198	26	54	5	7	0	3	0	0	0	0	282	0	0	0	0	98.72
BRAG 12	0.00	42.65	1.61	46.98	0.00	0.03	0.00	2.01	0.04	46	2764	0.12	9.08	94	2773	40	51	0	0	0	5	0	3	0	0	399	0	0	0	0	102.51
BRAG 45	1.28	15.37	15.73	46.83	0.09	0.00	0.14	15.36	0.23	152	1998	0.09	4.74	24	319	22	29	11	0	5	271	6	13	0	0	493	0	7	0	0	99.86
117BRG	0.00	41.14	0.64	47.57	0.00	0.03	0.00	2.30	0.03	73	2541	0.12	8.39	52	2490	108	43	0	5	0	14	0	2	0	0	267	0	0	0	0	100.21
BRAG20	0.67	46.42	0.43	47.86	0.03	0.03	0.00	0.47	0.00	54	3792	0.14	9.44	108	3282	0	52	5	0	0	9	0	1	0	0	292	0	0	0	0	105.47
Caminho Velho/Vinhas																														
187-BRG	0.64	32.87	10.25	45.13	0.03	0.09	0.13	6.16	0.10	75	1385	0.13	9.35	60	1037	117	58	7	0	7	89	0	8	2	0	372	145	0	0	0	104.85
72BRG	0.00	44.72	0.91	47.39	0.00	0.03	0.00	0.34	0.04	68	10913	0.17	9.00	101	2432	0	71	6	0	0	2	0	0	3	0	228	0	0	0	0	102.57
96-BRG	2.98	8.27	12.76	47.67	0.21	0.01	0.28	12.03	1.55	367	607	0.21	13.60	46	49	196	108	18	0	11	189	34	106	9	0	503	0	0	0	0	99.58
95-BRG	0.87	45.98	1.31	46.46	0.00	0.04	0.00	0.39	0.04	51	2581	0.08	7.51	61	2286	0	46	6	9	0	5	0	2	0	0	245	0	0	0	0	102.66
184-BRG	0.00	41.65	1.22	46.47	0.00	0.02	0.00	2.29	0.04	89	2952	0.13	8.63	82	2117	21	49	4	0	0	3	0	0	0	0	451	45	0	0	0	100.44
188-BRG	3.35	12.32	19.58	49.77	0.08	0.01	0.00	11.65	0.29	99	874	0.08	5.31	0	266	52	32	12	0	2	145	9	32	3	0	330	99	7	0	0	102.44
Morais																														
86-BRG	0.00	32.52	19.35	34.19	0.04	0.00	0.00	0.11	0.88	251	0	0.15	13.25	0	301	10	93	14	13	2	0	4	25	0	0	0	0	0	0	0	100.49
85-BRG	0.00	46.25	1.44	46.44	0.00	0.10	0.00	0.07	0.03	61	2303	0.07	8.25	75	2300	0	37	0	0	0	0	0	0	0	0	313	0	0	0	0	102.60

	Na2O	MgO	Al2O3	SiO2	P2O5	S	K2O	CaO	Ti	V	Cr	Mn	Fe	Co	Ni	Cu	Zn	Ga	As	Rb	Sr	Y	Zr	Nb	Mo	Ba	W	Pb	Th	U	Total
82-BRG	0.00	36.61	1.19	52.82	0.00	0.03	0.00	0.35	0.10	69	2696	0.13	9.56	102	3727	31	61	4	0	0	0	11	2	2	0	240	0	0	0	0	100.78
177-BRG	3.14	3.12	15.94	68.32	0.15	0.05	2.01	3.09	0.99	99	0	0.08	5.78	0	31	22	83	19	0	45	270	48	409	16	0	2062	0	22	30	0	102.64
175-BRG	4.85	3.47	17.36	65.28	0.11	0.17	1.67	2.30	0.81	169	0	0.06	5.97	0	29	35	96	20	0	54	331	32	207	12	0	1189	0	16	9	0	101.97
173-BRG	2.97	10.45	14.53	50.05	0.14	0.00	0.03	11.90	1.12	240	688	0.14	9.22	32	106	26	56	16	0	0	138	27	69	3	0	507	0	0	0	0	100.57
189-BRG	3.22	2.70	16.13	69.42	0.21	0.03	2.05	3.14	0.95	94	0	0.07	5.42	0	26	19	77	16	0	47	288	54	372	15	0	1613	0	21	25	0	103.34
190-BRG	2.16	10.31	13.91	47.88	0.13	0.01	0.00	12.14	1.01	279	696	0.17	9.15	0	102	17	66	15	0	2	134	26	57	3	0	683	0	0	0	0	96.85
186-BRG	0.00	44.96	1.37	47.61	0.03	0.07	0.00	1.34	0.03	53	2578	0.12	8.26	57	2089	0	53	0	0	0	0	2	1	0	0	408	0	0	0	0	103.16
Pyroxenite																															
BRAG 55	1.13	22.99	2.42	52.79	0.03	0.31	0.00	15.90	0.11	363	2805	0.14	7.21	37	306	136	34	4	0	0	15	0	3	3	0	304	73	7	0	0	102.88
BRAG 40	0.00	40.30	0.88	47.23	0.00	0.07	0.00	5.38	0.06	123	2676	0.14	9.12	79	1138	141	35	0	0	0	4	2	3	0	0	359	0	0	0	0	103.15
141BRG	0.62	23.82	1.19	51.97	0.05	0.18	0.00	13.70	0.08	232	5161	0.15	6.13	0	592	378	37	0	0	0	13	0	2	2	0	0	0	6	0	0	97.79
14BRG	0.00	23.54	1.07	50.73	0.06	0.25	0.00	12.31	0.09	348	4134	0.16	7.60	33	249	84	41	5	0	0	15	2	2	2	0	216	0	5	0	0	95.68
156-BRG	0.00	34.30	0.85	53.88	0.00	0.05	0.00	3.39	0.05	76	5034	0.16	8.41	46	756	47	42	4	0	0	26	0	2	0	0	230	196	0	0	0	101.07
BRAG89	0.00	31.96	1.21	50.20	0.05	0.02	0.00	7.25	0.08	149	3525	0.14	8.67	38	809	21	54	5	0	0	46	0	3	2	0	211	0	0	0	0	99.58
BRAG 21	0.00	45.53	1.16	45.21	0.00	0.05	0.00	0.89	0.04	0	2319	0.10	8.23	66	2351	0	38	0	0	0	4	0	0	2	0	420	0	0	0	0	101.18
43-BRG	0.00	33.18	1.28	56.31	0.00	0.36	0.00	2.74	0.04	123	3873	0.16	7.62	66	632	330	36	0	0	0	3	0	3	0	0	455	181	0	0	0	101.51
Dunite																															
BRAG58	0.00	45.34	0.00	48.48	0.00	0.03	0.00	0.09	0.02	0	2848	0.10	6.81	76	3432	0	23	5	0	0	3	0	2	0	0	212	0	4	0	0	100.86
BRAG6	0.00	49.43	0.00	46.70	0.00	0.04	0.00	0.10	0.00	41	2468	0.15	9.41	143	2591	0	50	4	6	0	4	0	2	0	0	208	0	0	0	0	105.81
BRAG15	0.00	55.44	0.00	43.05	0.00	0.09	0.00	0.05	0.03	0	1505	0.14	8.83	94	2555	0	34	4	0	0	1	0	2	0	0	255	0	0	0	0	107.58
BRAG 88	0.00	45.61	0.00	48.00	0.00	0.02	0.00	0.23	0.00	52	2083	0.12	7.57	73	2306	0	39	4	0	0	4	0	0	0	0	348	0	0	0	0	101.53
BRAG73	0.00	47.93	0.74	40.49	0.00	0.03	0.00	0.09	0.04	68	39420	0.19	9.66	116	2643	22	157	5	0	0	0	0	2	0	0	250	0	0	0	0	99.16
BRAG 19	0.00	46.36	1.65	42.27	0.00	0.10	0.00	3.25	0.04	72	6824	0.13	11.29	49	3868	575	70	6	9	0	176	0	6	0	0	409	0	0	0	0	105.04
Hornblendite/Garnet-pargasite-gneiss/Garnet-pyroxenite																															
BRAG 4	2.82	10.23	9.29	37.31	1.24	0.01	0.38	13.09	3.67	583	971	0.24	22.62	0	0	184	125	17	13	7	585	34	125	14	0	1280	0	0	0	0	100.89
54-BRG	2.72	11.01	11.77	39.91	2.33	0.00	1.17	14.44	1.50	310	589	0.20	15.36	0	31	83	117	16	13	10	1043	38	205	9	0	988	0	0	0	0	100.41
170-BRG	3.12	9.32	12.68	48.39	0.21	0.01	0.00	13.85	1.40	336	735	0.19	12.90	45	85	143	99	15	0	0	238	29	85	7	0	452	199	0	0	0	102.07
179-BRG	3.79	8.58	12.07	49.06	0.14	0.02	0.11	10.62	1.56	426	438	0.24	15.65	43	28	214	109	18	0	39	105	42	90	6	0	0	0	0	0	0	101.81
174-BRG	3.42	8.22	12.47	48.09	0.21	0.00	0.06	12.26	1.74	361	563	0.22	13.99	0	53	134	101	15	0	5	214	34	113	8	0	603	0	0	0	0	100.69
172-BRG	0.83	4.62	17.80	34.82	0.74	0.07	0.00	20.71	1.55	0	779	0.42	14.27	0	58	61	44	25	28	0	7024	170	3215	29	9	1367	0	14	29	156	95.79
178-BRG	2.19	6.24	10.75	45.10	0.18	0.00	0.00	21.45	1.41	356	1557	0.21	12.19	0	0	65	104	21	0	0	205	32	97	7	0	1321	0	0	0	0	99.72
169-BRG	2.20	10.39	11.04	43.20	0.27	0.01	0.29	15.35	2.01	368	1047	0.29	15.83	70	75	113	154	21	0	5	132	38	146	14	0	1277	524	0	0	0	100.87
185-BRG	2.98	8.78	13.20	48.09	0.12	0.01	0.09	12.44	1.17	339	569	0.22	12.17	0	56	157	86	17	0	6	162	27	56	5	0	829	0	0	0	0	99.25
132-BRG	2.35	15.07	11.17	40.82	2.29	0.00	0.70	13.59	1.31	330	531	0.14	11.94	0	85	159	76	19	0	4	879	41	103	6	0	817	0	0	0	0	99.36
Other Lithologies																															
167-BRG	0.72	34.83	0.91	58.19	0.02	0.01	0.00	2.00	0.08	121	4065	0.17	8.66	42	398	0	56	5	0	3	11	0	2	0	0	459	0	0	0	0	105.58
164-BRG	3.04	7.85	13.93	50.59	0.20	0.05	0.00	11.60	1.43	314	640	0.21	12.81	0	36	47	93	20	0	0	96	31	64	4	0	462	0	0	0	0	101.67
181-BRG	0.71	19.94	13.03	44.50	0.07	0.05	0.00	17.52	0.14	239	2070	0.11	5.82	29	800	91	83	15	0	0	18	5	4	0	0	355	0	4	0	0	101.88
168-BRG	4.21	2.72	17.40	71.92	0.13	0.00	2.08	1.64	0.52	89	0	0.07	3.80	0	44	9	61	17	0	52	381	15	130	8	3	968	677	17	6	0	104.49
137-BRAG	2.41	11.66	17.45	50.95	0.10	0.00	0.37	10.65	0.52	142	421	0.12	7.33	41	124	43	55	12	0	11	181	16	30	0	0	845	0	7	0	0	101.54
Standards																															
BHVO-1	2.84	6.03	14.75	48.92	0.21	0.01	0.40	11.07	2.61	281	714	0.17	11.66	0	95	129	105	19	0	9	385	27	176	18	0	856	0	0	0	0	98.67
MONGSP	2.66	1.90	15.54	68.86	0.33	0.04	5.56	2.13	0.62	0	0	0.03	4.08	0	0	34	105	22	0	248	232	28	489	24	0	1408	0	54	107	0	101.74

Cl, Ge, La, Ce, Nd analysed and in all samples found to be below detection limits

28/2/89	PPB						
Detect. Limits	2	0.5	0.5	0.5	0.5	0.5	
Sample	Os ppb	Ir ppb	Ru ppb	Rh ppb	Pt ppb	Pd ppb	SUMPGE
Brag2	42	57	110	– 20	83	66	378
BragX	200	420	510	160	690	340	2320
BragXDup	180	410	490	170	670	350	2270
BragX av.	190	415	500	165	680	345	2295
Brag28	88	250	390	120	510	340	1698
Brag52	34	50	69	13	52	83	301
Brag53	22	28	44	7.5	40	45	186.5
Brag57	670	1600	1200	590	4200	3200	11460
Brag57Dup	680	1500	1100	620	3900	3100	10900
Brag57 av.	675	1550	1150	605	4050	3150	11180
Brag58	4	14	14	3.5	10	11	56.5
Brag71	24	25	45	9	16	11	130
Brag78	160	180	310	46	51	18	765
Brag78Dup	200	220	320	48	49	15	852
Brag78 av.	180	200	315	47	50	16.5	808.5
Brag35	6	9	9	2.5	15	6.5	48
Standards							
SARM7	42	230	570	460	3100	2500	
SARM7repeat	40	210	560	430	3200	2400	
SARM7cert.	60	75	430	240	3740	1530	
(BX=B28repeat)							
	May-90						
	Os	Ir	Ru	Rh	Pt	Pd	SUMPGE
Detect. limit	2	2	2	1	2	2	
Harzburgite							
162B	2	2	4	2	8	12	30
133BRG	4	6	8	2	8	4	32
20BRG	4	6	8	2	8	8	36
Brag9	8	6	16	4	24	20	78
1BRG	4	4	8	2	4	4	26
Brag24	6	6	14	2	10	10	48
Pyroxenite							
Brag60	2	0	2	1	8	18	31
14BRG	2	4	4	2	8	6	26
20BRG	4	6	8	2	8	8	36
141BRG	2	2	4	2	22	24	56
Morais UATC							
72B	8	14	14	10	22	10	78
98B	22	16	44	7	14	10	113
Chromite-rich							
Brag39	34	32	72	10	20	44	
Brag64	70	56	140	36	86	180	
Brag70	4	2	12	2	2	2	
Brag73	28	26	54	5	8	8	
Brag76	46	42	185	8	6	14	
39BRG	18	18	58	7	-	2	
45BRG	78	118	225	45	155	90	
47BRG	20	12	40	3	4	6	
55BRG	38	32	86	6	2	4	
130BRG	20	20	66	6	4	2	
134BRG	34	32	60	5	2	2	
142BRG	960	1350	1500	240	1650	260	
145BRG	370	400	740	125	740	116	
Brag51	18	14	62	5	2	4	
152BRG	40	70	100	18	16	8	
154BRG	56	135	145	118	250	43	
155BRG	50	130	125	135	235	22	
Brag56	28	26	38	3	2	4	

7c PGE

Other	Os	Ir	Ru	Rh	Pt	Pd	
Brag6	4	2	6	1	2	4	
Brag8	2	-	4	-	-	2	
Brag15	6	4	12	1	- 6	6	
Brag18	2	-	4	1	-	2	-
Brag20	6	6	12	2	10	6	
Brag23	14	16	32	5	18	12	
Brag43	22	22	56	10	38	22	
Brag45	2	2	4	1	4	12	
Brag89	4	2	6	1	4	2	
1BRG	4	4	8	2	4	4	
10BRG	4	8	8	2	16	6	
29BRG	6	6	6	2	2	2	
30BRG	8	6	24	4	2	4	
62BRG	4	2	4	2	6	16	
82BRG	6	6	8	2	8	8	
85BRG	4	8	10	3	12	4	
88BRG	4	4	8	2	8	6	
92BRG	4	4	8	2	4	8	
94BRG	6	4	8	2	6	6	
105BRG	12	8	18	3	14	10	
131BRG	2	2	2	1	2	4	
147BRG	2	2	2	1	2	-	
149BRG	6	6	8	3	8	4	
Brag4	0	0	0	0	2	2	
Repeats							
Brag6	4	2	6	1	2	4	
Brag43	24	22	56	11	40	20	
Brag64	66	48	140	32	88	165	
Brag73	28	22	48	4	6	6	
Brag76	48	40	190	9	8	16	
29BRG	8	6	10	2	4	4	
45BRG	80	112	225	44	150	86	
47BRG	20	12	38	3	4	6	
105BRG	10	8	14	3	14	10	
142BRG	900	1300	1400	235	1600	240	
152BRG	44	62	108	19	16	12	
154BRG	62	140	150	120	235	44	
Standards							
1/5SARM7	12	18	84	48	760	300	
Repeat	16	20	94	48	860	295	
Certified	12	15	86	48	748	306	
HGM.1	140	110	380	130	390	940	
Repeat	150	110	420	140	390	1000	
Recommended	155	110	400	130	375	1000	
Mar-91							
43BRG	2	-	-	2	32	40	
191BRG	8	6	14	3	20	12	
166BRG	6	4	12	2	10	8	
Brag34	6	4	12	2	14	16	
Quartz(blank)	2	0	0	0	0	0	
1/5SARM7	12	18	88	47	700	295	
Certified	12	15	86	48	748	306	

Appendix 8 Pi-pole scatter analysis

The *Stereo* software programme calculates a set of statistical parameters (r1, r2 and K) from the data that has been input from an *Excel* spreadsheet to be plotted on a stereonet. On the graph below r1 is the value of the vertical axis and r2 the horizontal axis. If r1 and r2 are both small the data set has a random distribution. A large value for r1 with a small value for r2 indicates a grouping around a single point maxima. A large r2 and small r1 indicates a girdle disribution (McEachran 1988).

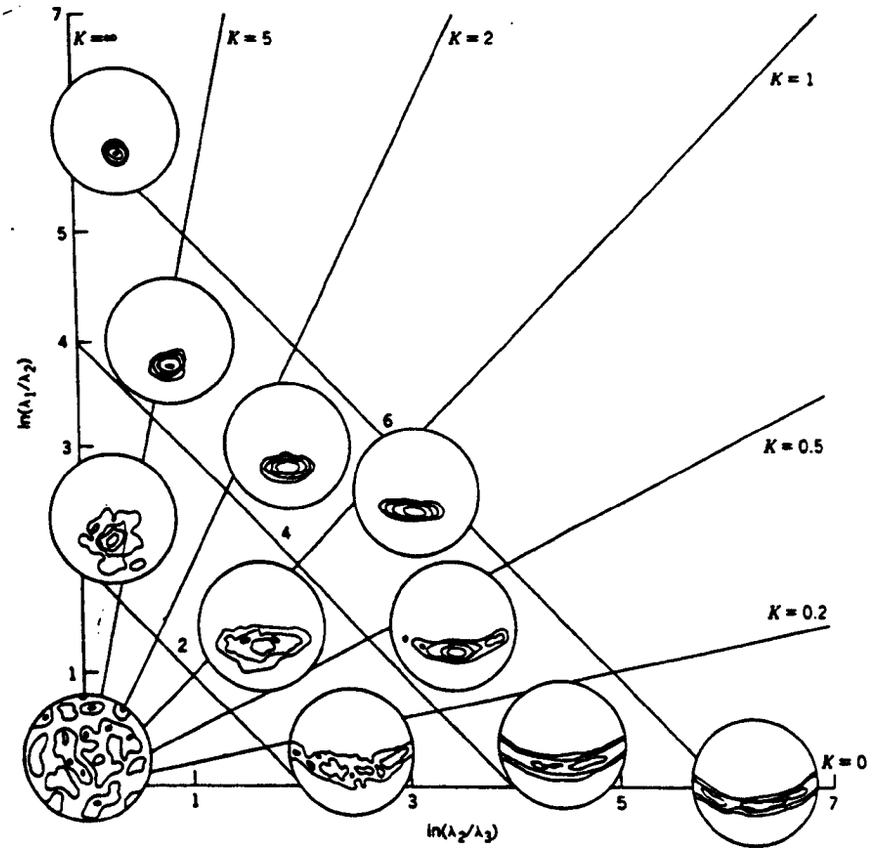

From Davis (1986)

References

Agiorgitis, G. and Wolf, R. 1978 Aspects of osmium, ruthenium and iridium contents in some Greek chromites. *Chemical Geology* **23**, 267-272.

Albrektsten, B.A., Furnes, H. and Pedersen, R.B. 1991 Formation of dunites in mantle tectonites, Leka Ophiolite Complex, Norway. *Journal of Geodynamics* **13**, 2-4.

Amossé, J., Allibert, M., Fischer, W. and Piboule, M. 1990 Experimental study of the solubility of platinum and iridium in basic silicate melts- implications for the differentiation of Platinum-group elements during magmatic processes. *Chemical Geology* **81**, 45-53.

Anthonioz, P.M. 1972 Les complexes polymétamorphiques précambriens de Morais et Bragança (NE du Portugal). Etude pétrographique et structurale. *Mem. Serv. Géol. Portugal* **20**, 192pp.

Arenas, R., Gil Ibarguchi, J.I., Gonzalez Lodeiro, F., Klein, E., Martinez Catalan, J.R., Ortega Girones, E., de Pablo Macia, J.G. and Peinado, M. 1986 Tectonostratigraphic units in the complexes with mafic and related rocks of the NW of the Iberian Massif. *Hercynica* **2**, 87-110.

Augé, T. and Roberts, S. 1982 Petrology and geochemistry of some chromitiferous bodies within the Oman ophiolite. *Ofioliti* **3** no. 2, 133-154.

Bacuta, G.C. (Jr), Kay, R.W., Gibbs, A.K. and Lipin, B.R. 1990 Platinum-group element abundances and distribution in chromite deposits of the Acoje Block, Zambales ophiolite complex, Philippines. *Journal of Geochemical Exploration* **37**, 113-145.

Barnes, Sarah-Jane, Naldrett, A.J. and Gorton, M.P. 1985 The origin of the fractionation of Platinum-Group Elements in terrestrial magmas. *Chemical Geology* **53**,303-323.

Basu, A.R. 1977 Textures, microstructures and deformation of ultramafic xenoliths from San Quintin, Baja California. *Tectonophysics* **43**, 213-246.

Bernard-Griffiths, J., Peucat, J-J., Cornichet, J., Iglesias Ponce de Léon, M. and Gil Ibarguchi, J., I. 1985 U-Pb, Nd Isotope and REE geochemistry in eclogites from the Cabo Ortegal Complex, Galicia, Spain: an example of REE immobility conserving MORB-like patterns during high-grade metamorphism. *Chemical Geology* **52**, 217-225.

Bodinier, J.L., Guirand, M., Fabriès, J., Dostal, J. and Dupuy, L. 1987 Petrogenesis of layered pyroxenites from the Lherz, Freychinède and Prades ultramafic bodies (Ariège, French Pyrénées). *G.C.A* **51**, 279-290.

Bowen, N.J. and Tuttle, O.F. 1949 The system MgO-SiO_2-H_2O. *Bulletin of the Geological Society of America* **60**, 439-460.

Boyd, F.R. 1989 Compositional distinction between oceanic and cratonic lithosphere. *E.P.S.L.* **96**, 15-26.

Boyd, F.R. and Schairer, J.F. 1964 The system MgSiO3-CaMgSi2O6. *Journal of Petrology* **5**, 275-309.

Brown, M. 1980 Textural and geochemical evidence for the origin of some chromite deposits in the Oman ophiolite. In *Ophiolites proceedings international ophiolite symposium Cyprus 1979* ed. Panayiotou, A. 714-721 Geological survey department Ministry of Agriculture and Natural Resources Republic of Cyprus 781pp.

Brown, M.A. 1982 Chromite deposits and their ultramafic host rocks in the Oman ophiolite. Unpub. PhD thesis The Open University 263pp.

Browning, P. 1982 The petrology, geochemistry, and structure of the plutonic rocks of the Oman ophiolite. Unpub. PhD thesis. The Open University 403pp.

Burgath, K.P. 1988 Platinum-group minerals in ophiolitic chromitites and alluvial placer deposits, Meratus-Bobaris area, SE Kalimantan. In *Geo-Platinum 87*, eds. Prichard, H.M., Potts, P.J., Bowles, J.F.W., and Cribb, S.J. 145-158 London Elsevier Applied Science 422pp.

Cameron, W.E., Nisbet, E.G. and Dietrich, V.J. 1980 Petrographic dissimilarities between ophiolitic and ocean-floor basalts. In *Ophiolites proceedings international ophiolite symposium Cyprus 1979* ed. Panayiotou, A. 182-192 Geological survey department Ministry of Agriculture and Natural Resources Republic of Cyprus 781pp.

Campbell, I.H. and Naldrett, A.J. 1979 The influence of silicate:sulphide ratios on the geochemistry of magmatic sulphides *Economic Geology* **74**, 1503-1506

Cannat, M., Bideau, D. and Bougalt, H. 1992 Serpentinized peridotites and gabbros in the Mid-Atlantic Ridge axial valley at 15°37'N and 16°52'N. *EPSL* **109**, 87-106.

Cassard, D., Nicolas, A., Rabinovitch, M., Moutte, J., Leblanc, M. and Prinzhofer, A. 1981 Structural classification of chromite pods in southern New Caledonia. *Economic Geology* **76**, 805-831.

Cawthorn, R.G. and Collerson, K.D. 1974 The recalculation of pyroxene end-member parameters and the estimation of ferrous and ferric iron content from electron microprobe analyses. *American Mineralogist* **59** 1203-1208.

Cheeney, R.F. 1983 *Statistical methods in geology*. London Allen and Unwin 169pp.

Christodolou, L. and Hirst, D.M. 1985 The chemistry of chromite from two mafic-ultramafic complexes in northern Greece. *Chemical Geology* **49**, 415-428.

Constantinides, C.C., Kingston, G.H. and Fisher, P.C. 1980 The occurrence of platinum-group minerals in the chromitites of the Kokkinorotsos chrome mine, Cyprus. In *Ophiolites* ed. Panayiotou, A. Proceedings International Ophiolite Symposium Cyprus 1979 781pp.

Cotelo Neiva, J.M. 1945 Possibilidade de ocorrencia de platina no distrito de Bragança. *Estudos, Notas e Trabalhos do Serviço de Fomento Mineiro* **1**, 6-12.

Cotelo Neiva, J.M. 1947 Platina no distrito de Bragança. *Estudos, Notas e Trabalhos do Serviço de Fomento Mineiro* **3**, 19-25.

Cox, K.G., Bell, J.D. and Pankhurst, R.J. 1979 The interpretation of igneous rocks. London Allen and Unwin 450pp.

Crawford, A.J., Falloon, T.J. and Green, D.H. 1989 Classification, petrogenesis and tectonic setting of boninites. In *Boninites* ed. Crawford, A.J. 1-44 London: Unwin Hyman 446pp.

Crocket, J.H. 1979 Platinum-group elements in mafic and ultramafic rocks: a survey. *Canadian Mineralogist* **17**, 391-402.

Crocket, J.H. 1981 Geochemistry of the platinum-group elements. In *Platinum-group elements: mineralogy, geology, recovery*, ed. Cabri, L.J. 47-64 The Canadian Inst. of Mining and Metallurgy special volume 23 pp267.

Crocket, J.H., Fleet, M.E. and Stone, W.E 1991 Experimental studies of the partitioning of PGE between sulphide liquid and basaltic melt. In *6th International Platinum Symposium Programme and Abstracts* ed,. Barnes, S.J. IAGOD Commission on Ore Deposits in Mafic and Ultramafic Rocks 56pp.

Dallmeyer, R.D. and Gil Ibarguchi, J.I. 1990 Age of amphibolitic metamorphism in the ophiolitic unit of the Morais allochthon (Portugal): implications for early Hercynian orogeneis in the Iberian Massif. *Journal of the Geological Society, London* **147**, 873-878.

Davis, D.C. 1986 *Statistics and data analysis in geology.* Wiley, New York, 646pp.

Den Tex, E., Engels, J.P. and Vogel, D.E. 1972 A high pressure intermediate temperature facies series in the Precambrian at Cabo Ortegal (Northwest Spain). *I.G.C.* **20**, 64-73.

Dick, H.J.B. and Bullen, T. 1984 Chromian spinel as a petrogenetic indicator in abyssal and alpine-type peridotites and spatially associated lavas. *Cont. Min. Pet.* **86**, 54-76.

Dickey, J.S. (Jr) 1975 A hypothesis of origin for podiform chromite deposits. *GCA* **39**, 1061-1074.

Drury, S.A. 1980 The geochemistry of high pressure gneisses from Cabo Ortegal (NW Spain): residues of deep anatexis. *Geologie en Mijnbouw* **59**, 61-64.

Duke, J.M. 1983 Ore deposit models 7. Magmatic segregation deposits of chromite. *Geoscience Canada* **10** no. 1, 15-24.

Eckstrand, O.R. 1975 The Dumont serpentinite: a model for control of nickeliferous opaque mineral assemblages by alteration reactions in ultramafic rocks. *Economic Geology* **70**, 183-201.

Economou, G. and Economou, M.I. 1986 Some chromite occurrences from the areas of Vermio and Veria, Macedonia Greece. In *Metallogeny of basic and ultrabasic rocks*, eds. Gallagher, M.J., Ixer, R.A., Neary, C.R. and Prichard, H.M, 351-354. London: The Institution of Mining and Metallurgy 522pp.

Economou, M.I. and Naldrett, A.J. 1984 Sulfides associated with podiform bodies of chromite at Tsangli, Eretria Greece. *Mineralium Deposita* **19**, 289-297.

Economou-Eliopoulos, M. and Paraskevopoulos, G. 1989 Platinum-group elements and gold in komatiitic rocks from the Agrilia Formation, Othrys ophiolite complex, Greece. *Chemical Geology* **77**, 149-158.

Edwards, S.J. 1990 Harzburgites and refractory melts in the Lewis Hills Massif, Bay of Islands Ophiolite complex: the base-metals and precious metals story. *Canadian Mineralogist* **28**, 537-552.

Elthon, D. and Scarfe, C.M. 1984 High pressure equilibria of a high-magnesia basalt and the genesis of primary oceanic basalts. *American Mineralogist* **69**, 1-15.

Elthon, D., Casey, J.F. and Komor, S. 1982 Mineral chemistry of ultramafic cumulates from the North Arm Mountain Massif of the Bay of Islands ophiolite: evidence for high-pressure crystal fractionation of oceanic basalts. *Journal of Geophysical Research* **87**, 8717-8730.

Evans, B.W. 1977 Metamorphism of alpine peridotite and serpentinite. *Ann. Rev. Earth Planet. Sci.* **5**, 397-447.

Fabriès, J. 1979 Spinel-olivine geothermometry in peridotites from ultramafic complexes. *Cont. Min. Pet.* **69**, 329-336.

Fabries, J., Bodinier, J.L., Dupuy, C., Lorand, J.P. and Benkerrou, C. 1989 Evidence for modal metasomatism in the orogenic-type spinel lherzolite body from Caussou (Northeastern Pyrenees, France). *Journal of Petrology* . **30**, 199-228.

Francis, R.D. 1990 Sulfide globules in mid-ocean ridge basalts (MORB), and the effect of oxygen abundance in Fe-S-O liquids on the ability of those liquids to partition metals from MORB and komatiite magmas. *Chemical Geology* **85**, 199-213.

Gain, S.B. 1985 The geologic setting of the platiniferous UG-2 Chromitite layer on the Maandagshoek, Eastern Bushveldt Complex. *Economic Geology* **80**, 925-943.

Garuti, G., Gorgoni, L. and Sighinolfi, G.P. 1984 Sulfide mineralogy and chalcophile and siderophile element abundances in the Ivrea-Verbano mantle peridotites (western Italian alps). *E.P.S.L.* **70**, 69-87.

Gass, I.G. 1990 Ophiolites and oceanic lithosphere. *In Ophiolites: oceanic crustal analogues proceedings of the symposium Troodos 1987.* eds. Malpas, J., Moores, E., Panayiotou, A. and Xenophontos, C. 1-10 The Geological Survey Dept. Nicosia 733pp.

Gass, I.G., Neary, C.R., Prichard, H.M. and Bartholomew, I.D. 1982 *The chromite of the Shetland ophiolite a re-appraisal in the light of new theory and techniques.* Unpub. report for the commission of European Communities The Open University 264pp.

Gil Ibarguchi, J.I. and Arenas, R. 1990 Metamorphic evolution of the allochthonous complexes from the northwest of the Iberian peninsula. In *Pre-Mesozoic Geology of Iberia*, eds. Dallmeyer, R.D. and Martinez Garcia, E. 237-246 Berlin Heidelberg Springer-Verlag 416pp.

Green, D.H. 1976 Experimental testing of "equilibrium" partial melting of peridotite under water-saturated, high pressure conditions. *Canadian Mineralogist* **14**, 255-268.

Green, D.H., Falloon, T.J. and Taylor, W.R. 1987 Mantle-derived magmas - role of variable source peridotite and variable C-H-O fluid compositions. In *Magmatic processes: physiochemical principles,* ed. Mysen, B.O. 139-154 Geochem. Soc. Spec. Publ. no.1.

Greenbaum, D. 1977 The chromitiferous rocks of the Troodos ophiolite complex, Cyprus. *Economic Geology* **72** 1175-1194.

Hamlyn, P.R. and Keays, R.R. 1986 Sulfur saturation and second stage melts; application to the Bushveld Pt metal deposits. *Economic Geology* **81**, 1431-1445.

Hamlyn, P.R., Keays, R.R. and Cameron, W.E. 1985 Precious metals in magnesian low-Ti lavas: implications for metallogenesis and sulfur saturation in primary magmas. *GCA* **49**, 1797-1811.

Hertogen, J., Janssens, M.J. and Palme, H. 1980 Trace elements in ocean ridge basalt glasses: implications for fractionations during mantle evolution and petrogenesis. *GCA* **44**, 2125-2143.

Hobbs, B.E., Means, W.D. and Williams, P.F. 1976 *An outline of structural geology.* New York Wiley 571pp.

Irvine, T.N. 1967 Chromian spinel as a petrogenetic indicator part 2. petrologic applications. *Canadian Journal of Earth Sciences* **4**, 71-103.

Irvine, T.N. 1974 Petrology of the Duke Island ultramafic complex southeastern Alaska. *Mem. Geol. Soc. Amer.* **138**, 240pp.

Jackson, E.D. and Thayer, T.P. 1972 Some criteria for distinguishing between stratiform, concentric and alpine peridotite-gabbro complexes. *24th IGC.*

Jan, Q.M. and Windley, B.F. 1990 Chromian spinel-silicate chemistry in ultramafic rocks of the Jijal complex, north west Pakistan. *Journal of Petrology* **31**, 667-715.

Jedwab, J., Cotelo Neiva, J.M. and Neiva, A.M.R. 1989 Platinum-group minerals of ultrabasic rocks from Abessedo, Carrazedo and Valongo (Bragança -Vinhais, Northern Portugal). *Memóriase Notícias Publ. Mus. Lab. Mineral. Geol Univ Coimbra* **107**.

Johan, Z. and Augé, T. 1986 Ophiolitic mantle sequences and their evolution: mineral chemistry constraints. In *Metallogeny of basic and ultrabasic rocks*, eds. Gallagher, M.J., Ixer, R.A., Neary, C.R. and Prichard, H.M., 305-317. London: The Institution of Mining and Metallurgy 522pp.

Keays, R.R. and Campbell, I.H. 1981 Precious metals in the Jimberlana intrusion, western Australia: implications for the genesis of platiniferous ores in layered intrusions. *Economic Geology* **76**, 1118-1141.

Kimball, K.L. 1990 Effects of hydrothermal alteration on the compositions of chromian spinel. *Cont. Min. Pet.* **105**, 337-346.

Lago, B.L., Rabinowicz and Nicolas, A. 1982 Podiform chromite ore bodies: a genetic model. *Journal of Petrology* **23**, 103-125.

Leake, B.E. 1978 Nomenclature of amphiboles. *Miner. Petrogr. Acta* **22**, 195-224.

Leblanc, M. 1980 Chromite growth, dissolution and deformation from a morphological view point: SEM investigations. *Mineral. Deposita.* **15**, 201-210.

Legendre, O. and Augé, T. 1986 Mineralogy of platinum-group mineral inclusions in chromitite from different ophiolitic complexes. In *Metallogeny of basic and ultrabasic rocks*, eds. Gallagher, M.J., Ixer, R.A., Neary, C.R. and Prichard, H.M., 361-375. London: The Institution of Mining and Metallurgy 522pp.

Lorand, J.P. 1988 Fe-Ni-Cu sulfides in tectonite peridotites from the Maqsad disrict, Sumail Ophiolite, southern Oman: implications for the origin of the sulfide component in the oceanic upper mantle. *Tectonophysics* **151**, 57-73.

Lorand, J.P. 1989 Abundance and distribution of Cu-Fe-Ni sulfides, sulfur, copper and platinum-group elements in orogenic-type spinel lherzolite massifs of Ariège (northeastern Pyrénées, France). *E.P.S.L.* **93**, 50-64.

Lorand, J.P. 1989a Sulfide petrology of spinel and garnet pyroxenite layers from mantle-derived spinel lherzolite massifs of Ariege, northeastern Pyrenees, France. *Journal of Petrology* **30**, 987-1015.

Lord, R.A. 1992 Platinum-group element mineralisation in the Shetland Ophiolite Complex. Unpub. Ph. D. thesis Open University.

Makovicky, M., Makovicky, E. and Rose-Hansen, J. 1986 Experimental studies on the solubility and distribution of Platinum-Group Elements in base metal sulphides in platinum deposits. In *Metallogeny of basic and ultrabasic rocks*, eds. Gallagher, M.J., Ixer, R.A., Neary, C.R. and Prichard, H.M., 415-425. London: The Institution of Mining and Metallurgy.

Marques, F.M.O.G. 1989 Estudo estrutural das rochas catazonais do sinforma de V. Boa de Ousilhão (Bragança, Trás-os-Montes). Unpub. MSc. thesis Universidade de Lisboa. 195pp.

McEachran, D.B. 1988 Stereo (TM) The stereographic projection program for the Macintosh. *Rockware Inc.* Philadelphia 38pp.

McElduff, B. and Stumpfl, E.F. 1990 Platinum-group minerals from the Troodos ophiolite, Cyprus. *Mineralogy and Petrology* **42**, 211-232.

Mercier, J-L.C. and Nicolas, A. 1975 Textures and fabrics of upper-mantle peridotites as illustrated by xenoliths from basalts. *Journal of Petrology* **16**, 454-487.

Misra, K.L. and Fleet, M.E. 1973 The chemical compositions of synthetic and natural pentlandite asemblages. *Economic Geology* **68**, 518-539.

Mitchell, R.H. and Keays, R.R. 1981 Abundance and distribution of gold, palladium and iridium in some spinel and garnet lherzolites: implications for the nature and origin of precious metal-rich intergranular components in the upper mantle. *G.C.A.* **45**, 2425-2442.

Moring, B.C., Page, N.J., Oscarson, R.L. 1988 Platinum-group element mineralogy of the Pole Corral podiform chromite deposit, Rattlesnake Creek terrane, northern California. Absract in *Geo-Platinum 87*, eds. Prichard, H.M., Potts, P.J., Bowles, J.F.W. and Cribb, S.J. 257 London Elsevier Applied Science 422pp.

Mountain, B.W. and Wood, S.A. 1988 Chemical controls on the solubility, transport and deposition of Platinum and Palladium in hydrothermal solutions: a thermodynamic approach, 1988 *Economic Geology* **83**, 492-510.

Munhá, J. and Ribeiro, A. 1986 Metamorphic evolution of kyanite-eclogites and related high grade rocks of the Bragança Massif (Tras-os-Montes, N.E. Portugal). *Maleo* **2**, 31.

Munhá, J., Ribeiro, A. and Ribeiro, M.L. 1984 Blueschists in the Iberian Variscan chain (Trás-os-Montes: NE Portugal). *Commun. Serv. Geol. Portugal* **70**, 31-53.

Murck, B.W. and Campbell, I.H. 1986 The effects of temperature, oxygen fugacity and melt composition on the behaviour of chromium in basic and ultrabasic melts. *GCA* **50**, 1871-1887.

Murton, B.J. 1988 *The tectonic evolution of the Western Limassol Forest Complex, Cyprus*. Unpub. PhD thesis The Open University 332pp.

Naldrett, A.J. and Duke, J.M. 1980 Platinum metals in magmatic sulfide ores. *Science* **208**, 1417-1424.

Naldrett, A.J. and Von Gruenewaldt, G. 1989 Association of Platinum-group elements with chromitite in layered intrusions and ophiolite complexes. *Economic Geology* **84**, 180-187.

Naldrett, A.J., Gasparrini, E.C., Barnes, S.J., Von Gruenewaldt, G. and Sharpe, M.R. 1986 *Economic Geology* **81**, 1105-1117.

Naldrett, A.J., Hoffman, E.L., Green, A.H., Chen-Lin Chou, Naldrett, S.R. and Alcock, R.A. 1979 The composition of Ni-sulfide ores, with particular reference to their content of PGE and Au. *Canadian Mineralogist* **17**, 403-415.

Neary, C.R. 1974 Chromitiferous ultrabasic rocks in the northern Hijaz of Saudi Arabia. Unpub. PhD. thesis, Univ. of Leeds, 380pp.

Neary, C.R. and Brown, M.A. 1979 Chromites from Al 'Ays complex Saudi Arabia and the Semail complex, Oman. In *Evolution and mineralisation of the Arabian-Nubian Shield*, ed. Al Shanti, A.M.S. *IAG Bulletin* **2**, 193-205.

Nicolas, A. 1986 A melt extraction model based on structural studies in mantle peridotites. *Journal of Petrology* **127**, 999-1022.

Nicolas, A. and Dupuy, C. 1984 Origin of ophiolites and oceanic lherzolites. *Tectonophysics* **110**, 177-187.

Nicolas, A. and Jackson, M. 1982 High temperature dikes in peridotites: origin by hydraulic fracturing. *Journal of Petrology* **23**, 569-582.

Nicolas, A., Bouchez, J.L., Boudier, F. and Mercier, J-L. 1971 Textures, structures and fabrics due to solid state flow in some European lherzolites. *Tectonophysics* **12**, 55-86.

Nilsson, L.P. 1990 Platinum-group mineral inclusions in chromitite from the Osthammeren ultramafic tectonite body, south central Norway. *Mineralogy and Petrology* **42**, 249-263.

Obata, M. 1980 The Ronda peridotite: garnet-, spinel-, and plagioclase-lherzolite facies and the P-T trajectories of a high-temperature mantle intrusion. *Journal of Petrology* **21**, 533-572.

Page, N.J, Aruscavage, P.J., Haffty, J. 1983 Platinum-group elements in rocks from the Voikar-Syninsky ophiolite complex, Polar Urals, USSR. *Mineralium Deposita* **18**, 443-455.

Page, N.J, Cassard, D., Haffty, J. 1982a Palladium, platinum, rhodium, ruthenium, and iridium in chromites from the Massif du Sud and Tiébaghi Massif, New Caledonia. *Economic Geology* **77** 1571-1577.

Page, N.J, Engin, T., Singer, D.A. and Haffty, J. 1984 Distribution of Platinum-group elements in the Bati Kef chromite deposit, Guleman-Elazig area, Eastern Turkey. *Economic Geology* **79** 177-184.

Page, N.J, Pallister, J.S., Brown, M.A., Smewing, J.D. and Haffty, J. 1982(b) Palladium, platinum, rhodium, iridium and ruthenium in chromite-rich rocks from the Samail ophiolite, Oman. *Canadian Mineralogist* **20**, 537-548.

Page, N.J, Singer, D.A., Moring, B.C., Carlson, C.A., McDade, J.M. and Wilson, S.A. 1986 Platinum-group element resources in podiform chromitites from California and Oregon. *Economic Geology* **81** 1261-1271.

Peach, C.L., Mathez, E.A. and Keays, R.R. 1989 Sulfide met-silicate melt distribution coefficients for the noble metals as deduced from MORBS. Abstract in *Bulletin of the Geological Society of Finland* **61**, part 1, 58.

Pearce, J.A., Lippard, S.J. and Roberts, S. 1984 Characteristics and tectonic significance of supra subduction zone ophiolites. In *Marginal Basin Geology*, eds. Kokelaar, B.P. and Howells, M.F. 77-94. Blackwell.

Pearson, D.G., Davies, G.R., Nixon, P.H., Greenwood, P.B. and Mattey, D.P. 1991 Oxygen isotope evidence for the origin of pyroxenites in the Beni Bousera peridotite massif, north Morocco: derivation from subducted oceanic lithosphere. *E.P.S.L.* **102**, 289-301.

Peck, D.C. and Keays, R.R. 1990 Geology, geochemistry, and origin of platinum-group element-chromitite occurrences in the Heazlewood River Complex, Tasmania. *Economic Geology* **85**, 765-793.

Perroud, H., Bonhommet, N. and Ribeiro, A. 1985 Palaeomagnetism of late Palaeozoic igneous rocks from southern Portugal. *Geophysical Research Letters* **12**, 45-48.

Peucat, J.J., Bernard-Griffiths, J., Gil Ibarguchi, J.I., Dallmeyer, R.D., Menot, R.P., Cornichet, J.and Iglesias Ponce de Leon, M. 1990 Geochemical and geochronological cross section of the deep variscan crust: the Cabo Ortegal high-pressure nappe (northwestern Spain). *Tectonophysics* **177**, 263-292.

Potts, P.J. 1984 Energy dispersive X-ray fluorescence analysis of silicate rocks for major and trace elements. *X-ray Spectrometry* **13**, 2-15.

Prewitt, C.T. (ed.) 1980 *Pyroxenes*.Reviews in Mineralogy **7** Mineralogical Society of America 525pp.

Prichard, H.M. and Neary, C.R. 1982 Some observations on the chromite in the Shetland Ophiolite complex. *Ofioliti* **2**, 455-466.

Prichard, H.M. and Neary, C.R. 1991 Platinum-group minerals in the chromitites of the Al 'Ays complex, Saudi Arabia. Abstract in *6th International Platinum Symposium Programme and Abstracts* (ed.) Barnes, S.J. 45 IAGOD Perth 56pp

Prichard, H.M. and Tarkian, M. 1988 Platinum and Palladium minerals from two PGE-rich localities in the Shetland ophiolite. *Canadian Mineralogist* **26**, 979-990.

Prichard, H.M., Neary, C.R. and Potts, P.J. 1986 Platinum-group minerals in the Shetland ophiolite. In *Metallogeny of basic and ultrabasic rocks*, eds. Gallagher, M.J., Ixer, R.A., Neary, C.R. and Prichard, H.M, 395-414. London: The Institution of Mining and Metallurgy 522pp.

Prichard, H.M., Neary, C.R., Potts, P.J., Lord, R.A. and Ward, G.R. 1987 Development of techniques for the determination of the PGE in ultramafic rock complexes of potential economic significance: mineralogical studies. Unpub. report for the European Economic Community, 162pp.

Prichard, H.M., Ribeiro, A., Bridges, J.C., Marques, F., Barriga, F., Munhá, J., Pereira, E., Meireles, C. and Ribeiro, L. 1991 Platinum-group mineralisation in two basic and ultrabasic complexes in northern Portugal. *Report for the EC Raw Materials Programme. Contract no. MAIM-075-C.* 122pp.

Queseda, C. 1991 Geological constraints on the Palaeozoic tectonic evolution of tectonostratigraphic terranes in the Iberian Massif. *Tectonophysics* **185**, 225-245.

Quick, J.E. 1981 The origin and significance of large, tabular dunite bodies in the Trinity peridotite, northern California. *Cont. Min. Pet.* **78**, 413-422.

Ribeiro, A, Pereira, E., Marques, F. and Meireles, C. 1987 A model for the lower continental crust (Morais and Bragança massifs, NE Portugal): 1. Portugal. *Terra Cognita* **7**, 161.

Ribeiro, A. 1974 Contribution a l'étude tectonique de Trás-os-montes oriental. *Serviços Geológicos de Portugal* **24** (Nova Série).

Ribeiro, A., Antunes, M.T., Ferreira, M.P., Rocha, R.B., Soares, A.F., Zbyszewski, G., Mointinho de Almeida, F., De Carvalho, D. and Monteiro, J.H. 1979 Introduction à la géologie générale du Portugal. *Serviços Geologicos de Portugal* Lisbon.

Ribeiro, A., Pereira, E. and Dias, R. 1990a Structure of Centro-Iberian Allochthon in the northwest of the Iberian peninsula. In *Pre-Mesozoic Geology of Iberia*, eds. Dallmeyer, R.D. and Martinez Garcia, E. 220-236 Berlin Heidelberg Springer-Verlag 416pp.

Ribeiro, A., Queseda, C. and Dallmeyer, R.D. 1990b Geodynamic evolution of the Iberian Massif. In *Pre-Mesozoic Geology of Iberia*, eds. Dallmeyer, R.D. and Martinez Garcia, E. 399-409 Berlin Heidelberg Springer-Verlag 416pp.

Ribeiro, M.L., Priem, H.N.A, Boelrijk, N.A.I.M. and Schermerhorn, L.J.G. 1985 Rb-Sr whole-rock age of peralkaline acidic volcanics in the Macedo de Cavaleiros area, Trás-os-Montes (NE Portugal). *Commun. Serv. Geol. Portugal* **71**, 171-174.

Ries, Alison C. and Shackleton, R.M. 1971 Catazonal complexes of N.W. Spain and N. Portugal, remnants of a Hercynian thrust plate. *Nature* **234**, 65

Robardet, M. and Gutierrez Marco, J.C. 1990 Sedimentary and faunal domains in the Iberian peninsula during Lower Palaeozoic times. In *Pre-Mesozoic Geology of Iberia*, eds. Dallmeyer, R.D. and Martinez Garcia, E. 383-395 Berlin Heidelberg Springer-Verlag 416pp.

Robardet, M., Paris, F. and Racheboeuf, P.R. 1990 Palaeogeographic evolution of southwestern europe during Early Palaeozoic times. In *Palaeozoic palaeogeography and biogeography*, eds McKerrow, W., S. and Scotese, C., R. 411-419 Geological Society Memoir no. 12 435pp.

Roberts, S. 1986 The role of igneous processes in the formation of ophiolitic chromitite. Unpub. PhD thesis The Open University 261pp.

Rock, N.M.S., Carroll, G.W. 1990 Mintab: a general purpose mineral recalculation and tabulation program for Macintosh microcompuers. *American Mineralogist* **75**, 424-430.

Roeder, P.L. and Reynolds, I. 1991 Crystallisation of chromite and chromium solubility in basaltic melts. *Journal of Perology* **32**, 909-934.

Roeder, P.L., Campbell, I.H., Jamieson, H.E.1979 A re-evaluation of the olivine-spinel geothermometer. *Cont. Min. Pet.* **68**, 325-334.

Sack, R.O. and Ghiorso, M.S. 1991 Chromian spinels as petrogenetic indicators: thermodynamics and petrological applications. *American Mineralogist* **76**, 827-847.

Saunders, A.D., Rogers, G., Marriner, G.F., Terrell, D.J. and Verma, S.P. 1987 Geochemistry of Cenozoic volcanic rocks, Baja California, Mexico: implications for the petrogenesis of post-subduction magmas. *Journ. of Volc. and Geothem. Research* **32**, 223-245.

Scotese, C.R., Bambach, R.K., Barton, C., Van der Voo, R. and Ziegler, A.M. 1979 *Journal of Geology* **87**, 217-277.

Sharpe, M.R. 1982 Noble metals in the marginal rocks of the Bushveld complex. *Economic Geology* **77**, 1286-1295.

Stockman, H.W. and Hlava, P.F. 1984 Platinum-Group Minerals in alpine chromitites from southwestern Oregon. *Economic Geology* **79**, 491-508.

Streckeisen, A. 1976 To each plutonic rock its proper name. *Earth Science Reviews* **12**, 1033.

Talkington, R.W. and Watkinson, D.H. 1986 Whole rock Platinum-group element trends in chromite rich rocks in ophiolitic and statiform igneous complexes. In *Metallogeny of basic and ultrabasic rocks*, eds. Gallagher, M.J., Ixer, R.A., Neary, C.R. and Prichard, H.M, 427-440. London: The Institution of Mining and Metallurgy 522pp.

Talkington, R.W., Watkinson, D.H., Whittaker, P.J. and Jones, P.C. 1984 Platinum-group minerals and other solid inclusions in chromite of ophiolitic complexes: occurrence and petrological significance. *Tschermaks Mineralogische und Petrographische Mitteilungen* **32**, 285-301.

Tarkian, M. and Prichard, H.M. 1987 Irarsite-hollingworthite solid solution series and other associated Os, Ir and Rh bearing PGM's from the Shetland ophiolite complex. *Mineral. Deposita* **22**, 178-184.

Thalhammer, O.A.R., Prochaska, W. and Mühlhaus, H.W. 1990 Solid inclusions in chrome spinels and platinum-group element concentrations from the Hochgrössen and Kraubath ultramafic massifs (Austria), their relationship to metamorphism and serpentinisation. *Cont. Min. Pet.* **105**, 66-80.

Thayer, T.P. 1964 Principal features and origin of podiform chromite deposits and some observations on the Guleman-Soridag disrict, Turkey. *Economic Geology* **59**, 1497-1524.

Umino, S. and Kushiro, I. 1989 Experimental studies on boninite genesis. In *Boninites* ed. Crawford, A.,J., 427-440. London: Unwin Hyman 446pp.

Van Calsteren, P.W.C. and Boelrijk, N.A.I.M, Hebeda, E.H., Priem, H.N.A., Den Tex, E., Verdurmen, E.A.Th. and Verschure, R.H. 1979 Isotopic dating of older elements (including the Cabo Ortegal mafic-ultramafic complex) in the Hercynian orogen of NW Spain: manifestations of a presumed early palaeozoic mantle-plume. *Chemical Geology* **24**, 35-56.

Van Calsteren, P.W.C.1978 Geochemistry of the polymetamorphic mafic-ultramafic complex at Cabo Ortegal (NW Spain). Lithos 11, 61-72.

Vaughan, D. (ed.) 1983 Energy-dispersive X-ray microanalysis an introduction. 52pp Kevex corporation: California.

Veblen, D.R. and Ribbe, P.H. 1982 *Amphiboles: petrology and experimental phase relations*. Reviews in Mineralogy .**9B** Mineralogical Society of America 390pp.

Vogel, D.E. and Abdel Monem, A.A. 1971 Radiometric evidence for a Precambrian metamorphic event in NW Spain. *Geol. Mijnbouw* **50**, 749-750.

Von Gruenevaldt, G., Hatton, C.J., Merkle, R.K.W.and Gain, S.B. 1986 Platinum-Group Element chromitite asociations in the Bushveldt complex. *Economic Geology* **81**, 1067-1079.

Walker, D., Shibata, T. and DeLong, S.E. 1979 Abyssal tholeites from the oceanographer fracture zone. *Cont. Min. Pet.* **70**, 111-125.

Wilson, A.H. and Tredoux, M. 1990 Lateral and vertical distribution of platinum-group elements and petrogenetic controls on the sulfide mineralisation in the P1 pyroxenite layer of the Darwendale subchamber of the Great Dyke, Zimbabwe. *Economic Geology* **85**, 556-584.

Wood, S.A. 1987 Thermodynamic calculations of the volatility of the Platinum-group elements (PGE): the PGE content of fluids at magmatic temperatures. *GCA* **51**, 3041-3050.

Wood, S.A. and Mountain, B.W. 1992 Hydrothermal solubility of palladium in chloride solutions from 300° to 700°C: preliminary experimental results-a discussion. *Economic Geology* **86**, 1562-1563.

Key to maps 1 to 3

Bragança Lithologies	Other work
Serpentinised peridotite (Dunite/harzburgite) and chromitite in dunite	Metaperidotites (1)
As above, abundant pyroxenite layers	
Garnet-feldspar-amphibole gneiss	Amphibolitised high P. granulites(2)
Hornblendite	
Garnet-feldspar-mica gneiss	Paragneiss (1)
Pargasite-peridotite	

Morais (Vinhas) Lithologies

Serpentinised, amphibolitised peridotite	Metaperidotites (1)
Garnet-feldspar-amphibole gneiss	Amphibolitised high P. granulites(2)
Granitic augen gneiss	Lagoa Gneiss (1)
Mica schist	Lagoa Schist (1)
Feldspar-amphibolite	

Symbols

- Foliation dip
- Axial plane dip (first generation folds)
- Fold hinge plunge (second generation folds)
- Vertical axial plane (second generation folds)
- Chromite lineation trend
- Tectonic contact, shear zone
- Axial trace
- Chromite mine
- Cross section ends
- Shear zone

1. Ribeiro (1974) 2. Munhá and Marques (1987)

MAP 1 DERRUIDA 1:10 000

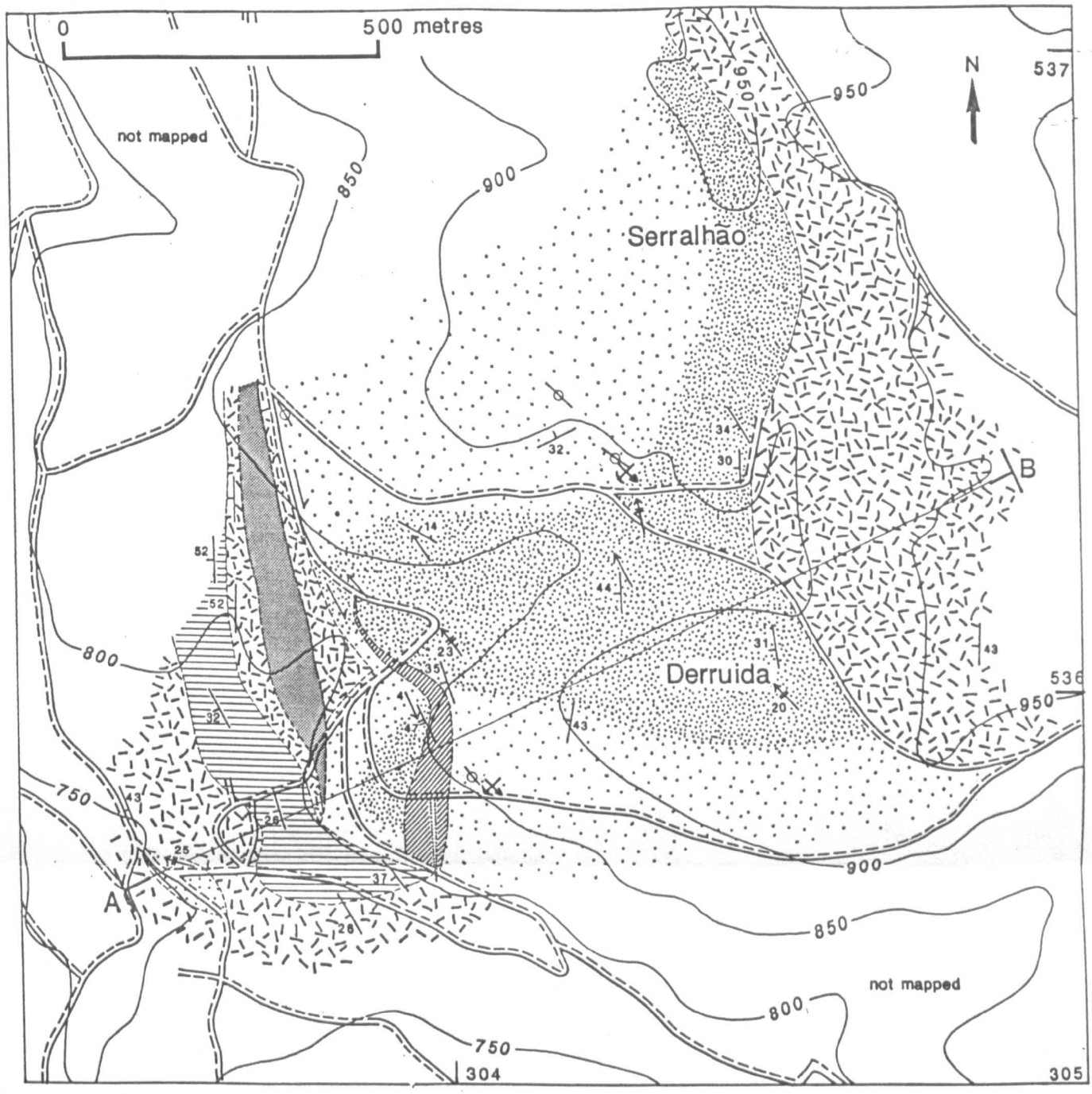

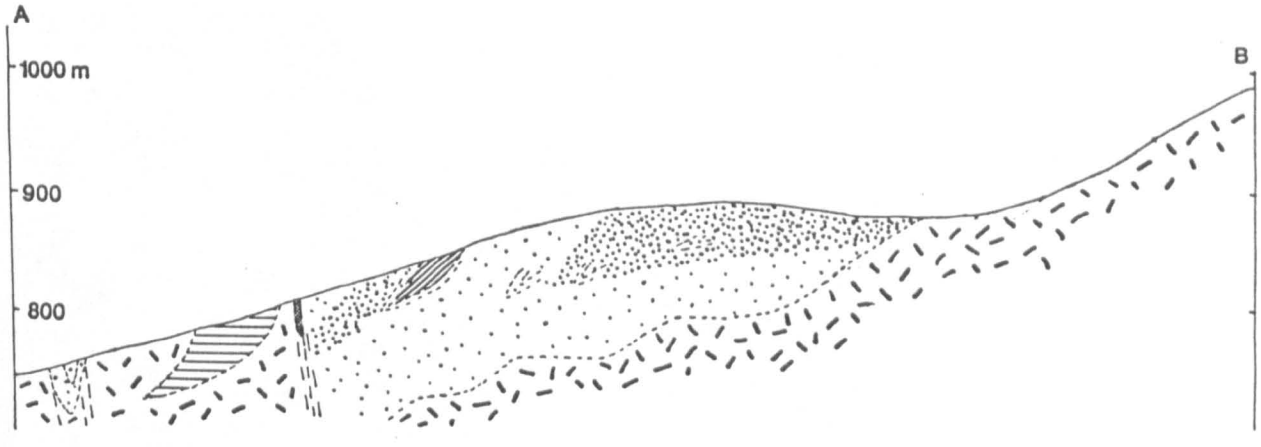

MAP 2 VILA VERDE 1:10 000

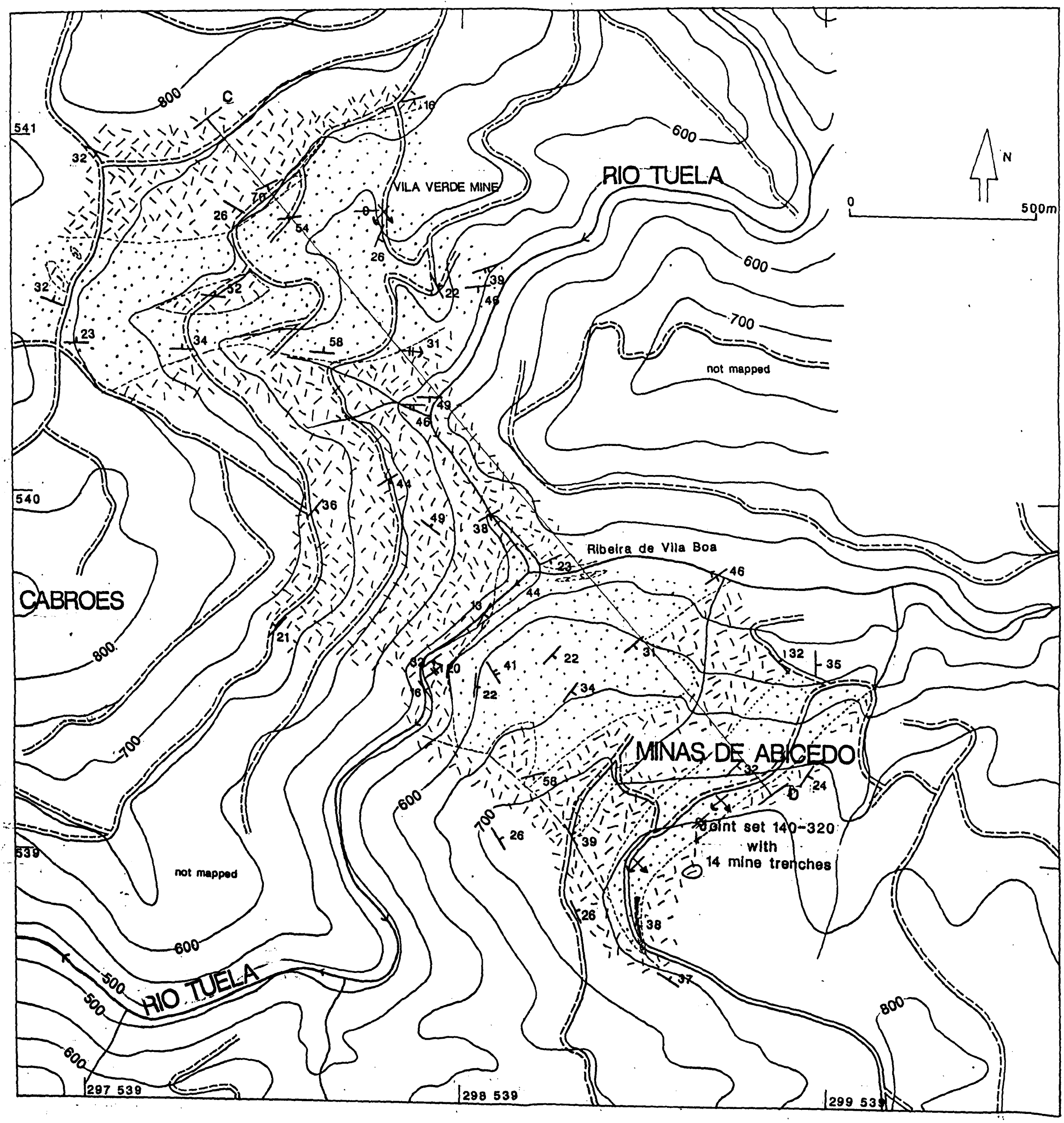

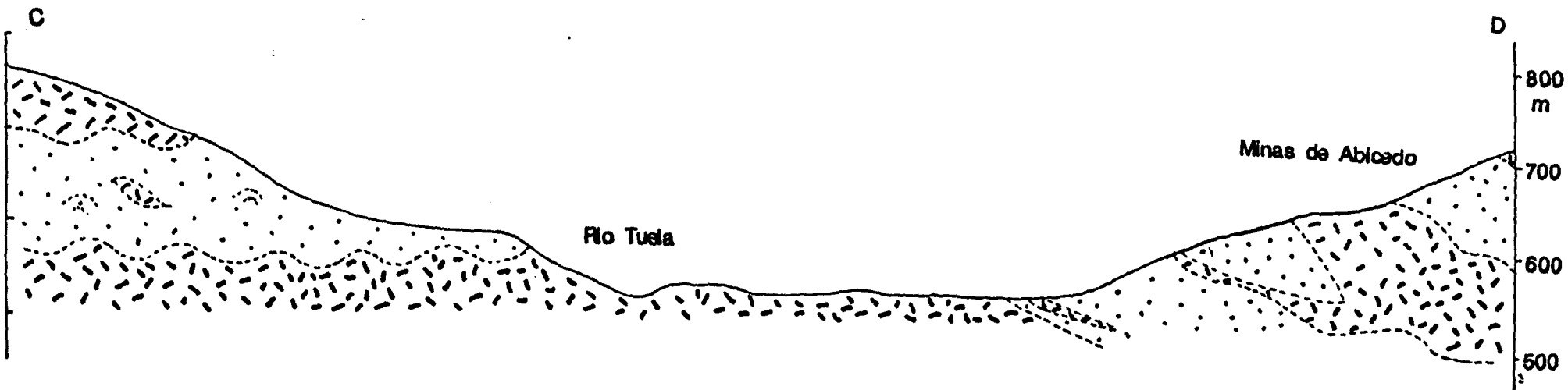

MAP 3 VINHAS (Morais massif) 1:10 000

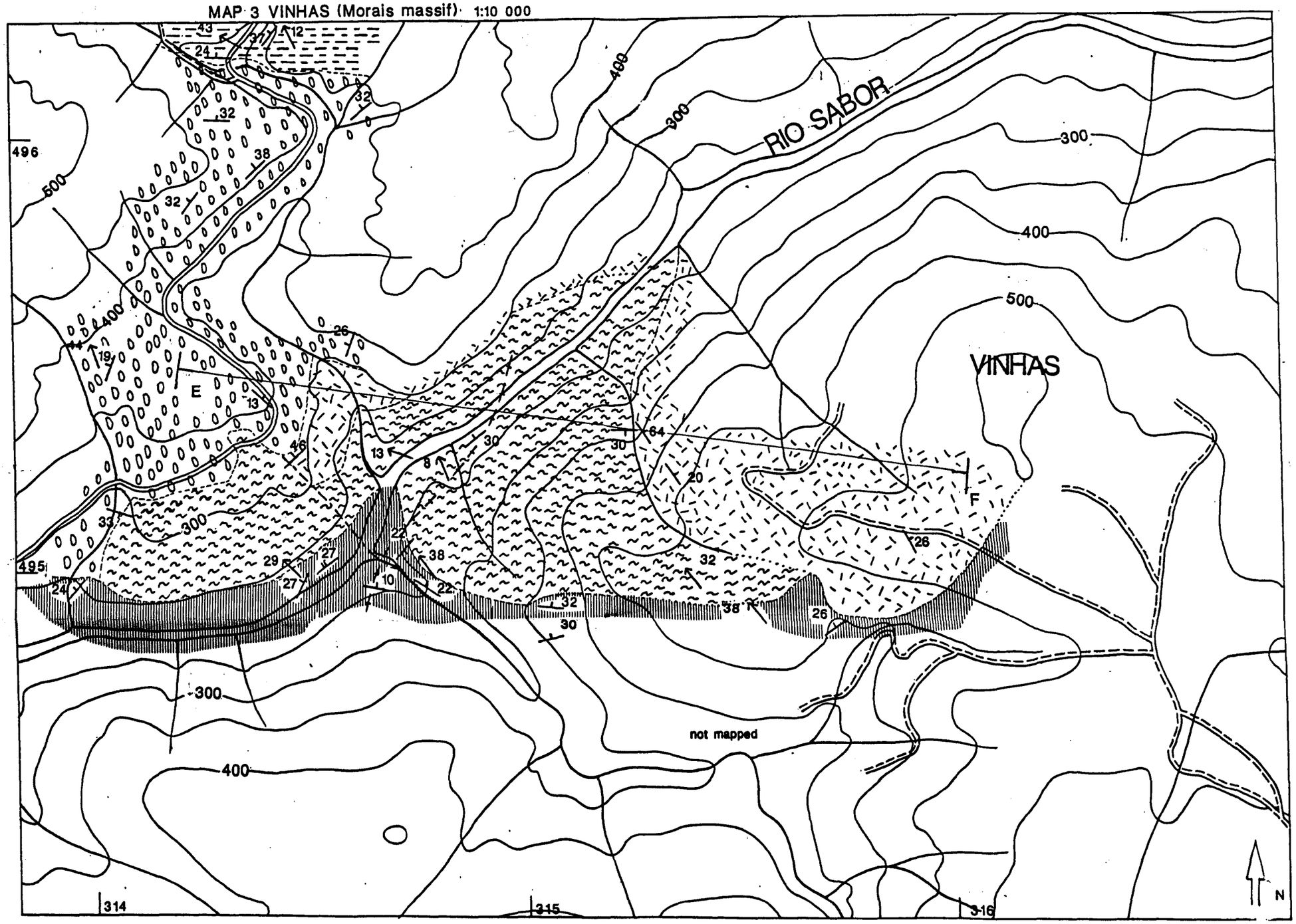

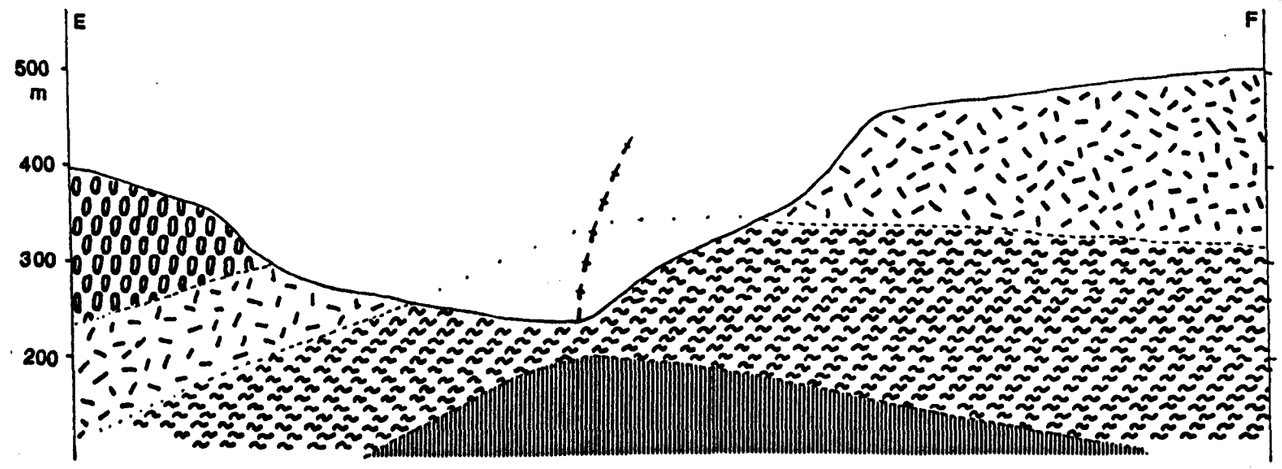

Map 4 The Bragança Ultrabasic Outline